Mathematical Modeling of Solid Oxide Fuel Cells

PhD dissertation submitted to
PhD School in Engineering "Leonardo da Vinci"
University of Pisa

Program in Chemical Engineering
(SSD: ING-IND/25)

presented by
Antonio Bertei

accepted on the recommendation of
Prof. Cristiano Nicolella

Pisa, 2013

Summary

Solid oxide fuel cells (SOFCs) are power units operating at 600–1000°C which produce electricity through the electrochemical conversion of the chemical energy of a fuel, thus providing a clean and efficient alternative for energy production in the near future. Although nowadays the first commercialization of residential and portable power units has just started, the optimization of this technology for bigger power system installations remains challenging. Indeed, SOFCs are complex systems, showing nonlinear interactions and strong coupling among phenomena occurring at different length scales. Therefore, modeling tools and simulation techniques offer a valid contribution to gain a deep understanding of the elementary processes in order to support the research in this field.

In this thesis, an integrated microstructural–electrochemical modeling framework for SOFCs is presented. At the microscale, the model numerically reconstructs the microstructure of the electrodes, which are random porous composite media wherein the electrochemical reactions occur. The effective properties of the electrodes are evaluated in the reconstructed microstructures and used, as input parameters, in physically–based electrochemical models, consisting of mass and charge balances written in continuum approach, which describe the transport and reaction phenomena at the mesoscale within the cell. Therefore, the strong coupling between microstructural characteristics and electrochemical processes can be conveniently taken into account by the integrated model.

The presented modeling framework represents a tool to fulfill a *from–powder–to–power* approach: it is able to reproduce and predict the SOFC macroscopic response, such as the current–voltage relationship, knowing only the powder characteristics and the operating conditions, which are the same measurable and controllable parameters available in reality. As a consequence, empirical, fitted or adjustable parameters are not required, feature which makes the model fully predictive and widely applicable in a broad range of conditions and fuel cell configurations as an interpretative tool of experimental data and as a design tool to optimize the system performance.

In this thesis several particle–based microstructural models are presented, covering all the main morphological features and electrode architectures adopted in SOFC technology (e.g., conventional composite electrodes, infiltrated electrodes, arbitrary particle shapes and agglomerates). Electrochemical models for the description of electrodes (button cell configuration) and cells (within a stack) are discussed. These models are applied for both conventional conducting materials, typically adopted in SOFC technology, and for innovative fuel cell configurations.

Each model is satisfactorily validated at the corresponding scale, then the whole framework is tested for the microstructural–electrochemical simulation of short stacks, showing an excellent agreement with experimental data. The application of the integrated model confirms that there is a strong coupling between electrode microstructure and cell electrochemical behavior: only by taking into account this interaction a model can provide quantitative information and sound predictions.

Concluding, this thesis provides an approach to fill the gap between the microstructural and the electrochemical modeling, offering a predictive tool which does not rely on empirical and adjustable parameters, capable to reproduce the macroscopic electrochemical behavior of an SOFC unit starting from the powder characteristics.

Preface

Solid oxide fuel cells offer a great opportunity for a young scientist who is interested in applied research: it is fast–growing topic, which requires a multi–disciplinary expertise and a multi–scale approach, involving a lot of excellent researchers worldwide in academia and industrial companies who are willing to disseminate their knowledge and findings. Especially if one wishes to model such a complex and intriguing system, he/she must know the fundamentals of a wide variety of physical and chemical phenomena while being aware of all the technological issues and market requirements. In a few words, solid oxide fuel cells represent a challenging test to improve the knowledge and apply all the skills that a good researcher should have.

Apart from being an interesting and fascinating topic, solid oxide fuel cells can represent one of the possible alternatives for a clean and sustainable energy production in the near future. Therefore, for me, it is a pleasure giving my contribution to help the research community in making solid oxide fuel cells available on the market as soon as possible. The enthusiasm that I have shown during these years is the same one that I noted in a lot of professors, researchers and students that I have met throughout the world.

Many people have contributed to the present thesis, directly and indirectly. First and foremost, I would like to express my gratitude to my supervisor Prof. Cristiano Nicolella for his support and confidence in me. He strongly encouraged me to continue my studies, supporting me in several ways. During these years, he actively participated in my modeling activities and gave me the possibility to gain further experience and to present my results in various conferences throughout the world.

Dr. Enzo Tricoli (University of Pisa) is gratefully acknowledged for being co–examiner of this thesis and for his periodic advices.

Special thanks to Dr. Jon G. Pharoah (Fuel Cell Research Centre of Kingston – Canada) for hosting me in his lab and sharing his knowledge and codes in a fruitful collaboration still active at the present. I am also really grateful especially to two collaborators of his team, Dr. Hae-Won Choi and Duncan A.W. Gawel. Heartfelt thanks to Dr. Chih-Che Chueh, who guided me in the topic of programming and worked very hard with me in these last three years.

I wish to express my gratitude to the staff who worked to provide high quality experimental results: Dr. Antonio Barbucci and Dr. M. Paola Carpanese (University of Genova), Dr. Massimo Viviani (National Research Council of Italy – IENI), Dr. Alessandra Sanson and Dr. Elisa Mercadelli (National Research Council of Italy – ISTEC).

Special thanks to Benedetta Nucci, for her dedication in assisting me in simulations and for nice chats.

I am really grateful to Prof. Wolfgang G. Bessler (Offenburg University of Applied Sciences) for inspiring this thesis with his physically–based approach to SOFC modeling.

Last but not least, I wish to thank all the colleagues at the Department of Civil and Industrial Engineering (University of Pisa), all my friends, my girlfriend and my family, who contributed to provide a peaceful environment during the last three years.

Antonio Bertei

Pisa, December 2013

Table of Contents

Chapter 1

Introduction

This Chapter represents the general introduction of the thesis, aimed to present the main features of solid oxide fuel cells and related modeling activities. The objective and structure of the thesis are described, focusing on the relationships among different chapters.

The main highlights discussed in this chapter are:

i. solid oxide fuel cells represent one of the possible alternatives to produce clean and sustainable energy in the future, despite to date this technology requires deeper understanding and further optimization;

ii. different phenomena occur in solid oxide fuel cells at different length scales, which can be modeled by using different approaches in order to guide research towards an optimal design;

iii. a multi–scale approach, integrating the different modeling tools at each scale level, practically is still lacking: this thesis aims to integrate the microstructural modeling into the cell–level model, in order to build a framework *from–powder–to–power* which does not require any empirical, fitted or adjustable parameter.

1.1 Solid oxide fuel cells

Fuel cells are electrochemical devices which convert the chemical energy of a fuel directly into electric energy [1,2], as schematically represented in Figure 1.1. The fuel and the oxidizer are kept separated in different compartments: the oxidation and reduction reactions proceed separately, charges flow through the system closing the circuit while feeding an external load. The electrochemical conversion is not limited by thermodynamic constraints (i.e., the Carnot cycle) as in heat engines, with clear benefits in terms of efficiency. In addition, since the combustion is avoided, the formation of pollutants is minimal, allowing an environmentally–friendly production of electric energy. Fuel cells allow for stationary operation since, unlike batteries, fuel and oxidizer can be continuously supplied.

When the fuel cell is fed with fuel and oxidizer, an electric potential difference *V* spontaneously arises at its terminals. This voltage is the driving force to produce dc current *I* and thus electric power for an external load. The basic elements of a typical fuel cell are the electrodes, namely the cathode and the anode, and the electrolyte. The cathode represents the positive electrode, wherein the oxidizer, typically oxygen, is reduced. The anode is the negative electrode, wherein the fuel is oxidized. The electrons produced at the anode flow in the external circuit, providing electric power. The electrolyte is insulating to electrons, it transfers charges within the cell through the transport of ions.

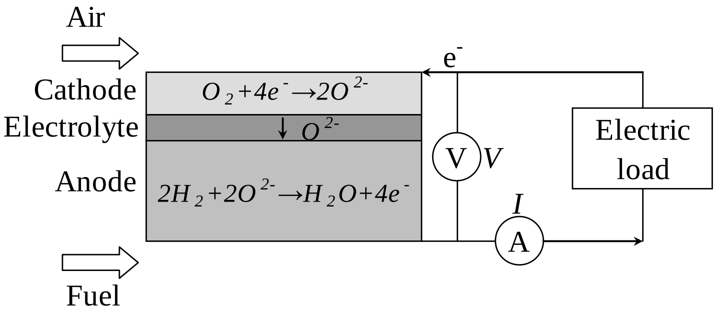

Figure 1.1 – Schematic representation of a solid oxide fuel cell fueled with hydrogen.

There exist different types of fuel cells, classified on the basis of the nature of the electrolyte material, which also determines the operating temperature and thus the state of reactants and products: alkaline fuel cells (AFC, 50–200°C), proton exchange membrane fuel cells (PEMFC, 30–100°C), direct methanol fuel cells (DMFC, 20–90°C), phosphoric acid fuel cells (PAFC, ~200°C), molten carbonate fuel cells (MCFC, ~200°C) and solid oxide fuel cells (SOFC, 600–1000°C) [1]. In this thesis only solid oxide fuel cells are considered, whose global electrochemistry is reported in Figure 1.1 for the case of hydrogen as a fuel.

Solid oxide fuel cells are characterized by a solid electrolyte, which transports oxygen ions from the cathode to the anode [3]. The transport in solid state limits the operating temperature in the range 600–1000°C, wherein the resistance to ionic transport is acceptably low. In such a temperature range, reactants and products are gaseous. In particular, gaseous water and carbon dioxide are produced at the anode when hydrogen–based (e.g., pure hydrogen, as in Figure 1.1) or carbon–based (e.g., carbon monoxide or hydrocarbons) fuels are used.

Despite the drawbacks connected to the high–temperature operation, SOFCs offer several advantages if compared with other types of fuel cells in terms of fuel flexibility, efficiency and adaptability. SOFCs can run with different fuels, such as hydrogen, carbon monoxide, methane and other hydrocarbons, also accommodating the possibility of internal reforming directly within the anode [3,4]. In addition, unconverted reactants can be feed to gas turbines: the hybrid SOFC–gas turbine system can reach efficiencies in the order of 60–70% [3–5]. The fuel flexibility makes this technology attractive in the next years for the transition between fossil and renewable fuels.

As anticipated above, SOFCs produce very low emissions of pollutants such as NO_x and SO_x because the combustion is avoided [3,4], which is an additional positive feature in comparison with heat engines. Then, since there are no moving parts, SOFCs also allow for silent, vibration–free operation [4,6], which also guarantees low maintenance costs. The modularity is another positive feature: big power plants, in the order of hundreds of megawatts [7], can be obtained by assembling small units [3], whose size can be even very small for miniaturized and portable applications [8,9].

Due to their inherent flexibility, nowadays SOFCs have been proposed for a broad range of applications. The U.S. Department of Energy has the objective of developing power system installations in the order of 100MW based on SOFC technology, fueled by syngas produced from coal gasification and accommodating the CO_2 capture [7]. Industrial teams, such as FuelCell Energy (formerly Versa Power Systems) and Bloom Energy, have demonstrated that SOFC systems for distributed power generation applications in the range 50–100kW can be manufactured and run with satisfactory efficiency [10]. Commercialization of combined heat and power systems for residential applications (~1kW–class units) started in Japan in 2011 under the framework of the NEDO project [11,12]. On the other hand, in North America Delphi has been developing and demonstrating SOFC–based auxiliary power units (3–5kW) for trucks and other vehicles [13]. Finally, micro–SOFCs (i.e., sub–kW class) are now used in military [8] and even portable applications, such as the nectar^{TM} mobile charging power system produced by Lilliputian Systems.

However, despite important achievements and although some SOFC systems are commercially available, to date the breakthrough of SOFC technology still faces significant challenges concerning cost reduction, long–term stability and performance improvement. SOFCs are complex systems, involving phenomena occurring at different length scales [14]. One of the major obstacles to further significant progress is the current poor understanding of the fundamental physical and electrochemical processes and how they influence each other [15]. An improved understanding, required to assist experimental interpretation and aid engineering of SOFCs, can be reached by using physically–based models, which are discussed in the following Section.

1.2 Multi–scale approach for SOFCs

SOFCs represent an outstanding example of multi–scale complex system: electrochemical reactions take place on particle surfaces on a nanometric scale while the whole SOFC unit, composed by several cells arranged in stacks, is usually integrated in power generation systems whose size is in the order of meters. What makes SOFCs a multi–scale system is the strong (often nonlinear) coupling among all the phenomena occurring at different length scales: processes taking place at the microscale can dominantly influence the macroscopic behavior [15]. As an example, the microstructural characteristics of the porous electrodes, such as the porosity and the particle size of conducting materials, influence the rate at which gaseous and charged species are transported and react at the microscale, producing significant macroscopic effects on the performance at the cell and system levels.

A schematic representation of the multiple length and time scales involved in an SOFC is reported in Figure 1.2.

At system level, the SOFC represents the power unit of the fuel cell system. In big stationary applications, the SOFC unit is connected with the so–called balance–of–plant, which consists of heat exchangers, blowers, fuel processors (e.g., a reformer, a desulfurization unit), exhaust gas treatment, ac/dc converter, electronic controls, etc. [1,16]. Thermal management [17], process control [18,19] and making the fuel cell system flexible to an unsteady power demand are some of the issues to be addressed at this level.

The stack consists of the assembly of multiple cells, along with interconnectors and gas manifolds for current and gas distribution. The main concerns at this level are ensuring a homogenous distribution of reactants to the cells through a proper manifold design in order to maximize the electrical output [20] and an even temperature distribution along the cells to minimize thermal stresses [21].

The cell level represents a single membrane–electrode assembly, that is, anode, cathode and electrolyte, including gas supply. At this scale, transport of reactants and electrochemistry within the electrodes govern the voltage and current produced, that is, the power generated by the cell [15]. The understanding of the interplay among cell geometry, operating conditions and physical–chemical processes is one of the most demanding tasks, where further improvements are still possible [22].

The electrode level is again ruled by transport and reaction phenomena, similarly to the cell level, but on a smaller scale [15]. These phenomena are strongly coupled to the microstructural characteristics of the electrode. Porosity, particle size, volume fractions of the conducting materials influence the effective transport properties of chemical and charged species as well as the density of reaction sites, therefore affecting the current and gas distribution. Experimental and theoretical studies have demonstrated that the electrode design has the major influence on the macroscopic system performance [23–26]. Therefore, the characterization and engineering of the electrode microstructure is nowadays one of the most intriguing activities in SOFC research [27].

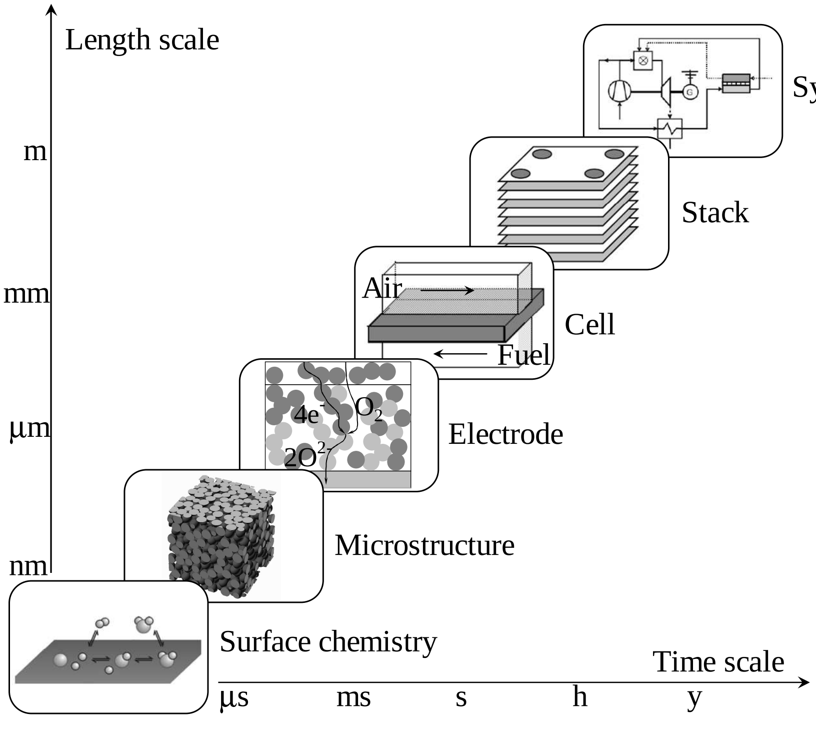

Figure 1.2 – Time and length scales involved in SOFCs (adapted from [15]).

Finally, chemical and electrochemical reactions take place on active particle surfaces and particle interfaces within the electrodes. As an example, the oxygen reduction reaction in a porous composite cathode occurs in the proximity of the contact perimeter between electron–conducting and ion–conducting particles exposed to the gas phase (see Section 2.1 in Chapter 2 for a comprehensive description). The main questions arising at this level concern the elementary kinetic chemistry, which means the identification of reaction mechanisms, intermediate species and rate–determining steps [15,28–30].

As anticipated at the end of Section 1.1, the mechanistic description of all the processes occurring in a cell and the understanding of their interplay is necessary for further improvement of this technology. In the last years, physically–based models and simulation techniques have been used to assist the SOFC development [14,31,32]. In particular, different modeling tools have been applied to fulfill the needs of each specific scale level.

At the most fundamental scales, *ab initio* methods, such as density functional theory (DFT) [33–35], have recently been applied to examine the quantum structure of atoms and their interactions. These types of models allow the simulation of the physics at the atomic scale, providing information useful to corroborate the soundness of detailed reaction mechanisms, such as the activation energies of elementary reactions or the chemical stability of reaction intermediates [36]. However, most of the kinetic parameters involved in the reaction schemes proposed to date have been obtained through the best fitting of the electrochemical response of patterned electrodes under different operating conditions [15,28–30,37,38].

The microstructural characteristics of porous electrodes have been analyzed at different degrees of sophistication with different modeling approaches, which aim to estimate the effective properties of porous electrodes on the basis of powder characteristics. Percolation theory has been adopted to estimate effective properties through the prediction of the number of contacts among the particles by using algebraic equations [39,40]. More accurate information can be obtained with detailed microstructural models such as particle–based numerical algorithms [41–44] and tomographic techniques [45–48]. While particle–based algorithms aim to numerically generate a virtual structure of the electrode by mimicking the packing process, techniques like focused ion beam (FIB) and X–ray tomography reconstruct the three–dimensional microstructure by scanning real samples.

While equivalent circuits are still used for a rapid interpretation of experimental data [49,50], nowadays physically–based models are employed to describe transport and reaction phenomena at both electrode and cell levels [22,51–56]. These models are based on balance equations, incorporating the electrochemistry of the reactions and the description of transport phenomena through the application of constitutive equations, such as the Ohm's law for charge transport, the Fick law for gas diffusion or more advanced models (e.g., Maxwell–Stefan gas transport theory [57], dusty–gas model [58], etc.). Electrode and cell–level models aim to predict the current–voltage relationship of the SOFC (i.e., *V–I* in Figure 1.1), usually providing also the spatial and temporal distribution of field variables (e.g., concentration, pressure, electric potential).

At the stack level the gas and temperature distributions are obtained by solving mass, heat and momentum conservation equations through computational fluid dynamics (CFD) codes [20,59,60]. This information is used to design manifolds and to modify the cell arrangement in order to minimize thermal stresses and optimize the distribution of reactants. Finally, system modeling is assisted by process simulations by using available commercial software in order to estimate the global electric and thermal efficiency of the whole fuel cell power system [5,61].

Despite the efforts made in developing specific modeling tools, to date a fully multi–scale framework integrating different models at different length scales is still lacking, although different authors have recognized this need [14,31,32]. Bessler and coworkers [15,62,63] have been one of the first research groups who are trying to fill this gap, although a lot of work is still necessary to reach this goal. This thesis shares the same aim and approach, as discussed in the following Section.

1.3 Aim and objective of this thesis

This aim of this thesis is the development and refinement of specific physically–based modeling tools and their coupling in order to provide an integrated framework able to describe the interplay of phenomena occurring at different length scales in SOFCs. More specifically, the study focuses on the integration of detailed microstructural models into electrode and cell–level models. Effective properties are estimated in electrode microstructures numerically reconstructed with particle–based packing algorithms and then used, as input parameters, into electrode and cell–level models based on mass and charge balances. Surface chemistry is not addressed in this thesis: where available, specific global kinetic expressions are taken from the literature.

As anticipated in Section 1.2, the microstructural characteristics of the electrodes play a major role in determining the global energetic performance of an SOFC: the cell electrochemical behavior is strongly dependent of porosity, particle size, volume fraction of conducting materials, as supported by a large number experimental evidences [23,26,64,65]. Modeling the interplay between electrode morphology and cell electrochemical behavior is crucial and represents an outstanding benefit in assisting SOFC development [14,27,31,32], especially considering that the microstructure of porous electrode is normally not included in cell–level models [32].

The integration of a detailed microstructural characterization into cell–level modeling allows a significant reduction of free parameters. Typically in macroscale models, effective properties such as gas phase tortuosity or effective conductivity are estimated using empirical correlations if not treated as fitting parameters to force simulation results to match experimental data [32]. In this way, the cell model will hardly provide realistic results when used to simulate conditions different from the data set on which its parameters have been tailored.

On the other hand, the integrated framework allows the development of a *from–powder–to–power* approach: given the material properties (e.g., the electric bulk conductivity of the materials), only the electrode porosity and the powder characteristics (i.e., the particle size and the solid volume fraction of the conducting phases), along with the operating conditions and cell geometry, are required to predict the global electrochemical response of the cell, as depicted in Figure 1.3.

With this approach, all the input parameters required by the integrated model are the same starting measurable and controllable variables used in reality when manufacturing or running an SOFC. In this way, the need for fitted, adjusted or empirical parameters is avoided, making the model extremely general and applicable to a wide variety of SOFC systems.

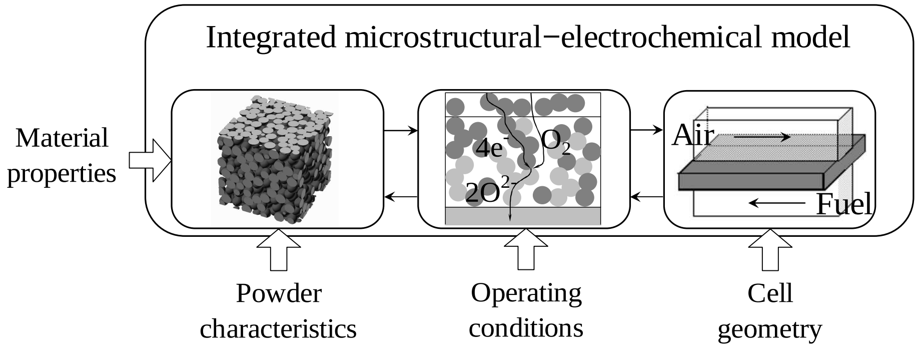

Figure 1.3 – Schematic representation of the integrated microstructural–electrochemical modeling approach with the required input parameters.

The integrated modeling approach is able to quantitatively describe how morphological modifications (e.g., reduction of particle size, increase in porosity) affect the cell electrochemical response (arrows from left to right in Figure 1.3). This feature is particularly amenable for electrode design, and an example is reported in Chapter 7.

In addition, the model can be used as interpretative tool of experimental data: the analysis of the macroscopic electrochemical behavior of the cell with the model allows a physical interpretation of specific features, whose cause can be attributed, with a reasonable confidence, to one or more phenomena occurring at microscopic scales (arrows from right to left in Figure 1.3), as discussed in Chapter 8.

Specific details on how the modeling framework is developed in this thesis are summarized in the next Section.

1.4 Structure of the thesis

The thesis is organized in three parts as follows:

i. electrochemical modeling (Chaps. 2 and 3): the models describing physical and chemical phenomena, such as the gas transport within the pores of the electrodes, the charge transport and the electrochemical kinetics are presented in Chapters 2 and 3. In both the chapters, the modeling is performed at the electrode level by applying conservation equations for mass and charge. Chapter 2 focuses on conventional electrodes and in particular on the composite cathode, consisting of well–characterized materials typically used in SOFCs. Chapter 3 describes the chemistry of a complex unconventional SOFC system, whose materials have not extensively studied to date, and which shows particular characteristics. In both the studies the effective properties of the porous media are estimated by using percolation models [40,66], whose validity and limits are further addressed in Chapter 4. It is worth noting that even the use of simple percolation models highlights the need of a detailed microstructural modeling in order to correctly describe the electrode electrochemical behavior;

ii. microstructural modeling (Chaps. 4–6): the description of the particle–based microstructural models used to numerically reconstruct the electrode microstructure is reported in this part. Packing algorithms used to reproduce random packings of spherical particles (Chapter 4), nonspherical particles (Chapter 5) and infiltrated electrodes (Chapter 6) are discussed. This set of algorithms is sufficiently general to reproduce all the main electrode morphologies currently adopted for SOFC applications;

iii. coupling between microstructural and electrochemical modeling (Chaps. 7 and 8): electrode (Chapter 7) and cell–level (Chapter 8) models benefit from the effective properties evaluated through the microstructural models. Chapter 7 shows an application at the electrode level, focusing on how the proposed integrated approach can be used to engineer the design of conventional composite cathodes. In Chapter 8 the same approach is used at the cell level, mainly focusing on the interpretation of the cell electrochemical response and on the effect of operating conditions on system efficiency. In addition, in this part the modeling framework is satisfactorily validated with specific data at both microstructural and cell levels.

Each chapter is organized to contain all the necessary information in order to be read as a standalone study. A short summary at the beginning of each chapter is provided to put in evidence the main results of the study in the context of the integrated framework discussed in this thesis. The general conclusions of the thesis are summarized in Chapter 9.

1.5 Summary of models developed

In order to reach the goal of the integrated modeling, during the preparation of this thesis several modeling tools and algorithms have been adapted and developed. Their list is summarized in Table 1.1, which is organized in order to distinguish the different length scales, purposes and chapters wherein the models are discussed.

Table 1.1 – List of models and algorithms discussed in this thesis.

Model (Platform)	*Purpose*	*Chapter*
Microstructure (C++)		
drop–and–roll algorithm	electrode reconstruction (spherical particles)	4, 7, 8
CR algorithm	electrode reconstruction (nonspherical particles)	5
infiltration algorithm	infiltrated electrode reconstruction	6
RW method	effective properties of reconstructed electrodes	7, 8
Electrode (Comsol)		
conv. electrode model	current–voltage characteristics	2, 7
unconv. SOFC model	current–voltage characteristics	3
Cell (Comsol)		
cell model	current–voltage characteristics	8

All the microstructural models have been developed in C++ program language.

The drop–and–roll algorithm numerically reconstructs the three–dimensional structure of porous electrodes assuming that particles are spherical. The original version of the code was provided by Dr. Jon G. Pharoah (Fuel Cell Research Centre of Kingston – Canada) [41]. In this thesis the algorithm has been adapted to simulate polydisperse phases and to take into account sintering phenomena (i.e., particle overlap) and the control of porosity with pore–formers, which are characteristic features of porous SOFC electrodes. The general structure of the algorithm is presented in Chapter 4, wherein its broad capabilities if compared with percolation theory are highlighted, and then applied in Chapters 7 and 8 for specific SOFC applications.

The collective rearrangement (CR) algorithm allows the three–dimensional numerical reconstruction of porous media by simulating particles of arbitrary shape and agglomerates. It is more general than the drop–and–roll algorithm since it does not rely on the assumption that particles are spherical. Therefore, it is able to accommodate specific morphological features of SOFC electrodes, such as particle agglomeration and the distortion of the particle shape from spherical to the ellipsoidal one as it may happen when adopting plasma spray techniques in the electrode manufacturing. The code was written in collaboration with Dr. Chih-Che Chueh (Fuel Cell Research Centre of Kingston – Canada) and it is presented in Chapter 5.

The infiltration algorithm is a packing algorithm specifically tailored for the numerical reconstruction of infiltrated electrodes. These electrodes, recently proposed for intermediate temperature SOFCs, are fabricated via an impregnation route in order to produce a nanostructured microstructure [67]. The algorithm mimics the deposition of nanoparticles onto the surface of micrometric particles proving a virtual three–dimensional structure of infiltrated electrodes. The study is summarized in Chapter 6.

The Monte Carlo random–walk (RW) method has been developed in order to calculate the effective properties of the electrodes reconstructed with the aforementioned packing algorithms. Effective transport properties, such as the effective electric conductivity and the gas phase tortuosity factor, are calculated by simulating the Brownian motion of tracers within the reconstructed microstructure. Other properties, such as the pore size distribution or the contact perimeter among different particles (that is, the so–called three–phase boundary length) are evaluated through geometric analysis. The method is presented in Chapter 7 and further applied in Chapter 8.

The electrode–level models have been implemented in Comsol Multiphysics [68], which is a commercial solver of systems of partial differential equations. Model solution provides the distribution of field variables which, in turn, are used to evaluate the current–voltage relationship.

The model for conventional electrodes consists of mass and charge balances written according to the continuum approach and applied along the thickness of the electrode, thus resulting in a 1D model. The model focuses on porous composite cathodes prepared with conventional conducting materials, taking into account the physical and chemical phenomena occurring at the micro and mesoscales. It is presented in Chapter 2 and also used in Chapter 7, wherein it is coupled with a detailed microstructural modeling.

A similar physically–based model is presented in Chapter 3, although it deals with the more complex chemistry involved in an unconventional SOFC showing mixed protonic–anionic conduction. Still based on mass and charge balances, the model takes into account some interesting chemical processes specific for the materials used in such a fuel cell, as the incorporation of gaseous water into the proton–conducting material, phenomenon which affects the electric conductivity.

The cell model extends the physically–based approach employed for electrodes to the higher level. The model describes the electrochemistry and the transport of mass and charge in the whole cell, including gas supply in the feeding channels. Unlike electrode models, which describe a button cell configuration, the cell model represents a single SOFC unit within a stack, resulting in a two–dimensional model along the thickness and the length of the cell. It is presented and applied in Chapter 8 to describe a well–known SOFC benchmark, taking advantage of a detailed microstructural representation.

Each model in Table 1.1 can be used standalone, even for broader applications than SOFCs: for example, the microstructural models could be used to represent granular porous media. However, the best benefits are reached when the models are integrated together, as already discussed in Section 1.3.

References

[1] J. Larminie, A. Dicks, Fuel Cell Systems Explained, Wiley, New York, 2003.

[2] S.C. Singhal, K. Kendall, High temperature solid oxide fuel cells: fundamentals, design and applications, Elsevier, Oxford, 2003.

[3] S.C. Singhal, Advances in solid oxide fuel cell technology, Solid State Ionics. 135 (2000) 305–313.

[4] R.J. Kee, H. Zhu, D.G. Goodwin, Solid-oxide fuel cells with hydrocarbon fuels, Proc. Combust. Inst. 30 (2005) 2379–2404.

[5] J. Palsson, A. Selimovic, L. Sjunnesson, Combined solid oxide fuel cell and gas turbine systems for efficient power and heat generation, J. Power Sources. 86 (2000) 442–448.

[6] S.C. Singhal, Solid oxide fuel cells for stationary, mobile, and military applications, Solid State Ionics. 152 (2002) 405–410.

[7] S.D. Vora, SECA program overview and status, ECS Trans. 57 (2013) 11–19.

[8] M. Kendall, A.D. Meadowcroft, K. Kendall, Microtubolar solid oxide fuel cells (mSOFCs), ECS Trans. 57 (2013) 123–131.

[9] H. Sumi, T. Yamaguchi, K. Hamamoto, T. Suzuki, Y. Fujishiro, Development of microtubular SOFCs for portable power sources, ECS Trans. 57 (2013) 133–140.

[10] B. Borglum, H. Ghezel-Ayagh, Development of solid oxide fuel cells at Versa Power Systems and FuelCell Energy, ECS Trans. 57 (2013) 61–66.

[11] K. Horiuchi, Current status of national SOFC projects in Japan, ECS Trans. 57 (2013) 3–10.

[12] A. Nanjou, Commercialization of SOFC micro-CHP in the Japanese market, in: F. Lefebvre-Joud (Ed.), 10th Eur. SOFC Forum, Lucerne - Switzerland, 2012: p. A0208.

[13] K. Haltiner, R. Kerr, Latest update on Delphi’s solid oxide fuel cell stack for transportation and stationary applications, in: F. Lefebvre-Joud (Ed.), 10th Eur. SOFC Forum, Lucerne - Switzerland, 2012.

[14] K.N. Grew, W.K.S. Chiu, A review of modeling and simulation techniques across the length scales for the solid oxide fuel cell, J. Power Sources. 199 (2012) 1–13.

[15] W.G. Bessler, Electrochemistry and transport in solid oxide fuel cells, Heidelberg University, Germany, 2007.

[16] D.J.L. Brett, A. Atkinson, N.P. Brandon, S.J. Skinner, Intermediate temperature solid oxide fuel cells, Chem. Soc. Rev. 37 (2008) 1568–1578.

[17] A. Faghri, Z. Guo, Challenges and opportunities of thermal management issues related to fuel cell technology and modeling, Int. J. Heat Mass Transf. 48 (2005) 3891–3920.

[18] B.M. Sanandaji, T.L. Vincent, A.M. Colclasure, R.J. Kee, Modeling and control of tubular solid-oxide fuel cell systems: II. Nonlinear model reduction and model predictive control, J. Power Sources. 196 (2011) 208–217.

[19] Y. Komatsu, S. Kimijima, J.S. Szmyd, Numerical analysis on dynamic behavior of a solid oxide fuel cell with a power output control scheme: study on fuel starvation under load-following operation, in: F. Lefebvre-Joud (Ed.), 10th Eur. SOFC Forum, Lucerne - Switzerland, 2012: pp. B10159–B10168.

[20] R.T. Nishida, S.B. Beale, J.G. Pharoah, Impact of manifolding on performance of a solid oxide fuel cell stack, ECS Trans. 57 (2013) 2495–2504.

[21] M. Peksen, A. Al-Masri, L. Blum, D. Stolten, 3D transient thermomechanical behaviour of a full scale SOFC short stack, Int. J. Hydrogen Energy. 38 (2013) 4099–4107.

[22] W.G. Bessler, S. Gewies, M. Vogler, A new framework for physically based modeling of solid oxide fuel cells, Electrochim. Acta. 53 (2007) 1782–1800.

[23] M. Juhl, S. Primdahl, C. Manon, M. Mogensen, Performance/structure correlation for composite SOFC cathodes, J. Power Sources. 61 (1996) 173–181.

[24] P.R. Shearing, Q. Cai, J.I. Golbert, V. Yufit, C.S. Adjiman, N.P. Brandon, Microstructural analysis of a solid oxide fuel cell anode using focused ion

beam techniques coupled with electrochemical simulation, J. Power Sources. 195 (2010) 4804–4810.

[25] M. Mogensen, S. Skaarup, Kinetic and geometric aspects of solid oxide fuel cell electrodes, Solid State Ionics. 86-88 (1996) 1151–1160.

[26] M.J. Jørgensen, S. Primdahl, C. Bagger, M. Mogensen, Effect of sintering temperature on microstructure and performance of LSM–YSZ composite cathodes, Solid State Ionics. 139 (2001) 1–11.

[27] P.R. Shearing, D.J.L. Brett, N.P. Brandon, Towards intelligent engineering of SOFC electrodes: a review of advanced microstructural characterisation techniques, Int. Mater. Rev. 55 (2010) 347–363.

[28] S.B. Adler, Factors governing oxygen reduction in solid oxide fuel cell cathodes., Chem. Rev. 104 (2004) 4791–4843.

[29] D.G. Goodwin, H. Zhu, A.M. Colclasure, R.J. Kee, Modeling electrochemical oxidation of hydrogen in Ni-YSZ pattern anodes, J. Electrochem. Soc. 156 (2009) B1004–B1021.

[30] M. Vogler, H. Störmer, D. Gerthsen, A. Utz, A. Weber, E. Ivers-Tiffée, et al., Electrochemistry and mechanism of hydrogen oxidation at Ni/YSZ patterned anodes, in: P. Connor (Ed.), 9th Eur. SOFC Forum, Lucerne - Switzerland, 2010: pp. 0994–09103.

[31] S.M.C. Ang, E.S. Fraga, N.P. Brandon, N.J. Samsatli, D.J.L. Brett, Fuel cell systems optimisation – Methods and strategies, Int. J. Hydrogen Energy. 36 (2011) 14678–14703.

[32] M. Andersson, J. Yuan, B. Sundén, Review on modeling development for multiscale chemical reactions coupled transport phenomena in solid oxide fuel cells, Appl. Energy. 87 (2010) 1461–1476.

[33] E.A. Carter, Challenges in modeling materials properties without experimental input, Science. 321 (2008) 800–803.

[34] M. Parkes, K. Refson, M. D’Avezac, G. Offer, N.P. Brandon, N. Harrison, Determining surface chemistry and vibrational properties of SOFC anode materials through ab initio calculations, ECS Trans. 57 (2013) 2419–2427.

[35] Y. Umeno, A.M. Iskandarov, A. Kubo, J.-M. Albina, Atomistic modeling and ab initio calculations of yttria-stabilized zirconia, ECS Trans. 57 (2013) 2791–2797.

[36] S. Liu, T. Ishimoto, H. Kohno, M. Koyama, First-principles calculations of the anodic oxidation reactions of solid oxide fuel cell: oxygen potential effect on nickel (111) surface, ECS Trans. 57 (2013) 2429–2436.

[37] R. Radhakrishnan, A. V. Virkar, S.C. Singhal, Estimation of charge-transfer resistivity of $La_{0.8}Sr_{0.2}MnO_3$ cathode on $Y_{0.16}Zr_{0.84}O_2$ electrolyte using patterned electrodes, J. Electrochem. Soc. 152 (2005) A210–A218.

[38] J. Mizusaki, H. Tagawa, T. Saito, K. Kamitani, T. Yamamura, K. Hirano, et al., Preparation of nickel pattern electrodes on YSZ and their electrochemical properties in H_2-H_2O atmospheres, J. Electrochem. Soc. 141 (1994) 2129–2134.

[39] D. Chen, Z. Lin, H. Zhu, R.J. Kee, Percolation theory to predict effective properties of solid oxide fuel-cell composite electrodes, J. Power Sources. 191 (2009) 240–252.

[40] A. Bertei, C. Nicolella, Percolation theory in SOFC composite electrodes: Effects of porosity and particle size distribution on effective properties, J. Power Sources. 196 (2011) 9429–9436.

[41] B. Kenney, M. Valdmanis, C. Baker, J.G. Pharoah, K. Karan, Computation of TPB length, surface area and pore size from numerical reconstruction of composite solid oxide fuel cell electrodes, J. Power Sources. 189 (2009) 1051–1059.

[42] Q. Cai, C.S. Adjiman, N.P. Brandon, Modelling the 3D microstructure and performance of solid oxide fuel cell electrodes: Computational parameters, Electrochim. Acta. 56 (2011) 5804–5814.

[43] J. Sanyal, G.M. Goldin, H. Zhu, R.J. Kee, A particle-based model for predicting the effective conductivities of composite electrodes, J. Power Sources. 195 (2010) 6671–6679.

[44] Y. Nishida, S. Itoh, A modeling study of porous composite microstructures for solid oxide fuel cell anodes, Electrochim. Acta. 56 (2011) 2792–2800.

[45] P.R. Shearing, J. Golbert, R.J. Chater, N.P. Brandon, 3D reconstruction of SOFC anodes using a focused ion beam lift-out technique, Chem. Eng. Sci. 64 (2009) 3928–3933.

[46] N.S.K. Gunda, H.-W. Choi, A. Berson, B. Kenney, K. Karan, J.G. Pharoah, et al., Focused ion beam-scanning electron microscopy on solid-oxide fuel-cell electrode: Image analysis and computing effective transport properties, J. Power Sources. 196 (2011) 3592–3603.

[47] H. Iwai, N. Shikazono, T. Matsui, H. Teshima, M. Kishimoto, Quantification of SOFC anode microstructure based on dual beam FIB-SEM technique, J. Power Sources. 195 (2010) 955–961.

[48] J. Joos, M. Ender, I. Rotscholl, N.H. Menzler, A. Weber, E. Ivers-Tiffée, Quantification of Ni/YSZ-anode microstructure parameters derived from FIB-tomography, in: F. Lefebvre-Joud (Ed.), 10th Eur. SOFC Forum, Lucerne - Switzerland, 2012: pp. B0578–B0589.

[49] D. Klotz, A. Weber, E. Ivers-Tiffée, Dynamic electrochemical model for SOFC-stacks, ECS Trans. 25 (2009) 1331–1340.

[50] A. Barbucci, M. Carpanese, A.P. Reverberi, G. Cerisola, M. Blanes, P.L. Cabot, et al., Influence of electrode thickness on the performance of composite electrodes for SOFC, J. Appl. Electrochem. 38 (2008) 939–945.

[51] P. Costamagna, P. Costa, V. Antonucci, Micro-modelling of solid oxide fuel cell electrodes, Electrochim. Acta. 43 (1998) 375–394.

[52] H. Zhu, R.J. Kee, Modeling distributed charge-transfer processes in SOFC membrane electrode assemblies, J. Electrochem. Soc. 155 (2008) B715–B729.

[53] V.M. Janardhanan, O. Deutschmann, Modeling diffusion limitation in solid-oxide fuel cells, Electrochim. Acta. 56 (2011) 9775–9782.

[54] T.X. Ho, P. Kosinski, A.C. Hoffmann, A. Vik, Modeling of transport, chemical and electrochemical phenomena in a cathode-supported SOFC, Chem. Eng. Sci. 64 (2009) 3000–3009.

[55] M. Andersson, H. Paradis, J. Yuan, B. Sundén, Three dimensional modeling of an solid oxide fuel cell coupling charge transfer phenomena with transport processes and heat generation, Electrochim. Acta. 109 (2013) 881–893.

[56] A. Pramuanjaroenkij, S. Kakaç, X. Yang Zhou, Mathematical analysis of planar solid oxide fuel cells, Int. J. Hydrogen Energy. 33 (2008) 2547–2565.

[57] R. Krishna, J.A. Wesselingh, The Maxwell-Stefan approach to mass transfer, Chem. Eng. Sci. 52 (1997) 861–911.

[58] E.A. Mason, A.P. Malinauskas, Gas transport in porous media: the dusty-gas model, Elsevier, Amsterdam, 1983.

[59] R.J. Kee, P. Korada, K. Walters, M. Pavol, A generalized model of the flow distribution in channel networks of planar fuel cells, J. Power Sources. 109 (2002) 148–159.

[60] M. Roos, E. Batawi, U. Harnisch, T. Hocker, Efficient simulation of fuel cell stacks with the volume averaging method, J. Power Sources. 118 (2003) 86–95.

[61] W.L. Becker, R.J. Braun, M. Penev, M. Melaina, Design and technoeconomic performance analysis of a 1MW solid oxide fuel cell polygeneration system for combined production of heat, hydrogen, and power, J. Power Sources. 200 (2012) 34–44.

[62] M.P. Eschenbach, R. Coulon, A.A. Franco, J. Kallo, W.G. Bessler, Multi-scale simulation of fuel cells: From the cell to the system, Solid State Ionics. 192 (2011) 615–618.

[63] W.G. Bessler, Multi-scale modelling of solid oxide fuel cells, in: M. Ni, T.S. Zhao (Eds.), Solid Oxide Fuel Cells From Mater. to Syst. Model., Royal Society of Chemistry, 2013: pp. 219–246.

[64] T. Tsai, S.A. Barnett, Effect of LSM-YSZ cathode on thin-electrolyte solid oxide fuel cell performance, Solid State Ionics. 93 (1997) 207–217.

[65] V.A.C. Haanappel, J. Mertens, D. Rutenbeck, C. Tropartz, W. Herzhof, D. Sebold, et al., Optimisation of processing and microstructural parameters of LSM cathodes to improve the electrochemical performance of anode-supported SOFCs, J. Power Sources. 141 (2005) 216–226.

[66] A. Bertei, C. Nicolella, A comparative study and an extended theory of percolation for random packings of rigid spheres, Powder Technol. 213 (2011) 100–108.

[67] Z. Jiang, C. Xia, F. Chen, Nano-structured composite cathodes for intermediate-temperature solid oxide fuel cells via an infiltration/impregnation technique, Electrochim. Acta. 55 (2010) 3595–3605.

[68] Comsol Inc., Comsol Multiphysics user’s guide, version 3.5, Burlington, MA, 2008.

Electrochemical Modeling

Chapter 2

Electrochemical Modeling of Conventional Electrodes

This Chapter presents a transient electrochemical model of transport and reaction applied for conventional composite electrodes. In particular, the study focuses on the LSM/YSZ cathode in comparison with experimental data. Effective properties are calculated using an extended percolation theory accounting for the linear distribution of porosity along the electrode thickness.

The study shows that:

i. the model is able to reproduce the experimental polarization behavior and impedance spectra in a wide range of temperatures and oxygen partial pressures;

ii. kinetic information regarding the oxygen reduction reaction can be obtained;

iii. even small variations of morphological characteristics can significantly affect the global electrochemical response.

This Chapter was adapted from the paper "Morphological and electrochemical modeling of SOFC composite cathodes with distributed porosity" by A. Bertei, A. Barbucci, M.P. Carpanese, M. Viviani and C. Nicolella, published in Chem. Eng. J. 207 (2012) 167–174, and the conference paper "Impedance simulation of SOFC LSM/YSZ cathodes with distributed porosity" presented at the 10th European SOFC Forum (Lucerne, 26–29 June 2012) by the same authors.

Abstract

A mathematical model of charge and mass transport and electrochemical reaction in porous composite cathodes for SOFC applications in transient conditions is presented. The model, based on local mass and charge balances, describes the domain as a continuum, characterizing kinetics as well as mass and charge transport using effective properties, related to cathode microstructure and material properties by percolation theory. The distribution of morphological properties along the electrode thickness, as experimentally observed on scanning electron microscope images of the samples investigated, is taken into account. This feature allows the model to reproduce the dependence of polarization resistance on electrode thickness and oxygen partial pressure in the range 600–850°C. It is found that for cathodes made of strontium–doped lanthanum manganite (LSM) and yttria–stabilized zirconia (YSZ), the exchange current, which represents the kinetic constant of the oxygen reduction reaction, follows an Arrhenius behavior with respect to the temperature and it is dependent on the square root of the oxygen partial pressure. Comparison with impedance spectra enables the evaluation of a specific capacitance which, however, does not show a clear dependence on temperature, suggesting that several phenomena may be gathered in such a specific parameter.

2.1 Introduction

Fuel cells are energy conversion devices in which the chemical energy of a fuel and a combustive agent (for example, hydrogen and air, respectively) is electrochemically transformed into electric energy. The electrochemical conversion avoids the use of a direct combustion process and of a Carnot thermodynamic cycle, thus reducing pollution levels in exhaust gases while increasing the energetic efficiency [1,2]. Solid oxide fuel cells (SOFCs), characterized by a solid electrolyte which transports oxygen ions at high temperature (usually higher than 600°C), have attracted research and technology interest due to the expected advantages if compared with other types of fuel cells, such as the broader fuel flexibility [3–5] and the high efficiency of energy conversion [6,7], which can be further increased by the possibility of co–generation with gas turbine power systems [8,9].

A single SOFC consists of two electrodes, namely the cathode and the anode, where the oxygen reduction and the fuel oxidation respectively occur, separated by a dense anion–conducting electrolyte, which is dedicated to the transport of oxygen ions from the cathode towards the anode. In hydrogen fed SOFCs, the cathode represents the main source of energy loss [10–12]. Porous composite cathodes, which consist of sintered random structures of electron–conducting (e.g., strontium–

doped lanthanum manganite, LSM) and ion–conducting particles (e.g., yttria–stabilized zirconia, YSZ), are often used in order to promote the oxygen reduction [13].

In a composite cathode, the molecular oxygen in gas phase reacts with electrons, transported by the electron–conducting phase, to form oxygen ions, which are transported by the ion–conducting particles towards the electrolyte. Therefore, the reaction occurs in the proximity of the contact perimeter between electron–conducting, ion–conducting and gas phase, where the reaction participants can coexist, which is called three–phase boundary (TPB) [10,14].

The rate at which the current is converted within the cathode, from the electronic form to the ionic form, depends not only on the catalytic activity of the materials and the extension of the reaction zone, but also on the relative facility at which charges and chemical species are transported to and from the reaction sites [15,16]. The effective transport properties of the composite structure, as well as the density of reacting sites, depend on the microstructural characteristics of the electrode, such as the particle diameter, the porosity and the composition [17]. Thus, the interplay of material, catalytic, geometric and microstructural characteristics determines the cathode efficiency [14,18], which is inversely proportional to its polarization resistance.

Electrochemical impedance spectroscopy analysis (EIS) is widely applied to distinguish the effects and the contributions of the multiple phenomena on the overall electrode performance [19]. However, in most cases the resulting impedance spectra are interpreted through equivalent electric circuits [20], which allow the identification of the elementary phenomena but without a direct link to the real phenomena and their physical description.

In this study, a mechanistic model, based on balance equations of the reaction participants, is developed and applied to porous composite LSM/YSZ cathodes in both steady–state and transient conditions. The conservation equations are applied to the domain modeled as a continuum phase (continuum approach) [15,21–26], characterized by effective transport and kinetic parameters (e.g., electric and ionic conductivity, gas permeability, TPB length per unit volume). The model accounts for a coherent description of the microstructure through the percolation theory [27], which is used to estimate the effective properties from the morphological cathode characteristics. As a new feature of the model herein presented, the variation of the porosity along the cathode thickness, as experimentally found on the electrodes investigated [28], is considered. The model represents the refinement of a previous work [29], in which the polarization behavior was interpreted without coherently relating the porosity distribution to the variation of morphological effective properties and, consequently, to the electrochemical performance (as, instead, developed here) and without taking into account the effects of the gas phase.

Comparing simulation results with experimental polarization curves and impedance spectra, information about the macrokinetics of oxygen reduction can be obtained, in particular regarding its dependence on temperature and oxygen partial pressure.

2.2 Modeling

2.2.1 General aspects and model assumptions

Within the cathode, the molecular oxygen in gas phase is reduced by the electrons, coming from the current collector and transported by the electron–conducting phase, into oxygen ions, transported by the ion–conducting phase, following the stoichiometry:

$$O_{2(g)} + 4e^{-}_{(el)} \rightarrow 2O^{2-}_{(io)}$$

The reaction, which represents the conversion of the current from the electronic form into the ionic form, may take place at any TPB, provided that the paths transporting the reaction participants are connected to the external sources of reactants (i.e., air for molecular oxygen and current collector for electrons) and to the sinks of products (i.e., the electrolyte for oxygen ions). A schematic representation of the cathode microstructure and geometry is reported in Figure 2.1a while a zoom on an active TPB is illustrated in Figure 2.1b.

The mathematical model describes, through conservation equations, the reaction and the transport of reaction participants within the electrode. The model is based on the following main assumptions:

i. model variables and parameters are uniform in any cross section of the cathode due to the button cell configuration, resulting in a mono–dimensional model in the electrode axial coordinate *x*;

ii. heat effects are neglected, resulting in uniform temperature in the whole cathode;

iii. the cathode structure is represented as a random composite packing of monosized spherical particles with a porosity distribution along the thickness. This assumption allows the application of the extended percolation theory [27] (see Section 2.2.3 for further details);

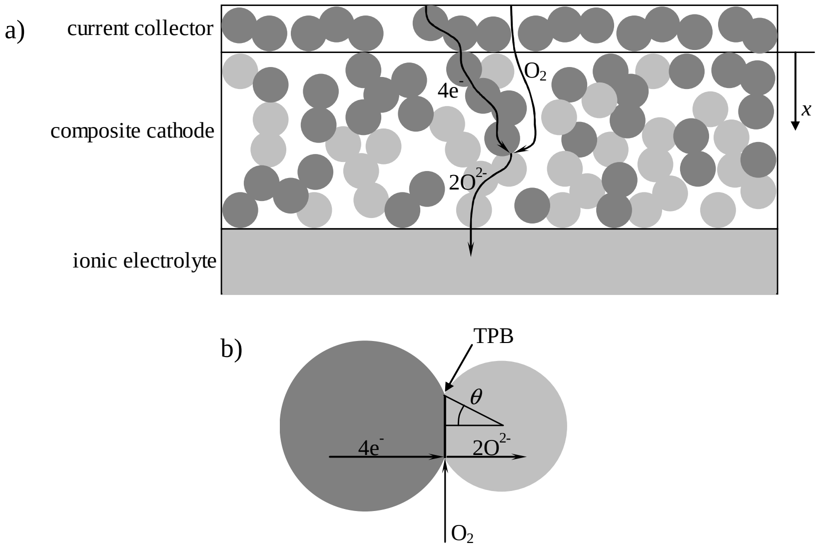

Figure 2.1 – a) Schematic view of a porous composite cathode; b) contact between electron–conducting and ion–conducting particles.

iv. no mixed ionic–electronic conduction in the electron–conducting phase and the ion–conducting phase;

v. it is assumed that the current collector, which is thinner and more porous than the electrode, does not affect the gas transport to the cathode, so that external gas conditions without any pressure drop are applied at the electrode–current collector interface.

2.2.2 Governing equations and boundary conditions

The model consists of the system of balance equations for the three species participating to the reaction (i.e., electrons, molecular oxygen and oxygen ions), coupled with the conservation of an inert gas fed with molecular oxygen (for example, nitrogen when the cathode is fed with air). Model equations are reported in Table 2.1 in dynamic conditions.

The source and consumption terms for reacting species are related, through stoichiometric coefficients and the Faraday constant F, to the current exchanged per unit volume ($i_{TPB}\lambda_{TPB}$), calculated as the product of the current density per unit TPB length i_{TPB} and the connected TPB length per unit volume λ_{TPB}. The kinetics of oxygen reduction is assumed to follow a Butler–Volmer expression without mass transfer effects [30]:

$$i_{TPB} = i_0\left[\exp\left(\alpha\frac{F}{RT}\eta\right) - \exp\left(-(1-\alpha)\frac{F}{RT}\eta\right)\right] \tag{2.1}$$

Table 2.1 – Model equations.

Species	*Balance equation*
E^{-}	$\frac{c_{dl}a_{dl}}{F}\frac{\partial(V_{io}-V_{el})}{\partial t}+\frac{\partial N_e}{\partial x}=-\frac{i_{TPB}\lambda_{TPB}}{F}$
O^{2-}	$-\frac{c_{dl}a_{dl}}{2F}\frac{\partial(V_{io}-V_{el})}{\partial t}+\frac{\partial N_o}{\partial x}=\frac{i_{TPB}\lambda_{TPB}}{2F}$
O_2	$\frac{\phi}{RT}\frac{\partial(Py_O)}{\partial t}+\frac{\partial N_O}{\partial x}=-\frac{i_{TPB}\lambda_{TPB}}{4F}$
I	$\frac{\phi}{RT}\frac{\partial(P(1-y_O))}{\partial t}+\frac{\partial N_I}{\partial x}=0$

where i_0 is the exchange current per unit of TPB length, α the transfer coefficient, R the gas constant and T the absolute temperature. In Eq. (2.1), η is the overpotential, calculated as follows [31]:

$$\eta=-\frac{RT}{4F}\ln\left(\frac{P^{ex}y_O^{ex}}{Py_O}\right)-V_{el}+V_{io} \tag{2.2}$$

where V_{el} and V_{io} represent the electric potential of, respectively, the electron–conducting phase and the ion–conducting phase, P the pressure and y_O the oxygen molar fraction. In Eq. (2.2), the subscript *ex* refers to external conditions, that is, the conditions of the gas mixture fed to the cathodic side of the cell. It is noteworthy that the first term in the right side of Eq. (2.2) represents the equilibrium potential step and that the kinetics is expressed in the direction of molecular oxygen consumption (i.e., $i_{TPB} > 0$) for positive overpotentials.

The time derivatives in Table 2.1 account for the local temporal variation of both molecular and charged species. In particular, electrons and oxygen ions can be accumulated at the interface between the electron–conducting phase and the ion–conducting phase: c_{dl} represents a specific capacitance per unit of interface area while a_{dl} is the connected contact area per unit volume between electron–conducting and ion–conducting particles. An ideal capacitive behavior is assumed [31], that is, linearly dependent on the first derivative of the potential difference between conducting phases, with a c_{dl} dependent on temperature only. In principle, the specific capacitance accounts for all the electric and surface capacitive phenomena occurring at the contact area between electron–conducting and ion–conducting particles.

The transport of charged species, that is electrons and oxygen ions within their respective conducting phases, is assumed to follow the Ohm law:

$$N_e = \frac{\sigma_{el}^{eff}}{F}\frac{\partial V_{el}}{\partial x} \tag{2.3a}$$

$$N_o = \frac{\sigma_{io}^{eff}}{2F}\frac{\partial V_{io}}{\partial x} \tag{2.3b}$$

where effective conductivities are considered.

The mass transport in porous phase is described according to the dusty–gas model [32,33], comprising in this way convection as well as ordinary and Knudsen diffusion. The molar fluxes of molecular oxygen and gaseous inert are calculated as a function of pressure and oxygen molar fraction as:

$$N_O\left(\frac{1}{D_O^{K,eff}}+\frac{1-y_O}{D_{O-I}^{eff}}\right)=\frac{y_O}{D_{O-I}^{eff}}N_I-\frac{P}{RT}\frac{\partial y_O}{\partial x}-\frac{y_O}{RT}\left(1+\frac{P}{\mu}\frac{B}{D_O^{K,eff}}\right)\frac{\partial P}{\partial x} \tag{2.4a}$$

$$N_I\left(\frac{1}{D_I^{K,eff}}+\frac{y_O}{D_{O-I}^{eff}}\right)=\frac{1-y_O}{D_{O-I}^{eff}}N_O+\frac{P}{RT}\frac{\partial y_O}{\partial x}-\frac{1-y_O}{RT}\left(1+\frac{P}{\mu}\frac{B}{D_I^{K,eff}}\right)\frac{\partial P}{\partial x} \tag{2.4b}$$

where the effective diffusion coefficients are calculated as follows:

$$D_i^{K,eff} = \frac{\phi}{\tau}\frac{4}{3}d_p\sqrt{\frac{RT}{2\pi M_i}} \quad \text{with } i = O, I \tag{2.5}$$

$$D_{O-I}^{eff} = \frac{\phi}{\tau}D_{O-I} \tag{2.6}$$

In these last equations, ϕ and τ represent, respectively, the porosity and the tortuosity factor of the gas phase, d_p the mean pore diameter while M_i is the molecular weight of the gas species. The binary diffusion coefficient D_{O-I} is calculated according to the Fuller expression [34].

The permeability coefficient B in Eqs. (2.4a) and (2.4b) is calculated by using the Blake–Kozeny form of the Darcy law [35]:

$$B = \frac{{D_p}^2}{150}\frac{\phi^3}{(1-\phi)^2} \quad \text{where} \quad D_p = \frac{3}{2}d_p\frac{1-\phi}{\phi} \tag{2.7}$$

The dynamic viscosity of the gas mixture μ, associated to the permeability in Eqs. (2.4a) and (2.4b), is calculated according to the Herning and Zipperer method [34].

Model equations in Table 2.1 are coupled with boundary conditions. At the current collector interface, the electric potential of the electron–conducting phase is set at 0V as reference and external conditions for total and oxygen partial pressure are imposed. At the electrolyte interface (i.e., $x = L_c$, where L_c is the electrode thickness), the electric potential of the ion–conducting phase is imposed equal to:

$$V_{io}(x = L_c) = \eta_c \cdot \sin(2\pi f t) \quad \text{in transient conditions} \qquad (2.8a)$$

$$V_{io}(x = L_c) = \eta_c \quad \text{in steady–state conditions} \qquad (2.8b)$$

where η_c is the cathode overpotential. Note that the boundary condition in Eq. (2.8) is applied in impedance simulations, in which a harmonically varying overpotential with a specified frequency f is imposed to the electrode [36]. On the other hand, Eq. (2.8b) refers to the boundary condition for steady–state simulations, that is, for the simulation of the stationary polarization behavior. In both steady–state and dynamic simulations, at $x = 0$ and $x = L_c$ the outgoing fluxes of reacting species are set by the electrochemical charge transfer reaction per unit surface [22], calculated considering the TPB length per unit surface [37].

The solution of model equations allows the calculation of the total current density at the current collector interface $x = 0$. In steady–state conditions, the current density I is used to calculate the polarization resistance as $R_p = \eta_c/I$ [21], which represents the main index of cathode efficiency of energy conversion. On the other hand, in impedance simulations a time–dependent current density $i(t)$ is obtained. By integrating $i(t)$ in a time interval $\Delta t = f^{-1}$ sufficiently far from the start time (i.e., $n >> 1$) as follows [36]:

$$\int_{nf^{-1}}^{(n+1)f^{-1}} i(t)\sin(2\pi f t)dt = \frac{I}{2f}\cos\varphi \qquad (2.9a)$$

$$\int_{nf^{-1}}^{(n+1)f^{-1}} i(t)\cos(2\pi f t)dt = \frac{I}{2f}\sin\varphi \qquad (2.9b)$$

the amplitude I and the phase φ of the current can be calculated. The real and imaginary components of the impedance Z_R and Z_I are calculated as $Z_R = \eta_c \cdot \cos(\varphi)/I$ and $Z_I = \eta_c \cdot \sin(\varphi)/I$, respectively. Note that Z_R and Z_I are functions of the frequency f: by varying the frequency and repeating the analysis, the impedance spectra of the electrode is simulated. It is noteworthy that the simulation reproduces the same procedure used in actual EIS measurements, unlike the frequency–resolved excitation [38] and the potential step [39] simulations, similarly to the Hofmann and Panopoulos work [40], although in such a study the effective properties were not related to the electrode microstructure.

2.2.3 Effective properties from microstructure characteristics

As reported in Table 2.1 and in Section 2.2.2, model equations require the estimation of effective properties, such as the connected TPB length per unit volume

λ_{TPB}, the effective conductivities σ_{el}^{eff} and σ_{io}^{eff} and the mean pore diameter d_p, in order to be solved. Such properties are related to the microstructure characteristics (i.e., particle diameter, porosity, composition) of the cathode by using an extended percolation theory [27]. With this approach, the spatial distribution of porosity, experimentally observed on cathode samples [28], can be accounted for in the estimation of effective properties.

In the extended percolation theory, the porosity distribution is attributed to a non–uniform distribution of pore–formers. Pore–formers are particles of materials, mixed with electron–conducting and ion–conducting particles during the electrode fabrication, which decompose at high temperatures during the sintering, leaving additional pores in the microstructure. This feature can be conveniently taken into account by the extended percolation theory [27], which is used to link the pore–former volume fraction to the final porosity ϕ and, subsequently, to calculate the effective properties from the electrode morphological characteristics.

Through the extended percolation theory [27], the pore–former volume fraction before sintering ψ_{pf}^{bs} leading to a final porosity ϕ can be calculated as follows:

$$\psi_{pf}^{bs} = \frac{\phi - \phi^{bs}}{1 - \phi^{bs}} \tag{2.10}$$

where ϕ^{bs} represents the porosity of the packing before sintering, when electron–conducting, ion–conducting and pore–former particles are present. For a random close mixture of monosized rigid spherical particles, ϕ^{bs} is equal to 0.36 [41,42].

The volume fraction before sintering of electron–conducting or ion–conducting particles can be calculated as a function of the final porosity and the volume fraction after sintering ψ_i as:

$$\psi_i^{bs} = \psi_i \frac{1 - \phi}{1 - \phi^{bs}} \quad \text{with } i = el, io \tag{2.11}$$

which, in turns, can be used to calculate the numbers of contacts between different particles, which assume the following simplified forms under the assumption that the phases are monosized [27]:

$$Z_{i,j} = \frac{\dfrac{\psi_j^{bs}}{d_j}}{\dfrac{\psi_{el}^{bs}}{d_{el}} + \dfrac{\psi_{io}^{bs}}{d_{io}} + \dfrac{\psi_{pf}^{bs}}{d_{pf}}} N_{i,j} \quad \text{with } i,j = el, io \tag{2.12}$$

$$N_{i,j} = \begin{cases} \dfrac{3\left(2-\sqrt{3}\right)\left(S_{i,j}+1\right)}{1+S_{i,j}-\sqrt{S_{i,j}\left(S_{i,j}+2\right)}} & if\ S_{i,j}=\dfrac{d_i}{d_j}\geq 1 \\ \dfrac{3\left(2-\sqrt{3}\right)\left(S_{i,j}^{-1}+1\right)S_{i,j}^{2}}{1+S_{i,j}^{-1}-\sqrt{S_{i,j}^{-1}\left(S_{i,j}^{-1}+2\right)}} & if\ S_{i,j}=\dfrac{d_i}{d_j}<1 \end{cases} \tag{2.13}$$

In Eqs. (2.12) and (2.13), d_i represents the diameter of the particles belonging to the phase *i*.

The number of contacts between *j* and *i*–particles $Z_{i,j}$ is an important parameter related to the particle connectivity. When $j = i$, $Z_{i,i}$ represents the number of contacts between homolog particles, which is related to the percolation probability γ_i that the *i*–th phase be entirely percolating throughout the electrode thickness [43] providing a conducting path for charge transport. On the other hand, when $j \neq i$, $Z_{i,j}$ (i.e., $Z_{el,io}$ and $Z_{io,el}$) is related to the number of contacts between electron–conducting and ion–conducting particles, which is associated to the TPB where reaction occurs.

The percolation probability γ_i takes into account the connectivity of the conducting phase *i* as a whole. Even though percolation theory allows the estimation of a local probability γ_i as a function of the local $Z_{i,i}$ as follows [44]:

$$\gamma_i = 1-\left(\frac{4.236-Z_{i,i}}{2.472}\right)^{3.7} \quad \text{with } i = el,\ io \tag{2.14}$$

when the morphology varies along the thickness, the local probability is fictitious. Instead, only the minimum value $\gamma_i^o = \min\limits_x \gamma_i$ is meaningful and characterizes the conducting phase throughout the whole electrode thickness.

The percolation probability takes part in the evaluation of the effective conductivities of electron–conducting and ion–conducting phases, according to the Nam and Jeon correlation [45]:

$$\sigma_i^{eff} = \sigma_i\left(\left(1-\phi\right)\psi_i\gamma_i^o\right)^{1.5} \quad \text{with } i = el,\ io \tag{2.15}$$

and in the estimation of the connected TPB length λ_{TPB} and the contact area a_{dl} per unit volume as follows [27]:

$$\lambda_{TPB} = 6\left(1-\phi^{bs}\right)\gamma_{el}^o\gamma_{io}^o\frac{\psi_{el}^{bs}}{d_{el}^{\ 3}}Z_{el,io}d_c \tag{2.16a}$$

$$a_{dl} = \frac{3}{2}\left(1-\phi^{bs}\right)\gamma_{el}^o\gamma_{io}^o\frac{\psi_{el}^{bs}}{d_{el}^{\ 3}}Z_{el,io}d_c^2 \tag{2.16b}$$

$$d_c = \min(d_{el}, d_{io}) \sin\theta \tag{2.16c}$$

where θ represents the contact angle between electron–conducting and ion–conducting particles (see Figure 2.1b).

The last parameter affected by the porosity distribution is the mean pore diameter (where mean is related to the cross section and not to the thickness), which characterizes the gas phase. According to the extended percolation theory [27], it is calculated as a function of the local porosity, particle diameters and electrode composition as follows:

$$d_p = \frac{2}{3}\frac{\phi}{1-\phi^{bs}}\frac{d_{el}d_{io}}{\psi_{el}^{bs}d_{io}+\psi_{io}^{bs}d_{el}} \tag{2.17}$$

2.3 Results and discussion

The model of the cathode described in Section 2.2 is used to interpret the experimental data, provided by Barbucci et al. [28], regarding porous composite cathodes of different thicknesses in different operating conditions. LSM was used as electronic conductor and YSZ as ion–conducting phase. From scanning electron microscope images, all the samples were found to show a porosity linearly distributed along the thickness, increasing up from the current collector to the electrolyte interface as follows:

$$\phi = \phi^{cc} + \kappa x \tag{2.18}$$

where ϕ^{cc} represents the porosity at the current collector and κ the porosity gradient. Such a porosity distribution was not originally desired by Barbucci et al., it resulted as a consequence of the shaping method used by the researchers.

Sample and operating conditions used in the model are listed in Table 2.2, coupled with physical properties and model parameters. The transfer coefficient α, which affects the symmetry of the i_{TPB}–η relationship in Eq. (2.1) with respect to positive and negative overpotentials, is assumed to be equal to 0.5 because experimental polarization curves were found to be symmetrical for different temperatures and thicknesses [28]. On the other hand, there are no sound indications about the mean contact angle among particles θ, therefore it is assumed equal to 15° as commonly accepted in several modeling works [15,21,45,46].

Table 2.2 – Material properties, design and operating conditions of the cathodes.

Parameter	*Value*
Materials	
Electron–conducting phase	LSM [28]
Electric conductivity σ_{el}	$8.855\cdot 10^{7}/T\cdot\exp(-1082.5/T)$ $\mathrm{S\cdot m^{-1}}$ [47]
Ion–conducting phase	YSZ [28]
Ionic conductivity σ_{io}	$3.34\cdot 10^{4}\cdot\exp(-10300/T)$ $\mathrm{S\cdot m^{-1}}$ [48]
Morphological parameters	
Volume fraction electron–conducting phase ψ_{el}	0.5 (after sintering) [28]
Mean particle diameter $d_{el} = d_{io} = d_{pf}$	0.3μm [28]
Porosity at current collector ϕ^{cc}	0.40 [29]
Porosity gradient κ	1.03mm^{-1} [28]
Contact angle θ	15° [15,21,45]
Tortuosity factor τ	2.083 [49]
Geometric parameters	
Thickness L_c	5–85μm [28]
Diameter	5mm [28]
Operating conditions	
Temperature T	600–850°C [28]
Gas feed	air (0.79 vol N_2, 0.21 vol. O_2) [28]
Pressure P^{ex}	1atm [28]
Applied overpotential η_c	20mV [28]

Model equations were implemented and solved by using the commercial solver of systems of partial differential equations COMSOL Multiphysics 3.5, based on the finite element method. The model solution includes the values of field variables (e.g., pressure, electric fields, overpotential), fluxes and other desired quantities within the domain, which are used to obtain meaningful outcomes such as the total current density I.

2.3.1 Effective properties along the cathode thickness

The linear porosity distribution along the cathode thickness, according to Eq. (2.18) and taken into account in the percolation model described in Section 2.2.3, affects the effective properties, which are not uniform along the axial coordinate.

According to the morphological parameters ϕ^{cc} and κ reported in Table 2.2, in Figure 2.2a the porosity linearly increases with the axial coordinate x from the current collector ($x = 0$) towards the electrolyte interface. The mean pore diameter d_p increases more quickly than the porosity because, according to Eq. (2.17), at the denominator the volume fractions before sintering linearly decrease as results of combining Eq. (2.18) and Eq. (2.11).

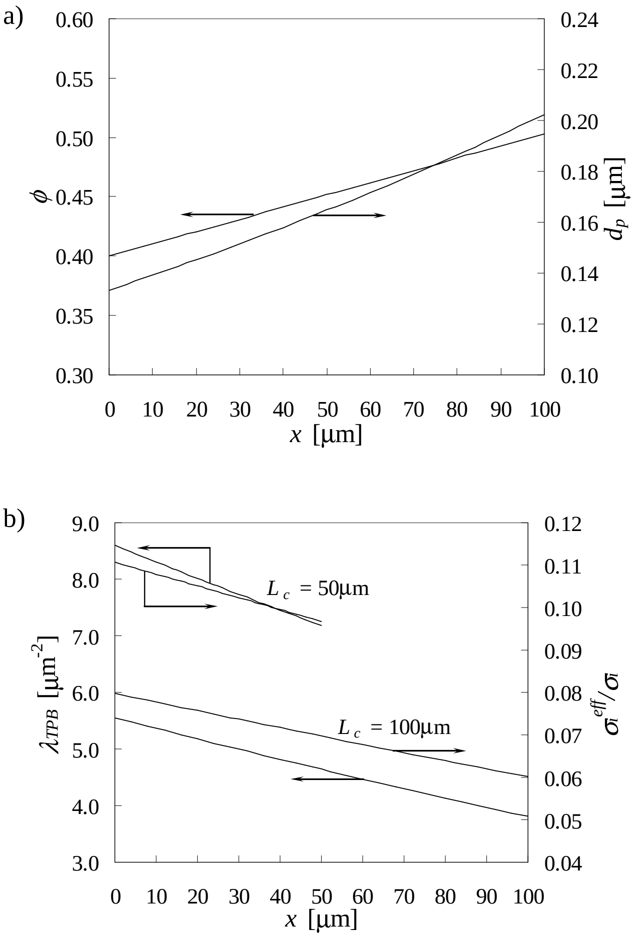

Figure 2.2 – Effective properties as a function of the axial coordinate for a porosity gradient $\kappa = 1.03\mathrm{mm}^{-1}$*: a) porosity and mean pore diameter; b) TPB length per unit volume and relative effective conductivity (that is, the ratio between the effective and the material conductivities) for two electrode thicknesses.*

On the other hand, the effective properties regarding the conducting phases, that is, the TPB length per unit volume λ_{TPB} and the effective conductivities σ_{el}^{eff} and σ_{io}^{eff}, decrease with the axial coordinate as represented in Figure 2.2b. In addition, it is noteworthy that they also strongly depend on the electrode thickness: as the thickness increases, both λ_{TPB}, σ_{el}^{eff} and σ_{io}^{eff} decrease. The dependency of λ_{TPB} and σ_{i}^{eff} on the electrode thickness is due to the percolation probability since, according to Eqs. (2.15) and (2.16a), both these parameters depend on the minimum percolation probabilities γ_{el}^{o} and γ_{io}^{o}. As the electrode thickness increases, the minimum percolation probabilities γ_i^o, which occur at the cathode–electrolyte interface, decrease, leading to a decrease in λ_{TPB} and σ_i^{eff} .

Concluding, due to the distribution of porosity, the electrodes become less conductive and offer a smaller density of reacting sites as the thickness increases.

2.3.2 Polarization resistance and thickness

The dependence of the effective properties on the axial coordinate leads to a peculiar behavior of the polarization resistance as a function thickness as experimentally observed by Barbucci et al. [28]. For the sake of clarity, an example is reported in Figure 2.3, corresponding to a representative operating temperature, equal to 750°C.

In Figure 2.3 the polarization resistance decreases as the thickness increases reaching a minimum value, after which it starts to increase almost linearly. This behavior is well reproduced by the mathematical model when the porosity distribution in Eq. (2.18) is taken into account (solid line), offering a straightforward interpretation based on the observations made in Section 2.3.1 regarding the effective properties. For thin electrodes, the total TPB length available for the reaction within the cathode is low, thus the oxygen reduction is limited by the lack of reaction sites leading to a high polarization resistance. On the other hand, thick electrodes are less conductive and, even if they offer a larger TPB length (although locally the TPB per unit volume is lower), the cathode performance is limited by the charge transport.

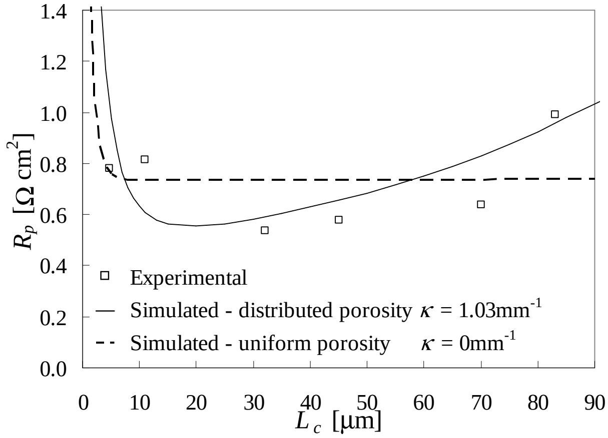

Figure 2.3 – Polarization resistance as a function of thickness at 750°C: experimental data [28] are represented with squares, simulation results with lines (solid line for distributed porosity, dotted line for uniform porosity).

Note that assuming uniform porosity ($\kappa = 0$, dotted line), which would result in uniform effective properties along the electrode thickness, would not allow the model to catch the increase in polarization resistance for thicknesses larger than the optimal one. In fact, if κ was equal to 0, there would not be any decrease in TPB length and effective conductivity as discussed in Section 2.3.1.

The full set of experimental and simulation results are reported in Figure 2.4 in the range of temperature 600–850°C. Model results are obtained by assigning, given the temperature, the value of the exchange current per unit of TPB length i_0 (*a priori* unknown) which results from the least square method herein described. Called $L_{c,k}$ the thickness of the k–th cathode investigated, let $R^e_{p,k}$ be the experimental polarization resistance and $R^s_{p,k}(i_0)$ be the corresponding simulated polarization resistance, which is a function of the exchange current i_0 through Eq. (2.1). The optimal best fit value of i_0 corresponds to the one which leads to the minimum of the sum of the quadratic errors between simulated and experimental data, which means:

$$\min_{i_0} \sum_{k=1}^{N} \left(R^s_{p,k}(i_0) - R^e_{p,k} \right)^2 \tag{2.19}$$

where N represents the number of cathodes investigated (equal to 6 in this case).

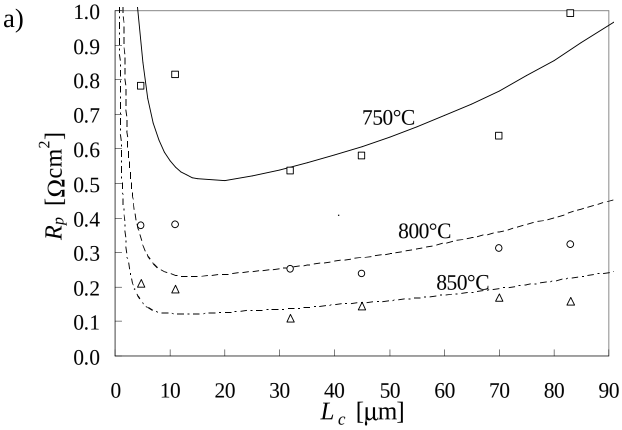

Figure 2.4 – Simulated (lines) and experimental [28] (marks) cathode polarization resistance in air as a function of thickness for different operating temperatures assuming a linear distribution of porosity with $\kappa = 1.03\text{mm}^{-1}$.

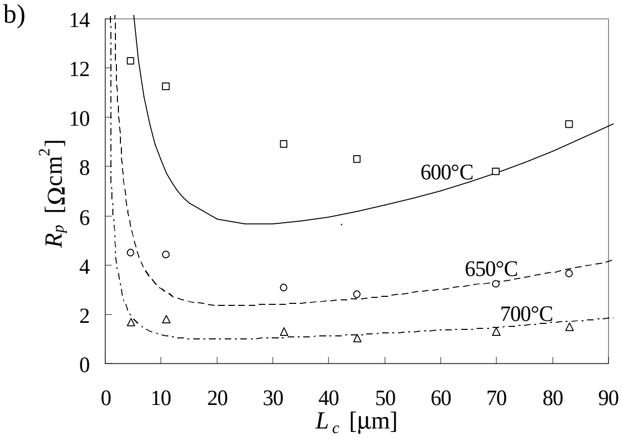

Figure 2.4 (continued) – Simulated (lines) and experimental [28] (marks) cathode polarization resistance in air as a function of thickness for different operating temperatures assuming a linear distribution of porosity with $\kappa = 1.03mm^{-1}$.

The values of exchange current per unit of TPB length, estimated by this procedure on the data corresponding to Figure 2.4, are reported in Figure 2.5 as a function of temperature. The exchange current i_0 shows to follow an Arrhenius behavior with an activation energy of 163.4kJ·mol^{-1}, which is fairly in agreement with the value of 144.7kJ·mol^{-1} obtained by Radhakrishnan et al. [50] in specific kinetic studies on patterned electrodes performed within the same range of temperature.

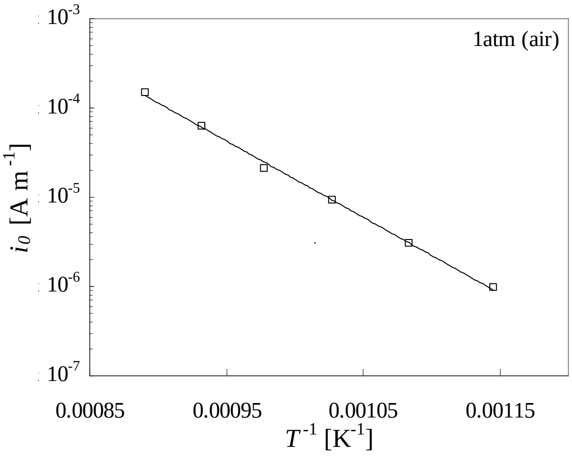

Figure 2.5 – Arrhenius plot of the exchange current per unit of TPB length as estimated by the model through the best fitting of experimental data.

2.3.3 Effect of oxygen partial pressure

Experimental studies were performed to assess the dependence of the polarization resistance on the oxygen partial pressure in the gas stream fed to the cathode. In such studies, performed at different temperatures in a sample 40µm thick, the air was replaced with a mixture of pure oxygen and argon for different relative compositions at 1atm [28].

Theoretically, since molecular oxygen is a participant of the electrochemical reduction, the effect of a different partial pressure in the feed on R_p may be related to i) a concentration effect affecting the kinetic rate and ii) a different contribution due to the gas transport resistance. The latter contribution seems negligible according to Figure 2.6, which shows the profile of oxygen partial pressure along the axial coordinate for a 85µm thick cathode, fed with air at 1atm with an applied overpotential of 20mV, for the upper and lower bounds of temperature (850°C and 600°C respectively) as results from the simulation. Even at 850°C, where the oxygen consumption rate is larger due to a faster kinetics, the profile of oxygen partial pressure is almost flat and equal to the external conditions within the electrode thickness, revealing that the mass transport is fast enough to ensure a continuous supply of molecular oxygen to reaction sites. This consideration, drawn also by other authors in similar situations [21], supports the choice of neglecting mass transport effects in the Butler–Volmer expression (Eq. (2.1)) as well as the contribution to gas transfer resistance related to the current collector (see Section 2.2.1).

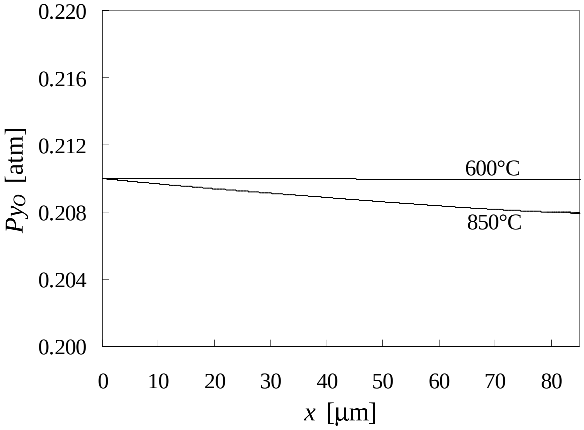

Figure 2.6 – Oxygen partial pressure as a function of axial coordinate in a cathode of 85µm at different temperatures in air as evaluated by the model for an applied overpotential of 20mV.

Hence, the significant effect of the oxygen partial pressure in the feed stream on the polarization resistance, as experimentally observed by Barbucci et al. [28] and reported with marks in Figure 2.7, must be attributed to a kinetic effect. In order to catch this phenomenon in the model, the dependency of the exchange current i_0 on the oxygen partial pressure is taken into account in a slightly different formulation of the kinetic expression in Eq. (2.1), which is:

$$i_{TPB} = i_{00}\left(Py_O\right)^{\beta}\left[\exp\left(\alpha\frac{F}{RT}\eta\right)-\exp\left(-(1-\alpha)\frac{F}{RT}\eta\right)\right] \tag{2.20}$$

where β is an exponent factor to be determined.

It is noteworthy that since the gas conditions are uniform throughout the electrode thickness as discussed above (see Figure 2.6), the kinetic results obtained in the previous Section in air regarding the parameter i_0 are still valid and useful. In particular, given β, in order to be coherent with the previous results (and, therefore, in agreement with experimental data), i_{00} must be evaluated as:

$$i_{00} = i_0 / \left(0.21 atm\right)^{\beta} \tag{2.21}$$

Simulations were performed for the same conditions used in the experiments (i.e., thickness equal to 40µm, mixtures of argon and oxygen at 1atm, temperature of 800°C and 700°C) for different values of the parameter β. Simulation results are reported with lines in Figure 2.7 along with the experimental data. While for $\beta = 0$ there are no significant effects on R_p as expected, for $\beta = 0.5$ the simulation results match very well the experimental data at both 800°C (Figure 2.7a) and 700°C (Figure 2.7b). Table 2.3 reports the values of i_{00} at different temperatures, calculated from the values of i_0 reported in Figure 2.5 through Eq. (2.21) considering $\beta = 0.5$.

Following the derivation of the Butler–Volmer expression for a single rate–determining charge transfer step, which is the kinetics assumed in both Eq. (2.1) and (2.20), a value of β equal 0.5 means that for the electrochemical rate–determining step the transfer coefficient is equal to 0.5 [30]. Hence, $\beta = 0.5$ as found in this Section is consistent with the assumption of $\alpha = 0.5$, made in Section 2.3.1 according to the symmetry of the polarization behavior. Nevertheless, deeper and more specific experimental and theoretical studies on the reaction mechanism were carried out by different authors in the past [5,10,15,22]. Such a detail of sophistication is out of the scope of this study, which instead provides a semi–empirical macrokinetics of oxygen reduction in LSM/YSZ cathodes and its dependency on temperature and oxygen partial pressure for use in micro–macroscale models.

Table 2.3 – Kinetic parameter i_{00} of the oxygen reduction kinetic expression Eq. (2.20) as a function of temperature as evaluated by the model for $\beta = 0.5$.

Temperature [°C]	*Kinetic parameter i_{00} [$A \cdot m^{-1} \cdot atm^{-0.5}$]*
600	$2.14 \cdot 10^{-6}$
650	$6.57 \cdot 10^{-6}$
700	$2.01 \cdot 10^{-5}$
750	$4.57 \cdot 10^{-5}$
800	$1.38 \cdot 10^{-4}$
850	$3.26 \cdot 10^{-4}$

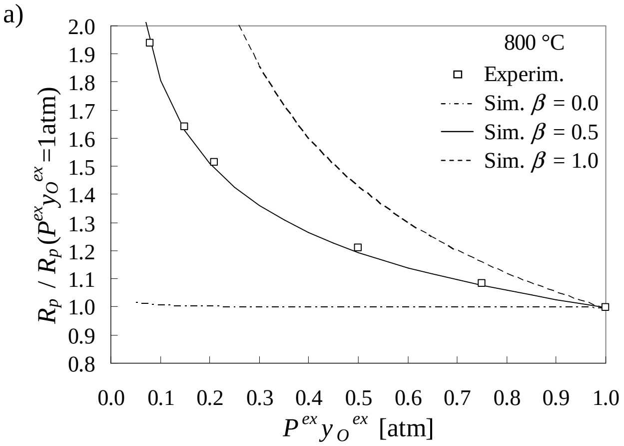

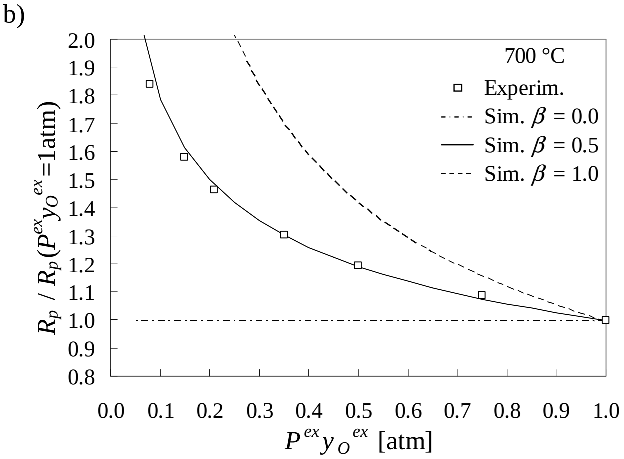

Figure 2.7 – Polarization resistance, normalized to the resistance at oxygen partial pressure of 1atm, for a 40μm thick cathode as a function of the oxygen partial pressure in the feed, which is a mixture of oxygen and argon: experimental data [28] are represented with squares while simulation results with lines.

2.3.4 Impedance simulations

Impedance spectra are simulated solving the model in time domain imposing Eq. (2.8a) as boundary condition. Simulation results are reported in Figure 2.8 along with experimental data for three characteristic electrode thicknesses at three operating temperatures. Since there is not a perfect match between experimental and simulated polarization resistances, as shown in Figure 2.4, for each temperature and thickness the real and imaginary components of impedance in simulation results are uniformly scaled to obtain the same polarization resistance given by the experimental data. In other words, the simulated $Z_R(f$=0Hz) is forced to match the experimental $Z_R(f$=0Hz) by using a constant multiplier coefficient, which is used to scale all the simulation data of Z_R and Z_I at each frequency. This linear transformation does not change the shape of the curves but only helps to make an easier comparison.

Given the temperature, the specific capacitance c_{dl} is evaluated by best fitting with experimental data and kept constant with the thickness. The capacitance does not have any influence on the shape of the curve, it only affects the speed at which the curves are covered in terms of frequency. Thus, c_{dl} is fitted in order to have the best possible agreement in terms of frequency.

Figure 2.8 shows that simulated spectra match fairly well the shape and the frequencies of experimental data, especially for high temperatures and for cathodes 32 and 83μm thick. Indeed, larger discrepancies are expected for the 4.7μm thick electrode due to the stronger sensitivity of experimental data on geometrical and morphological defects in such a small thickness. In all the range of temperature and thickness, the shape of the spectra is depressed, which means that the maximum of Z_I is smaller than the maximum of Z_R (note that in Figure 2.8 the scales of axes are not equal). At 850°C there is only a single arc of impedance with characteristic frequency of about 250Hz, while, as the temperature decreases, a second smaller contribution, corresponding to a much higher frequency, appears.

In the mathematical model (see Table 2.1) there are basically two phenomena which are dependent on a time derivative and that can give a response in the Nyquist plot: the gas transport and the specific capacitance. The former is found to be responsible of the high frequency contribution while the latter produces the larger low frequency arc (from 250 to 3.5Hz for temperatures of 850 and 650°C respectively).

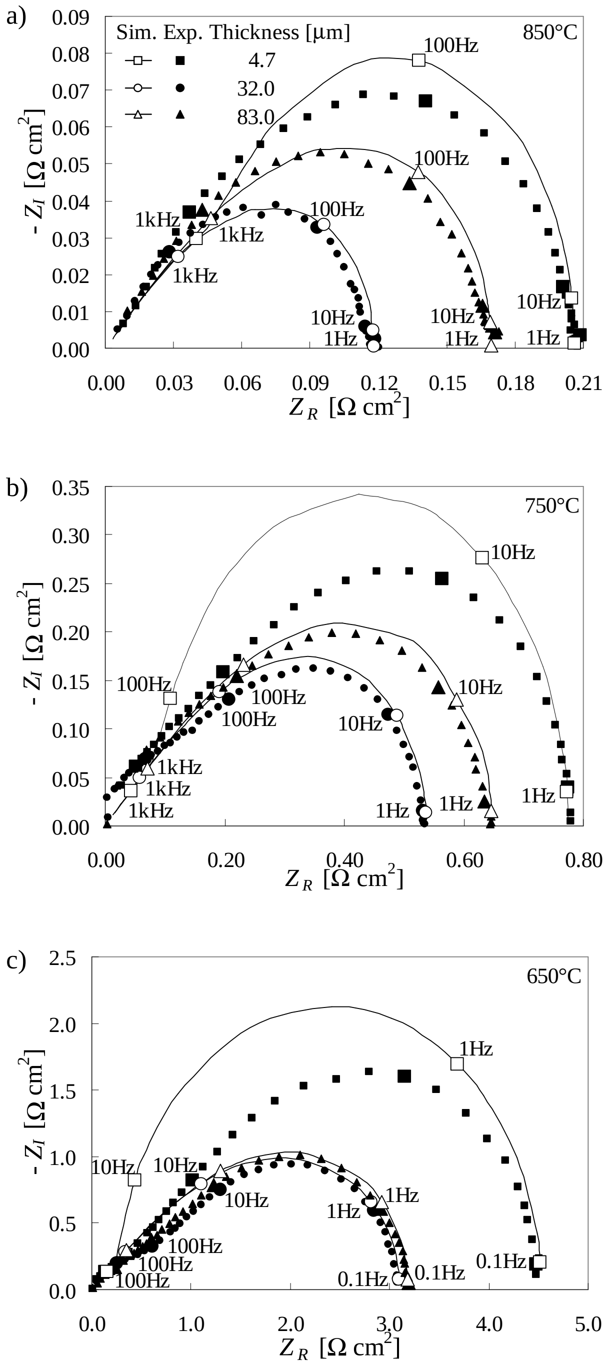

Figure 2.8 – Simulated (lines and open marks) and experimental [28] (solid marks) impedance spectra for three different electrode thicknesses at different temperatures.

The model predicts that the gas transport contribution to the whole cathode polarization resistance is negligible due to the large porosity and the small electrode thickness, as also discussed in Section 2.3.3 (see Figure 2.6). In addition, the model predicts that the oxygen is transported in the pores mainly by diffusion (about the 80% of the flux is diffusive). By using the Bosanquet formula [45] to calculate an overall oxygen diffusivity D_O^{eff} from the effective ordinary and Knudsen diffusivities, it is possible to estimate the characteristic frequency of the gas transport as D_O^{eff}/L_c^2, which is about 1100Hz for a thickness of 83μm and rises to 6200Hz for 32μm. This confirms that the high frequency contribution is related to the gas transport.

On the other hand, the model suggests to attribute the low frequency arc of impedance to the specific capacitance at the LSM/YSZ interface. The values of the specific capacitance c_{dl} obtained by best fitting at the investigated temperatures are reported in Table 2.4. Contrary to what happened with the kinetic constant i_{00} (see Table 2.3 and Figure 2.5), the capacitance c_{dl} does not show a clear relationship with respect to the temperature. Moreover, the specific capacitance, which ranges between 115 and 210μF·mm^{-2}, is about two orders of magnitude higher than the typical value associated to a double layer electric capacitive phenomenon in a SOFC electrode [25,51].

All these considerations lead to draw the conclusion that the parameter c_{dl} is not related to a single electric phenomenon, rather it gathers in itself several overlapping contributions which have different behaviors with respect to the temperature but about the same time constants. In other words, c_{dl} represents only a global capacitance which is the sum of different phenomena related to the local time variation of the overpotential at the LSM/YSZ interface. Just to make an example, c_{dl} could gather the electric capacitance and the surface diffusion of reaction intermediates, which are both related to the time derivative of V_{io} and V_{el} at the LSM/YSZ interface.

Table 2.4 – Specific capacitance as evaluated by best fitting of experimental spectra.

Temperature T [°C]	*Capacitance c_{dl} [μF·mm^{-2}]*
850	125
800	133
750	115
700	210
650	180

2.4 Conclusions

A mathematical model of porous composite SOFC cathodes, based on the application of local mass and charge balance equations, was developed. The model also comprised, through the extended percolation theory, a coherent morphological description, which allowed non–uniform effective properties along the cathode thickness to be taken into account. The model was applied to interpret experimental data of polarization resistance and impedance spectra as a function of thickness, temperature and oxygen partial pressure of porous LSM/YSZ cathodes, which showed to be characterized by a linear porosity distribution along the thickness.

The mathematical morphological description showed that the distributed porosity mainly led to a decrease in the effective properties related to the conducting phases, such as the density of reaction sites (that is, the TPB length per unit volume) and the effective electric and ionic conductivities, as the thickness increased. This phenomenon was found to be responsible of the dependence of the polarization resistance on the electrode thickness as experimentally observed.

The comparison of simulation results with experimental polarization curves allowed the estimation of the exchange current per unit of TPB length of the oxygen reduction reaction, which was found to be well correlated by an Arrhenius law with an activation energy of $164.3\mathrm{kJ \cdot mol^{-1}}$ in the range 600–850°C. From the comparison between experimental data and simulations for different gas feed compositions, the exchange current was found to depend on the square root of the oxygen partial pressure in the range 0.05–1atm, providing in this way a more detailed macrokinetics of oxygen reduction.

The comparison between experimental and simulated impedance spectra, the latter obtained by solving model equations in time domain, provided a physically–based interpretation of the impedance plots. In particular, the high frequency arc was attributed to the capacitive behavior related to the accumulation of gas species within the pores. On the other hand, the low frequency arc (characteristic frequency from 250 to 3.5Hz for temperatures of 850 and 650°C, respectively) was found to be related to capacitive phenomena at the LSM/YSZ interface. However, the specific capacitance did not show a clear relationship with temperature, suggesting that multiple chemical (i.e., surface diffusion) and electrical (i.e., electric double layer capacitance) phenomena could be gathered in such a global specific parameter.

With the proposed approach, which couples a coherent and flexible morphological description within the electrode mass and charge balances, even non–homogeneous microstructures can be considered. The approach can be used to assist the interpretation experimental data with physically–based considerations, as discussed here, or to optimize the cell performance through the engineering of geometry and microstructure. Schneider et al. [52] studied the effects of functionally graded SOFC electrodes; similarly, other kinds of non–uniform distributions could be considered, such as a distribution of particle size [53]. In particular, an *ad hoc* porosity distribution may be helpful in optimizing very complex SOFC systems, such as the IDEAL–Cell [49].

Nomenclature

Glossary

a_{dl}	connected contact area between *el*– and *io*–particles per unit volume [m^{-1}]
B	permeability coefficient [m^{2}]
c_{dl}	specific capacitance [F$\cdot$m^{-2}]
d_i	mean particle diameter (i = *el*, *io*, *pf*) [m]
d_p	mean pore diameter [m]
D_i^K	Knudsen diffusivity for species i ($i = O, I$) [m$^{2}\cdot$s^{-1}]
$D_{O\text{–}I}$	binary diffusion coefficient for oxygen–inert gas [m$^{2}\cdot$s^{-1}]
f	frequency [s^{-1}]
F	Faraday constant [C$\cdot$mol^{-1}]
i_0	exchange current per unit of TPB length [A$\cdot$m^{-1}]
i_{00}	kinetic parameter in Eq. (2.20) per unit of TPB length [A$\cdot$m$^{-1}\cdot$atm$^{-\beta}$]
i_{TPB}	current density per unit of TPB length [A$\cdot$m^{-1}]
I	current density per unit of electrode area [A$\cdot$m^{-2}]
L_c	electrode thickness [m]
M_i	molecular weight of species i ($i = O, I$) [kg$\cdot$mol^{-1}]
N_e	molar flux of electrons [mol$\cdot$m$^{-2}\cdot$s^{-1}]
N_I	molar flux of inert gas [mol$\cdot$m$^{-2}\cdot$s^{-1}]
N_o	molar flux of oxygen ions [mol$\cdot$m$^{-2}\cdot$s^{-1}]
N_O	molar flux of molecular oxygen [mol$\cdot$m$^{-2}\cdot$s^{-1}]
P	pressure [Pa]
R	ideal gas constant [J$\cdot$mol$^{-1}\cdot$K^{-1}]
R_p	cathode polarization resistance [$\Omega\cdot$m^{2}]
t	time [s]
T	temperature [K]
V	electric potential [V]
x	axial coordinate along the thickness [m]
y_O	oxygen molar fraction in gas phase
$Z_{i,j}$	number of contacts between j and i–particles (i,j = *el*, *io*)
Z_I	imaginary component of the impedance [$\Omega\cdot$m^{2}]
Z_R	real component of the impedance [$\Omega\cdot$m^{2}]
α	transfer coefficient
β	exponent of oxygen partial pressure in Eq. (2.20)
γ_i^o	minimum percolation probability of phase i (i = *el*, *io*)

η	overpotential [V]
η_c	overpotential applied to the cathode [V]
θ	contact angle [rad]
κ	porosity gradient [m^{-1}]
λ_{TPB}	connected TPB length per unit volume [m^{-2}]
μ	dynamic viscosity of the gas mixture [$\mathrm{kg}\cdot\mathrm{m}^{-1}\cdot\mathrm{s}^{-1}$]
σ_i	electric conductivity of phase i ($i = el, io$) [$\mathrm{S}\cdot\mathrm{m}^{-1}$]
τ	tortuosity factor of the gas phase
ϕ	porosity
ϕ^{bs}	porosity before sintering
ϕ^{cc}	porosity at the current collector
φ	phase of the impedance [rad]
ψ_i	solid volume fraction of phase i ($i = el, io$) after sintering
ψ_i^{bs}	solid volume fraction of phase i ($i = el, io, pf$) before sintering

Superscripts

bs	before sintering
cc	current collector
eff	effective
ex	external conditions

Subscripts

e	electrons
el	electron–conducting phase
io	ion–conducting phase
I	inert gas
o	oxygen ions
O	molecular oxygen
pf	pore–formers
TPB	three–phase boundary

Abbreviations

LSM	strontium–doped lanthanum manganite
TPB	three–phase boundary
YSZ	yttria–stabilized zirconia

References

[1] J. Larminie, A. Dicks, Fuel Cell Systems Explained, Wiley, New York, 2003.

[2] S.C. Singhal, K. Kendall, High temperature solid oxide fuel cells: fundamentals, design and applications, Elsevier, Oxford, 2003.

[3] R.J. Kee, H. Zhu, D.G. Goodwin, Solid-oxide fuel cells with hydrocarbon fuels, Proc. Combust. Inst. 30 (2005) 2379–2404.

[4] E. Achenbach, E. Riensche, Methane/steam reforming kinetics for solid oxide fuel cells, J. Power Sources. 52 (1994) 283–288.

[5] H. Zhu, R.J. Kee, V.M. Janardhanan, O. Deutschmann, D.G. Goodwin, Modeling elementary heterogeneous chemistry and electrochemistry in solid-oxide fuel cells, J. Electrochem. Soc. 152 (2005) A2427–A2440.

[6] S.C. Singhal, Advances in solid oxide fuel cell technology, Solid State Ionics. 135 (2000) 305–313.

[7] S.C. Singhal, Solid oxide fuel cells for stationary, mobile, and military applications, Solid State Ionics. 152 (2002) 405–410.

[8] J. Palsson, A. Selimovic, L. Sjunnesson, Combined solid oxide fuel cell and gas turbine systems for efficient power and heat generation, J. Power Sources. 86 (2000) 442–448.

[9] F. Leucht, W.G. Bessler, J. Kallo, K.A. Friedrich, Pressurized SOFC system simulation for hybrid power plant operation, in: P. Connor (Ed.), 9th Eur. SOFC Forum, Lucerne - Switzerland, 2010: pp. 0353–0362.

[10] S.B. Adler, Factors governing oxygen reduction in solid oxide fuel cell cathodes., Chem. Rev. 104 (2004) 4791–4843.

[11] J. Gao, X. Liu, D. Peng, G. Meng, Electrochemical behavior of $Ln_{0.6}Sr_{0.4}Co_{0.2}Fe_{0.8}O_{3-\delta}$ (Ln=Ce, Gd, Sm, Dy) materials used as cathode of IT-SOFC, Catal. Today. 82 (2003) 207–211.

[12] M.T. Colomer, B.C.H. Steele, J.A. Kilner, Structural and electrochemical properties of the $Sr_{0.8}Ce_{0.1}Fe_{0.7}Co_{0.3}O_{3-\delta}$ perovskite as cathode material for ITSOFCs, Solid State Ionics. 147 (2002) 41–48.

[13] M.J. Jørgensen, S. Primdahl, C. Bagger, M. Mogensen, Effect of sintering temperature on microstructure and performance of LSM–YSZ composite cathodes, Solid State Ionics. 139 (2001) 1–11.

[14] M. Mogensen, S. Skaarup, Kinetic and geometric aspects of solid oxide fuel cell electrodes, Solid State Ionics. 86-88 (1996) 1151–1160.

[15] B. Kenney, K. Karan, Engineering of microstructure and design of a planar porous composite SOFC cathode: A numerical analysis, Solid State Ionics. 178 (2007) 297–306.

[16] W. Lehnert, J. Meusinger, F. Thom, Modelling of gas transport phenomena in SOFC anodes, J. Power Sources. 87 (2000) 57–63.

[17] A. Barbucci, M. Viviani, M. Panizza, M. Delucchi, G. Cerisola, Analysis of the oxygen reduction process on SOFC composite electrodes, J. Appl. Electrochem. 35 (2005) 399–403.

[18] M. Juhl, S. Primdahl, C. Manon, M. Mogensen, Performance/structure correlation for composite SOFC cathodes, J. Power Sources. 61 (1996) 173–181.

[19] B.A. Boukamp, Electrochemical impedance spectroscopy in solid state ionics: recent advances, Solid State Ionics. 169 (2004) 65–73.

[20] Y.L. Yang, A.J. Jacobson, C.L. Chen, G.P. Luo, K.D. Ross, C.W. Chu, Oxygen exchange kinetics on a highly oriented $La_{0.5}Sr_{0.5}CoO_{3-\delta}$ thin film prepared by pulsed-laser deposition, Appl. Phys. Lett. 79 (2001) 776.

[21] P. Costamagna, P. Costa, V. Antonucci, Micro-modelling of solid oxide fuel cell electrodes, Electrochim. Acta. 43 (1998) 375–394.

[22] H. Zhu, R.J. Kee, Modeling distributed charge-transfer processes in SOFC membrane electrode assemblies, J. Electrochem. Soc. 155 (2008) B715–B729.

[23] T.X. Ho, P. Kosinski, A.C. Hoffmann, A. Vik, Numerical modeling of solid oxide fuel cells, Chem. Eng. Sci. 63 (2008) 5356–5365.

[24] P. Aguiar, C.S. Adjiman, N.P. Brandon, Anode-supported intermediate temperature direct internal reforming solid oxide fuel cell. I: model-based steady-state performance, J. Power Sources. 138 (2004) 120–136.

[25] H. Zhu, R.J. Kee, Modeling electrochemical impedance spectra in SOFC button cells with internal methane reforming, J. Electrochem. Soc. 153 (2006) A1765–A1772.

[26] S. Campanari, P. Iora, Definition and sensitivity analysis of a finite volume SOFC model for a tubular cell geometry, J. Power Sources. 132 (2004) 113–126.

[27] A. Bertei, C. Nicolella, Percolation theory in SOFC composite electrodes: Effects of porosity and particle size distribution on effective properties, J. Power Sources. 196 (2011) 9429–9436.

[28] A. Barbucci, M. Paola Carpanese, M. Viviani, N. Vatistas, C. Nicolella, Morphology and electrochemical activity of SOFC composite cathodes: I. Experimental analysis, J. Appl. Electrochem. 39 (2009) 513–521.

[29] C. Nicolella, A. Bertei, M. Viviani, A. Barbucci, Morphology and electrochemical activity of SOFC composite cathodes: II. Mathematical modelling, J. Appl. Electrochem. 39 (2008) 503–511.

[30] A.J. Bard, L.R. Faulkner, Electrochemical methodes: fundamentals and applications, Wiley, New York, 2001.

[31] W.G. Bessler, S. Gewies, M. Vogler, A new framework for physically based modeling of solid oxide fuel cells, Electrochim. Acta. 53 (2007) 1782–1800.

[32] E.A. Mason, A.P. Malinauskas, Gas transport in porous media: the dusty-gas model, Elsevier, Amsterdam, 1983.

[33] D. Arnošt, P. Schneider, Dynamic transport of multicomponent mixtures of gases in porous solids, Chem. Eng. J. Biochem. Eng. J. 57 (1995) 91–99.

[34] B. Todd, J.B. Young, Thermodynamic and transport properties of gases for use in solid oxide fuel cell modelling, J. Power Sources. 110 (2002) 186–200.

[35] R.B. Bird, W.E. Steward, E.N. Lightfoot, Transport phenomena, Wiley, New York, 1960.

[36] W.G. Bessler, A new computational approach for SOFC impedance from detailed electrochemical reaction–diffusion models, Solid State Ionics. 176 (2005) 997–1011.

[37] D. Chen, Z. Lin, H. Zhu, R.J. Kee, Percolation theory to predict effective properties of solid oxide fuel-cell composite electrodes, J. Power Sources. 191 (2009) 240–252.

[38] A. Bieberle, L.J. Gauckler, State-space modeling of the anodic SOFC system Ni , H2–H2O|YSZ, Solid State Ionics. 146 (2002) 23–41.

[39] W.G. Bessler, Rapid impedance modeling via potential step and current relaxation simulations, J. Electrochem. Soc. 154 (2007) B1186–B1191.

[40] P. Hofmann, K.D. Panopoulos, Detailed dynamic solid oxide fuel cell modeling for electrochemical impedance spectra simulation, J. Power Sources. 195 (2010) 5320–5339.

[41] D.G. Scott, Packing of spheres: Packing of equal spheres, Nature. 188 (1960) 908–909.

[42] G.T. Nolan, P.E. Kavanagh, Computer simulation of random packing of hard spheres, Powder Technol. 72 (1992) 149–155.

[43] D. Bouvard, F.F. Lange, Relation between percolation and particle coordination in binary powder mixtures, Acta Metall. Mater. 39 (1991) 3083–3090.

[44] A. Bertei, C. Nicolella, A comparative study and an extended theory of percolation for random packings of rigid spheres, Powder Technol. 213 (2011) 100–108.

[45] J.H. Nam, D.H. Jeon, A comprehensive micro-scale model for transport and reaction in intermediate temperature solid oxide fuel cells, Electrochim. Acta. 51 (2006) 3446–3460.

[46] J. Sanyal, G.M. Goldin, H. Zhu, R.J. Kee, A particle-based model for predicting the effective conductivities of composite electrodes, J. Power Sources. 195 (2010) 6671–6679.

[47] W. Kiatkittipong, T. Tagawa, S. Goto, S. Assabumrungrat, P. Praserthdam, Oxygen transport through LSM/YSZ/LaAlO system for use of fuel cell type reactor, Chem. Eng. J. 106 (2005) 35–42.

[48] J.R. Ferguson, J.M. Fiard, R. Herbin, Three-dimensional numerical simulation for various geometries of solid oxide fuel cells, J. Power Sources. 58 (1996) 109–122.

[49] A. Bertei, Chapter 3 of this Thesis, 2013.

[50] R. Radhakrishnan, A. V. Virkar, S.C. Singhal, Estimation of charge-transfer resistivity of $La_{0.8}Sr_{0.2}MnO_3$ cathode on $Y_{0.16}Zr_{0.84}O_2$ electrolyte using patterned electrodes, J. Electrochem. Soc. 152 (2005) A210–A218.

[51] M.G.H.M. Hendriks, J.E. Elshof, H.J.M. Bouwmeester, H. Verweij, The electrochemical double-layer capacitance of yttria-stabilised zirconia, Solid State Ionics. 146 (2002) 211–217.

[52] L.C.R. Schneider, C.L. Martin, Y. Bultel, L. Dessemond, D. Bouvard, Percolation effects in functionally graded SOFC electrodes, Electrochim. Acta. 52 (2007) 3190–3198.

[53] A. Bertei, B. Nucci, C. Nicolella, Engineered electrode microstructure for optimization of solid oxide fuel cells, Chem. Eng. Trans. 32 (2013) 2293–2298.

Chapter 3

Electrochemical Modeling of Unconventional SOFCs

This Chapter presents a steady–state electrochemical model of an innovative SOFC, called IDEAL–Cell, which shows mixed ionic conduction. Other interesting phenomena are considered, such as the incorporation of water in the proton–conducting phase and the dependence of protonic conductivity from water partial pressure. The thermodynamics and electrochemistry of the system are analyzed. Effective properties are calculated with the extended percolation theory.

The study highlights that:

i. the presented electrochemical modeling framework is applicable also to unconventional SOFCs;

ii. empirical correlations for the estimation of effective conductivity, which do not take into account particle overlap (i.e., the contact angle), are inappropriate;

iii. the cell performance can be substantially enhanced by optimizing the morphological parameters.

This Chapter was adapted from the paper "Mathematical modeling of mass and charge transport and reaction in a solid oxide fuel cell with mixed ionic conduction" by A. Bertei, A.S. Thorel, W.G. Bessler and C. Nicolella, published in Chem. Eng. Sci. 68 (2012) 606–616.

Abstract

A mathematical model for the description of transport phenomena and reactions in an innovative solid oxide fuel cell (called IDEAL–Cell) under steady–state conditions is presented. This cell is characterized by an intermediate porous composite layer, called central membrane, between cathodic and anodic compartments, which shows mixed conduction of protons and oxygen ions and offers active sites for their recombination to form water vapor. This study presents an original model of charge transport and reaction in the central membrane. The model, based on local mass and charge balances, accounts for mixed conduction in the solid phases, diffusion and convection in the gas phase, and reaction at the solid/gas interface. The model domain is resolved in a continuum approach by using effective properties related to morphology and material properties through percolation theory. The model predictions are successfully compared with experimental data, which provide an estimate of the kinetic parameter of the water recombination reaction. Simulations show a strong dependence of predicted results on the kinetic constant of the water incorporation reaction and the effective conductivities. A design analysis on porosity, thickness, particle dimension, composition of central membrane and cell radius is performed and an optimal membrane design is obtained.

3.1 Introduction

Fuel cells are electrochemical devices which convert the chemical energy of a combustible and a combustive agent (e.g., hydrogen and air, respectively) directly into electric energy, without passing through a Carnot thermodynamic cycle, thus increasing the energetic efficiency of the process and reducing pollution levels in exhaust gases [1]. Among various types of fuel cells, Solid Oxide Fuel Cells (SOFCs) and Proton Conducting Solid Oxide Fuel Cells (PCFCs) have attracted research and technology interest due to high expected performance and efficiency.

The Innovative Dual mEmbrAne fueL Cell (IDEAL–Cell) is a new SOFC concept operating in the temperature range of 600–700°C [2]. It consists in the junction between the anodic part of a PCFC (i.e., anode and dense protonic electrolyte) and the cathodic part of an SOFC (i.e., cathode and dense anionic electrolyte) through a porous composite layer, called central membrane (CM), made of proton–conducting and anion–conducting phase. At the anode, hydrogen is converted into protons while at the cathode molecular oxygen is converted into oxygen ions. Protons and oxygen ions migrate through their respective electrolytes towards the CM wherein they react to produce water vapor (Figure 3.1).

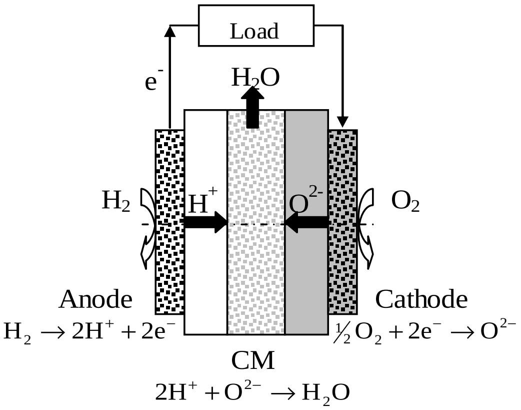

Figure 3.1 – Schematic diagram of the IDEAL–Cell (Innovative Dual mEmbrAne fueL Cell) configuration.

The water recombination reaction occurs in the CM rather than at one of electrodes as in common SOFC and PCFC configurations. As a consequence, the generation of corrosive mixtures of water with hydrogen or oxygen is avoided, safeguarding the interconnect materials. At the electrodes water vapor does not dilute reactants, thus they can be recycled without any treatment, while pure water and heat can be recovered from the CM. In principle, the IDEAL–Cell performance can be improved beyond either SOFC and PCFC performance since anode, cathode and CM are independent and can therefore be fully optimized for their individual purposes, that is, the delivery and conversion of reactants into ions at the electrodes and production and discharge of water vapor in the CM.

The CM represents the main innovative component of the IDEAL–Cell since electrodes are similar to those used in SOFC and PCFC configurations. The CM shows mixed conduction of oxygen ions and protons. Within the layer, ions react at the active sites to produce water vapor, which leaves the CM through the pores. The CM is an electrochemical system in which mixed ionic conduction, mass transport in the gas phase and reaction simultaneously occur. Mixed ionic conduction and water recombination from protons and oxygen ions are the peculiar features of the IDEAL–Cell. They do not occur neither in SOFC nor in PCFC, and for this reason they have not attracted attention before.

Due to mixed ionic–protonic conduction in the CM, the IDEAL–Cell is an original concept of a fuel cell with three chambers for separately feeding fuel (at the anode) and air (at the cathode) and removing produced water (at the CM). This cell concept was demonstrated by a set of dedicated experiments [2]. Being the objective of these experiments the proof of concept of the IDEAL–Cell, the cell design was not optimized, resulting in thick layers for different compartments and poor electrochemical performance. Much effort is currently being dedicated to the shaping of more efficient cells, and the objective of the presented model is, besides allowing more fundamental interpretation of the experimental findings, to provide a tool to support material and cell design. To this end, a mathematical model for the description of simultaneous mixed ionic conduction and electrochemical reaction in a porous composite layer is developed. The model is based on charge and mass balances in a continuum approach, which describes the porous composite structure as a continuum characterized by effective transport and kinetic parameters (conductivities, reaction constants, gas diffusivities, etc.). Despite its simplifications, this approach has been employed in several modeling studies of composite electrodes yielding valuable results [3–8]. The continuum model is then a mechanistic model, that is, based on the physical and chemical representation of the phenomena involved in the cell, which describes the reacting system by local partial–differential balance equations for species participating to the reactions.

The presented model is the extension and the refinement of a previous model of the CM [9]. In particular, the current model is able to reproduce the experimental behavior of the IDEAL–Cell and to elucidate the key factors (e.g., structural and geometrical parameters, operating conditions, etc.) governing the cell performance. Hence, this refined model has been developed in order to reach a better physical description of the system, to focus on sensitive parameters, to perform design analyses for the improvement of cell performances, and finally to extend the results of the existing model (specifically tailored on the CM of the IDEAL–Cell) for description of a general porous composite system showing simultaneous mixed ionic conduction and electrochemical reaction.

3.2 Modeling

3.2.1 General aspects

The CM is a composite layer made of proton–conducting and anion–conducting particles randomly distributed and sintered to give enough porosity for water removal. The recombination reaction between protons, coming from the anodic compartment and carried by the proton–conducting phase (PCP), and oxygen ions, coming from the cathodic compartment and carried by the anion–conducting phase (ACP), occurs at the three–phase boundary (TPB) among PCP, ACP and gas phase where reactants and products may coexist (Figure 3.2a):

$$2H^{+}_{(PCP)} + O^{2-}_{(ACP)} \leftrightarrow H_2O_{(g)} \tag{3.1}$$

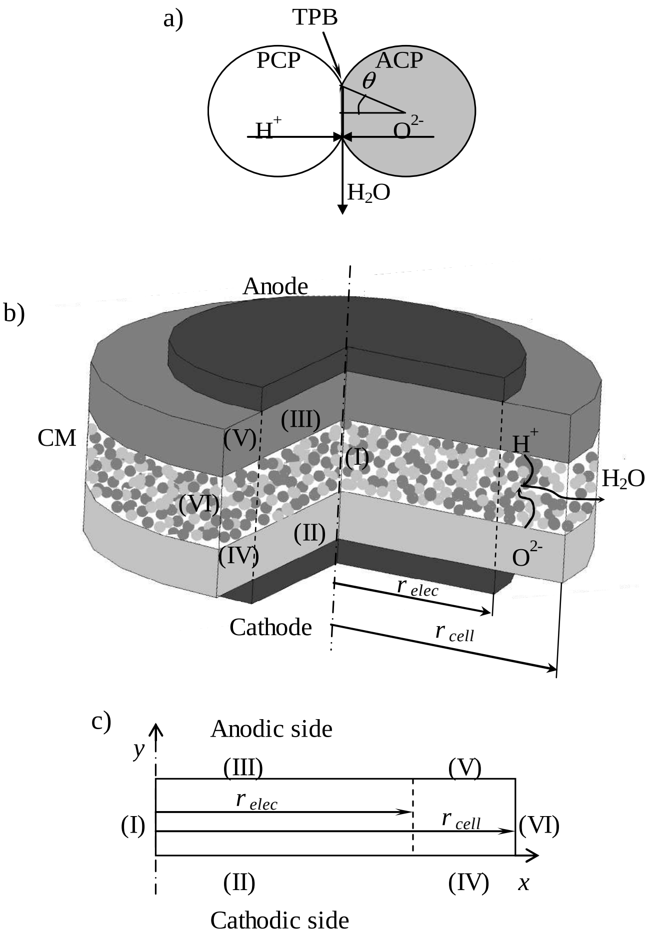

Figure 3.2 – a) Recombination reaction at the three–phase boundary (TPB). b) schematic diagram of the cylindrical geometry of the IDEAL–Cell. In the central membrane, protons and oxygen ions react at the TPBs and the produced water vapor leaves in the radial direction. c) Schematic representation of the CM domain in the continuum approach with boundary identification numbers (the dotted line represents the electrode projection).

The recombination reaction can take place at any TPB location provided that the gas phase and the two conducting phases are connected with their respective bulk phases via percolating networks (Figure 3.2b). As a consequence, transport of both molecular and ionic species through their respective conducting phases must be considered.

Due to large length–scale disparities (ranging from tenths of millimeters at cell level to fractions of micrometers at particle level) and complex microscopic structure, the model is developed by using the continuum (also called macro–homogeneous) approach, which describes the composite structure as a homogeneous continuum. Homogenization enables an approximate representation within a representative volume of the CM that is small relative to the overall dimensions but large compared to the microstructure. The composite structure is characterized by effective properties (e.g., conductivities, mean pore diameter, TPB length per unit volume) related to microstructure and material properties through percolation theory. As a result, the model consists of a set of continuum partial–differential equations, with particle–level detail represented through effective material properties [5,10].

The CM model is based on the following main assumptions (further assumption will be given in the following Sections):

i. steady–state conditions;

ii. the CM is modeled as a continuum and its morphology is assimilated to a random packing of monosized spherical particles partly overlapping; effective parameters are assumed to be uniform throughout the CM;

iii. isothermal conditions: temperature is uniform throughout the CM and heat effects are neglected;

iv. mixed conduction of both ionic species is neglected in both solid phases, that is, PCP conducts only protons and ACP only oxygen ions.

In the following Sections, the submodels regarding morphology, electrochemistry, and transport phenomena are developed and discussed.

3.2.2 Morphological model

In order to obtain parameters required for the continuum approach, we apply particle–based morphological models and percolation theory. The CM is assumed to be a random binary packing of monosized spherical particles of the two conducting phases. Assuming that the gas phase is entirely connected in the range of porosity investigated [11], the connected TPB length per unit volume λ^v_{TPB}, the PCP surface area exposed to gas phase per unit volume a^v_{TPB} and the mean pore diameter d_p are estimated by using percolation theory according to Bertei and Nicolella [12,13] as a function of particle size and volume fraction of conducting phases.

Effective conductivities are estimated by computer simulations of random packings of overlapping spheres. The composite microstructure is generated by assembling a relatively small set of particles (hundreds of particles) into a cubical region. A random position for each PCP and ACP particle is assigned in a body–centered cubic structure according to their relative volume fraction providing porosity and coordination number of particles consistent to those related to close random packings of spheres [14]. Particle radii are then expanded to achieve an overlap characterized by the contact angle θ (see Figure 3.2a). Effective conductivities are evaluated by using the finite element method solving the Ohm law within the conducting phases as a function of composition and contact angle.

In Figure 3.3, the effective conductivity factor, defined as the ratio between the effective and the material–specific conductivities, estimated according to the method described above, is compared to that evaluated by Sanyal et al. [15], who used a computer simulation method based on a numerical reconstruction to generate a random packing of particles. Results are referred to a binary mixture of particles of the same size with a contact angle of 15 °, as often used in mathematical models of composite electrodes [3,4,15,16], and a porosity of 32 %. The results obtained by using our simplified simulation method are consistent and in quite good agreement with Sanyal et al. [15] results.

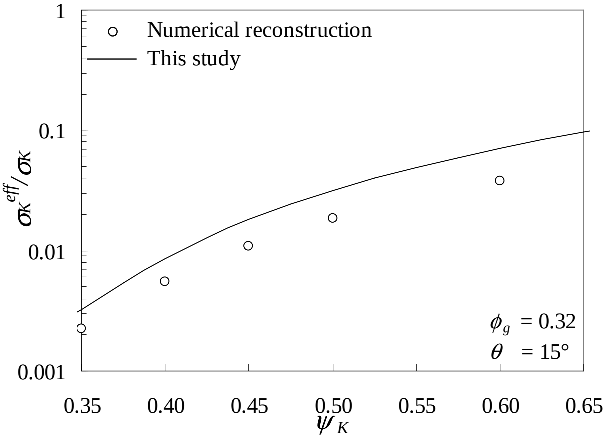

Figure 3.3 – Comparison between effective conductivity factors obtained by numerical reconstruction method [15] and by our simulation method for a binary mixture of monosized particles with contact angle 15° and porosity 32%.

3.2.3 Thermodynamics and kinetics

The local equilibrium of the reaction reported in Eq. (3.1) is described by the balance of electrochemical potentials of species participating to the reaction [17]:

$$2\tilde{\mu}^{eq}_{H^+(PCP)} + \tilde{\mu}^{eq}_{O^{2-}(ACP)} = \tilde{\mu}^{eq}_{w(g)} \tag{3.2}$$

in which each electrochemical potential is the sum of the standard chemical potential, the activity term and the electric potential term:

$$\tilde{\mu}^{eq}_{i(K)} = \mu^{0}_{i(K)} + R_g T \ln(a^{eq}_{i(K)}) + j_i F V^{eq}_{K} \tag{3.3}$$

where i refers to the species, j_i to its charge, $a_{i(K)}$ to its activity, K to the phase to which the species belongs, V_K is the electric potential of the phase. By rewriting Eq. (3.2) through Eq. (3.3), the local absolute equilibrium voltage difference between conducting phases may be expressed as:

$$\Delta V_{abs}^{eq} = V_{ACP}^{eq} - V_{PCP}^{eq} = -\frac{\Delta G_{CM}^{0}}{2F} - \frac{R_g T}{2F} \ln\left(\frac{p_w / p_w^0}{a_{H^+(PCP)}^2 \, a_{O^{2-}(ACP)}} \right) \tag{3.4}$$

where water activity is explicitly expressed as the ratio of water vapor partial pressure (p_w) and standard pressure (p_w^0) while the standard Gibbs free energy is the algebraic sum of standard chemical potentials of participating species. Note that Eq. (3.4) represents the Nernst law for the reaction in Eq. (3.1).

Eq. (3.4), which represents the local voltage difference at equilibrium, can be used to calculate the open–circuit voltage difference for the CM. At open–circuit equilibrium, local conditions are uniform and, in particular, the local water vapor partial pressure is equal to the external water vapor partial pressure p_w^{ex}. Application of Eq. (3.4) under these conditions yields:

$$\Delta V_{abs}^{eq,ex} = -\frac{\Delta G_{CM}^{0}}{2F} - \frac{R_g T}{2F} \ln\left(\frac{p_w / p_w^0}{a_{H^+(PCP)}^2 \, a_{O^{2-}(ACP)}} \right) \tag{3.5}$$

By subtracting Eq. (3.5) from Eq. (3.4) and assuming that activities of protons and oxygen ions are unity since they are not function of external conditions (i.e., activities are assumed to depend only on temperature and material properties), a relative local equilibrium voltage difference is obtained:

$$\Delta V^{eq} = -\frac{R_g T}{2F} \ln\left(\frac{p_w}{p_w^{ex}} \right) \tag{3.6}$$

In the following model, we use only the relative equilibrium voltage difference given in Eq. (3.6) since the Gibbs free energy of reaction Eq. (3.1) is unknown.

Since kinetic studies on the materials used in the IDEAL–Cell have not been developed yet, a macroscopic Butler–Volmer type kinetic approach without mass–transfer effects is assumed [17]:

$$i_{TPB} = i_0 \left\{ \exp\left(\alpha \frac{F}{R_g T} \eta \right) - \exp\left(-(1-\alpha) \frac{F}{R_g T} \eta \right) \right\} \tag{3.7}$$

where i_{TPB} represents the current density per unit of TPB length (related to the current density exchanged per unit volume through a morphological parameter, i.e., the TPB length per unit volume λ^{v}_{TPB}), i_0 the exchange current per unit of TPB length, α the transfer coefficient and η the overpotential, which is defined as:

$$\eta = \Delta V^{eq} - \left(V_{ACP} - V_{PCP}\right) \tag{3.8}$$

The reaction kinetics is expressed in the direction of water production for positive overpotentials.

3.2.4 Gas transport

Water vapor is produced according to Eq. (3.1) and it is removed from the cell through the porosity of the CM. In the pores, a carrier inert gas (e.g., nitrogen) could also be present, which is used to carry away water from the cell in order to reduce concentration losses in the CM and to increase the open–circuit voltage according to the Nernst law. On the other hand, as discussed later in Section 3.2.6, a decrease in water partial pressure may lead to a decrease in proton conductivity. However, in principle the overall cell performance increases if the gain in the open–circuit voltage is higher than the polarization loss due to the decrease in proton conductivity.

Mass transport is described according to the dusty–gas model for transition region [18,19], taking into account convection (Darcy flow) and diffusion (both ordinary and Knudsen diffusion) of water vapor and carrier gas. Surface diffusion of adsorbed species is neglected and the gas phase is assumed to be ideal considering the high temperature and the relatively low pressure.

According to the dusty–gas model, the net molar fluxes of water (*w*) and carrier (*c*) are described as a function of pressure P and water vapor molar fraction x_w:

$$N_{w,g}\left(\frac{1}{D_w^{K,eff}} + \frac{1-x_w}{D_{wc}^{eff}}\right) = \frac{x_w}{D_{wc}^{eff}} N_{c,g} - \frac{P}{R_g T}\nabla x_w - \frac{x_w}{R_g T}\left(1 + \frac{P}{\mu}\frac{B}{D_w^{K,eff}}\right)\nabla P \tag{3.9}$$

$$N_{c,g}\left(\frac{1}{D_c^{K,eff}} + \frac{x_w}{D_{wc}^{eff}}\right) = \frac{1-x_w}{D_{wc}^{eff}} N_{w,g} + \frac{P}{R_g T}\nabla x_w - \frac{1-x_w}{R_g T}\left(1 + \frac{P}{\mu}\frac{B}{D_c^{K,eff}}\right)\nabla P \tag{3.10}$$

Effective diffusion coefficients, both ordinary and Knudsen, are used, by correcting for the porosity ϕ_g and the tortuosity factor τ_g of the gas phase [19]:

$$D_{wc}^{eff} = \frac{\phi_g}{\tau_g} D_{wc} \tag{3.11}$$

$$D_i^{K,eff} = \frac{\phi_g}{\tau_g} D_i^K \quad \text{where } D_i^K = \frac{4}{3} d_p \sqrt{\frac{R_g T}{2\pi M_i}} \quad \text{for } i = w, c \tag{3.12}$$

where the binary diffusion coefficient in Eq. (3.11) is calculated by using the Fuller correlation [20]. In Eq. (3.12) M_i is the molecular weight of the species (water or carrier).

In Eqs. (3.9) and (3.10), μ is the dynamic viscosity of the gaseous mixture, calculated by using the Herning and Zipperer method [20], while B represents the permeability coefficient, which is calculated using the Blake–Kozeny form of the Darcy law [21]:

$$B = \frac{{D_p}^2}{150} \frac{\phi_g^3}{\left(1-\phi_g\right)^2} \tag{3.13}$$

where D_p represents the mean particle diameter, related to the mean pore diameter as [21]:

$$D_p = \frac{3}{2} \frac{\left(1-\phi_g\right)}{\phi_g} d_p \tag{3.14}$$

The Blake–Kozeny form is an empirical form of the Darcy law specifically developed for porous media, such as packing of spherical particles. The numerical constant 150 in Eq. (3.13) is empirically determined as the average of hundreds of measurements on systems with different particle size and porosity.

In this work, we propose to estimate the tortuosity factor in Eqs. (3.11) and (3.12) by comparing the permeability given by the Blake–Kozeny correlation (Eq. (3.13)) with the corresponding expression used for estimating the viscous (non–separative) component of flow (i.e., due to gradient of total pressure [22]), as defined by the dusty–gas model [18,19]:

$$B = \frac{\phi_g}{\tau_g} \frac{{d_p}^2}{32} \tag{3.15}$$

By comparing Eqs. (3.13) and (3.15), the tortuosity factor results as:

$$\tau_g = \frac{2^2 \cdot 150}{3^2 \cdot 32} = 2.083 \tag{3.16}$$

3.2.5 Water incorporation and transport in PCP

Some proton–conducting materials, in particular those based on the perovskite structure, show to incorporate and transfer water in the solid phase [23–26]. This is the case for the PCP material used in the present study.

Water is incorporated into the PCP bulk in the form of protonic defects according to the following reaction [24], written in Kröger–Vink notation:

$$H_2O_{(g)} + V^{\bullet\bullet}_{O(PCP)} + O^{x}_{O(PCP)} \leftrightarrow 2OH^{\bullet}_{O(PCP)} \tag{3.17}$$

where $V_O^{\cdot\cdot}$ represents an oxygen vacancy, O_O^x an oxygen ion in the lattice and $OH_O^{\bullet}$ a protonic defect. According to Eq. (3.17), the concentration of incorporated water is equal to a half of protonic defect concentration. Molar concentrations of oxygen ions in the lattice (c_O) and oxygen vacancies (c_{VO}) can be expressed as a function of molar concentration of protonic defects per unit mole of perovskite cell (c_{OH}) as follows [24]:

$$c_{VO} = \frac{S - c_{OH}}{2} \tag{3.18}$$

$$c_{VO} = \frac{S - c_{OH}}{2} \tag{3.19}$$

where S represents the dopant level of the proton–conducting perovskite material. Hence, the thermodynamic constant of the water incorporation reaction becomes [24]:

$$K_w = \frac{{c_{OH}}^2}{p_w c_O c_{VO}} = \frac{4{c_{OH}}^2}{p_w\left(S - c_{OH}\right)\left(6 - S - c_{OH}\right)} \tag{3.20}$$

To the best of our knowledge, the kinetics of the water incorporation reaction is unknown. Consequently, a global kinetic expression, consistent with the equilibrium stated in Eq. (3.20), is assumed for the molar rate of water incorporation per unit of PCP surface:

$$v_{inc} = k_d\, p_w c_{VO} c_O - \frac{k_d}{K_w} {c_{OH}}^2 \tag{3.21}$$

where k_d is the kinetic constant of water incorporation reaction and c_{VO} and c_O are expressed as in Eqs. (3.18) and (3.19).

The diffusion of protonic defects (i.e., water) within the PCP can be described by the Fick law [25]:

$$N_{w,PCP} = -D^{eff}_{w,PCP} \nabla C_{w,PCP} \tag{3.22}$$

The water diffusion coefficient is estimated according to Coors [25] as a function of self–diffusivities of protonic defects and oxygen vacancies as well as of protonic defects concentration. It is corrected for porosity and tortuosity of the PCP phase in the same way described in Section 3.2.2 for the PCP conductivity. The volume concentration of incorporated water $C_{w,PCP}$ is related to the molar concentration of protonic defects as:

$$c_{OH} = 2\frac{C_{w,PCP}}{\delta} \tag{3.23}$$

where δ is the molar density of perovskite unit cells per unit volume. Eq. (3.23) allows the calculation of molar concentration, thermodynamic constant and kinetic rate of water incorporation reaction (Eqs. (3.18–3.21)) as a function of $C_{w,PCP}$.

Both water incorporation kinetics and diffusion are assumed to be independent of the electric potential of the PCP phase.

3.2.6 Charge transport

Transport of protons and oxygen ions in PCP and ACP, respectively, is assumed to follow the Ohm law:

$$N_{H^+} = -\frac{\sigma_{PCP}^{eff}}{F}\nabla V_{PCP} \tag{3.24}$$

$$N_{O^{2-}} = \frac{\sigma_{ACP}^{eff}}{2F}\nabla V_{ACP} \tag{3.25}$$

where effective conductivities are considered.

The PCP conductivity is not spatially constant. Instead, the local PCP conductivity is linearly dependent on the concentration of protonic defects according to the Nernst–Einstein equation [17]:

$$\sigma_{PCP} = \sigma_{PCP}^{sat}\frac{c_{OH}}{S} \tag{3.26}$$

in which σ_{PCP}^{sat} is the conductivity at the saturation limit, that is, when the concentration of protonic defects is maximum and equal to S. According to Eqs. (3.20) and (3.17), given the temperature and the material, at equilibrium the molar concentration of protonic defects is a non–linear function of water vapor partial pressure. In particular, c_{OH} increases as the water vapor partial pressure increases until a saturation limit, determined by the dopant level S, is approached. Beyond this limit, a further increase in the water vapor partial pressure does not lead to any increase in c_{OH}, that is, in proton conductivity. As already stated in Section 3.2.4, in such a case the use of a carrier gas in the CM can increase the cell performance since the lack of water vapor leads to a gain in the open–circuit voltage without any decrease in the proton conductivity.

3.2.7 Governing equations and boundary conditions in the CM

The model consists of the system of molar balance equations for the five species involved in the CM (protons in PCP, oxygen ions in ACP, water incorporated in PCP, water vapor and carrier gas in gas phase):

$$\nabla \cdot N_{H^+} = -\frac{i_{TPB}\lambda_{TPB}^{v}}{F} \qquad \text{(protons in PCP)} \qquad (3.27)$$

$$\nabla \cdot N_{O^{2-}} = -\frac{i_{TPB}\lambda_{TPB}^{v}}{2F} \qquad \text{(oxygen ions in ACP)} \qquad (3.28)$$

$$\nabla \cdot N_{w,PCP} = v_{inc} a_{PCP}^{v} \qquad \text{(water incorporated in PCP)} \qquad (3.29)$$

$$\nabla \cdot N_{w,g} = \frac{i_{TPB}\lambda_{TPB}^{v}}{2F} - v_{inc} a_{PCP}^{v} \qquad \text{(water vapor in gas phase)} \qquad (3.30)$$

$$\nabla \cdot N_{c,g} = 0 \qquad \text{(carrier in gas phase)} \qquad (3.31)$$

The model is developed for a cylindrical cell design (see Figure 3.2b). Due to the axial symmetry, the governing equations are applied to the CM domain in 2D (Figure 3.2c).

Boundary conditions are applied according to Figure 3.2c. The boundary identification numbers are also reported in Figure 3.2b for the sake of clarity. Symmetry conditions are considered at boundary (I), insulating conditions at boundaries (IV) and (V). At boundary (II) we define V_{ACP} as reference potential (V_{ACP} = 0) while at boundary (III) the condition $V_{PCP} = \eta_{CM}$ is set, where η_{CM} represents the overpotential applied to the whole CM. External conditions are applied at boundary (VI) ($P = P^{ex}$ and $x_w = x_w^{ex}$) coupled with the desorption of water from PCP ($\hat{n} \cdot N_{w,PCP} = -\phi_{PCP} v_{inc}$, where ϕ_{PCP} is the fraction of PCP volume to the total volume, including void volume, and $\hat{n}$ the exiting unitary vector). Transport of incorporated water inside PCP is considered at boundary (III) in a simplified form as:

$$\hat{n} \cdot N_{w,PCP} = \phi_{PCP} \overline{D}_{w,PCP} \frac{C_{w,PCP} - C_{w,PCP}^{an}}{t_{AE}} \qquad (3.32)$$

where $\overline{D}_{w,PCP}$ represents the mean water diffusivity in PCP across the electrolyte, t_{AE} the anodic electrolyte thickness and $C_{w,PCP}^{an}$ the concentration of incorporated water at anode–anodic electrolyte interface.

3.3 Results and discussion

The model of the CM, that is, the system of Eqs. (3.27–3.31) coupled with relationships of fluxes and kinetics, is implemented and solved by using COMSOL Multiphysics 3.5 (based on the finite element method) in 2D due to the symmetry of the geometry. The main model outcome is i_{tot}, that is, the total current density flowing through the axial direction of the CM referred to electrode or cell area. Cell and CM polarization resistances (Rp_{cell} and Rp_{CM}), that is, the main performance indexes, are respectively defined as the ratio of either cell or CM overpotential and the total current density. In addition, the model solution includes the values of field variables (e.g., pressure, overpotential, PCP and ACP electric potentials, etc.), fluxes and other desired quantities in the domain.

3.3.1 Comparison with experimental data

The IDEAL–Cell concept was proven in a single set of dedicated experiments [2], which are used in this work as a term of comparison in order to verify model assumptions.

The model is compared with experimental data measured at 873K on a non–optimized cell used for proofing the IDEAL–Cell concept [2]. In the same test series, also the polarization resistances of platinum electrodes were singularly measured. Yttria–doped barium cerate (BCY15) was used as PCP, yttria–doped ceria (YDC15) as ACP and nitrogen as carrier gas. Although BCY15 is known to be a good conductor for both protons and oxygen ions, its oxygen ion conductivity will be significantly lower than proton conductivity due to the absence of molecular oxygen and the presence of water vapor [27]. Therefore, mixed conduction of both ionic species in PCP can reasonably be neglected accordingly with the assumption done in Section 3.2.1.

Sample and working conditions are shown in Table 3.1, and the main model parameters used in simulation are shown in Table 3.2. Physical properties for gas and water transport in PCP are taken respectively from Todd and Young [20] and from Coors [25], while the thermodynamic constant K_w is taken from Kreuer [24] for BCY10. Since BCY15 is used as PCP, the density of perovskite–cells δ is equal to $19594 \mathrm{mol \cdot m^{-3}}$. The contact angle is assumed equal to 15° as commonly accepted [3,4,15,16] for calculation of effective morphological parameters as described in Section 3.2.2.

Table 3.1 – Sample and working conditions used for the comparison of the model with experimental data [2].

Parameter	*Value*
Materials	
PCP	BCY15
ACP	YDC15
Electrodes	Platinum
Cell geometric parameters	
CM thickness	600μm
Anodic electrolyte thickness	1400μm
Cathodic electrolyte thickness	1000μm
Cell radius	5mm
Electrode radius	2mm
CM morphological parameters	
Proton–conducting particle radius	0.15μm
Anion–conducting particle radius	0.15μm
Pore–former radius	0.75μm
Porosity	0.53
PCP solid volume fraction	0.50
Working conditions	
Temperature	873K
CM external pressure	1bar
CM external water vapor molar fraction	$5.406\cdot 10^{-4}$
Water vapor partial pressure at anode	0.03bar

Table 3.2 – Main model parameters used in the comparison of the model with experimental data.

Parameter	*Value*
Conductivities	
PCP (saturation)	$1.9844\mathrm{S}\cdot\mathrm{m}^{-1}$ [28]
ACP	$1.5488\mathrm{S}\cdot\mathrm{m}^{-1}$ [29]
Polarization resistances	
Anode	$3.0\cdot 10^{-4}\Omega\cdot\mathrm{m}^2$ [2]
Cathode	$4.2\cdot 10^{-4}\Omega\cdot\mathrm{m}^2$ [2]
Morphological parameters	
Contact angle	15° [3,4,15,16]
Kinetic parameters	
Exchange current	$3\cdot 10^{-8}\mathrm{A}\cdot\mathrm{m}^{-1}$
Kinetic constant water incorporation reaction	$5\cdot 10^{-12}\mathrm{mol}\cdot\mathrm{m}^{-2}\cdot\mathrm{Pa}^{-1}\cdot\mathrm{s}^{-1}$
Transfer coefficient	0.5

In the following, we compare our own method to estimate effective conductivity (see Section 3.2.2) with two different formulations that have been proposed earlier:

$$\frac{\sigma_K^{eff}}{\sigma_K} = \frac{0.5 \cdot (\zeta_K - \zeta_{K-th})^2}{(1 - \zeta_{K-th})^2} \tag{3.33}$$

$$\frac{\sigma_K^{eff}}{\sigma_K} = \left((1 - \phi_g) \psi_K \gamma_K \right)^{1.5} \tag{3.34}$$

Eq. (3.33) is the Costamagna et al. [3] correlation in which ζ_K represents the numerical fraction of K–phase particles and ζ_{K-th} the numerical fraction corresponding to the percolation threshold, while Eq. (3.34) is the Nam and Jeon [16] correlation where ψ_K represents the solid volume fraction of phase K and γ_K its connection probability, calculated according to Bertei and Nicolella [13].

Figure 3.4 shows the comparison between experimental and simulated polarization curves; current density is normalized to electrode area. The exchange current i_0 of the recombination reaction Eq. (3.1) is evaluated as the best fit to experimental data for each individual method used for the estimate of effective conductivity factors. Table 3.3 shows effective conductivity factors and kinetic parameters obtained from the different methods.

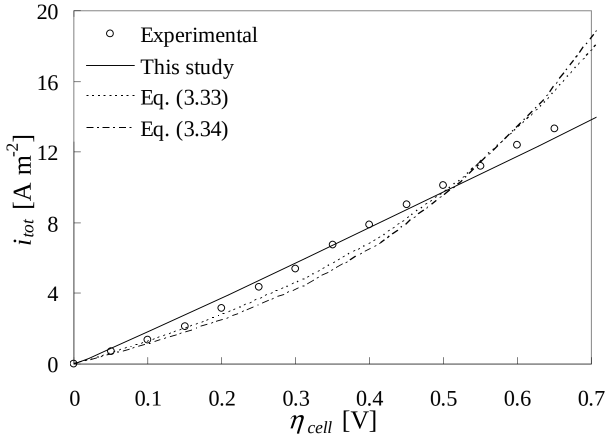

Figure 3.4 – Comparison of models using different correlations for the effective conductivity with experimental data [2].

The highest exchange current results from using our morphological model since it predicts the lowest effective conductivity providing an ohmic regime condition as reflected by experimental data. In particular, the kinetic contribution to CM polarization resistance is 9.7% as calculated from simulation. In addition, the simulation predicts that the 95.5% of the cell polarization losses are due to the CM.

On the other hand, the two morphological models in Eqs. (3.33) and (3.34) predict higher effective conductivity providing a lower exchange current, which yields a higher kinetic contribution to the cell polarization resistance and an exponential shape of simulated polarization curves.

Because our own morphological model yields good agreement with experimental data, it will be used in the remainder of this Section.

Being the experimental data on IDEAL–Cell available so far rather limited, the comparison shown here cannot provide a thorough validation of the model. In particular, the model was not tested on different cell designs and operating conditions. More detailed experimental information is required to estimate unknown parameters and to extensively validate the model. However, the satisfactory comparison with available experimental results (see Figure 3.4), as well as the rigorous phenomenological derivation of the model (see Section 3.2), suggest that the model provides sound indications on the effects of key design and structural parameters and operating conditions on cell behavior and performance. To support these indications, a sensitivity analysis and a design analysis are presented in the following Sections.

Table 3.3 – Effective conductivity factors and exchange currents as a result of the best fitting of experimental data used in Section 3.3.1 for different methods used to predict the effective conductivity factor.

Method	σ_K^{eff}/σ_K	i_0
Our method (Section 3.2.2)	$4.653\cdot10^{-3}$	$3\cdot10^{-8}\mathrm{A\cdot m^{-1}}$
Eq. (3.33)	$3.609\cdot10^{-2}$	$8\cdot10^{-11}\mathrm{A\cdot m^{-1}}$
Eq. (3.34)	$9.167\cdot10^{-2}$	$4\cdot10^{-11}\mathrm{A\cdot m^{-1}}$

3.3.2 Sensitivity analysis

The model contains two key parameters for which no reliable values are available, that is, the kinetic constant of water incorporation reaction k_d and the contact angle θ. As reported in Table 3.2, while the latter was set to 15° as commonly accepted in several modeling studies [3,4,15,16], the kinetic constant of water incorporation reaction was set equal to $5\cdot10^{-12}\mathrm{mol\cdot m^{-2}\cdot Pa^{-1}\cdot s^{-1}}$ because, as discussed later in Section 3.3.2.1, it yields a conservative estimate of the cell performance. In order to study the choice of parameter values on the electrochemical behavior, a parameter study was performed as follows. Polarization curves, corresponding to the same conditions used in Section 3.3.1, were simulated individually varying the two unknown parameters. Using a value for the exchange current i_0 equal to $3\cdot10^{-8}\mathrm{A\cdot m^{-1}}$ (see Table 3.2), the cell polarization resistance, calculated in the linear range (in particular, for cell overpotential equal to 0.2V), is simulated as a function of the tested parameter. Subsequently, the exchange current i_0 is determined again as a function of the tested parameter as the best fit to experimental data in order to evaluate how the estimate of the exchange current would have been changed if a different model parameter had been used. In the following figures, simulations using the standard parameters (Table 3.2) are marked with a solid symbol.

3.3.2.1 Variation of water incorporation kinetics

Figure 3.5a shows the cell polarization resistance as a function of the kinetic constant k_d of the PCP water incorporation reaction. As can be observed in this figure, as k_d increases as the cell polarization resistance increases. Two asymptotes, corresponding to an upper and a lower regime of k_d, are identified. At high k_d, water incorporation reaction is fast and the PCP tends to be in equilibrium with the gas phase. The low value of water vapor partial pressure used in the simulations (see Table 3.1 regarding external water vapor molar fraction x_w^{ex}) leads to a low protonic defect concentration, resulting in low proton conductivity of PCP (see Eq. (3.26)) and in high cell polarization resistance. On the other hand, for low k_d values, protonic defect concentration (and PCP conductivity) tends to become independent of gas phase conditions, and to be mainly determined by the mass transport of the incorporated water. As a consequence, the PCP conductivity in the CM is influenced by the anode conditions, where a certain level of humidity has to be maintained to ensure proton conductivity (see Eq. (3.17)). If the water vapor partial pressure in the CM is lower than at the anode (as in the simulations performed in this work, based on the experimental conditions used, see Table 3.1), the overall polarization resistance levels off for low k_d. This situation occurs just in case of low water vapor partial pressure in the CM, and it will not occur for other operating conditions. Low water vapor partial pressure in the gas chamber connected to the CM was required in the experiments performed to prove that water in the IDEAL–Cell is produced in the CM and not at the electrodes [2]. Higher water vapor partial pressure in CM should be expected for normal operation of the cell.

Figure 3.5b shows that for low k_d the refitting to experimental data reduces the exchange current. On the other hand, it becomes impossible to fit experimental data over $k_d = 5 \cdot 10^{-11} \mathrm{mol \cdot m^{-2} \cdot Pa^{-1} \cdot s^{-1}}$ by further increasing i_0. Provided the validity of the model and of the experimental data, and despite other uncertainties that might affect the model comparison with such experimental data (Section 3.3.1), Figure 3.5b states that the kinetic parameter of water incorporation reaction k_d is physically limited below this critical value.

These results show that the water incorporation kinetics into PCP plays an important role in model validation and in simulation results, therefore an accurate estimate is required. Due to the lack of specific kinetic studies, the chosen kinetic constant $k_d = 5 \cdot 10^{-12} \mathrm{mol \cdot m^{-2} \cdot Pa^{-1} \cdot s^{-1}}$ is precautionary since, according to Figure 3.5b, it yields a low estimate of the exchange current i_0.

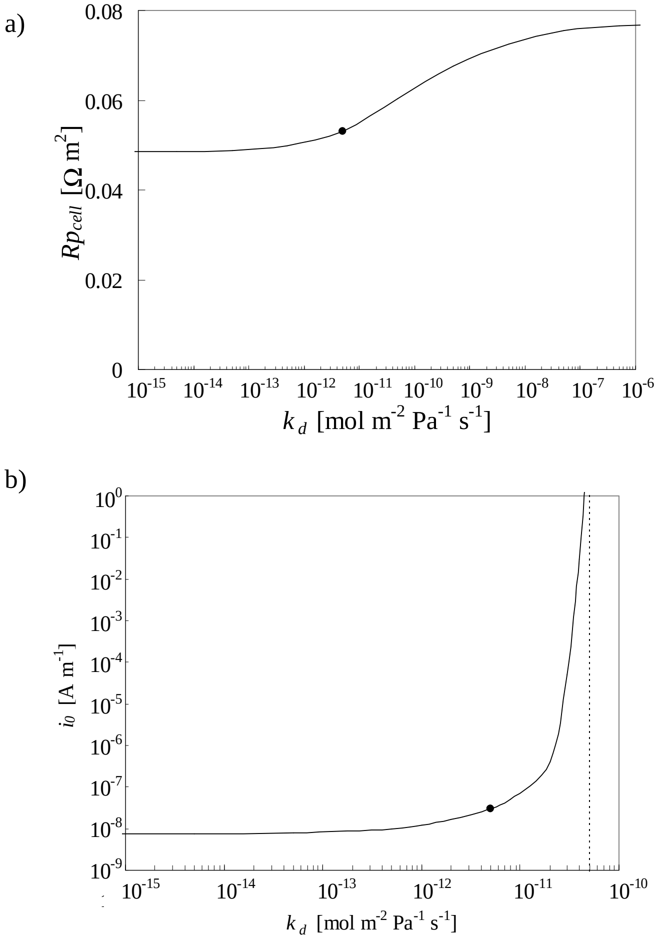

Figure 3.5 – Parameter study of the kinetic constant k_d. a) Cell polarization resistance calculated as a function of k_d under reference conditions; b) sensitivity of exchange current i_0 on k_d resulting from the refitting of experimental data.

3.3.2.2 Variation of contact angle

The contact angle θ affects the estimate of the TPB length per unit volume and the effective conductivity factors, both of which decrease as θ decreases. Regarding the cell polarization behavior, since the kinetic contribution to CM polarization resistance is almost negligible (Section 3.3.1), the effects of contact angle variation will be mainly attributed to the change in effective conductivity.

In Figure 3.6a the almost hyperbolic decrease in cell polarization resistance as θ decreases reflects the linear dependence of the effective conductivity factor (equal for both PCP and ACP since composition and particles dimensions are the same) on the contact angle in the range investigated. Figure 3.6b shows the dependence of the best fit exchange current as a function of contact angle. As θ increases, i_0 decreases because the increase in both effective conductivities and TPB length forces, during refitting, the choice of a lower exchange current to reproduce the experimental behavior. For the same reason, as θ decreases, i_0 increases strongly until reaching a limiting value at $\theta = 13.2°$. Below this limit value it is impossible to obtain good fitting of experimental data since the effective conductivities become too low.

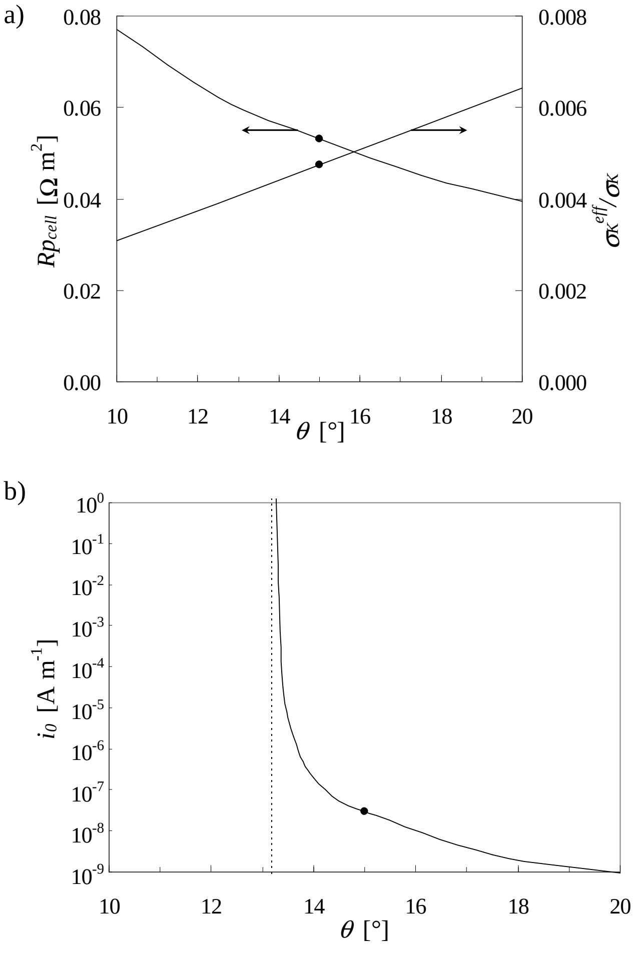

Figure 3.6 – Parameter study of the contact angle θ. a) Cell polarization resistance calculated as a function of θ under reference conditions; b) sensitivity of exchange current i_0 on θ resulting from the refitting of experimental data.

As a conclusion, the contact angle is a key model parameter as it affects primarily the effective conductivity factors which play the main role in determining cell performance since the CM is in ohmic regime. In the following simulations, the standard value of 15° is used [3,4,15,16].

3.3.3 Design analysis

Keeping in mind the need for more rigorous model validation (see Section 3.3.1), the present model is nevertheless used here to determine the best CM design which leads to the minimum CM area–specific polarization resistance, as an indication about how the design parameters affect the CM performance. In this Section, the CM area–specific polarization resistance is referred to the CM area, while in the previous Sections (see Sections 3.3.1 and 3.3.2) it was referred to the electrode area. In the following, the model parameters listed in Table 3.1 and Table 3.2 are used, except for the cell radius (10mm), electrode radius (8mm, i.e., 2mm are left free for sealing), anodic electrolyte thickness (40μm) and external water vapor molar fraction (0.2), as these conditions are more realistic for an optimal design study under realistic conditions.

Figure 3.7 shows the dependence of the CM polarization resistance as a function of porosity and thickness. The minimum porosity investigated is 0.36, corresponding to the porosity of a dense random packing of homologue particles [14,30,31] theoretically obtainable without using pore–formers. At any given porosity, CM polarization resistance shows a minimum (i.e., optimum) with respect to thickness. For lower thicknesses the total number of reaction sites decreases giving an increase in Rp_{CM} due to kinetic activation losses, while for higher thicknesses the ohmic losses become dominant. As the porosity decreases also the minimum polarization resistance decreases due to an increase in PCP and ACP effective conductivities. As a result, the optimum porosity corresponds to the minimum value investigated, i.e., 0.36.

Fixing the porosity to 0.36, Figure 3.8 shows the minimum CM polarization resistance as a function of PCP solid volume fraction. The increase in PCP solid volume fraction leads to an increase in PCP effective conductivity and a decrease in the ACP effective conductivity and vice versa. The combination of these two opposite effects leads again to a minimum of polarization resistance. Since PCP and ACP show similar bulk conductivities under these working conditions and both kinds of particles have the same dimension, the optimal composition corresponds to 50% PCP and 50% ACP of the total volume of solid phases with an optimal CM thickness of 146μm. In addition, this composition corresponds the maximum TPB length per unit volume for monosized particles [13].

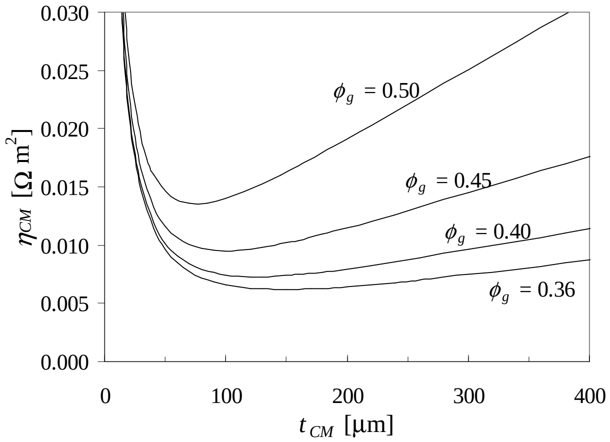

Figure 3.7 – Design analysis on porosity and thickness.

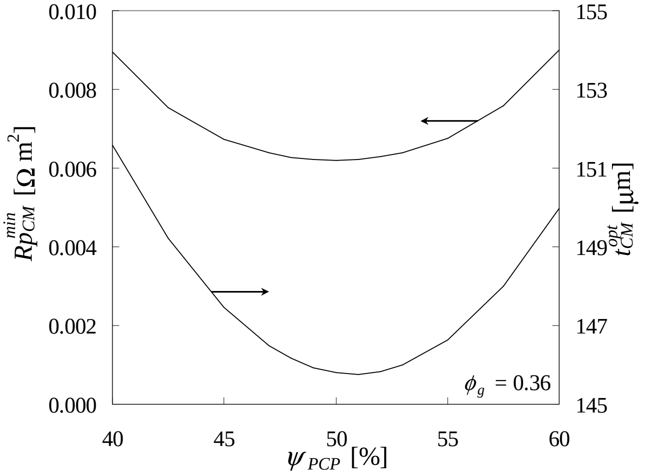

Figure 3.8 – Design analysis on composition: minimum CM polarization resistance and optimal CM thickness as a function of the solid volume fraction of PCP.

The influence of particle size on CM polarization resistance is shown in Figure 3.9. As shown in Figure 3.9a, decreasing particle dimension leads to an improvement in CM performance since both CM polarization resistance and the optimal thickness decrease due to the increased TPB length. Nevertheless, as shown in Figure 3.9b for a reasonable CM overpotential of 0.1V, also the mean pore dimension decreases yielding an increase in total pressure since the permeability becomes smaller (Eq. (3.15)). High pressures within the CM should be avoided to guarantee the mechanical stability of the membrane. Moreover, actually small particles could lead to problems during the sintering, resulting in a smaller porosity that reduces both gas transport and kinetics due to a lower TPB length as a result of a non–percolating pore space. For these reasons, we suggest to avoid decreasing the particle size below 0.15μm.

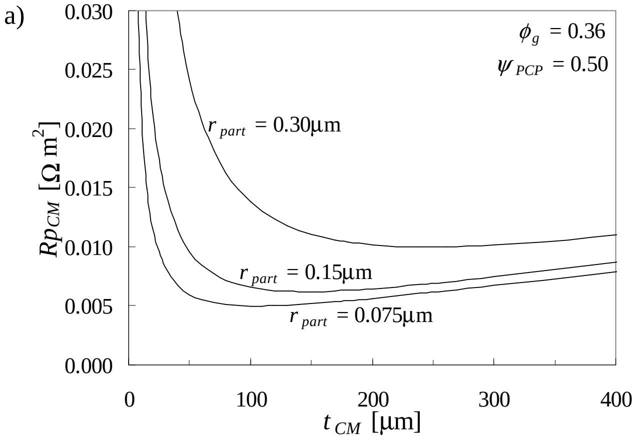

Figure 3.9 – Design analysis on particle dimension. a) CM polarization resistance as a function of thickness for different particle radii; b) maximum pressure inside the CM at a given CM overpotential.

The cell radius is another important design parameter; technologically, larger cells are preferred due to their higher absolute power output. In the following, we assume that due to sealing requirements, the electrode radius is 2mm smaller than cell radius:

$$r_{elec} = r_{cell} - 2mm \tag{3.35}$$

Using the best design parameters as identified above and a reasonable CM overpotential of 0.1V, Figure 3.10a shows the influence of cell radius and CM thickness on CM gas pressure. As the cell radius increases, the maximum pressure inside the CM increases due to the increased transport distance that water vapor has to cover to leave the CM in the radial direction. This results in a larger CM concentration overpotential yielding a lower CM performance. However, the active region available for the recombination reaction, corresponding to the electrode projection, increases. Figure 3.10b shows the influence of cell geometry on polarization resistance. Here, an optimal design is obtained for r_{cell} = 13mm and a CM thickness of 156μm where the minimum CM polarization resistance, equal to $6.065\cdot10^{-3}\Omega\cdot m^2$, is observed. In addition, Figure 3.10b shows that higher cell radii could be used without significant increase in CM polarization resistance, if also the CM thickness is increased accordingly.

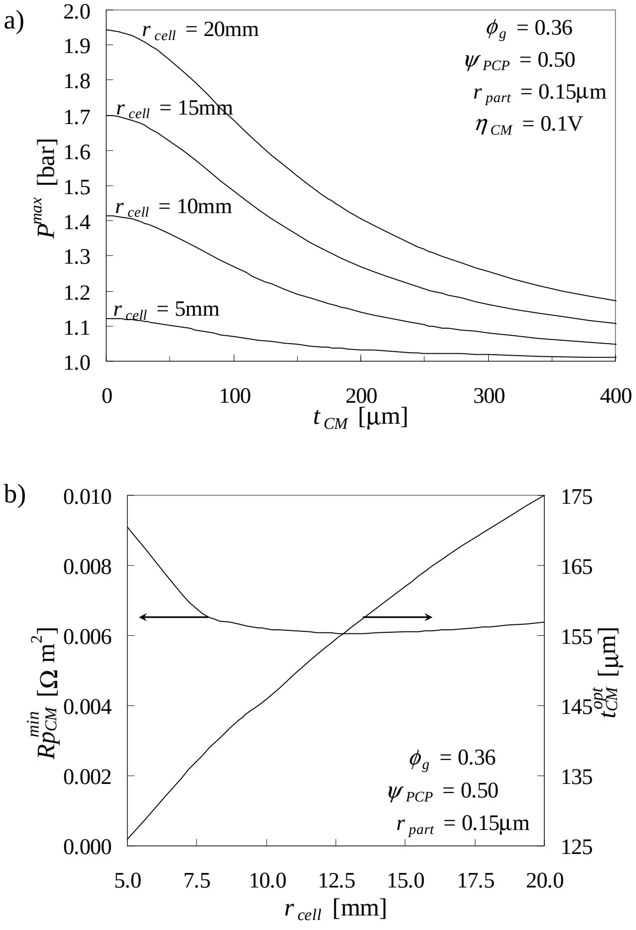

Figure 3.10 – Design analysis on cell radius. a) Maximum pressure inside the CM at a given CM overpotential for different cell radii; b) minimum CM polarization resistance and optimum CM thickness as a function of cell radius.

The little increase shown by the polarization resistance for thicknesses higher than the optimum condition gives comfortable latitude for shaping efficient cells with mechanical reliability and for advanced design (e.g., grid channels) to enhance water vapor outflux.

3.4 Conclusions

A mathematical model of the central membrane (CM) of the IDEAL–Cell was developed in this study. The CM was modeled using a continuum approach describing a mixed ionic conduction layer where chemical and electrochemical reactions, coupled with charge and mass transports of reacting species, occur. The model consists of a system of local charge and mass balance differential equations under steady–state conditions. Geometrical parameters were obtained using morphological models based on percolation theory.

The model was successfully compared with experimental data from literature. The kinetics of the recombination reaction was estimated by best fitting revealing that the CM was in ohmic regime under the investigated conditions.

A variation of uncertain parameters, in particular the kinetic constant of water incorporation into the proton–conducting phase and the contact angle between particles, showed a strong influence on the estimated exchange current, suggesting that an accurate estimate is required in order to obtain reliable results from the model. Despite this limitation, a design analysis allowed the identification of how geometrical and morphological parameters affect the cell performance, revealing that an increase in cell efficiency is expected when using lower porosity, smaller thickness and higher cell radius compared to the reference condition. In particular, the optimized parameters yield a decrease in CM polarization resistance from $0.32\Omega\cdot\mathrm{m}^2$ of the reference to $6.065\cdot10^{-3}\Omega\cdot\mathrm{m}^2$ in the optimized condition.

After further experimental comparisons and more rigorous validation in order to get reliable values of the so far unknown parameters, the presented model may be used as a valuable tool to interpret experimental data, to help optimizing cell design and to predict future performance and development. The predicted optimum performance relies on the model chosen for the packing (random packing of single–size spheres), and it may improve when features not considered in this study (e.g., channeled porosity, mixed conduction in a single phase, better shaping and better materials) were taken into account.

Nomenclature

Glossary

$a_{i(K)}$	activity of species *i* in phase *K*
a_{PCP}^{v}	PCP surface area exposed to gas phase per unit volume [m^{-1}]
B	permeability coefficient [m^{2}]
c_O	molar ratio of oxygen ions to perovskite cells
c_{OH}	molar ratio of protonic defects to perovskite cells
c_{VO}	molar ratio of oxygen vacancies to perovskite cells
$C_{w,PCP}$	volume concentration of water incorporated in PCP [mol$\cdot$m^{-3}]
d_p	mean pore diameter [m]
D_i^K	Knudsen diffusivity for species *i* (*i* = *w*, *c*) [m$^{2}\cdot$s^{-1}]
D_p	mean particle diameter [m]
D_{wc}	binary diffusion coefficient for water vapor–carrier gas [m$^{2}\cdot$s^{-1}]
$D_{w,PCP}$	diffusivity of water incorporated in PCP [m$^{2}\cdot$s^{-1}]
F	Faraday constant [C$\cdot$mol^{-1}]
G	Gibbs free energy [J$\cdot$mol^{-1}]
i_0	exchange current [A$\cdot$m^{-1}]
i_{tot}	total current density per unit of electrode or cell area [A$\cdot$m^{-2}]
i_{TPB}	current density per unit of TPB length [A$\cdot$m^{-1}]
k_d	kinetic constant of water incorporation reaction in PCP [mol$\cdot$m$^{-2}\cdot$Pa$^{-1}\cdot$s^{-1}]
K_w	thermodynamic constant of water incorporation reaction [Pa^{-1}]
$\hat{n}$	normal versor
$N_{c,g}$	molar flux of carrier gas in gas phase [mol$\cdot$m$^{-2}\cdot$s^{-1}]
N_{H^+}	molar flux of protons in PCP [mol$\cdot$m$^{-2}\cdot$s^{-1}]
$N_{O^{2-}}$	molar flux of oxygen ions in ACP [mol$\cdot$m$^{-2}\cdot$s^{-1}]
$N_{w,g}$	molar flux of water vapor in gas phase [mol$\cdot$m$^{-2}\cdot$s^{-1}]
$N_{w,PCP}$	molar flux of water incorporated in PCP [mol$\cdot$m$^{-2}\cdot$s^{-1}]
P	pressure [Pa]
p_w	water partial pressure within the CM [Pa]
r_{cell}	cell radius [m]
r_{elec}	electrode radius [m]
r_{part}	particle radius [m]
R_g	ideal gas constant [J$\cdot$mol$^{-1}\cdot$K^{-1}]
Rp_{cell}	area–specific cell polarization resistance [$\Omega\cdot$m^{2}]
Rp_{CM}	area–specific CM polarization resistance [$\Omega\cdot$m^{2}]
S	dopant level
T	temperature [K]

t_{AE}	thickness of the anodic electrolyte [m]
t_{CM}	thickness of the CM [m]
V	electric potential [V]
v_{inc}	rate of water incorporation reaction in PCP [$\mathrm{mol \cdot m^{-2} \cdot s^{-1}}$]
x_w	molar fraction of water vapor in gas phase
α	transfer coefficient
γ	percolation fraction
δ	molar density of perovskite cells [$\mathrm{mol \cdot m^{-3}}$]
ΔV_{abs}^{eq}	absolute equilibrium voltage difference between ACP and PCP [V]
ΔV^{eq}	relative equilibrium voltage difference between ACP and PCP [V]
ζ	numerical fraction of ACP of PCP particles
η	overpotential [V]
η_{cell}	cell overpotential [V]
η_{CM}	overpotential applied to the whole CM [V]
θ	contact angle [rad]
λ_{TPB}^{v}	connected TPB length per unit volume [$\mathrm{m^{-2}}$]
μ	dynamic viscosity of the gas mixture [$\mathrm{kg \cdot m^{-1} \cdot s^{-1}}$]
$\tilde{\mu}_{i(K)}$	electrochemical potential of species *i* in phase *K* [$\mathrm{J \cdot mol^{-1}}$]
σ	ionic conductivity [$\mathrm{S \cdot m^{-1}}$]
τ_g	tortuosity factor of the gas phase
ϕ_g	porosity
ϕ_{PCP}	volume fraction of PCP
ψ	solid volume fraction of ACP or PCP

Superscripts

0	standard conditions
an	anodic conditions
eff	effective
eq	equilibrium condition
ex	external condition
sat	saturation limit

Subscripts

c	carrier gas
H^+	protons
O^{2-}	oxygen ions
w	water

Abbreviations

ACP	anion–conducting phase
BCY	yttria–doped barium cerate
CM	central membrane
PCFC	proton conducting solid oxide fuel cell
PCP	proton–conducting phase
TPB	three–phase boundary
YDC	yttria–doped ceria

Acknowledgements

This research has received funding from the European Community's FP7 Programme under grant agreement No 213389.

References

[1] J. Larminie, A. Dicks, Fuel Cell Systems Explained, Wiley, New York, 2003.

[2] A.S. Thorel, A. Chesnaud, M. Viviani, A. Barbucci, S. Presto, P. Piccardo, et al., IDEAL-Cell, a high temperature Innovative Dual mEmbrAne Fuel-Cell, ECS Trans. 25 (2009) 753–762.

[3] P. Costamagna, P. Costa, V. Antonucci, Micro-modelling of solid oxide fuel cell electrodes, Electrochim. Acta. 43 (1998) 375–394.

[4] B. Kenney, K. Karan, Engineering of microstructure and design of a planar porous composite SOFC cathode: A numerical analysis, Solid State Ionics. 178 (2007) 297–306.

[5] H. Zhu, R.J. Kee, Modeling distributed charge-transfer processes in SOFC membrane electrode assemblies, J. Electrochem. Soc. 155 (2008) B715–B729.

[6] C. Nicolella, A. Bertei, M. Viviani, A. Barbucci, Morphology and electrochemical activity of SOFC composite cathodes: II. Mathematical modelling, J. Appl. Electrochem. 39 (2008) 503–511.

[7] T.X. Ho, P. Kosinski, A.C. Hoffmann, A. Vik, Modeling of transport, chemical and electrochemical phenomena in a cathode-supported SOFC, Chem. Eng. Sci. 64 (2009) 3000–3009.

[8] W.G. Bessler, S. Gewies, C. Willich, G. Schiller, K.A. Friedrich, Spatial distribution of electrochemical performance in a segmented SOFC: a combined modeling and experimental study, Fuel Cells. 10 (2010) 411–418.

[9] T. Ou, F. Delloro, C. Nicolella, W.G. Bessler, A.S. Thorel, Mathematical modelling of mass and charge transport and reaction in the central membrane of the IDEAL-Cell, ECS Trans. 25 (2009) 1295–1304.

[10] S. Gewies, W.G. Bessler, Physically based impedance modeling of Ni/YSZ cermet anodes, J. Electrochem. Soc. 155 (2008) B937–B952.

[11] B. Kenney, M. Valdmanis, C. Baker, J.G. Pharoah, K. Karan, Computation of TPB length, surface area and pore size from numerical reconstruction of

composite solid oxide fuel cell electrodes, J. Power Sources. 189 (2009) 1051–1059.

[12] A. Bertei, C. Nicolella, A comparative study and an extended theory of percolation for random packings of rigid spheres, Powder Technol. 213 (2011) 100–108.

[13] A. Bertei, C. Nicolella, Percolation theory in SOFC composite electrodes: Effects of porosity and particle size distribution on effective properties, J. Power Sources. 196 (2011) 9429–9436.

[14] G.T. Nolan, P.E. Kavanagh, Computer simulation of random packing of hard spheres, Powder Technol. 72 (1992) 149–155.

[15] J. Sanyal, G.M. Goldin, H. Zhu, R.J. Kee, A particle-based model for predicting the effective conductivities of composite electrodes, J. Power Sources. 195 (2010) 6671–6679.

[16] J.H. Nam, D.H. Jeon, A comprehensive micro-scale model for transport and reaction in intermediate temperature solid oxide fuel cells, Electrochim. Acta. 51 (2006) 3446–3460.

[17] A.J. Bard, L.R. Faulkner, Electrochemical methodes: fundamentals and applications, Wiley, New York, 2001.

[18] E.A. Mason, A.P. Malinauskas, Gas transport in porous media: the dusty-gas model, Elsevier, Amsterdam, 1983.

[19] D. Arnošt, P. Schneider, Dynamic transport of multicomponent mixtures of gases in porous solids, Chem. Eng. J. Biochem. Eng. J. 57 (1995) 91–99.

[20] B. Todd, J.B. Young, Thermodynamic and transport properties of gases for use in solid oxide fuel cell modelling, J. Power Sources. 110 (2002) 186–200.

[21] R.B. Bird, W.E. Steward, E.N. Lightfoot, Transport phenomena, Wiley, New York, 1960.

[22] W. Kast, C.-R. Hohenthanner, Mass transfer within the gas-phase of porous media, Int. J. Heat Mass Transf. 43 (2000) 807–823.

[23] K.D. Kreuer, Aspects of the formation and mobility of protonic charge carriers and the stability of perovskite-type oxides, Solid State Ionics. 125 (1999) 285–302.

[24] K.D. Kreuer, Proton-conducting oxides, Annu. Rev. Mater. Res. 33 (2003) 333–359.

[25] W.G. Coors, Protonic ceramic steam-permeable membranes, Solid State Ionics. 178 (2007) 481–485.

[26] W. Suksamai, I.S. Metcalfe, Measurement of proton and oxide ion fluxes in a working Y-doped BaCeO3 SOFC, Solid State Ionics. 178 (2007) 627–634.

[27] T. Ou, Mathematical modeling of mass transfer and reaction in an innovative solid oxide fuel cell, University of Pisa, Italy, 2011.

[28] K. Katahira, Y. Kohchi, T. Shimura, H. Iwahara, Protonic conduction in Zr-substituted BaCeO3, Solid State Ionics. 138 (2000) 91–98.

[29] J. Van herle, T. Horita, T. Kawada, N. Sakai, H. Yokokawa, M. Dokiya, Sintering behaviour and ionic conductivity of yttria-doped ceria, J. Eur. Ceram. Soc. 16 (1996) 961–973.

[30] D.G. Scott, Packing of spheres: Packing of equal spheres, Nature. 188 (1960) 908–909.

[31] W.S. Jodrey, E.M. Tory, Computer simulation of isotropic, homogeneous, dense random packing of equal spheres, Powder Technol. 30 (1981) 111–118.

Microstructural Modeling

Chapter 4

Numerical Reconstruction of Random Packings of Spheres

This Chapter presents the numerical reconstruction method used to simulate random packings of spherical particles, which is also applied in Chapters 6–8. The method is compared with percolation theory in sintered composite packings of particles, that is, in composite SOFC electrodes.

The numerical reconstruction algorithm allows the identification of the range of validity of percolation theory, showing that:

i. percolation theory predictions are inaccurate for contact angles larger than 23°, which means porosities smaller than 28% according to Chapter 7, which are typically used in the anode functional layer just to make an example;

ii. the assumption that particles retain their position upon sintering when pore–formers are used is generally valid for porosities smaller than 60%, therefore it is satisfied in typical SOFC electrodes;

iii. within these conditions, percolation theory fairly agrees with the results of the packing algorithm, although broader information can be obtained from the latter.

This Chapter was adapted from the paper "Percolating behavior of sintered random packings of spheres" by A. Bertei, H.-W. Choi, J.G. Pharoah and C. Nicolella, published in Powder Technol. 231 (2012) 44–53.

Abstract

This study investigates the effects of sintering in random composite packings of spherical particles, with focus on structures with relatively low densification where the sintering is used to obtain desired catalytic and transport properties. The effects of the degree of sintering (particle–particle contact angle) and of additional porosity created by pore–former particles on coordination numbers and percolation probabilities are addressed by using both the extended percolation theory and the drop–and–roll numerical reconstruction method. The comparison of the two methods allows the assessment of two key assumptions on which percolation theory relies when applied to sintered structures: i) particles retain their position during the sintering, ii) coordination numbers in the sintered structure are evaluated as the particles were rigid spheres. The former assumption is assessed by calculating, using the drop–and–roll method, the fraction of collapsing particles, which belong to clusters completely surrounded by pore–formers. Numerical simulations show that the fraction of collapsing particles is less than 1% for porosities as high as 60%. Within the range of validity of the first assumption, the theoretical and numerical methods predict that pore–formers decrease the number of contacts and so the percolation probability. The latter assumption is assessed by comparing simulated and theoretical results for different contact angles. The comparison shows that for contact angles smaller than 15° particles behave as they were rigid. For contact angles larger than 23°, sintering effects are no longer negligible, leading to a relative error between the two methods larger than 10% in contact number estimations. This study also shows that percolation theory and numerical simulations provide very similar results over a wide range of conditions, suggesting that the two methods can be used interchangeably for describing sintered random packings.

4.1 Introduction

Random packings of spherical particles have attracted research and technology interest due to their several theoretical and practical applications. They are used in many particulate systems such as packed beds in oil and chemical applications, cermets and ceramics. In several applications the packing undergoes a sintering process. Depending on the desired resulting properties and the involved materials, the sintering has two different aims: i) the densification of the packing, leading to a highly compact structure, closing the pores among the particles, hereafter called structural sintering, ii) the stabilization of the position of the particles in the packing without closing the pores, hereafter called functional sintering.

The goal of the structural sintering is the enhancement of the mechanical properties (e.g., the tensile strength), as desired in the densification of metal–ceramic powder mixtures as in powder metallurgy [1,2]: in such a situation the residual porosity is undesired. Powder densification has been addressed experimentally [3–5], theoretically [6,7] and numerically [8–11]. These studies were mainly dedicated to investigate very high packing densities (up to 90–95%).

In functional sintering the mechanical properties have a marginal role and the sintering process is used to get the desired catalytic and transport properties (e.g., the specific surface area exposed to the gas phase, the effective electric conductivity, the effective gas diffusivity), in particular for composite mixtures. This is the case of porous composite electrodes for solid oxide fuel cells, in which the optimization of the cell performance requires the tailoring of the microstructural functional properties [12–17]. In such applications the packing porosity can be controlled by addition of pore–formers in the particle mixture before sintering. Pore–formers are particles of materials which decompose at high temperature during the sintering, leaving additional pores in the microstructure thus increasing the packing porosity and, as a consequence, the gas transport properties. On the other hand, the degree of densification can be tailored to enhance the degree of particle overlap, thus increasing the effective electric conductivity of the solid phase. This study focuses on structures obtained by such a type of functional sintering.

In these applications the main goal of studying the packing morphology is the prediction of the effective functional properties starting from measurable parameters such as the granulometric distribution of the powders and their composition. Among theoretical and numerical methods, percolation theory [18,19] and particle based numerical reconstruction methods [20,21] have been widely applied to characterize the microstructural properties of random packings of spherical particles. The former, due to its simple implementation, can be easily integrated in more advanced macroscopic models [14,22] but it does not provide all the effective properties like, for example, the effective thermal and electric conductivities. On the other hand, numerical methods reconstruct the microstructure of the media, which can be used to evaluate broader information than percolation theory can predict about solid and gas phase properties, at the expense of a higher computational cost.

Particle based numerical packing algorithms have been widely adapted in the context of the microstructural reconstructions. There is a variety of available numerical techniques for simulating random structures of spherical particles, ranging from random loose to random close packings: Monte Carlo [23–25], collective rearrangement [20,26,27], drop–and–roll [21,28–31] and discrete element methods [32–34] to cite the most common methods. Among many others, this article adapts the drop–and–roll algorithm due to its easy implementation and because it is usually faster than collective rearrangement and discrete element methods, nevertheless ensuring consistent results at the particle level [35].

In this study, several improvements over our previous approaches [36–38] have been introduced in the packing algorithm in order to provide a better representation of the microstructure of composite sintered structures. Pore–former particles can be added into the reconstruction process in order to increase the porosity of the packing. Furthermore, the model is capable of preserving the same particle–particle contact angle between the rolling and the packed particles throughout the whole structure. Different degrees of sintering are numerically simulated by varying the contact angle, providing structures ranging from overlap–free (i.e., rigid spheres having a contact angle approaching zero) to substantially highly sintered packings (i.e., overlapping spheres having a contact angle up to 40°).

Percolation theory [18,19,39,40] is a stochastic theory regarding the particle arrangement in the packing, which relies on the prediction of average contact numbers of particles, that is, the number of contacts made by a particle with its neighboring particles. Functional properties, related to the connectivity among particles, are then predicted starting from the evaluation of the contact numbers [14,18,19]. Several percolation models have been developed [18,39,40], based on different basic relationships used to calculate contact numbers as a function of particle size and composition. Recently Bertei and Nicolella [41] showed a critical comparison of existing percolation theories and proposed new relationships to obtain a better agreement with simulated and experimental results. The theory was extended to take into account polydisperse powders and the control of porosity by addition of pore–formers in the mixture of particles [19].

Despite recent improvements [19,41], percolation theory relies on some assumptions which require careful verification and it has some possible limitations when applied to sintered structures:

i. it is assumed that pore–former particles, which decompose during the sintering, leave holes in the structure of the same shape of the pore–former particle that occupied such position before sintering. Under this assumption, the remaining particles retain their position, and their percolation properties as well, during the sintering;

ii. the particle coordination numbers are evaluated considering particles as rigid spheres, i.e., neglecting overlaps.

The first assumption is valid only if the structure does not locally collapse. When a solid particle or a cluster of solid particles is surrounded by pore–former particles, after sintering they cannot retain the same position they had before sintering. Structure collapse logically occurs in the case of a high volume fraction of pore–formers in the starting mixture, although a quantitative estimate has not yet been proposed. Regarding the second assumption, to what extent particles can be considered as rigid is still an open issue.

The main goal of this article is to investigate the sintering effects in the applications where a functional sintering is required (e.g., porous composite electrodes). The assessment is performed by using percolation theory and the particle based numerical reconstruction method. Mean coordination numbers and the phase percolation probabilities are evaluated, which are the primary information required for the calculation of more advanced effective packing properties related to particle connectivity. Furthermore, this article evaluates the limiting particle–particle contact angle over which particles do not behave as rigid spheres as well as the amount of pore–former particles leading to local structure collapses, providing the range of validity of the extended percolation theory as well as practical indications for the mixture preparation.

4.2 Methodology

The extended percolation theory used in this work has been extensively described in Ref. [19], thus only the equations strictly required for the comprehension of the study will be briefly recalled in this section.

The particle based reconstruction procedure used in this study follows the random sequential addition method better known as drop–and–roll algorithm [21,28–31]. The procedure is applied to a ternary mixture of polydisperse powders, namely *a*–, *b*– and *f*–particles. The latter type represents pore–former particles, which decompose during the sintering and are not present in the final sintered structure. The granulometric distribution of the powders is discretized into particle sizes [18]: m_a for *a*–particles (i.e., different radii r_{a_1}, r_{a_2}, …, $r_{a_{ma}}$), m_b for *b*–particles and m_f for *f*–particles.

The packing is numerically generated by adding one particle at a time into a box domain of specified dimensions with periodic boundary conditions in the horizontal directions [21,31]. Each particle is dropped from the top of the domain randomly choosing its horizontal coordinates. The falling particle is allowed to roll over one or two already packed particles without friction, adhesion or inertia, provided that its z–coordinate is higher than the z–coordinate of the center of rotation. The particle comes into rest when either it is stably supported by three other particles, that is, the projection on the floor of the center of the falling particle is located inside the projection of the triangle formed by the contact points with the three contacting spheres [20,42–44], or it reaches the bottom of the domain. As the particle comes into rest, its position is fixed and a new particle is dropped into the domain repeating the same procedure, reported in Figure 4.1. The desired volume fractions of the *a*–, *b*– and *f*–phases, indicated as ψ_a, ψ_b and ψ_f, are enforced by assigning a weighted probability to the particle selection before the particle is dropped. In a similar way, the size of the falling particle is randomly determined before the dropping considering an occurrence probability according to the desired particle size distribution for such phase.

A desired particle–particle contact angle is used as input parameter of the algorithm, in order to simulate different degrees of sintering. The contact angle is a property of the pair of contacting particles: for each couple of spheres, the contact angle depends upon the smaller particle [18] as represented in Figure 4.2. Given the contact angle and the radii of the contacting particles, the minimum allowable distance between them is directly calculated, allowing the rolling of the particle holding the same distance (i.e., the same particle–particle contact angle) between the rolling particle and the packed one. This feature represents an improvement of the previous version of the algorithm [36] since the contact angle is constant throughout the structure. Structures with overlap–free (i.e., rigid spheres) or overlapping particle configurations are obtained by using small (usually below 5°) or larger contact angles, respectively.

As the box domain has been entirely filled with particles, the structure generation is completed. Since during the sintering process pore–former particles undergo decomposition (e.g., they burn in an oxidizing atmosphere), it is assumed that they leave holes of the same shape of the pore–former particle that occupied that position before sintering. Even though pore–former particles are not present in the final structure, constituted by only *a*– and *b*–particles, they do have an effect on the number of contacts of *a*– and *b*–particles. Indeed, due to this assumption, the remaining particles hold their position during the sintering, so that they retain, upon sintering, the same percolation properties they had before sintering. In order to characterize the final packing composition, the volume fractions of *a*– and *b*–particles after sintering ψ_a^{as} and ψ_b^{as} are evaluated on the basis of the volume fractions before sintering as $\psi_a^{as} = \psi_a / (\psi_a + \psi_b)$ and $\psi_b^{as} = \psi_b / (\psi_a + \psi_b)$.

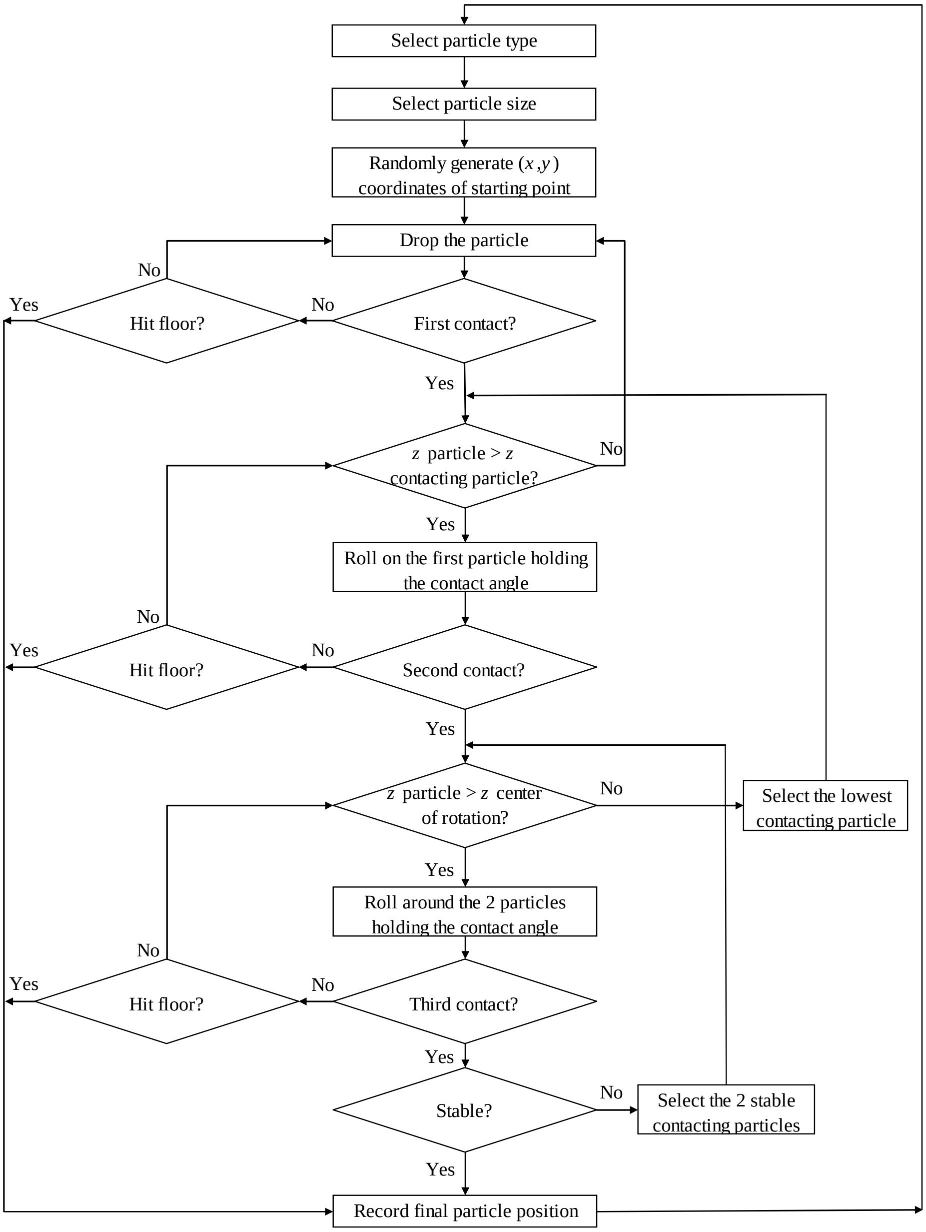

Figure 4.1 – Program flow chart.

Using the numerical reconstruction method, the type, the radius and the center coordinates of each packed particle within the domain are known. Based on that information, the number and type of contacting particles can be easily determined for each particle. Taking as reference the *l*–th particle of the n_{h_i} particles belonging to the *i*–th particle size of the phase *h*, the individual number of contacts of this particle with particles belonging to the *j*–th particle size of phase *k* is indicated as

$z_{h_i,k_j}^{(l)}$. The average number of contacts between the h_i–particle size with the k_j–particle size, called Z_{h_i,k_j}, is then calculated by summing all the individual contacts of each h_i–particle with k_j–particles and dividing by the number of particles belonging to the h_i–particle size n_{h_i}:

$$Z_{h_i,k_j} = \frac{\sum_{l=1}^{n_{h_i}} z_{h_i,k_j}^{(l)}}{n_{h_i}} \tag{4.1}$$

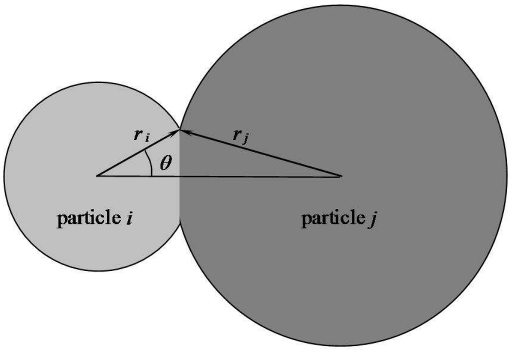

Figure 4.2 – Definition of contact angle between two overlapping particles: the contact angle θ is defined upon the smaller particle.

The average coordination number of h_i–particles Z_{h_i} is defined as the total number of contacts that an h_i–particle makes with its neighboring particles. Thus, the coordination number Z_{h_i} is equal to the sum of the number of contacts that the h_i–particles make with *a*– and *b*–particles as:

$$Z_{h_i} = \sum_{j=1}^{m_a} Z_{h_i,a_j} + \sum_{j=1}^{m_b} Z_{h_i,b_j} \tag{4.2}$$

These average numbers of contacts are comparable to those calculated, in the same conditions (i.e., composition and particle size distributions), by using percolation theory according to Ref. [19].

The contact information of the resulting structure also allows the determination of how many clusters of particles are present in the simulated packing. A cluster is defined as a group of homolog particles (i.e., of the same type) connected to each other. The number of clusters as well as the number and particle index of particles belonging to each cluster can be identified. Then, following the notation given by Costamagna et al. [14] (see Figure 4.3), each cluster is marked as entirely percolating (A–cluster), if it provides a connected network through the thickness (that is, the *z* direction) of the structure, partly percolating (B–cluster) if connected to either the top or the bottom of the domain for *a*–particles and *b*–particles, respectively, and completely isolated (C–cluster) if it is not connected with either the top or the bottom of the domain for *a*–particles and *b*–particles, respectively. According to Refs. [14,39], for each phase only the particles belonging to A–clusters are considered percolating. The percolation probability in the simulated packing is calculated as the ratio between the number of percolating particles and the total number of particles belonging to the considered phase.

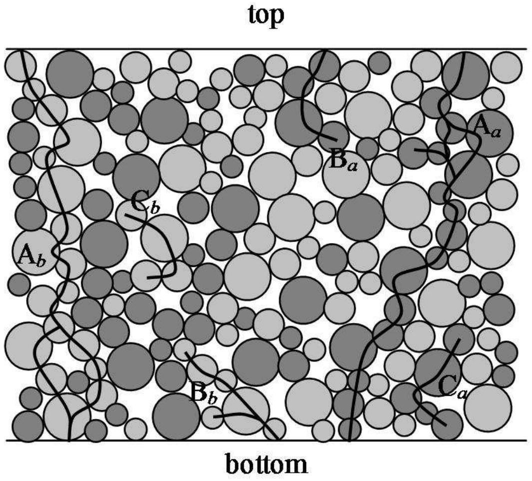

Figure 4.3 – 2D schematic representation of a composite random structure made of a–particles (dark gray) and b–particles (light gray). Entirely percolating (A), partly percolating (B) and completely isolated (C) clusters are shown for both the phases.

Regarding percolation theory, the percolation probability p_h of the phase *h* is estimated as:

$$p_h = 1 - \left(\frac{4.236 - Z_{h,h}}{2.472} \right)^{3.7} \quad (4.3)$$

where $Z_{h,h}$ represents the overall average number of contacts for all *h*–particles, i.e., the average number of contacts that an *h*–particle makes with other homolog *h*–particles, calculated according to:

$$Z_{h,h} = \frac{\sum_{i=1}^{m_h} \zeta_{h_i} \sum_{j=1}^{m_h} Z_{h_i,h_j}}{\sum_{i=1}^{m_h} \zeta_{h_i}} \tag{4.4}$$

where ζ_{h_i} represents the numerical fraction before sintering of h_i–particles.

The same routine described for the determination of clusters of homolog particles is also used to individuate the local structure collapse. It is assumed that, due to the interactions among particles that the sintering process provides, after sintering a particle is stable provided that it makes at least a contact with another stable particle. A particle is considered unstable if it belongs to a cluster of *a*– or *b*–particles or a mixture of them (in the following, we will refer to a solid particle if such a particle belongs independently to the *a* or *b* phase, but obviously not to the pore–former phase) not connected to the bottom of the domain and completely surrounded by pore–former particles before sintering. After sintering such a cluster is unstable and it will drop downward without retaining its initial configuration. Thus, the structure collapse is related to the presence of C–clusters of solid particles isolated from the bottom of the domain. In the following, the ratio between the number of unstable solid particles and the total number of solid particles in the structure after sintering will be taken into account as a reference for the structure collapse.

4.3 Results and discussion

4.3.1 Effect of pore–formers on percolation properties

Polydisperse mixtures of rigid particles were simulated by using the numerical reconstruction algorithm with a small contact angle among particles (4°, smaller than the one used by Nolan and Kavanagh [20]). Numerical Gaussian distributions were used for each phase in order to highlight the differences between a polydisperse and a monodisperse case, emphasizing in this way the gap between small and big particles in the packing [19]. In particular, each distribution was discretized into 9 particle sizes in the range $\left(\bar{r} - \sigma\sqrt{3}, \bar{r} + \sigma\sqrt{3}\right)$ with a step size of 2σ where $\bar{r}$ and σ are the mean radius and the standard deviation of the distribution, respectively [45]. The cases investigated considered $\bar{r} = \bar{r}_a = \bar{r}_b = \bar{r}_f$ and $\sigma_a = \sigma_b = \sigma_f = 0.2\bar{r}$ with an increasing volume fraction before sintering of pore–formers, thus leading to an increasing final porosity starting from 0.41 for $\psi_f = 0$. In all the simulations, the dimension of the cubic domain was chosen to encompass an average of 10 000 particles in order to provide an adequate number of particles for each particle size n_{h_i} in Eq. (4.1) (40 particles as suggested by Bouvard and Lange [39]). The same starting input parameters were considered for percolation theory.

In Figure 4.4, the coordination numbers of the smallest (a_1), mean (a_5) and biggest (a_9) particle size are shown for *a*–particles as a function of the final porosity. Since $\bar{r}_a = \bar{r}_b$ and $\sigma_a = \sigma_b$, the coordination numbers of *b*–particles are coincident to those of *a*–particles. Numerical simulation results are represented with marks while the estimates of percolation theory are reported with lines.

Figure 4.4 shows a good agreement between theoretical and simulation results for the range of porosity considered. Numerical simulation results show that, as predicted by percolation theory, in a polydisperse mixture the coordination number of the biggest particle size (a_9) is larger than the coordination number of the smallest particle size (a_1). Both percolation theory and numerical simulation results show that increasing the volume fraction of pore–former particles, i.e., increasing the final porosity, leads to a decrease in the coordination numbers of *a*–particles (and *b*–particles too). Hence, as stated by Bertei and Nicolella [19], the numerical simulation highlights the fact that the presence of pore–formers not only increases the packing porosity but it also reduces the number of particle contacts. Furthermore, the agreement between percolation theory estimates and simulation results suggests that both methods provide consistent results with respect to the contact numbers in polydisperse mixtures of rigid particles with and without pore–formers.

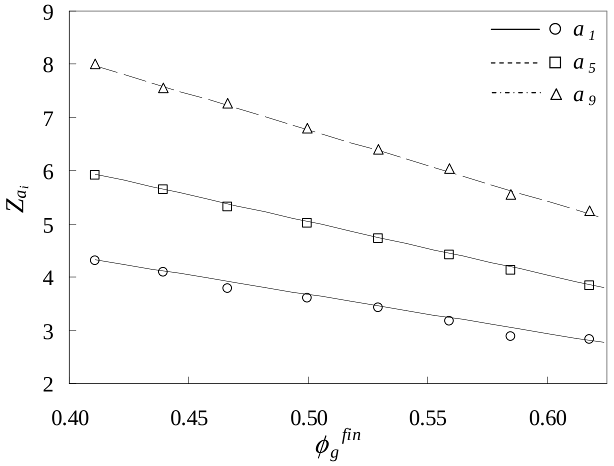

Figure 4.4 – Coordination numbers of smallest (a_1), mean (a_5) and biggest (a_9) a–particle size calculated by the percolation theory and the numerical model as a function of the final porosity. Lines are used for percolation theory results, marks for the numerical model.

The percolation probability of *a*–particles as a function of the packing composition was numerically evaluated for four representative final porosities (ϕ_g^{fin} = 0.41, 0.45, 0.50, 0.55, corresponding to ψ_f =0, 0.066, 0.151, 0.235). In numerical simulations, for each setting four structures containing more than 10 000 particles were simulated in order to have sufficient data for each case. A single simulation per case is not enough to get a reliable representation of the mean value due to the randomness of the structure generation. Simulation results are reported in Figure 4.5.

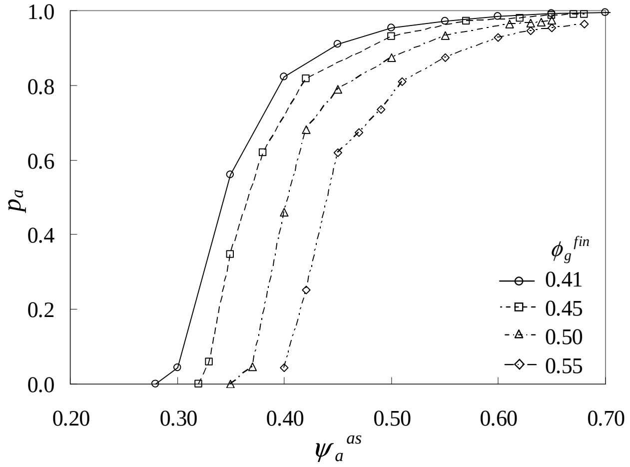

Figure 4.5 – Percolation probability of a–particles as a function of the volume fraction after sintering of a–particles for different final porosities calculated by the numerical model.

For each final porosity, the percolation probability of *a*–particles is equal to 0 until a critical composition, called percolation threshold [39,46], is reached. This means that below the percolation threshold *a*–particles are grouped in B– and C–clusters but there is not any A–cluster entirely percolating. Above the threshold, as the volume fraction ψ_a^{as} increases, p_a increases reaching 1 when all *a*–particles belong to one or more entirely percolating clusters.

Given a composition after sintering above the percolation threshold, increasing the packing porosity by adding a larger volume fraction of pore–formers before sintering leads to a decrease in percolation probability. This result, predicted by percolation theory [19] and confirmed by numerical simulations, is expected since the decrease in the number of contacts as previously observed (Figure 4.4) with an increasing amount of pore–formers is logically connected to a decrease in particle connectivity. Indeed, Eq. (4.3) highlights that there is a direct relationship between the number of contacts of homolog particles $Z_{h,h}$ and the percolation probability p_h. Furthermore, as the packing porosity increases, the percolation threshold of *a*–

particles moves towards a larger volume fraction ψ_a^{as}, from ψ_a^{as} = 0.29 when no pore–formers are added to ψ_a^{as} = 0.38 for ϕ_g^{fin} = 0.55.

These results show that increasing the amount of pore–formers leads to an increase in packing porosity, which may logically increase the effective gas transport properties of the sintered packing such as the effective diffusivity and the permeability. On the other hand, the additional porosity leads to a decrease in the number of contacts in the solid phase, resulting in a smaller particle connectivity represented by a smaller percolation probability which will reduce the effective electrical conductivity.

4.3.2 Structure collapse

As discussed in Section 4.1, the local structure collapse occurs when, before sintering, a cluster of solid particles is completely surrounded by pore–former particles. After sintering this cluster is unstable and its particles cannot retain their position. Local structure collapse should be avoided when a functional sintering is required because it leads to non homogeneous microstructures. Furthermore, the resulting microstructure and its percolation properties are not the same of those that could be expected and predicted. Indeed, the extended percolation theory cannot be used since it relies on the assumption that particles retain their position during the sintering while the numerical reconstruction method should be adjusted in order to take into account the dropping and rolling of the unstable clusters after sintering. In other words, both percolation theory and numerical reconstruction method are valid within the range where local collapse does not occur.

In this Section, the local structure collapse is identified when at least 1% of solid particles are unstable after sintering. This condition does not identify when a sintered composite packing is practically feasible, rather it determines the limit below which the presence of collapsing clusters can be neglected when evaluating microstructural properties by percolation theory or numerical reconstruction method.

The local structure collapse was investigated by using the numerical algorithm because such a type of information cannot be obtained from percolation theory. Given the *a*–, *b*– and *f*–particle distributions as well as the volume fraction of *a*–particles after sintering, the volume fraction of pore–former particles before sintering was increased in the numerical simulations until structure collapse occurred. In particular, for each setting, three structures were created: if collapse occurred in at least one of them the current volume fraction of pore–former particles was stored and related to that setting, otherwise three new structures were generated with an increased pore–former volume fraction. In each structure, the domain size was varied for each setting in order to get at least 5000 particles after sintering, that is, at least 50 unstable particles when the collapse occurred. During the structure generation pore–former particles were also considered, so the total number of particles per structure was actually much larger than 5000.

Monosized rigid particles (i.e., $\theta < 4°$) were used in these simulations. Obviously, polydisperse mixtures might be used, however the attention was focused on monodisperse phases in order to get the general, and not distribution–specific, behavior of the local structure collapse as a function of composition and particle size. The radius of *b*–particles was fixed to a constant value r_b. Three pore–former sizes were investigated, that is, r_f/r_b = 0.5, 1 and 2. For each pore–former size, three simulations were performed using three different radii for *a*–particles, that is, r_a/r_b = 0.5, 1 and 2. In total, 9 different cases were simulated. It is important to note that the actual powder sizes are not important, only the ratios of particle radii affect the volume fraction of pore–former particles at collapse. Figures 4.6 and 4.7 show the volume fraction of pore–formers before sintering required to get the local structure collapse and the porosity after sintering as a function of the volume fraction of *a*–particles after sintering, respectively.

a)

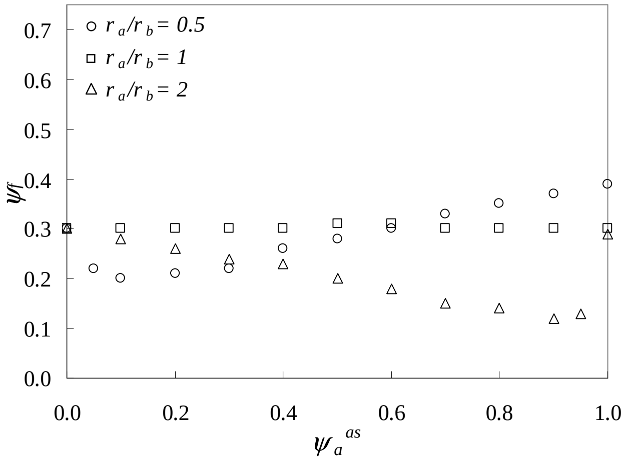

Figure 4.6 – Local structure collapse: pore–former volume fraction at collapse as a function of a–particle volume fraction after sintering for different pore–former sizes: a) r_f/r_b = 0.5; b) r_f/r_b = 1; c) r_f/r_b = 2.

b)

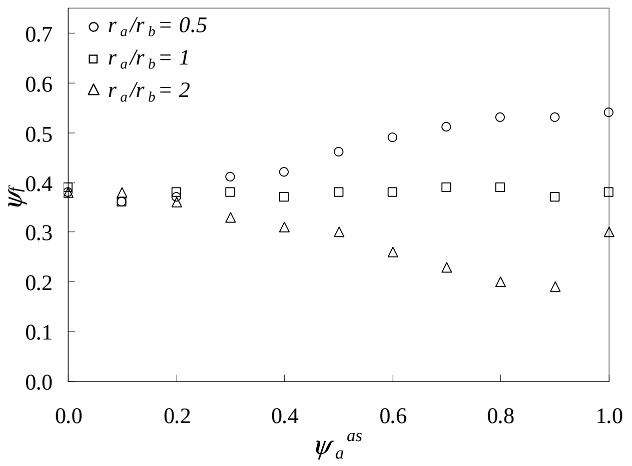

c)

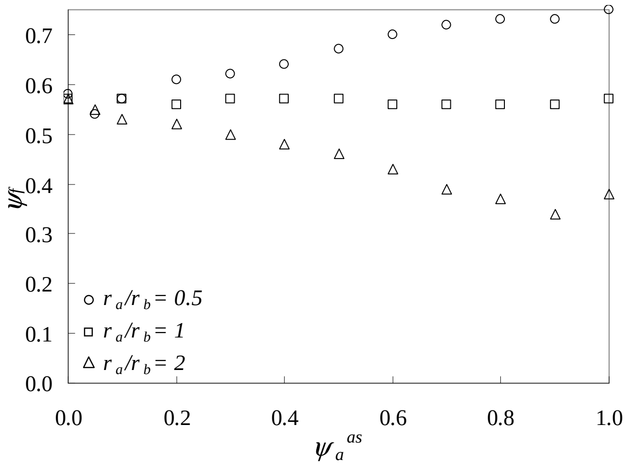

Figure 4.6 (continued) – Local structure collapse: pore–former volume fraction at collapse as a function of a–particle volume fraction after sintering for different pore–former sizes: a) $r_f/r_b = 0.5$; b) $r_f/r_b = 1$; c) $r_f/r_b = 2$.

Figure 4.6 shows that, given the radii of *a*– and *b*–particles and the composition after sintering, as the pore–former radius increases, a larger volume fraction of pore–formers is required to get the collapse as already predicted by Bertei and Nicolella [19]. This behavior is reasonable because in a packing smaller particles surround and isolate bigger particles [47]. Accordingly, given the radius of pore–former particles, when smaller *a*–particles are used (circles), a higher amount of pore–former particles is required to get the collapse if compared with the case in which larger *a*–particles are used (triangles). As shown in Figure 4.6, this is true at least for compositions close to $\psi_a^{as} = 1.0$. Indeed, except in the cases where $r_a = r_b$ (squares), the volume fraction of pore–former particles at collapse shows a minimum ψ_a^{as} a function of the volume fraction of *a*–particles after sintering.

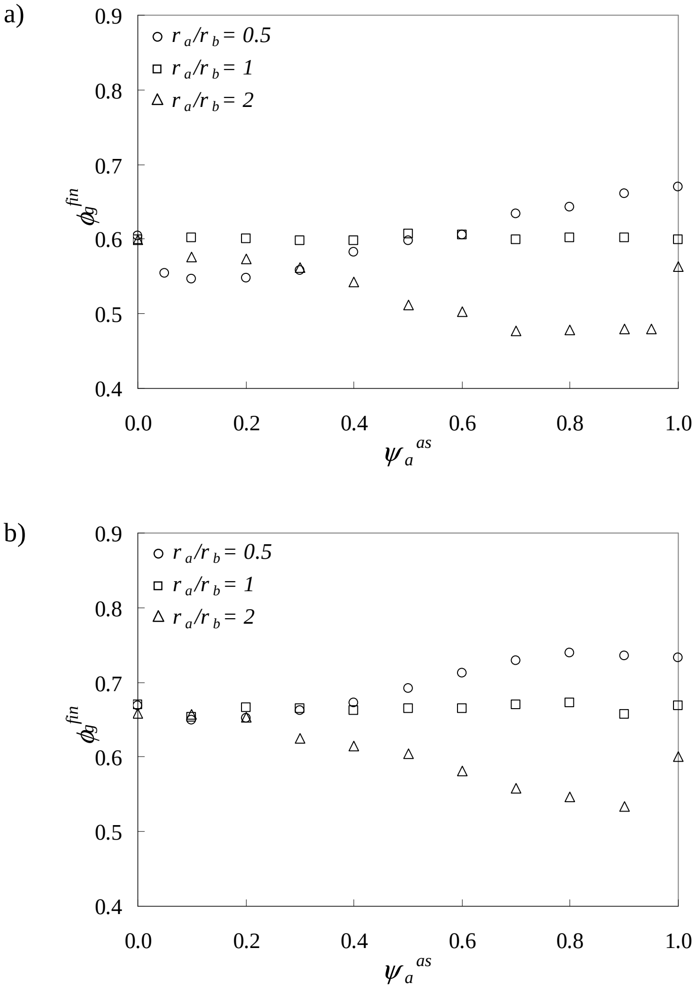

Figure 4.7 – Local structure collapse: porosity after sintering at collapse as a function of a–particle volume fraction after sintering for different pore–former sizes: a) $r_f/r_b = 0.5$; b) $r_f/r_b = 1$; c) $r_f/r_b = 2$.

c)

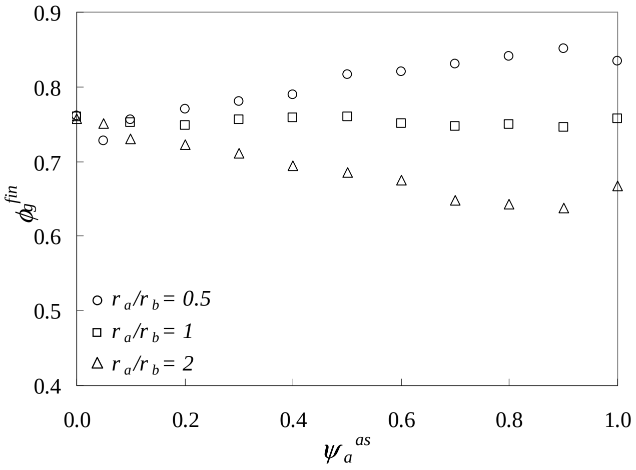

Figure 4.7 (continued) – Local structure collapse: porosity after sintering at collapse as a function of a–particle volume fraction after sintering for different pore–former sizes: a) $r_f/r_b = 0.5$*; b)* $r_f/r_b = 1$*; c)* $r_f/r_b = 2$*.*

In order to explain why there is a minimum ψ_f at collapse as a function of ψ_a^{as}, take as an example the case $r_f/r_b = 1$ with $r_a/r_b = 2$ (marked with triangles in Figure 4.6b): we would expect that the minimum ψ_f occurred at $\psi_a^{as} = 1.0$ because, in such a situation, there is the highest ratio of radii between bigger solid particles and smaller pore–former particles, which surround and isolate the first ones and lead to collapse. But actually, bigger *a*–particles make more contacts than the smaller *b*–particles, which will make just a few contacts, for example just one with a bigger *a*–particle and the remaining contacts with pore–former particles. Taking as an example the situation represented in Figure 4.8a, a bigger *a*–particle (dark gray) makes three contacts with smaller *b*–particles (light gray) which make the remaining contacts with pore–former particles (white): in this situation, the whole cluster, made up of 4 particles in total, is completely isolated. Figure 4.8b shows exactly the same situation where *b*–particles were replaced by pore–former particles, so the volume fraction of pore–formers was increased at the expense of the volume fraction of *b*–particles: here only one particle, i.e., the bigger *a*–particle, is isolated, so the total number of isolated particles is 1 instead of 4.

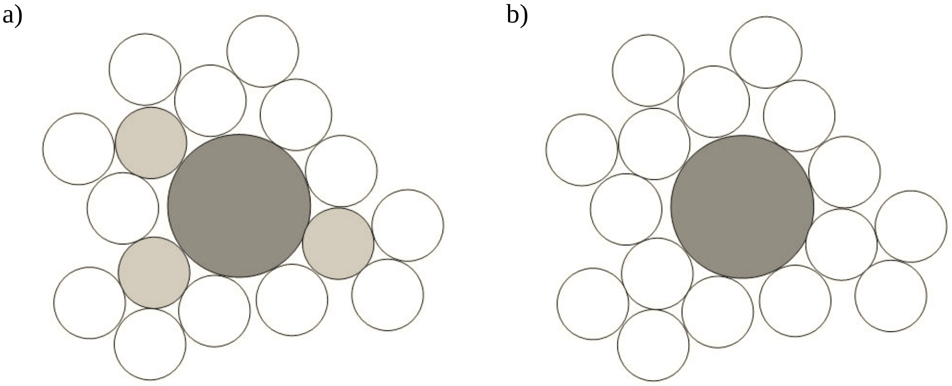

Figure 4.8 – 2D schematic representation of a local structure collapse with a–particles marked in dark gray, b–particles in light gray and f–particles in white: a) b–particles present in the mixture; b) b–particles replaced by f–particles.

Hence, bigger solid particles are surrounded by smaller solid particles which make few contacts: reasonably, smaller solid particles will make the remaining contacts with pore–former particles, bringing themselves, the bigger solid particle and the related other smaller particles into contact with an isolated region. The combination of this effect with the general rule that smaller particles surround bigger ones yields the minimum ψ_f at collapse as a function of ψ_a^{as} when $r_a \neq r_b$ as shown in Figure 4.6.

The same considerations could be repeated for the porosity at collapse (Figure 4.7). In general, the relationship between the final porosity and ψ_a^{as} reflects the dependence of ψ_f at collapse as a function of ψ_a^{as}. However, the porosity at collapse is a function of both the volume fraction of pore–formers at collapse and the initial porosity of the ternary mixture before sintering. In some cases the overlap of the two opposite effects yields a maximum ϕ_g^{fin} as a function of ψ_a^{as} (circles in Figures 4.7b and 4.7c), which is not present in the corresponding figures concerning ψ_f at collapse as a function of ψ_a^{as}.

Figures 4.6 and 4.7 show that local structure collapse occurs at relatively high volume fraction of pore–formers, that is, for very high expected final porosities, in particular when pore–former particles are as large as or larger than solid particles. Accordingly, the extended percolation theory and the numerical reconstruction model, which are based on the assumption that local collapse does not occur, are valid over the range of practical compositions normally used, for example, in sintered electrodes for solid oxide fuel cells. These results can be seen from another point of view: given the particle dimension and the composition, Figures 4.6 and 4.7 show the limiting volume fraction of pore–formers and the maximum porosity in order to avoid local structure collapse of more than 1% of solid particles after sintering. The knowledge of these limits is essential in the design of sintered composite microstructures.

4.3.3 Effects of contact angle

Even though particles were rigid after the packing preparation, the sintering process introduces overlaps among the particles. In the numerical reconstruction this effect was simulated by increasing the contact angle θ among the particles. In order to evaluate how the particle overlap affects the average number of contacts of particles and the percolation properties, binary mixtures of more than 6000 monosized spheres with $r_a = r_b = 0.25\mu m$ without pore–formers were simulated. In this situation, the overlaps have the highest effect ion particle shape [19]. Indeed, since the contact angle is defined based upon the smaller particle in a contact, in polydisperse packings the fraction of volume of bigger particles lost in contacts with smaller particles would be much less than what would happen in a mixture of monosized spheres, where in each contact the fraction of volume lost by each particle is maximum.

Figure 4.9 shows the mean coordination number of *a*–particles in the mixture as a function of the contact angle as obtained by the numerical simulation: increasing the contact angle leads to an increase in the mean coordination number. This behavior is expected since the increase in contact angle leads to larger overlaps among particles, therefore increasing the number of contacts they make. It is noteworthy that for small contact angles particles behave as almost rigid, that is, the mean coordination number is close to 6 as it is for rigid spheres. In particular, for $\theta = 15°$, which is a contact angle often assumed in simulating sintered structures [13,14,25,48], the simulated mean coordination number is equal to 6.21, which is only 3.5% higher than the value of 6 predicted by percolation theory for rigid spheres. Hence, percolation theory, although it does not consider the particle overlaps, is still suited to estimate the number of contacts.

On the other hand, for large contact angles the sintering effects are no longer negligible and the increase in coordination number becomes significant. For $\theta = 23°$, the simulated coordination number equals 6.6, that is, 10% higher than the corresponding value for rigid spheres. Therefore, $\theta = 23°$ is considered as the limiting contact angle, which represents the upper value over which particles no longer behave as rigid spheres. Figure 4.10 shows the mean numbers of contacts (Figure 4.10a) and the percolation probability (Figure 4.10b) of *a*–particles as a function of the volume fraction of *a*–particles after sintering for a contact angle of 23°.

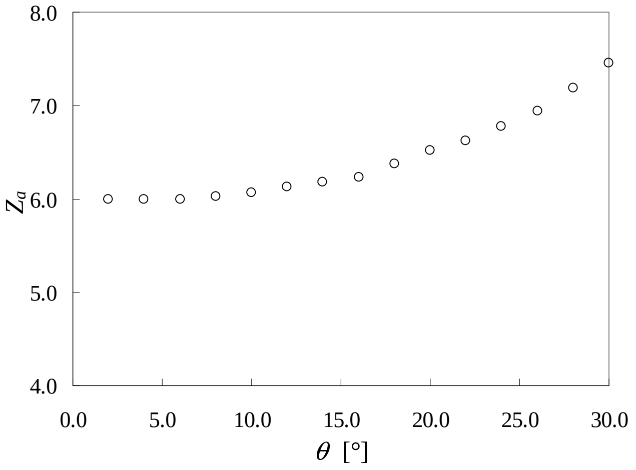

Figure 4.9 – Mean coordination number of a–particles as a function of the contact angle in a binary mixture of monosized spheres.

In Figure 4.10a, numerical simulation results (marks) are compared with percolation theory calculations (lines) of the mean number of *a–a* contacts $Z_{a,a}$ (squares and dashed line), mean number of *a–b* contacts $Z_{a,b}$ (triangles and dot–dashed line) and mean coordination number of *a*–particles Z_a (circles and solid line). The mean relative error between percolation theory and simulation results is in the order of 10% for all the numbers of contacts, revealing that the assumption of rigid spheres in calculating the contact numbers is no longer applicable.

Figure 4.10b shows the comparison between numerical simulation results (marks) and predicted results (lines) regarding the percolation probability of *a*–particles. In particular, Eq. (4.3) was used to predict percolation probability, where the average number of contacts of homolog particles $Z_{a,a}$ was either predicted starting from particle radii and composition (solid line) or directly evaluated from the numerical packing simulation (dashed line). Simulation results show that, given the composition, the percolation probability of the *a*–phase is higher than the percolation theory prediction (solid line), in which sintering effects are not considered. This result is expected due to the larger number of contacts made by particles as a consequence of the allowed overlaps (see $Z_{a,a}$ in Figure 4.10a). However, if the actual $Z_{a,a}$ is used in Eq. (4.3) (dashed line), the predicted percolation probability is in very good agreement with simulated results, suggesting that Eq. (4.3) can reasonably predict the percolation probability in binary mixtures of monosized spheres even if partly overlapped, provided that the correct $Z_{h,h}$ is used.

a)

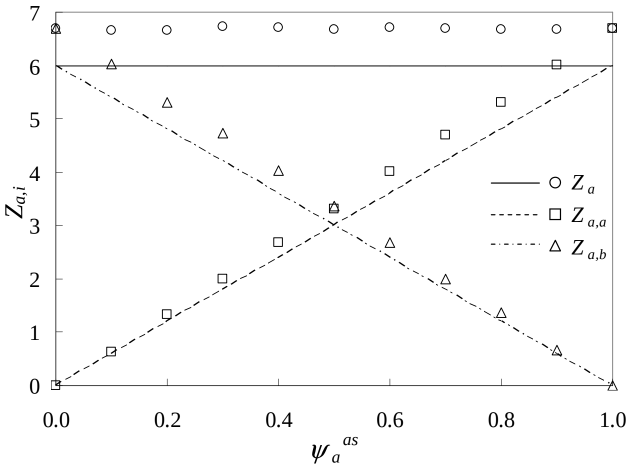

b)

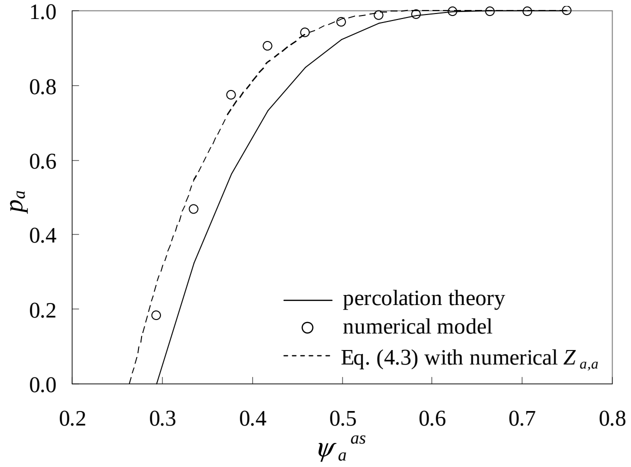

Figure 4.10 – Comparison between percolation theory and numerical reconstruction model for a–particles in a binary mixture of monosized spheres with a contact angle of 23°: a) numbers of contacts for a–particles (Z_a, $Z_{a,a}$ and $Z_{a,b}$) and b) percolation probability as a function of the volume fraction of a–particles.

As a practical application of these results, the contact perimeter between percolating *a*– and *b*–particles and the gas phase was evaluated in two reference cases, that is, θ = 15° and θ = 23°, as a function of packing composition. Such contact perimeter, usually called three–phase boundary (TPB), is an important geometrical parameter in solid oxide fuel cell (SOFC) applications, which has to be maximized in order to promote the electrochemical reaction taking place at the composite electrodes [19,36,48]. The TPB–length depends on both the numbers of contacts of particles and the percolation probability of the two phases. In the numerical simulations, the contact perimeter between *a*– and *b*–particles was analytically evaluated from the knowledge of the center–coordinates and the size of each particle [36]. Concerning percolation theory, the connected TPB length per unit volume λ_{TPB}^{v} was calculated according to Ref. [19] as:

$$\lambda_{TPB}^{v} = \frac{1-\phi_g^{in}}{\frac{4}{3}\pi\left(\zeta_a r_a^3 + \zeta_b r_b^3\right)} p_a p_b \zeta_a Z_{a,b} 2\pi r_a \sin(\theta) \tag{4.5}$$

It is noteworthy that in Eq. (4.5) the contact angle θ is considered only in the sine computation, while it cannot be considered, as previously discussed, in the evaluation of the contact number $Z_{a,b}$ and in the probabilities of percolation p_a and p_b. Therefore, the accounting of the contact angle in percolation theory is only partial and not properly self–consistent.

Initial porosities of 0.404 and 0.329, evaluated in numerical simulations, for θ = 15° and 23°, respectively, were used into Eq. (4.5). In both methods, only the particles belonging to A–clusters were considered as percolating and the gas phase was considered entirely percolating according to Kenney et al. [36] because the porosity was higher than 30% in both cases.

Figure 4.11 shows that there is a satisfactory agreement between percolation theory predictions (solid line) and numerical results (circles) for θ = 15°, that is consistent with the results at the particle level shown above (see Figure 4.9). On the other hand, for θ = 23°, the TPB length estimated by percolation theory (dashed line) is on average 22% smaller than the TPB length evaluated in numerically reconstructed microstructures (squares). This result was expected due to the larger number of contacts per particle in numerical simulations, which leads to an increase of *a–b* contacts as well as to an increase in percolation probability than predicted by percolation theory.

Thus, for $\theta \leq$ 15°, numerical simulations and percolation theory provide very similar results at the particle level (that is, the number of contacts) as well as at the macroscopic level (that is, percolation probability and TPB length per unit volume), although the latter neglects the particle overlaps in the calculation of the contact numbers. The good agreement between the two methods is due to the fact that for contact angles smaller than or equal to 15° these sintering effects are negligible and particles still behave as rigid spheres. Over 23° the overlapping of particles should be considered because the assumption of rigid spheres is no longer reasonable. Regarding percolation theory, theoretical approaches as used for the structural sintering should be used [6,7]. It is worth reminding that in the case studied (i.e., monosized particles with $r_a = r_b$ without pore–formers) sintering of particles yields the highest effects, which will be lower in polydisperse mixtures with pore–formers, so in these cases the agreement between the two methods could be fairly good and the assumption of rigid spheres could hold even for contact angles slightly larger than 15°.

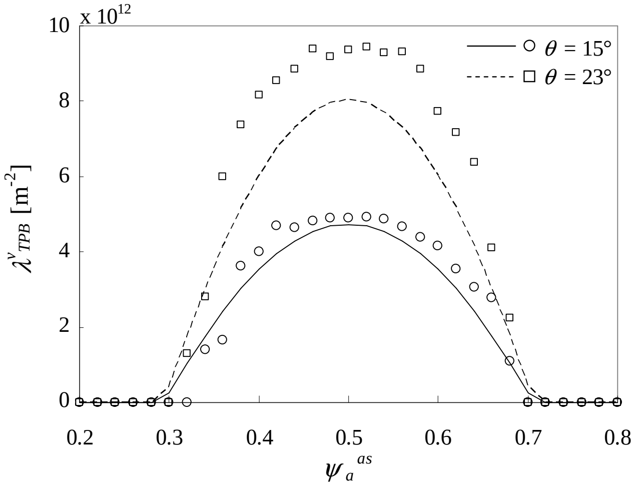

Figure 4.11 – TPB length per unit volume for different contact angles calculated from the percolation theory (lines) by using Eq. (4.5) and the numerical reconstruction model (marks) in a binary mixture of monosized spheres with $r_a = r_b = 0.25\mu m$.

4.4 Conclusions

Contact numbers and percolation probabilities of phases, which are the primary information to calculate more advanced packing properties, were evaluated by both the extended percolation theory and the numerical reconstruction method (namely, drop–and–roll algorithm) in random polydisperse and monodisperse mixtures of spherical particles. The effects of pore–former particles and of the particle–particle contact angle were investigated in random packings of spherical particles in order to assess the effect of the functional sintering on the packing properties and the validity of the assumptions on which the theoretical and numerical methods rely.

Numerical simulations confirmed the theoretical prediction of percolation theory that the presence of pore–former particles not only increases the packing porosity, but it also reduces the numbers of contacts among particles, which decrease as the volume fraction of pore–formers increases. Consequently, the reduced number of contacts among homolog particles leads to a decrease in particle connectivity, that is, a reduction of percolation probability. This phenomenon occurs because pore–formers decompose during the sintering, leaving holes where they were positioned before the sintering.

As the volume fraction of pore–formers increases, solid particles could lose particle–particle connectivity and do not retain their position during the sintering since they could become unstable. The local structure collapse of a sintered microstructure, introduced by the addition of pore–formers in the mixture of powders, was defined as the numerical fraction of unstable solid particles after sintering. In this study, a limit of 1% was used. Numerical simulations enabled the identification of local collapse given the composition and the particle distribution of the mixture. Since both the extended percolation theory and the numerical reconstruction model rely on the assumption that local collapse does not occur in order to predict packing properties, the range of validity of these methods was individuated, which is reasonably wide because, except for some limited cases, the local structure collapse did not occur for final porosities smaller than 60%.

Numerical simulations with partly overlapped spheres helped to assess the effect of particle overlap on contact numbers and percolation probability. Numerical results showed that for a contact angle smaller than 15° the particles behave as they were rigid, so that sintering effects are negligible. In this situation, percolation theory, which assumes that particles are rigid in the calculation of contact numbers, provided results in good agreement with numerical simulation results. For contact angles larger than 23°, particle overlaps become significant, so that the average contact numbers are at least 10% higher than what could be expected in a similar situation with rigid spheres. In such a case, percolation theory underestimates the contact and percolation information.

This study also highlighted that, for practical purposes, percolation theory and numerical reconstruction algorithm provide comparable and consistent results even for sintered random structures. Thus, they can be used interchangeably to estimate the effective properties strictly connected to the contact information.

Nomenclature

Glossary

m	number of particle sizes
n_{h_i}	number of particles belonging to the *i*–th particle size of *h*–particles
p	percolation probability
r	radius of a type of particles [μm]
$\bar{r}$	mean radius of a distribution [μm]
$z^{(l)}_{h_i,k_j}$	number of contacts of the *l*–th h_i–particle with k_j–particles
$Z_{h,h}$	overall mean number of contacts for all *h*–particles (see Eq. (4.4))
Z_{h_i}	mean coordination number of h_i–particles (see Eq. (4.2))

ζ	numerical fraction of a type of particles (before sintering)
θ	contact angle (see Figure 4.2)
λ_{TPB}^{v}	three–phase boundary length per unit volume [m^{-2}]
σ	standard deviation of normal distribution [μm]
ϕ_g^{fin}	final porosity (after sintering)
ϕ_g^{in}	initial porosity (before sintering)
ψ	volume fraction of a type of particles relative to the total solid (before sintering)

Superscripts

as	after sintering

Subscripts

a	*a*–particles
b	*b*–particles
f	pore–former particles
h	particles of type *h* (with *h* = *a*, *b* or *f* if not otherwise specified)
h_i	*i*–th particle size of *h*–particles
k	particles of type *k* (with *k* = *a*, *b* or *f* if not otherwise specified)

Acknowledgements

This research was supported by the NSERC Solid Oxide Fuel Cell Canada Strategic Research Network from the Natural Science and Engineering Research Council (NSERC) and other sponsors listed at www.sofccanada.com.

References

[1] S.J. Kang, Sintering: densification, grain growth and microstructure, Elsevier, Oxford, 2005.

[2] L. Olmos, C.L. Martin, D. Bouvard, Sintering of mixtures of powders: Experiments and modelling, Powder Technol. 190 (2009) 134–140.

[3] F.F. Lange, L. Atteraas, F. Zok, J.R. Porter, Deformation consolidation of metal powders containing steel inclusions, Acta Metall. Mater. 39 (1991) 209–219.

[4] C.D. Turner, M.F. Ashby, The cold isostatic pressing of composite powders, I. Experimental investigations using model powders, Acta Mater. 44 (1996) 4521–4530.

[5] C.L. Martin, O. Lame, D. Bouvard, Cohesion and dilatation of powder compacts containing hard phase particles under highly deviatoric stress states, Machanics Mater. 32 (2000) 405–421.

[6] E. Arlt, The influence of an increasing particle coordination on the densification of spherical powders, Acta Metall. 30 (1982) 1883–1890.

[7] D. Bouvard, Modelling the densification of powder composites by power law creep, Acta Metall. Mater. 41 (1993) 1413–1420.

[8] C.L. Martin, D. Bouvard, Study on the cold compaction of composite powders by the discrete element method, Acta Mater. 51 (2003) 373–386.

[9] C.L. Martin, D. Bouvard, S. Shima, Study of particle rearrangement during powder compaction by the Discrete Element Method, J. Mech. Phys. Solids. 51 (2003) 667–693.

[10] C.L. Martin, D. Bouvard, Isostatic compaction of bimodal powder mixtures and composites, Int. J. Mech. Sci. 46 (2004) 907–927.

[11] C.L. Martin, L.C.R. Schneider, L. Olmos, D. Bouvard, Discrete element modeling of metallic powder sintering, Scr. Mater. 55 (2006) 425–428.

[12] M. Juhl, S. Primdahl, C. Manon, M. Mogensen, Performance/structure correlation for composite SOFC cathodes, J. Power Sources. 61 (1996) 173–181.

[13] J.H. Nam, D.H. Jeon, A comprehensive micro-scale model for transport and reaction in intermediate temperature solid oxide fuel cells, Electrochim. Acta. 51 (2006) 3446–3460.

[14] P. Costamagna, P. Costa, V. Antonucci, Micro-modelling of solid oxide fuel cell electrodes, Electrochim. Acta. 43 (1998) 375–394.

[15] S.B. Adler, Factors governing oxygen reduction in solid oxide fuel cell cathodes., Chem. Rev. 104 (2004) 4791–4843.

[16] P. Costamagna, M. Panizza, G. Cerisola, A. Barbucci, Effect of composition on the performance of cermet electrodes. Experimental and theoretical approach, Electrochim. Acta. 47 (2002) 1079–1089.

[17] M. Mogensen, S. Skaarup, Kinetic and geometric aspects of solid oxide fuel cell electrodes, Solid State Ionics. 86-88 (1996) 1151–1160.

[18] D. Chen, Z. Lin, H. Zhu, R.J. Kee, Percolation theory to predict effective properties of solid oxide fuel-cell composite electrodes, J. Power Sources. 191 (2009) 240–252.

[19] A. Bertei, C. Nicolella, Percolation theory in SOFC composite electrodes: Effects of porosity and particle size distribution on effective properties, J. Power Sources. 196 (2011) 9429–9436.

[20] G.T. Nolan, P.E. Kavanagh, Computer simulation of random packing of hard spheres, Powder Technol. 72 (1992) 149–155.

[21] E.M. Tory, B.H. Church, M.K. Tam, M. Ratner, Simulated random packing of equal spheres, Can. J. Chem. Eng. 51 (1973) 484–493.

[22] A. Bertei, Chapter 3 of this Thesis, 2013.

[23] N. Metropolis, A.W. Rosenbluth, M.N. Rosenbluth, A.H. Teller, E. Teller, Equation of state calculations by fast computing machines, J. Chem. Phys. 21 (1953) 1087–1092.

[24] D. He, N.N. Ekere, L. Cai, Computer simulation of random packing of unequal particles, Phys. Rev. E. 60 (1999) 7098–7104.

[25] J. Sanyal, G.M. Goldin, H. Zhu, R.J. Kee, A particle-based model for predicting the effective conductivities of composite electrodes, J. Power Sources. 195 (2010) 6671–6679.

[26] J. Finney, Fine structure in randomly packed, dense clusters of hard spheres, Mater. Sci. Eng. 23 (1976) 199–205.

[27] D. He, N.N. Ekere, Computer simulation of powder compaction of spherical particles, J. Mater. Sci. Lett. 17 (1998) 1723–1725.

[28] E.M. Tory, N.A. Cochrane, S.R. Waddel, Anisotropy in simulated random packing of equal spheres, Nature. 220 (1968) 1023–1024.

[29] W.M. Visscher, M. Bolsterli, Random packing of equal and unequal spheres in two and three dimensions, Nature. 239 (1972) 504–507.

[30] W.S. Jodrey, E.M. Tory, Simulation of random packing of spheres, J. Simul. 32 (1979) 1–12.

[31] M. Suzuki, K. Makino, M. Yamada, K. Iinoya, Study on the coordination number in a system of randomly packed, uniform-sized spherical particles, Int. Chem. Eng. 21 (1981) 482–488.

[32] P.A. Cundall, O.D.L. Strack, A discrete numerical model for granular assemblies, Géotechnique. 29 (1979) 47–65.

[33] L.F. Liu, Z.P. Zhang, A.B. Yu, Dynamic simulation of the centripetal packing of mono-sized spheres, Phys. A Stat. Mech. Its Appl. 268 (1999) 433–453.

[34] Z.P. Zhang, L.F. Liu, Y.D. Yuan, A.B. Yu, A simulation study of the effects of dynamic variables on the packing of spheres, Powder Technol. 116 (2001) 23–32.

[35] A. Bezrukov, M. Bargiel, D. Stoyan, Statistical analysis of simulated random packings of spheres, Part. Part. Syst. Charact. 19 (2002) 111–118.

[36] B. Kenney, M. Valdmanis, C. Baker, J.G. Pharoah, K. Karan, Computation of TPB length, surface area and pore size from numerical reconstruction of composite solid oxide fuel cell electrodes, J. Power Sources. 189 (2009) 1051–1059.

[37] H.-W. Choi, A. Berson, J.G. Pharoah, S.B. Beale, Effective transport properties of the porous electrodes in solid oxide fuel cells, Proc. Inst. Mech. Eng. Part A J. Power Energy. 225 (2011) 183–197.

[38] A. Berson, H.-W. Choi, J.G. Pharoah, Determination of the effective gas diffusivity of a porous composite medium from the three-dimensional reconstruction of its microstructure, Phys. Rev. E. 83 (2011) 026310.

[39] D. Bouvard, F.F. Lange, Relation between percolation and particle coordination in binary powder mixtures, Acta Metall. Mater. 39 (1991) 3083–3090.

[40] M. Suzuki, T. Oshima, Estimation of the co-ordination number in a multi-component mixture of spheres, Powder Technol. 35 (1983) 159–166.

[41] A. Bertei, C. Nicolella, A comparative study and an extended theory of percolation for random packings of rigid spheres, Powder Technol. 213 (2011) 100–108.

[42] M.M. Roozbahani, B.B.K. Huat, A. Asadi, The effect of different random number distributions on the porosity of spherical particles, Adv. Powder Technol. 24 (2013) 26–35.

[43] M.M. Roozbahani, B.B.K. Huat, A. Asadi, Effect of rectangular container's sides on porosity for equal-sized sphere packing, Powder Technol. 224 (2012) 46–50.

[44] Y. Shi, Y. Zhang, Simulation of random packing of spherical particles with different size distributions, Appl. Phys. A. 92 (2008) 621–626.

[45] D. Chen, L. Lu, J. Li, Z. Yu, W. Kong, H. Zhu, Percolation micro-model to predict the effective properties of the composite electrode with poly-dispersed particle sizes, J. Power Sources. 196 (2011) 3178–3185.

[46] C.-H. Kuo, P.K. Gupta, Rigidity and conductivity percolation thresholds in particulate composites, Acta Metall. Mater. 43 (1995) 397–403.

[47] J.H. Yu, G.W. Park, S. Lee, S.K. Woo, Microstructural effects on the electrical and mechanical properties of Ni–YSZ cermet for SOFC anode, J. Power Sources. 163 (2007) 926–932.

[48] B. Kenney, K. Karan, Engineering of microstructure and design of a planar porous composite SOFC cathode: A numerical analysis, Solid State Ionics. 178 (2007) 297–306.

Chapter 5

Numerical Reconstruction of Random Packings of Non–Spherical Particles

This Chapter presents the numerical reconstruction method used to simulate random packings of nonspherical particles and arbitrary shapes. The method must be considered as an extension of the drop–and–roll algorithm described in Chapter 4, to be used when the particle shape cannot be approximated as a sphere.

The study shows that:

i. the proposed algorithm is able to produce close packings, whose properties are in fair agreement with more consolidated algorithms;

ii. in the resulting microstructure particles touch each other, which is a desired feature often not guaranteed by other packing algorithms;

iii. sintering phenomena and packings composed by mixtures of polydisperse particles and agglomerates can be simulated.

This Chapter was adapted from the paper "Modified collective rearrangement sphere–assembly algorithm for random packings of nonspherical particles: Towards engineering applications" by A. Bertei, C.-C. Chueh, J.G. Pharoah and C. Nicolella, in press in Powder Technology (doi: 10.1016/j.powtec.2013.11.034).

Abstract

A modified collective rearrangement algorithm, based on the sphere–assembly representation of the particle shape, is presented for simulating random packings of nonspherical particles and arbitrary shapes. Compared to other collective rearrangement methods, the modification introduced by this algorithm consists in i) avoiding the particle–to–container shrinking procedure by allowing particles to sequentially settle down and ii) in a stability constraint applied to all the particles in the packing. The coupling of these criteria ensures that all the particles are stable and contacting each other, allowing for an unambiguous detection of contacts, which is important in the evaluation of the effective properties desired in many engineering applications, such as percolation thresholds and effective conductivity. The effect of the internal parameters of the algorithm is investigated, showing that random close packings can be obtained. The algorithm is applied to simulate packings of rigid ellipsoids and cylinders with different aspect ratios, which are compared with simulation results provided by other packing algorithms, showing the consistency of our method. Simulations of inter–penetrating particles, mixtures of particles with different shapes and packings of agglomerates are shown, which confirm the applicability of the method to a broad range of packing problems of practical interest and, in particular, for fuel cell applications.

5.1 Introduction

Random packings of particles are widely considered in science and engineering applications: they have been suggested as models for liquid and glass structure [1,2] and they are used to represent granular materials [3], packed beds, cermets [4] as well as in many other applications. In the last decades, several packing algorithms have been developed to represent the packing microstructure and for the evaluation of effective properties. Many algorithms have been developed in particular for spherical particles: Monte Carlo [5–7], drop–and–roll and sequential deposition algorithms [8–13], collective rearrangement [14–16], discrete element methods [17–19] and molecular dynamics [20,21] to cite the most common ones.

Recently, in order to have a better representation of particulate systems, and mainly due to the availability of increased computational resources, the attention has shifted to the simulation of random packings of nonspherical particles. The first problem arising with nonspherical particles is the more complex shape than the spherical form. Different approaches have been proposed to account for nonspherical shapes. In several methods the analytical equation of the particles is considered in the algorithm: packings of ellipsoids [22–25], spherocylinders [26], superballs [27,28], superellipsoids [29] and general convex particles [30] have been investigated. The use of the analytical equation to represent the particle has the clear advantage that the exact shape of the particles is considered. Although such a method is elegant and rigorous, the detection of overlaps is non–trivial and may lead to detection errors in some critical situations [31]. In addition, the algorithm is tailored for the specific shape under consideration and, clearly, particles with a shape that cannot be represented analytically cannot be simulated.

Another approach consists of tessellating the container and the particle shape with a grid, digitizing both the domain and the particles [32–35]. In this way, any particle shape can be approximated with a coherent collection of pixels (2D) or voxels (3D), and the collision and overlap detection is simply noting whether two objects occupy the same site in the grid. On the other hand, quantitative predictions of packing characteristics, such as packing density, are sensitive to the resolution used and increasing the resolution through a finer grid leads to too much higher memory requirements than other methods [32]. Moreover, the movement of the particles is discretized, such that particle trajectories are affected by the resolution of the grid.

The third method is the so–called multi–sphere (or sphere–assembly) approach [36–40], in which particles are represented by an assembly of component spheres reproducing their shape. As the digitizing method, general particle shapes, analytical or otherwise, can be reproduced by varying the position and the size of the component spheres within the particle. The detection of particle overlaps is carried out by checking if two component spheres, belonging to different particles, overlap, which is much easier if compared with the first approach where the analytical particle equations are used. On the other hand, higher resolutions, obtained with a larger number of component spheres, slow down the algorithm and require more computer memory, though usually less than in the case of the digitizing method.

The packing procedure is the second important feature to consider and it can affect the resulting packing properties. Existing physical simulation models include the discrete element method (DEM) [29,39,40] and the molecular dynamics method (MD) [23,24,28]. In these algorithms the real interaction forces are taken into account, rigorously simulating the dynamics of the packing generation in time domain. While even jammed configurations can be obtained [22,41], these methods are usually very complex and, although specific technical solutions can be used to speed up the simulations, they are less computationally efficient than many purpose designed packing algorithms, at least for spheres [42]. Furthermore, for some engineering applications such a highly detailed physical representation is not necessary.

In Monte Carlo methods [31], each particle is added to the domain one by one by selecting a random position and orientation and checking the overlaps with previously placed particles: if there are no overlaps, the current particle is accepted, otherwise a new position is tried and, after a predefined number of trials, the particle is rejected if an acceptable placement has not been found. Though this algorithm is straightforward, it is very time consuming and no rearrangement of particles is permitted (i.e., the orientation is completely random). This usually results in loose packings, and when rigid particles are simulated the majority if not all the particles are not in contact with one another.

Another packing algorithm, which has been widely adapted for nonspherical random packings [36,38], is the collective rearrangement method (CR). In this algorithm all the particles are randomly distributed and oriented in a domain which is smaller than the volume that all the particles may occupy. At the beginning particles experience large overlaps, which are individually removed by iteratively moving and rotating each particle under the action of a restoring force and a restoring moment generated in consideration of the overlaps. The rearrangement of particles is usually coupled with a process of particle to domain reduction, consisting of either reducing (i.e., scaling down) the particle size or increasing (i.e., scaling up) the domain volume. When simulating hard particles, the algorithm stops when all the overlaps have been removed. This technique is expected to run faster than DEM and MD, since the physics is only approximated in order to save computational time. While this method usually provides close packings, these are generally not strictly jammed. Moreover, there is no check about the contact information of particles during the rearrangement process: typically, in the final configuration particles are arranged in unstable positions or are isolated, feature which is pronounced by the particle–to–container shrinking procedure.

Finally, in principle each packing algorithm could be coupled with one of the three approaches described above to represent the particle shape, although some concerns have been recently arisen when the sphere–assembly approach is coupled with the discrete element method [39,40].

In this study, a collective rearrangement method coupled with the sphere–assembly approach is used, sharing some features in common with the Nolan and Kavanagh work [36]. However, in the present algorithm both the particles and the container maintain their dimensions, avoiding the particle shrinking procedure. A constraint has been introduced and applied to each particle in order to provide packings in which all the particles are stable. The coupling of these two characteristics ensures that all the particles contact each other in the final configuration, characteristics that cannot be generally guaranteed by conventional

CR algorithms [21]. The unambiguous detection of contacts is a desired feature in many engineering applications because percolation thresholds and conduction properties of the packing are strictly related to the number of contacts [7,43–45]. In addition, the algorithm has been generalized to allow for multiple polydisperse phases and to a controlled degree of particle overlap in order to simulate deformable particles and sintered multi–phase packings.

The study focuses on the application to rigid and non–rigid ellipsoids, cylinders and agglomerates, though the algorithm is sufficiently general that any particle shape can in principle be used. The chosen sub–set of shapes are common in several engineering applications, such as in polymer electrolyte [46] and solid oxide [47–49] fuel cells which, in part, motivated the developments described herein. In these applications it is important that in the reconstructed microstructure the packing is representative of a stable configuration and the particles experience a desired degree of overlap, in order to ensure that charges can be transported and converted throughout the packing [47,48,50–53].

The study is organized as follows: in Section 5.2 the algorithm is presented in detail; in Section 5.3, the algorithm is first explored by assessing the effects of its internal parameters, then simulation results for rigid spheres, ellipsoids and cylinders are compared to those obtained by other algorithms, and finally some results regarding the broader possibilities of the algorithm are shown.

5.2 Algorithm

5.2.1 General aspects

The algorithm was written in C++ programming language with the use of some functions provided in an open source finite element deal.II library [54]. The code was generalized to account for both 2D and 3D packings with one or more polydisperse or monodisperse phases of rigid or deformable particles: in this study only the three dimensional problem is described.

The algorithm begins with the definition of the domain size and the number, types and sizes of particles. The domain consists of a box of specified dimensions having a rigid floor and periodic boundary conditions in the horizontal directions. Based on the desired volume composition, the initial porosity and the particle size distribution of each phase, the number of particles for each phase is calculated. A very small and unrealistic initial porosity is used in order to fill the domain with more particles than there will be in the final configuration: in this way, packings that do not completely fill the chosen domain are excluded.

All the particles are labeled with a progressive index *i*, from 1 to the total number of particles N_{part}. Apart from its type and size, each particle *i* is characterized by its center coordinates $\underline{c}_i$ (i.e., the coordinates of its center of mass) and two axial directions, $\hat{\underline{x}}_i$ and $\hat{\underline{z}}_i$, which identify the orientation of the particle with respect to the global system of reference (see Figure 5.1). Note that the third axis $\hat{\underline{y}}_i$ is not independent and can be easily calculated as $\hat{\underline{y}}_i = \hat{\underline{z}}_i \times \hat{\underline{x}}_i$.

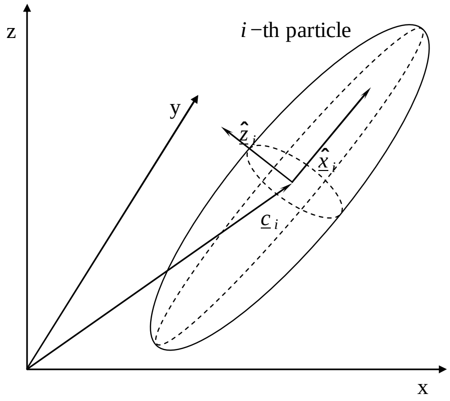

Figure 5.1 – Center coordinates and orientation axes of a generic particle (here an ellipsoid) in the domain.

Each particle is represented by an assembly of $n_c^{(i)}$ component spheres, which means that the radius ($r_k^{(i)}$) and relative position of each $k^{(i)}$ component sphere with respect to the local particle coordinate system ($\tilde{\underline{c}}_k^{(i)}$) are stored. Note that $\tilde{\underline{c}}_k^{(i)}$ represents the center of the $k^{(i)}$ component sphere in the local frame, which is centered on the particle center of mass and oriented along the particle axes. The center coordinate of the component sphere in the global frame is indicated with $\underline{c}_k^{(i)}$. There is a one–to–one correspondance between the center of the component sphere in the global (i.e., $\underline{c}_k^{(i)}$) and in the local (i.e., $\tilde{\underline{c}}_k^{(i)}$) coordinate systems as reported in Eq. (5.1).

$$\underline{c}_k^{(i)} = \underline{c}_i + \begin{vmatrix} \hat{\underline{x}}_i^T \\ \hat{\underline{y}}_i^T \\ \hat{\underline{z}}_i^T \end{vmatrix}^{-1} \cdot \tilde{\underline{c}}_k^{(i)} \quad \text{and} \quad \tilde{\underline{c}}_k^{(i)} = \begin{vmatrix} \left(\underline{c}_k^{(i)} - \underline{c}_i\right) \cdot \hat{\underline{x}}_i \\ \left(\underline{c}_k^{(i)} - \underline{c}_i\right) \cdot \hat{\underline{y}}_i \\ \left(\underline{c}_k^{(i)} - \underline{c}_i\right) \cdot \hat{\underline{z}}_i \end{vmatrix} \tag{5.1}$$

Eq. (5.1) shows that the component sphere center in the global frame $\underline{c}_k^{(i)}$ can be calculated from the local one $\tilde{\underline{c}}_k^{(i)}$ by applying a rotation matrix, given by the versors identifying the particle orientation, and adding the particle center $\underline{c}_i$. On the other hand, given the component sphere center in the global frame $\underline{c}_k^{(i)}$, the projection of the vector $\left(\underline{c}_k^{(i)} - \underline{c}_i\right)$ on the orientation axes provides the center of the component sphere in the local particle frame.

At the beginning particles are randomly and uniformly distributed and oriented in the domain. The random orientation is determined by using the Marsaglia method [55] to find an axis of rotation and by randomly choosing a rotation angle between 0 and 2π (details on how to rotate a particle are given in Section 5.2.4). The randomness is checked calculating the nematic order parameter from the alignment matrix $\underline{\underline{Q}}$ [56]:

$$\underline{\underline{Q}} = \frac{1}{N_{part}} \sum_{i=1}^{N_{part}} \left(\frac{3}{2} \hat{\underline{x}}_i \otimes \hat{\underline{x}}_i - \frac{1}{2} \underline{\underline{I}} \right) \tag{5.2}$$

where $\underline{\underline{I}}$ is the identity matrix and $\otimes$ is the tensor product. The nematic order parameter is equal to $-2\lambda_2$, where λ_2 is the middle eigenvalue of the orthogonal matrix $\underline{\underline{Q}}$. The orientation of particles is repeated, if necessary, until the absolute value of the nematic order parameter of the initial configuration is lower than 0.1, which means that the initial configuration is disordered and isotropic [38], which helps to speed up the rearrangement process.

After the initial placement, the configuration of particles has a lot of undesired overlaps and the packing is, in general, unstable. In order to get the final packing configuration, a collective rearrangement procedure, following the flow chart represented in Figure 5.2, is used.

At each iteration, provided that the number of internal cycles has not been exceeded leading to the application of the reallocation or the reposition procedures (details are given hereafter in this Section), the yet to be placed particle with the lowest *z*–coordinate is selected. By choosing the lowest particle at each iteration, and manipulating it to find a stable fixed position, the packing of stable particles grows vertically from the bottom to the top of the domain. Neighboring particles are then identified (see Section 5.2.2 for further details) and considered as overlapping if the degree of overlap with the current particle is larger than desired, otherwise they are labeled as contacting particles. Each overlapping particle generates a force and a moment which lead to translation and rotation of the particles. On the other hand, the contacting particles, which are the already placed neighboring particles with a degree of overlap equal to or smaller than what is desired, do not cause particle movements. Contacting particles are considered only to check the stability of the current particle (see Section 5.2.5).

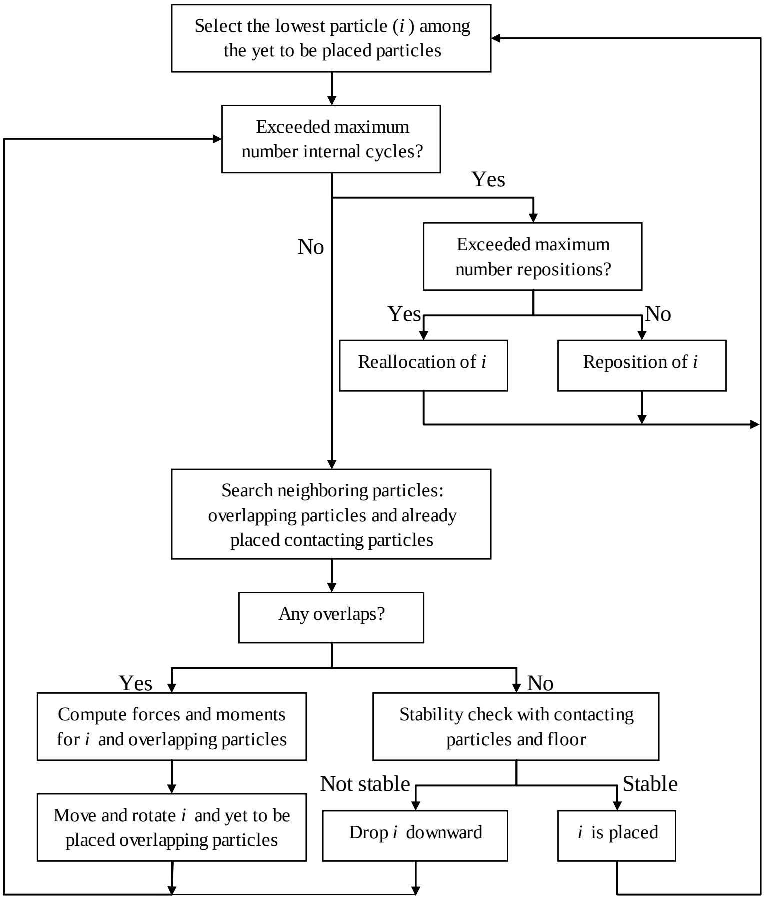

Figure 5.2 – Flow chart of the algorithm.

If the current particle has at least one overlap, the resultant forces and moments between the current and the overlapping particles are calculated (see Section 5.2.3 for details). The current and the yet to be placed overlapping particles are then translated and rotated according to the respective resultant forces and moments (see Section 5.2.4). The placed particles are neither moved nor rotated since they are considered as fixed in their final (stable) configuration. After the movement of the particles, the process is repeated.

If the current particle does not experience any overlap, its stability is checked with regard to contacting particles and the floor (see Section 5.2.5). If the current particle is stable, it is considered as placed, that is, fixed in its final position, and a new particle is selected, otherwise the particle is dropped downward a bit and the procedure is repeated. Note that fixing the particle position and orientation as soon as a stable position for the current particle is reached represents a simplification of the packing procedure. In fact, in reality the placement of following particles may destabilize the previously placed ones. This destabilization phenomenon is not considered in our method for the sake of simplicity and to save computational cost, therefore each placed particle is fixed in its position until the end of the rearrangement process. Note that this simplification is adopted also in well–established packing algorithms, such as the drop–and–roll method for spherical particles [9–12].

If after a predefined number of internal cycles (i.e., several movements and rotations) the current particle has not yet found a stable placement, it is considered as stuck in an unstable configuration. For example, the particle could be surrounded by already placed particles, which generate forces and moments that might cancel each other. In such a case, the current particle is repositioned, which means that it is slightly and randomly translated and rotated from its position. After this repositioning, the overlapping and contacting particles are again identified and the rearrangement process is repeated until either the particle finds a stable position or the maximum number of internal cycles is again exceeded, so that the particle will be repositioned once again. If after a predefined number of repositioning attempts the particle is still stuck, it is reallocated. The reallocation consists of removing the particle from the current position and randomly reallocating it with a random orientation in another point of the domain. Since the domain could be full of already placed particles, the z–coordinate of the particle is chosen between 0 and 2 times the domain height. However, the algorithm parameters should be tailored in order to minimize as much as possible the repositioning and the reallocation of particles.

It is worth noting that during the rearrangement process both the particles and the domain maintain their dimensions in contrast to other collective rearrangement algorithms, wherein the particles or the domain are respectively shrunk or increased at each iteration [15,36,38,57]. In our algorithm, the choice of not using this operation depends on this consideration: when a particle experiences overlaps and contacts, the effects (i.e., the movements) should be limited to the neighborhood of the current particle while the condition of other particles should remain unchanged. If the current particle is stuck somewhere, the other particles are unaffected (for example, they are not shrunk) because of this undesired situation. The particle shrinking or the container growing operations have been replaced in our algorithm by the reposition and reallocation procedures.

5.2.2 Checking the overlaps and the contacts

The most time consuming step in the algorithm is that of checking if the current particle has overlaps or contacts with other particles. In order to obtain packings of non–rigid particles, the distinction between overlapping and contacting particles is made by using a kernel scale factor and a contact allowance. Basically, it is assumed that each particle has a hard kernel which cannot be penetrated by surrounding particles, as in Figure 5.3a, which defines the permitted contact. The kernel scale factor κ_f represents the volume fraction of the kernel to the particle volume, the contact allowance is similarly defined. A particle is marked as overlapping if its kernel intersects the kernel of the current particle (see Figure 5.3b, bottom left). On the other hand, the neighboring particle, provided it is placed, is defined as contacting if there is an intersection of the contact allowance volumes (Figure 5.3b, bottom right), otherwise it is considered as neither overlapping nor contacting (Figure 5.3b, top), that is, there is no effect on the current particle.

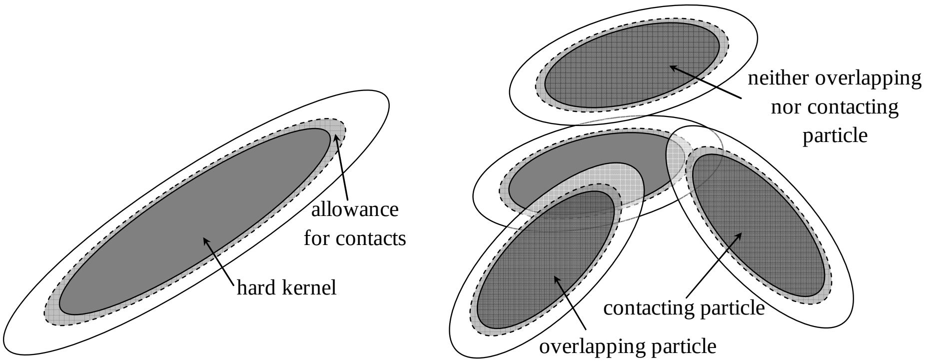

Figure 5.3 – a) Definition of hard kernel and allowance for contacts. b) Example of overlaps and contacts (the current particle is in the middle).

The check of overlaps and contacts is made by scaling down each particle to its hard kernel and its kernel plus the contact allowance. Since the particles are represented by an assembly of component spheres, this is done by scaling the radius and the center of each component sphere in the local frame. When the particle shape is convex, such as for ellipsoids, cylinders and for many other geometries of interest in engineering applications, the kernel is identified by reducing the radius and the distance of each component sphere from the particle center. In this scaling procedure, the kernel is just a smaller copy of the original particle, with the same center and orientation, as represented in Figure 5.3a. For particles having a non–convex shape, for example a hollow cylinder, such a simplified scaling law cannot be used. However, the concept of hard kernel and its identification through component spheres still hold, although not considered in this study.

As the particles have been scaled down to their kernels, overlaps and contacts between adjacent particles can easily be detected by checking each component sphere within one particle with every component sphere in the other particle. This check may be very time consuming when a large number of particles and component spheres per particle are used, but it is sped up by conveniently dividing the domain into cubical sectors and checking only the particles belonging to sectors adjacent to that occupied by the current particle. In addition, each particle is characterized by a bounding sphere [23], whose radius is equal to the maximum distance of the particle external surface from the particle center of mass. If two bounding spheres do not overlap, the two particles are not neighboring, thus there is no need to check in detail component sphere by component sphere.

The result of this step is the list of indices of each neighboring particle, indicating if they are overlapping or contacting the current particle.

5.2.3 Computing forces and moments

Each particle which overlaps the current particle produces forces and moments which are calculated by using the component spheres. Taking into account two component spheres $h^{(i)}$ and $k^{(j)}$, belonging to two different particles, $h^{(i)}$ to the current particle i while $k^{(j)}$ to the overlapping one j, the shared volume $V_{h^{(i)},k^{(j)}}$ between the two component spheres produces a repulsive force $\underline{F}_{h^{(i)},k^{(j)}}$, as represented in Figure 5.4. Such a force is oriented along the direction connecting the two component sphere centers and proportional to the shared volume as follows:

$$\underline{F}_{h^{(i)},k^{(j)}} = \rho_F V_{h^{(i)},k^{(j)}} \frac{\underline{c}_h^{(i)} - \underline{c}_k^{(j)}}{\left|\underline{c}_h^{(i)} - \underline{c}_k^{(j)}\right|} \delta_{h^{(i)},k^{(j)}} \tag{5.3}$$

where ρ_F is a force factor and $\delta_{h^{(i)},k^{(j)}}$ is the Kronecker delta, equal to 1 if the two component spheres overlap, 0 otherwise. The force applied on the overlapping particle is merely equal in magnitude but opposite in direction.

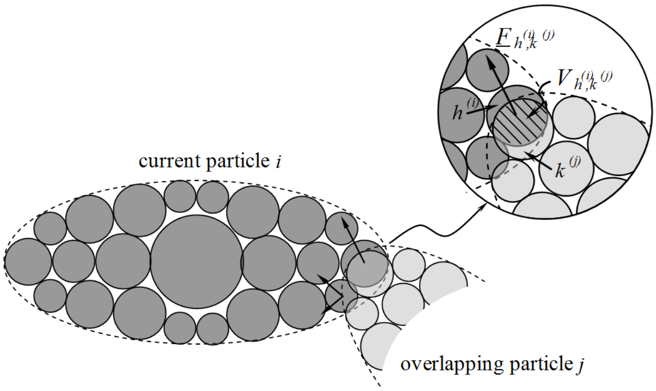

Figure 5.4 – Forces created by the overlap of two particles calculated by using the component spheres.

The force produced by the overlap of component spheres $h^{(i)}$ and $k^{(j)}$ produces also a moment $\underline{M}_{h^{(i)},k^{(j)}}$, applied to the center of mass of particles *i* and *j*, equal to:

$$\underline{M}_{h^{(i)},k^{(j)}} = \left(\underline{c}_h^{(i)} - \underline{c}_i\right) \times \underline{F}_{h^{(i)},k^{(j)}} \tag{5.4}$$

The resultant force ($\underline{F}_i$) and moment ($\underline{M}_i$) on the particle are obtained by summing up the contributions of each component sphere for all the $N_o^{(i)}$ particles overlapping the current particle *i* as follows:

$$\underline{F}_i = \sum_{j=1}^{N_o^{(i)}} \sum_{h=1}^{n_c^{(i)}} \sum_{k=1}^{n_c^{(j)}} \underline{F}_{h^{(i)},k^{(j)}} \quad \text{and} \quad \underline{M}_i = \sum_{j=1}^{N_o^{(i)}} \sum_{h=1}^{n_c^{(i)}} \sum_{k=1}^{n_c^{(j)}} \underline{M}_{h^{(i)},k^{(j)}} \tag{5.5}$$

Particle friction is not accounted for in this work, though in principle it could be considered, because friction is often associated to the generation of loose packings [58] while the study focuses on random close packings. Similarly, the gravity is not considered in calculating the resultant forces and moments: in principle, it corresponds to neglect the gravity force contribution in comparison to the restoring forces while particles are overlapping.

5.2.4 Moving and rotating the particles

Based on the calculated resultant force and moment, at each iteration the current and its overlapping particles are translated and rotated, with the exception of the already placed overlapping particles, which are considered fixed in their configuration.

The translation is made by applying a displacement $\underline{d}_i = \underline{F}_i/V_i$, where V_i represents the particle volume, to both the particle center of mass and the centers of its component spheres. The rotation, along the direction given by the moment $\underline{M}_i$, is made by using the rotation matrix:

$$\underline{\underline{R}} = \cos\theta_i \underline{\underline{I}} + \sin\theta_i \left\lfloor \hat{\underline{M}}_i \right\rfloor_\times + \left(1 - \cos\theta_i\right) \hat{\underline{M}}_i \otimes \hat{\underline{M}}_i \tag{5.6}$$

where $\hat{\underline{M}}_i = \underline{M}_i / \left|\underline{M}_i\right|$ represents the axis of rotation and $\left\lfloor \hat{\underline{M}}_i \right\rfloor_\times$ the cross product matrix of $\hat{\underline{M}}_i$. The magnitude of the rotation angle θ_i is calculated as $\theta_i = \left|\underline{M}_i\right| / J_i$, where J_i is the scalar moment of inertia of the particle calculated with respect to the axis of rotation $\hat{\underline{M}}_i$. Knowing the rotation matrix, the rotation of the orientation axes $\hat{\underline{x}}_i$ and $\hat{\underline{z}}_i$ as well as of the coordinates of the center of each component sphere is performed as $\hat{\underline{x}}_i = \underline{\underline{R}} \cdot \hat{\underline{x}}_i$, $\hat{\underline{z}}_i = \underline{\underline{R}} \cdot \hat{\underline{z}}_i$ and $\underline{c}_k^{(i)} = \underline{c}_i + \underline{\underline{R}} \cdot \left(\underline{c}_k^{(i)} - \underline{c}_i\right)$.

For analytical shapes, such as ellipsoids and cylinders, both the particle volume V_i and the particle moment of inertia J_i are calculated by considering their analytical expression. For non–analytical shapes, such as agglomerates of spheres, V_i and J_i are calculated by using the component spheres (see Appendix 5.A for details).

Note that linking the displacement to the force through the particle volume and the rotation angle to the moment through the moment of inertia represents a *quasi*–physical approach to the particle movement. However, in the proposed algorithm, unlike DEM and MD approaches, the magnitude of forces and moments experienced by particles does not have a real physical meaning: only the relationship between the amount of overlap and the displacement and rotation necessary to remove the overlap matters. In addition, in order to get closer packings, independently of the magnitude of the resultant force and moment, the magnitude of the displacement $|d_i|$ and of the angle θ_i are predefined. In particular, both $|d_i|$ and θ_i are chosen to be sufficiently small to produce a movement of the same order of magnitude of the contact allowance used for defining the contact region (see Section 5.2.2). As an additional consequence of assigning predefined magnitudes of displacement and rotation angle, the specific value set to the force factor ρ_F in Eq. (5.3) is not important and it does not play any role in the packing generation. In other words, the force factor ρ_F influences the magnitude of forces and moments, but not the magnitude of displacement and rotation angle, which are assigned *a priori*, therefore ρ_F does not affect the simulation results.

5.2.5 The stability check

If the current particle does not make any overlaps, its stability with respect to already placed contacting particles and the domain floor is checked.

The current particle is classified as stable if i) its kernel is placed on the floor or ii) it has a supporting contacting particle and experiences positive and negative moments and forces in both horizontal directions. Moments and forces on the current particle are calculated according to Section 5.2.3 by considering the already placed contacting particles. Note that such forces and moments are only used to check the stability and do not produce any movement of particles. In addition, their magnitude is not important, only their sign and orientation matter, therefore also in the stability check the specific value of the force factor ρ_F does not play any role. A contacting particle is considered supporting if it provides a resultant force on the current particle with a vertical component oriented upward.

Note that the proposed stability check does not exactly satisfy the condition of mechanical equilibrium against the gravity force (for example, there is no check if the weight of the particle can be really sustained by the contacting particles), it represents a simplified geometrical constraint. Although generally, but not strictly always, such a geometrical constraint ensures that a particle cannot move or roll downward, the gravitational stability is a stronger condition than the implemented one. However, although not rigorous, eventually the adopted geometrical constraint prevents a particle from being completely isolated (i.e., suspended in the space without any contact), which is one of the main improvements introduced by the algorithm. Note that this stability constraint is slightly stronger than the one implemented by Nolan and Kavanagh [36]. In principle, provided that the stability constraint could be satisfied, the more restrictive the stability check, the closer the packing. In addition, in our algorithm each placed particle in the packing is stable, unlike in the Nolan and Kavanagh algorithm where the packing was considered stable if more than 95% of its particles were stable [36]. This improvement is crucial in some applications where the contact among the particles is important, such as in fuel cell simulation for the identification of percolation thresholds [59,60].

If after the stability check the particle is found to be unstable, it is dropped downward of a small distance equal to the contact allowance used for defining the contact region.

5.2.6 Getting the outputs

Once the structure generation has been completed, the packing occupies more than the initial domain volume. The particles which are completely outside from the domain are removed, so that the final packing consists of an assembly of particles within the predefined domain. For each particle in the domain the center coordinates, the orientation, the type and size are known. The packing properties are then determined in a central portion of the packing, far from both the domain floor and the top in order to avoid wall effects.

The coordination number of each particle is calculated by using the same procedure described to check the overlaps and the contacts during the packing generation (see Section 5.2.2). All the neighboring particles are considered at this stage. Then, the mean coordination numbers for each phase and for the whole packing (Z) can be easily calculated as the algebraic average of the coordination numbers of the relative particles.

The nematic order parameter is calculated as described in Section 5.2.1 in order to check if the final packing is disordered or if particles show a preferential orientation and long–range ordering as a result of the rearrangement process. The alignment matrix in Eq. (5.2) can be calculated by considering all the particles, irrespective of their type, as well as considering only the particles belonging to individual phases, providing in this way the nematic order parameter of the individual phases.

The porosity ϕ is estimated by using a Monte Carlo method: a sufficient number of test points are randomly selected in the central portion of the packing. The porosity is then equal to the ratio between the number of test points not belonging to a particle and the total number of test points. The packing density is the complement to 1 of the porosity.

For non–analytical shapes, component spheres are used to check if a test point is within a particle: it is sufficient that the test point belongs to at least a component sphere. It is clear that the particle volume must be entirely filled with component spheres, even in overlapping configuration, in order to avoid fictitious empty regions within the particle. Hence, two different filling methods can be used: one during the packing generation, usually with a smaller number of component spheres in overlap–free configuration, and another one to estimate the packing density, consisting in even a larger number of component spheres in overlapping configuration. On the other hand, for analytical shapes the check can be performed by using the analytical particle equation (see Appendix 5.B).

5.3 Results and discussion

5.3.1 Exploring the algorithm

In this Section the effects of the main internal parameters of the algorithm (such as the number of iterations before reposition and the number of repositions before reallocation) and of the constraints (i.e., the stability check) are assessed.

Random packings of monodisperse rigid cylinders with diameter to height ratio equal to 1 were simulated. Rigid means that the kernel scale factor approached 1, with a contact allowance of 1.5% as a maximum. The starting porosity used was 0.1, which was found to be small enough to allow, at the end of the rearrangement, the filling of the whole domain volume. A cubic domain volume with a side equal to about 16 times the particle diameter was used, encompassing approximately 5000 particles. The cylinders were represented by 3 layers of 7 component spheres each with a radius $r_k = R/3$. Each layer was composed of a central sphere and adjacent component spheres in the same plane, forming a hexagon. The middle layer was rotated of 30° with respect to the cylinder axis (see Figure 5.5a). A similar approach is later used to represent ellipsoids (see Figure 5.5b).

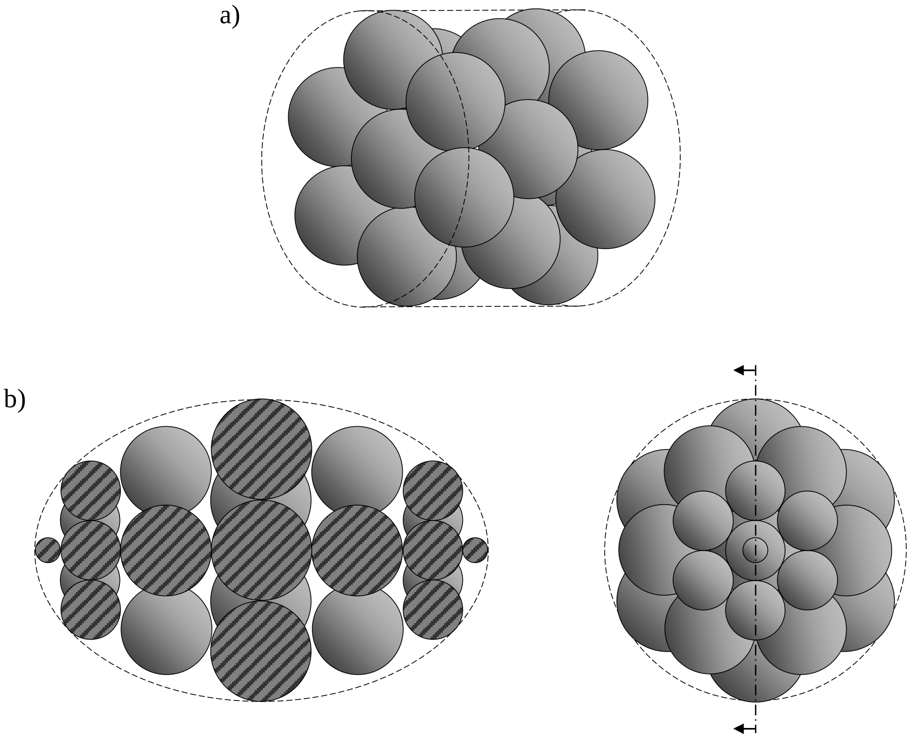

Figure 5.5 – Representation of a) a cylinder (diameter to height ratio equal to 1) and b) a prolate ellipsoid (aspect ratio equal to 1.5) by means of a layer of 7 component spheres each arranged in hexagon configuration.

5.3.1.1 The effect of the stability check

The effect of the constraint given by the stability check was assessed by simulating packings of 5000 rigid cylinders, with a diameter to height ratio of 1, with and without using the stability check in the algorithm. The internal parameters were chosen in order to get the closest packing the algorithm could produce. When the stability check was not used, a particle was considered stable if it did not experience any overlaps. This situation is the analogous of the CR methods in which the stability check is not applied [38,57], though in our method the reposition and reallocation procedures substitute for the particle–to–container shrinking.

When the stability check was used, the final packing density was 0.693 while the mean coordination number was 5.43. On the other hand, removing the stability check, the resulting packing density was 0.664 and the mean coordination number 4.71. The decrease in both packing density and mean coordination number means that the resulting packing was looser than that obtained when the constraint on stability was taken into account. Thus, in our modified algorithm the stability check, apart from ensuring that all the particles (and hence the packing) are stable and contacting each other, is also a necessary constraint to be applied to get random close packings, therefore it will be used in the reminder of this study. However, some limitations introduced by the stability constraint will be presented and discussed in Section 5.3.3. It is noteworthy that in both cases the nematic order parameter of the final configurations was smaller than 0.025 in absolute value, revealing that the packings were disordered.

5.3.1.2 The effect of the internal parameters

The main internal parameters which affect the final packing properties are the maximum number of internal cycles before reposition (N_{int}^{max}) and the maximum number of repositions before reallocation (N_{rep}^{max}). Reasonably, these numbers should be large enough to minimize spurious reallocations, while not unreasonably increasing the computational time.

Figure 5.6 shows the effect of the maximum number of internal cycles and the maximum number of repositions before reallocation on the packing porosity.

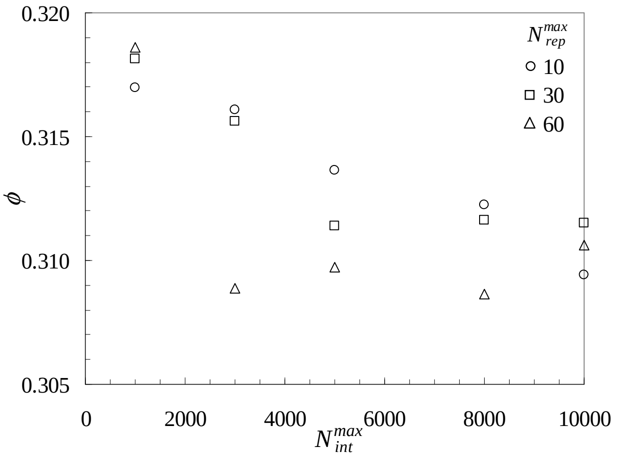

Figure 5.6 – Porosity of a packing of 5000 cylinders, with diameter to height ratio equal to 1, as a function of the maximum number of internal cycles for different maximum numbers of repositions before reallocation.

Although the randomness of the generation did not produce smooth results, Figure 5.6 shows that given N_{rep}^{max}, as N_{int}^{max} increased, the packing porosity decreased. It is noteworthy that the curves seem to approach asymptotic limits for large N_{int}^{max}, indicating that after an optimal number of internal cycles there is no significant improvement in the packing properties, that is, the number of internal cycles allowed are enough to find a stable position. Similarly, an increase in N_{rep}^{max} led to a decrease in the porosity. The percentage of particles reallocated decreased from 2.26 to 0.52 and 0.24% for, respectively, N_{rep}^{max} equal to 10, 30 and 60. Thus, increasing N_{int}^{max} and N_{rep}^{max} leads to closer packings until asymptotic limits are reached. It is important to note that the nematic order parameter was smaller than 0.05 in absolute value in all the conditions, attesting the randomness of the particle distribution.

Another adjustable internal parameter is the contact volume allowance defined in Section 5.2.2: it should be small enough to precisely define the desired overlap (which should be zero in the case of rigid particles), but large enough to allow the numerical detection of contacting particles. By decreasing it from 1.5% to 1.0% and 0.5%, the packing density decreased from 0.693 to 0.689 and 0.687, respectively. The computational time, however, increased by approximately a factor 2 and 6 as the degree of overlap decreased, as a consequence of the larger N_{int}^{max} and N_{rep}^{max} required by the decrease in the magnitude of movement, which is proportional to the contact allowance as described in Section 5.2.4. Therefore, a contact allowance of 1.5% was used in this work as a compromise between computational time and accuracy of the desired amount of overlap.

Other internal parameters, such as the initial porosity, as well as the relaxation of some constraints, such as a looser stability check or removing the fixed rotation and displacement, affect the final packing properties. In particular, looser packings can be obtained by increasing the initial porosity and ρ_F without assigning fixed displacements and rotations. Even though random loose packings can be generated by the algorithm, they are outside of the scope of this study.

5.3.2 Methods of filling a shape

In a sphere–assembly model, the approximation of the particle shape using component spheres is crucial to obtain good results. Each component sphere represents a portion of the particle volume, thus the whole particle volume should be filled with component spheres to the largest degree possible. This results in a large number of small component spheres with the drawback of high computational costs. A compromise should be reached: the number and arrangement of component spheres within the particle shape should be chosen large enough to ensure a good resolution but small enough to reduce the computational cost. Hence, the optimization of the particle representation is a demanding task.

Component spheres can be positioned either allowing for overlaps or not within the particle shape and their size distribution can vary. Significantly overlapping configurations should be avoided during the packing generation, although they could provide a larger particle coverage. The reason is that forces and moments generated by the overlapping regions are applied twice, and this is not physical and may distort the particle movement. Thus, overlap–free configurations should be preferred during the packing generation. However, as already stated in Section 5.2.6, after that the packing has been generated, the particle representation can be switched to an overlapping configuration in order to correctly estimate the packing properties.

The filling method used in this study for both cylinders and ellipsoids has already been presented in Figure 5.5. While ellipsoids are characterized by a round and smooth external surface, which can be well represented by the filling method adopted, cylinders present very sharp edges at the their bases, which cannot be exactly approximated with component spheres even when increasing their number or varying their size (Figure 5.7). This approximation may affect the resulting packing properties, in particular the packing density, which is calculated by the Monte Carlo method described in Section 5.2.6 by considering the analytical particle equation rather than its representation through component spheres. In such a case, it is reasonable that particles overlap more than what desired, therefore increasing the packing density.

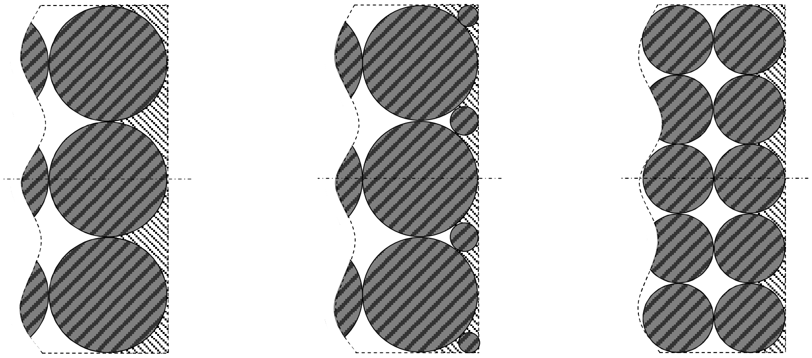

Figure 5.7 – Filling a cylinder with component spheres leaves regions close to the bases which are not accurately represented: even if smaller spheres are introduced (in the middle) or the number of component spheres is increased (on the right), these regions (highlighted in light grey) are reduced but not completely filled.

The effect of the approximation is evaluated by using the Monte Carlo method in order to determine the fraction of volume shared by more particles, calculated as the number of test points belonging to two or more kernels over the number of test points belonging to the solid phase. The calculation was performed for a packing of 5000 cylinders, with diameter to height ratio equal to 1, and a packing of about 2500 rigid prolate ellipsoids, with a aspect ratio equal to 1.5. In both cases, the particles were nominally rigid, although a contact allowance of 1.5% was used to define a contact (see Section 5.3.1.2).

In the case of ellipsoids, only 1.6% of total particles volume was found to be shared by two or more ellipsoids: considering that the contact tolerance was specified as 1.5%, the particle representation used is adequate to avoid significant undetected overlaps. On the other hand, in the case of cylinders, 3.5% of total particle volume was shared by more than one particle, which is significantly higher than the assigned allowance. This difference is attributed to the rough approximation of the sharp edges, which may be somewhat improved by increasing the number of component spheres, even though the exact shape cannot be perfectly captured. Indeed, even when adopting improved component sphere configurations, as those illustrated in Figure 5.7, the fraction of particle overlap decreased to 2.7% as a minimum, while the computational cost increased by even an order of magnitude.

In conclusion, while ellipsoids and, in general, smooth particles are well represented by component spheres, cylinders and particles with sharp edges cannot be well approximated. More importantly, in the latter case the resulting degree of overlap (i.e., the resulting kernel scale factor) may be different than desired. As an additional consequence, fully rigid sharp particles cannot be directly simulated. Note that the problem of the accurate representation of particle shape is also shared by the digitizing method [32] while undesired penetration of particles can affect even methods in which the analytical shape of the particle is employed [31]. However, this is not a significant limitation for our method: the effective kernel factor can always be calculated on the generated packing and compared with the desired one, while results for rigid particles can be extrapolated as shown in Section 5.3.4.1.

5.3.3 Comparison with other algorithms

In order to check the consistency of the algorithm, packings of nominally rigid spheres, ellipsoids and cylinders are compared with simulation results obtained by other authors as a function of, respectively, the composition for binary mixtures of spheres and the aspect ratio α in monodisperse packings of ellipsoids and cylinders. In each case, the internal parameters were chosen in order to get the closest packing. For spherical particles the algorithm was run in a simplified version: particle rotation, associated to the resultant moment in Eq. (5.4), was ignored and, instead of applying the stability condition described in Section 5.2.5, each sphere was considered stable if it was in contact with the floor or supported by three other placed contacting spheres [61]. Note that, since the analysis focuses on random close packings, friction was ignored in all the simulations in this study as well as in those performed by other authors and used for comparison.

Figure 5.8 shows the packing porosity of about 1000 rigid spheres in binary mixtures with a size ratio of 2 as a function of the volume fraction of smaller particles ψ_s. Our results (circles) are compared with experimental data [62] (triangles) and computational results (squares) provided by the drop–and–roll algorithm [57]. Even though the porosity of simulated packings produced by our algorithm does not match experimental values, the proposed algorithm provided closer packings than the drop–and–roll method. In addition, the coordination number of smaller particles calculated in the simulated packings with our algorithm (bullets) was in good agreement with percolation theory estimates [63] (solid line). These results suggest that our modified CR algorithm provides random close packings affected by a certain degree of angular separation [15] due to the preferential direction created by the combination of the stability constraint (see Section 5.2.5) and the procedure of selecting the lowest particle at each iteration (see Section 5.2.1). In other words, the packings produced by the algorithm are slightly looser along the vertical direction if compared with the horizontal ones. On the other hand, bridging of particles, which contributes to decrease the packing density and, mainly, the coordination number [15], is excluded since particles are placed one by one.

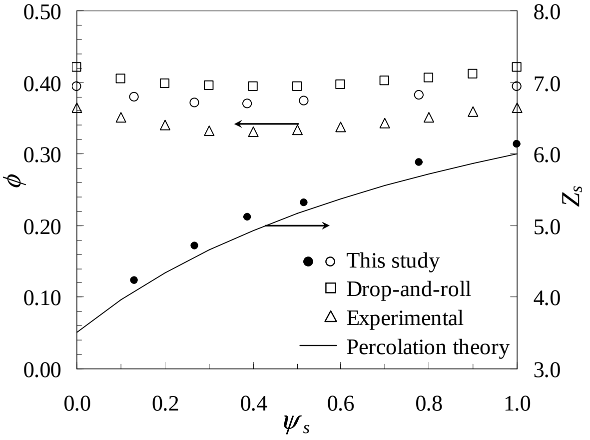

Figure 5.8 – Packing porosity and mean coordination number of smaller particles in a binary mixture of hard spheres with size ratio 2. Regarding packing porosity, results obtained in this study are represented with circles, while results from drop–and–roll algorithm [57] and experimental data [62] are represented with squares and triangles, respectively. The mean coordination number of smaller particles calculated in this study is represented with bullets and compared with percolation theory estimates [63] in solid line.

Figure 5.9 shows the packing density of about 2500 rigid prolate ellipsoids as a function of the aspect ratio α, defined as the ratio between the larger and the smaller semiaxis. Our results (circles) are compared with Donev et al. [25] results (squares), who used a molecular dynamics algorithm to get maximally jammed packings. The dependence of the packing density as a function of the aspect ratio is similar in both the series of results: the packing density increases reaching a maximum at an aspect ratio of 1.5, after which it decreases almost linearly. However, for each aspect ratio, the packing density obtained by Donev et al. was higher than ours, which is in agreement with the results obtained with spheres, where our algorithm provided looser packings than those experimentally observed. This is reasonable because the molecular dynamics algorithm proposed by Donev et al. was developed to obtain jammed packings while our algorithm implements a weaker stability constraint (see Section 5.2.5). In a jammed packing, each particle as well as any subset of particles are trapped by their neighbors so that they cannot be moved [41]. On the other hand, in our algorithm, even if a particle is marked as stable, it may be free to move upward, therefore generally it is not jammed. Since the jamming constraint is more strict than the simplified geometrical stability constraint described in Section 5.2.5, it is reasonable that Donev et al. obtained closer packings.

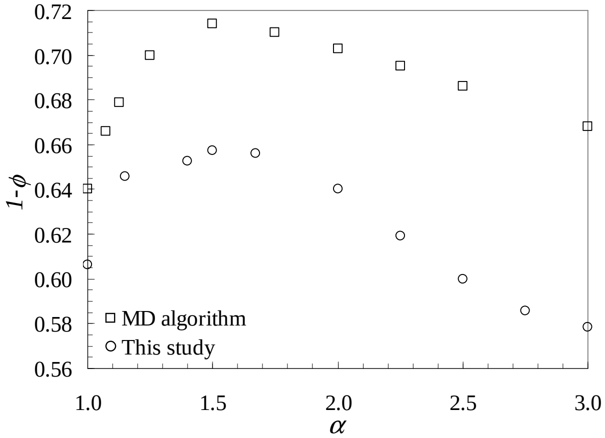

Figure 5.9 – Packing density of rigid prolate ellipsoids as a function of the aspect ratio as obtained by our modified CR algorithm (circles) and by MD algorithm (squares) developed by Donev et al. [25].

In Figure 5.10, the packing density of about 5000 rigid cylinders as a function of the aspect ratio is compared with the results obtained by Zhao et al. [38], who used a sphere–assembly CR algorithm to simulate 200 particles without stability check and using a particle–to–container shrinking procedure. The aspect ratio α is here defined as height to diameter ratio. Our simulated results (circles) are in good agreement with Zhao et al. results (squares): the relative error is smaller than 1.5%. It is important to note that the packing density calculated in our study is for nominally rigid cylinders, which were found to be affected by the 3.5% of overlap in Section 5.3.2. Zhao et al. [38] used the sphere–assembly method, hence their results could also be affected by a certain degree of overlap which was not declared in their study. Therefore, the present results are not corrected to account for the degree of overlap.

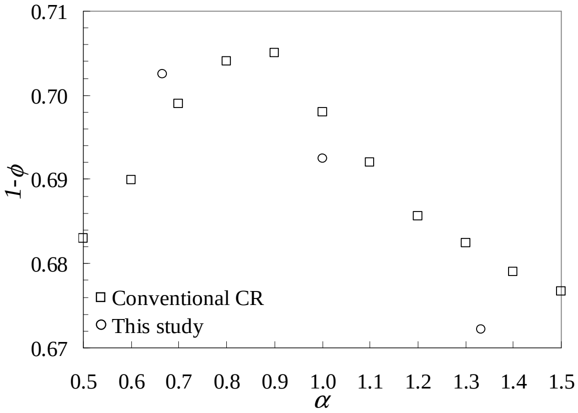

Figure 5.10 – Packing density of rigid cylinders as a function of the aspect ratio as obtained by our modified CR algorithm (circles) and by the conventional CR algorithm (squares) developed by Zhao et al. [38].

In conclusion, our modified CR algorithm provides consistent results with other algorithms, although jammed packings of spheres and ellipsoids cannot be obtained. This is due to the sequential selection of the lowest particle at each iteration and by the imposed stability condition, which produce a preferential direction during the packing generation along which the packing is slightly looser.

5.3.4 Overview on the applicability of the algorithm

In the previous Sections, we considered packings of monosized rigid particles, but the main advantages of our modified sphere–assembly CR method consist in accommodating soft (i.e., not rigid) particles, polydisperse phases, mixtures of particles and agglomerates. These features make the algorithm very attractive for engineering applications: the simulated microstructures can be easily implemented in CFD or similar tools for evaluating packing effective properties [50]. In the following Sections some examples will be given as an overview of the capabilities of the algorithm, without the purpose of being exhaustive: studies on specific particle shapes and conditions will be subject of future investigations.

5.3.4.1 Overlapped particles

As described in Section 5.2.2, the kernel scaling factor κ_f represents the portion of the volume of the kernel of the particle which cannot be overlapped by other particles in the final configuration. A kernel factor of 1 is used to get rigid particles, otherwise as the kernel factor decreases, the particles experience larger overlaps and behave as if they were softer. It is expected that small kernel factors will lead to closer packings.

In Figure 5.11, the effects of the kernel scale factor κ_f on porosity ϕ and mean coordination number Z are shown in packings of prolate ellipsoids with aspect ratio of 1.15 (Figure 5.11a) and of cylinders with aspect ratio of 1 (Figure 5.11b). Each packing encompassed about 2000 particles for prolate ellipsoids and 4500 particles for cylinders. The predicted kernel factors were corrected with the Monte Carlo method in order to account for both the effects of the filling method and of the contact allowance as discussed in Section 5.3.2, therefore the effective kernel scale factors are used in the plot.

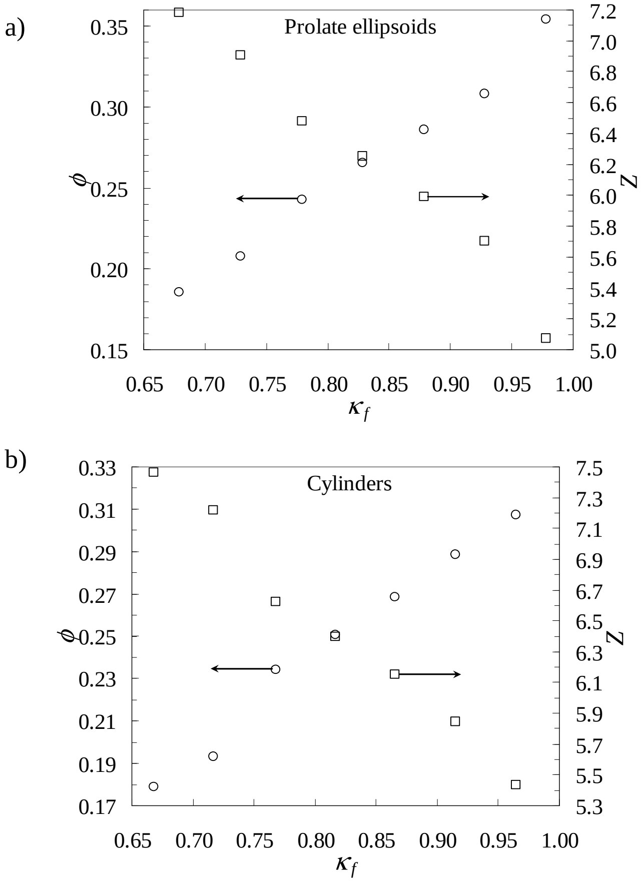

Figure 5.11 – Effect of the kernel scale factor on packing porosity and mean coordination number in a packing of a) prolate ellipsoids (aspect ratio equal to 1.15) and b) cylinders (aspect ratio equal to 1).

In both the figures, as the kernel factor κ_f decreased, the porosity ϕ decreased and the mean coordination number Z increased. This means that decreasing the kernel factor leads to closer packings, as expected. Portions of the packings of cylinders are represented in Figure 5.12. Figure 5.12a shows the case of nominally rigid particles (kernel factor approaching 1, equal to 0.965) while Figure 5.12b is representative of a kernel factor of 0.668: in the latter case, particles are packed in a closer configuration than in the former.

Note that the one–to–one correspondance between porosity and kernel scale factor reported in Figure 5.11 can be applied to find an empirical correlation between kernel scale factor, particle shape, material properties and sintering conditions by comparing simulation results with measurements of porosity in sintered packings. The assessment of quantitative criteria to set *a priori* the value of the kernel scale factor in specific situations was not analyzed because out of the scope of this study.

These results are also useful to assess the effect of representing cylinders with component spheres, which was discussed in Section 5.3.2. The porosity of a packing of effectively rigid cylinders, corresponding to kernel scale factor equal to 1, can be extrapolated from Figure 5.11b assuming linearity to be conservative (in reality, the dependence of porosity on the kernel factor appears to be parabolic with downwards concavity). The porosity of a packing of rigid cylinders would approach a value of 0.327, which means a packing density of 0.673. Therefore, the packing density of 0.693, which was used in the previous sections and, in particular, in Section 5.3.3 as representative of rigid cylinders, is about 3% higher than the extrapolated value, which is a reasonable error for many engineering applications and the algorithm is reasonably fast due to the small number of component spheres.

Hence, the kernel scale factor is a parameter which can be varied in the algorithm in order to obtain packings of overlapped particles. In this way, sintering effects can be simulated, which are important in several engineering applications such as powder metallurgy and sintering of ceramics and cermets [48,64–66].

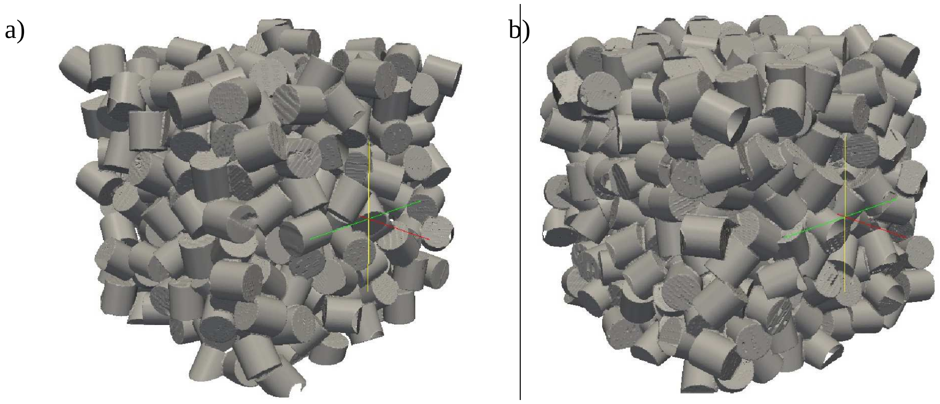

Figure 5.12 – Portion of the packings of cylinders (aspect ratio equal to 1) at different kernel factors: a) kernel factor = 0.965 (440 particles) and b) kernel factor = 0.668 (603 particles).

5.3.4.2 Combination of particles

The algorithm can accommodate particles of different shapes and sizes. As an example, binary mixtures of about 1000 rigid prolate ellipsoids with the same aspect ratio, equal to 1.15, and size ratio equal to 2 were generated at different compositions.

In Figure 5.13 the porosity of the mixture as a function of the volume fraction of smaller particles ψ_s is shown. The porosity decreased reaching a minimum for a composition between 0.4 and 0.5, similar to what is observed experimentally and numerically in the case of packings of spheres (see Figure 5.8), because smaller particles fill the voids left by bigger particles. A precise minimum could not be numerically determined since the standard deviation of the results, created by the randomness of the packing generation, was of the same order of magnitude of the gap between the porosities corresponding to a volume fraction of smaller particles of 0.4 and 0.5. Figure 5.14 shows the representation of a portion of the packing for a volume fraction of smaller particles equal to 0.6.

The algorithm can be applied to more than two phases of different shapes, making it amenable for use in many diverse applications, especially in modeling granular and composite materials where mixtures of particles are common.

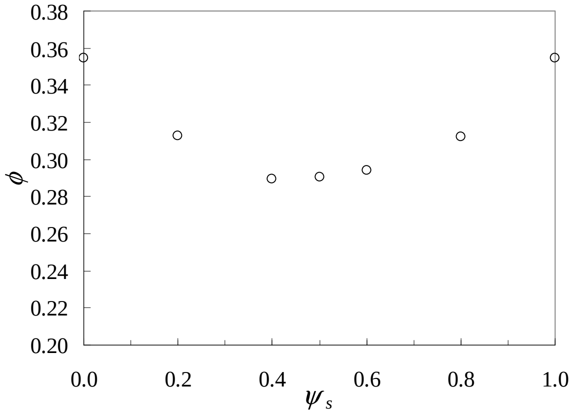

Figure 5.13 – Porosity as a function of the volume fraction of smaller particles in a binary mixture of prolate ellipsoids with same aspect ratio, equal to 1.15, and size ratio equal to 2.

5.3.4.3 Simulations for fuel cell applications

Fuel cells, especially polymer electrolyte [46] and solid oxide [47–49] fuel cells, offer a research field to explore all the capabilities supported by the proposed algorithm. As an example, a polymer electrolyte fuel cell electrode is simulated in this Section.

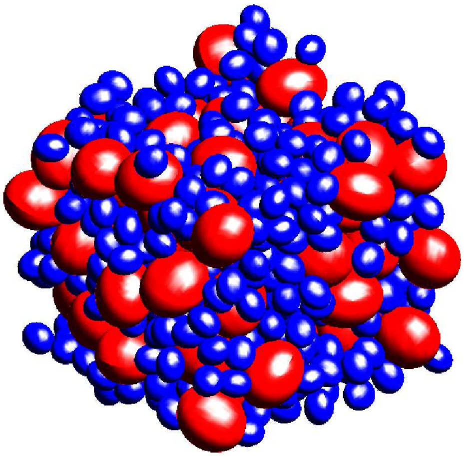

Figure 5.14 – Representation of a mixture of rigid prolate ellipsoids with aspect ratio 1.15 and size ratio 2. The solid volume fraction of smaller particles is 0.6.

A porous polymer electrolyte fuel cell electrode is made of a catalyst layer, composed by sintered agglomerates of catalyst particles, and a porous transport layer, typically made of carbon fibers [67]. Therefore the electrode can be schematically represented as a bi–layer structure: a random packing of sintered agglomerates of spherical particles (i.e., the catalyst layer) plus a loose random packing of long cylinders.

Figure 5.15 shows an example of microstructure generated with our algorithm: the lower layer is composed by about 600 monosized agglomerates of spheres while the upper layer consists of about 1500 monosized randomly packed long cylinders (aspect ratio equal to 5). The bi–layer structure was built first by generating the layer of agglomerates and then by adding the packing of cylinders. Note that in the whole structures there are not isolated particles, that is, each particle makes at least 2 contacts.

A single simulation is not enough to confirm that the algorithm be able to quantitatively reproduce all the microstructural characteristics of fuel cell electrodes, however Figure 5.15 suggests that the proposed method has the capability to accommodate these needs. The use of the algorithm to specific fuel cell applications will be subject of future investigations.

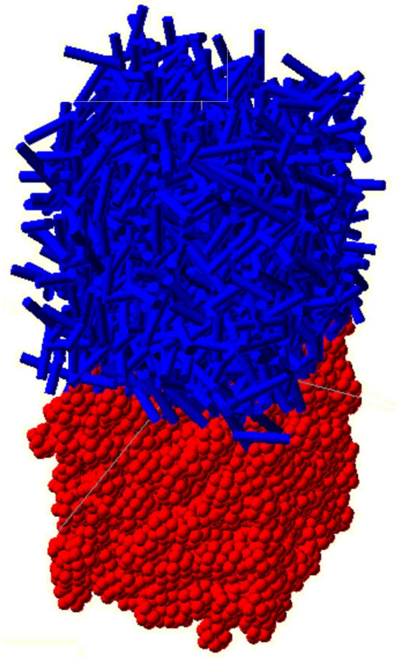

Figure 5.15 – Representation of a polymer electrolyte fuel cell electrode, consisting of a layer of agglomerates of spheres (the catalyst layer) and a layer of long cylindrical particles (the porous transport layer), simulated with the proposed packing algorithm. The picture looks similar to the schematic representation of a polymer electrolyte fuel cell electrode reported in [67].

5.4 Conclusions

A modified collective rearrangement algorithm for simulating random packings of nonspherical particles, represented as an assembly of component spheres, was presented and discussed in this study.

Unlike previous CR methods, a stability constraint was introduced while the particle–to–container shrinking procedure was removed. In this way, during the packing generation the rearrangement process concerned only the neighborhood of the particle taken in consideration. More importantly, this ensured that in the final packing all the particles were stable and contacting each other, overcoming one of the limits of conventional CR algorithms. This makes this method attractive for engineering applications because many effective properties of practical interest, such as conduction properties, strictly depend on the nature of contacts among the particles.

A study regarding the internal parameters of the algorithm showed that packings ranging from random loose to random close can be obtained. In particular, simulation results showed that the stability constraint is necessary in this algorithm to obtain closer packings.

The packing density of random packings of rigid cylinders and prolate ellipsoids as a function of the aspect ratio was calculated and compared with results obtained by other packing algorithms. The good agreement pointed out in the comparison suggests that our algorithm provides results consistent with other consolidated packing algorithms, although the implemented geometric stability constraint cannot produce jammed configurations as showed for packings of spheres and ellipsoids.

The algorithm was generalized to be used in several engineering applications. By using a kernel scale factor, non–rigid particles can be simulated, leading to packings where the particles experience overlaps of the desired degree, enabling the simulation of structural changes due to sintering or melting. Simulations with cylinders and ellipsoids showed that as the kernel factor decreased (i.e., the particles become softer), the packing became closer as highlighted by the increase in both the packing density and the mean coordination number.

The algorithm enabled the simulation of packings with more polydisperse phases of different particle shapes and sizes, as shown in a simulation of binary mixtures of rigid prolate ellipsoids. In addition, since particles are represented by an assembly of component spheres, packings of agglomerates of spheres or nonspherical and non–analytical particles can in principle be generated.

The applications of the algorithm are wide, in particular for simulating granular, sintered and composite materials for engineering purposes. The generated packing structures can be used in CFD computations to determine effective properties such as the thermal conductivity and the gas phase permeability of composite polydisperse nonspherical particles and aggregates.

Simulations showed that the resolution of the shape, that is, the representation of the particle with component spheres, is crucial to get reliable and consistent results. This feature is shared by all the methods which adapt a sphere–assembly or a digital approach. Future work will be dedicated to the optimization of the particle representation and to the evaluation of effective properties in random packings of nonspherical particles, especially for specific fuel cell applications.

Nomenclature

Glossary

$\underline{c}_i$	coordinates of the *i*–th particle center of mass
$\underline{c}_k^{(i)}$	center of the *k*–th component sphere on the *i*–th particle in the global frame

$\underline{\tilde{c}}_k^{(i)}$	center of the *k*–th component sphere on the *i*–th particle in the local frame
$\underline{d}_i$	displacement of the *i*–th particle due to the force $\underline{F}_i$
$\underline{F}_{h^{(i)},k^{(j)}}$	force created by the *k*–th component sphere of the *j*–th particle on the *h*–th component sphere of the *i*–th particle
$\underline{F}_i$	resultant force on the *i*–th particle
i	particle index (*i*–th particle), usually considered as the current particle
$\underline{\underline{I}}$	identity matrix
j	particle index (*j*–th particle)
J_i	scalar moment of inertia of the *i*–th particle
$k^{(i)}$	*k*–th component sphere of the *i*–th particle
$\underline{\hat{M}}_i$	axis of rotation of the *i*–th particle due to the moment $\underline{M}_i$
$\underline{M}_{h^{(i)},k^{(j)}}$	moment created by the *k*–th component sphere of the *j*–th particle on the *h*–th component sphere of the *i*–th particle
$\underline{M}_i$	resultant moment on the *i*–th particle
$n_c^{(i)}$	number of component spheres representing the *i*–th particle
N_{int}^{max}	maximum number of internal cycles before reposition
$N_o^{(i)}$	number of particles overlapping the *i*–th particle
N_{part}	total number of particles
N_{rep}^{max}	maximum number repositions before reallocation
$\underline{\underline{Q}}$	alignment matrix
$r_k^{(i)}$	radius of the *k*–th component sphere of the *i*–th particle
$\underline{\underline{R}}$	rotation matrix
$V_{h^{(i)},k^{(j)}}$	shared volume between the *k*–th component sphere of the *j*–th particle and the *h*–th component sphere of the *i*–th particle
V_i	volume of the *i*–th particle
$\underline{\hat{x}}_i$	vector used to define the orientation of the *i*–th particle (local *x*–axis)
$\underline{\hat{y}}_i$	vector used to define the orientation of the *i*–th particle (local *y*–axis)
$\underline{\hat{z}}_i$	vector used to define the orientation of the *i*–th particle (local *z*–axis)
Z	coordination number
α	aspect ratio
θ_i	rotation angle applied to the *i*–th particle
κ_f	kernel scale factor
ρ_F	force factor

ϕ	porosity
ψ_s	solid volume fraction of smaller particle

Mathematical notation

^{T}	transpose
$\otimes$	tensor product
$[\underline{v}]_\times$	cross product matrix of vector $\underline{v}$

Abbreviations

CFD	computational fluid dynamics
CR	collective rearrangement algorithm
DEM	discrete element method
MD	molecular dynamics method

Acknowledgements

This research was supported by the NSERC Solid Oxide Fuel Cell Canada Strategic Research Network from the Natural Science and Engineering Research Council (NSERC) and other sponsors listed at www.sofccanada.com. Special thanks to Sandro Pintus, who helped us in configuring the machines used to run the simulations at the Department of Civil and Industrial Engineering of the University of Pisa. Thanks to Olivier Blake, Fuel Cell Research Centre of Kingston, who assisted us in the production of Figure 5.15.

References

[1] J.D. Bernal, A geometrical approach to the structure of liquids, Nature. 183 (1959) 141–147.

[2] F.H. Stillinger, E.A. DiMarzio, R.L. Kornegay, Systematic approach to explanation of the rigid disk phase transition, J. Chem. Phys. 40 (1964) 1564–1576.

[3] H.A. Makse, J. Kurchan, Testing the thermodynamic approach to granular matter with a numerical model of a decisive experiment., Nature. 415 (2002) 614–617.

[4] P. Costamagna, P. Costa, V. Antonucci, Micro-modelling of solid oxide fuel cell electrodes, Electrochim. Acta. 43 (1998) 375–394.

[5] N. Metropolis, A.W. Rosenbluth, M.N. Rosenbluth, A.H. Teller, E. Teller, Equation of state calculations by fast computing machines, J. Chem. Phys. 21 (1953) 1087–1092.

[6] D. He, N.N. Ekere, L. Cai, Computer simulation of random packing of unequal particles, Phys. Rev. E. 60 (1999) 7098–7104.

[7] J. Sanyal, G.M. Goldin, H. Zhu, R.J. Kee, A particle-based model for predicting the effective conductivities of composite electrodes, J. Power Sources. 195 (2010) 6671–6679.

[8] E.M. Tory, N.A. Cochrane, S.R. Waddel, Anisotropy in simulated random packing of equal spheres, Nature. 220 (1968) 1023–1024.

[9] W.M. Visscher, M. Bolsterli, Random packing of equal and unequal spheres in two and three dimensions, Nature. 239 (1972) 504–507.

[10] E.M. Tory, B.H. Church, M.K. Tam, M. Ratner, Simulated random packing of equal spheres, Can. J. Chem. Eng. 51 (1973) 484–493.

[11] W.S. Jodrey, E.M. Tory, Simulation of random packing of spheres, J. Simul. 32 (1979) 1–12.

[12] M. Suzuki, K. Makino, M. Yamada, K. Iinoya, Study on the coordination number in a system of randomly packed, uniform-sized spherical particles, Int. Chem. Eng. 21 (1981) 482–488.

[13] V. Mourzenko, J.-F. Thovert, O. Vizika, P.M. Adler, Geometrical and transport properties of random packings of polydisperse spheres, Phys. Rev. E. 77 (2008) 066306.

[14] J. Finney, Fine structure in randomly packed, dense clusters of hard spheres, Mater. Sci. Eng. 23 (1976) 199–205.

[15] G.T. Nolan, P.E. Kavanagh, Computer simulation of random packing of hard spheres, Powder Technol. 72 (1992) 149–155.

[16] W.S. Jodrey, E.M. Tory, Computer simulation of close random packing of equal spheres, Phys. Rev. A. 32 (1985) 2347–2351.

[17] P.A. Cundall, O.D.L. Strack, A discrete numerical model for granular assemblies, Géotechnique. 29 (1979) 47–65.

[18] L.F. Liu, Z.P. Zhang, A.B. Yu, Dynamic simulation of the centripetal packing of mono-sized spheres, Phys. A Stat. Mech. Its Appl. 268 (1999) 433–453.

[19] Z.P. Zhang, L.F. Liu, Y.D. Yuan, A.B. Yu, A simulation study of the effects of dynamic variables on the packing of spheres, Powder Technol. 116 (2001) 23–32.

[20] B.D. Lubachevsky, F.H. Stillinger, Geometric properties of random disk packings, J. Stat. Phys. 60 (2000) 561–583.

[21] S. Torquato, T. Truskett, P. Debenedetti, Is random close packing of spheres well defined?, Phys. Rev. Lett. 84 (2000) 2064–2067.

[22] A. Donev, I. Cisse, D. Sachs, E.A. Variano, F.H. Stillinger, R. Connelly, et al., Improving the density of jammed disordered packings using ellipsoids., Science. 303 (2004) 990–993.

[23] A. Donev, S. Torquato, F.H. Stillinger, Neighbor list collision-driven molecular dynamics simulation for nonspherical hard particles. I. Algorithmic details, J. Comput. Phys. 202 (2005) 737–764.

[24] A. Donev, S. Torquato, F.H. Stillinger, Neighbor list collision-driven molecular dynamics simulation for nonspherical hard particles. II. Applications to ellipses and ellipsoids, J. Comput. Phys. 202 (2005) 765–793.

[25] A. Donev, R. Connelly, F.H. Stillinger, S. Torquato, Underconstrained jammed packings of nonspherical hard particles: Ellipses and ellipsoids, Phys. Rev. E. 75 (2007) 051304.

[26] D.W. Rebertus, K.M. Sando, Molecular dynamics simulation of a fluid of hard spherocylinders, J. Chem. Phys. 67 (1977) 2585–2590.

[27] Y. Jiao, F.H. Stillinger, S. Torquato, Optimal packings of superballs, Phys. Rev. E. 79 (2009) 041309.

[28] Y. Jiao, F.H. Stillinger, S. Torquato, Distinctive features arising in maximally random jammed packings of superballs, Phys. Rev. E. 81 (2010) 041304.

[29] G.W. Delaney, P.W. Cleary, The packing properties of superellipsoids, Europhys. Lett. 89 (2010) 34002.

[30] D. Coelho, J.-F. Thovert, P.M. Adler, Geometrical and transport properties of random packings of spheres and aspherical particles, Phys. Rev. E. 55 (1997) 1959–1978.

[31] W.X. Xu, H.S. Chen, Z. Lv, An overlapping detection algorithm for random sequential packing of elliptical particles, Phys. A Stat. Mech. Its Appl. 390 (2011) 2452–2467.

[32] X. Jia, R.A. Williams, A packing algorithm for particles of arbitrary shapes, Powder Technol. 120 (2001) 175–186.

[33] X. Jia, M. Gan, R.A. Williams, D. Rhodes, Validation of a digital packing algorithm in predicting powder packing densities, Powder Technol. 174 (2007) 10–13.

[34] X. Jia, R. Caulkin, R.A. Williams, Z.Y. Zhou, A.B. Yu, The role of geometric constraints in random packing of non-spherical particles, Europhys. Lett. 92 (2010) 68005.

[35] T. Byholm, M. Toivakka, J. Westerholm, Effective packing of 3-dimensional voxel-based arbitrarily shaped particles, Powder Technol. 196 (2009) 139–146.

[36] G.T. Nolan, P.E. Kavanagh, Random packing of nonspherical particles, Powder Technol. 84 (1995) 199–205.

[37] J.F. Favier, M.H. Abbaspour-Fard, M. Kremmer, A.O. Raji, Shape representation of axi-symmetrical, non-spherical particles in discrete element simulation using multi-element model particles, Eng. Comput. 16 (1999) 467–480.

[38] J. Zhao, S. Li, P. Lu, L. Meng, T. Li, H. Zhu, Shape influences on the packing density of frustums, Powder Technol. 214 (2011) 500–505.

[39] H. Kruggel-Emden, S. Rickelt, S. Wirtz, V. Scherer, A study on the validity of the multi-sphere Discrete Element Method, Powder Technol. 188 (2008) 153–165.

[40] D. Höhner, S. Wirtz, H. Kruggel-Emden, V. Scherer, Comparison of the multi-sphere and polyhedral approach to simulate non-spherical particles within the discrete element method: Influence on temporal force evolution for multiple contacts, Powder Technol. 208 (2011) 643–656.

[41] S. Torquato, F.H. Stillinger, Jammed hard-particle packings: From Kepler to Bernal and beyond, Rev. Mod. Phys. 82 (2010) 2633–2672.

[42] S. Raschdorf, M. Kolonko, A comparison of data structures for the simulation of polydisperse particle packings, Int. J. Numer. Methods Eng. 85 (2011) 625–639.

[43] M.J. Powell, Site percolation in random networks, Phys. Rev. B. 21 (1980) 3725–3728.

[44] M. Ahmadzadeh, A.W. Simpson, Critical concentrations for site percolation in the dense-random-packed hard-sphere Bernal model, Phys. Rev. B. 25 (1982) 4633–4638.

[45] D. Bouvard, F.F. Lange, Relation between percolation and particle coordination in binary powder mixtures, Acta Metall. Mater. 39 (1991) 3083–3090.

[46] N.P. Siegel, M.W. Ellis, D.J. Nelson, M.R. von Spakovsky, Single domain PEMFC model based on agglomerate catalyst geometry, J. Power Sources. 115 (2003) 81–89.

[47] A.M. Gokhale, S. Zhang, M. Liu, A stochastic geometry based model for total triple phase boundary length in composite cathodes for solid oxide fuel cells, J. Power Sources. 194 (2009) 303–312.

[48] H.-W. Choi, A. Berson, J.G. Pharoah, S.B. Beale, Effective transport properties of the porous electrodes in solid oxide fuel cells, Proc. Inst. Mech. Eng. Part A J. Power Energy. 225 (2011) 183–197.

[49] H.-W. Choi, D.A.W. Gawel, A. Berson, J.G. Pharoah, K. Karan, Comparison between FIB-SEM experimental 3-D reconstructions of SOFC electrodes and random particle-based numerical models, ECS Trans. 35 (2011) 997–1005.

[50] A. Berson, H.-W. Choi, J.G. Pharoah, Determination of the effective gas diffusivity of a porous composite medium from the three-dimensional reconstruction of its microstructure, Phys. Rev. E. 83 (2011) 026310.

[51] J.H. Yu, G.W. Park, S. Lee, S.K. Woo, Microstructural effects on the electrical and mechanical properties of Ni–YSZ cermet for SOFC anode, J. Power Sources. 163 (2007) 926–932.

[52] K. Chen, L. Zhe, N. Ai, X. Chen, X. Huang, W. Su, Experimental study on effect of compaction pressure on performance of SOFC anodes, J. Power Sources. 180 (2008) 301–308.

[53] A. Bertei, Chapter 3 of this Thesis, 2013.

[54] W. Bangerth, R. Hartmann, G. Kanschat, deal.II - A general purpose object oriented finite element library, ACM Trans. Math. Softw. 33 (2007) 24.

[55] G. Marsaglia, Choosing a point from the surface of a sphere, Ann. Math. Stat. 43 (1972) 645–646.

[56] A. Wouterse, S.R. Williams, A.P. Philipse, Effect of particle shape on the density and microstructure of random packings, J. Phys. Condens. Matter. 19 (2007) 406215.

[57] A. Bezrukov, M. Bargiel, D. Stoyan, Statistical analysis of simulated random packings of spheres, Part. Part. Syst. Charact. 19 (2002) 111–118.

[58] G.W. Delaney, J.E. Hilton, P.W. Cleary, Defining random loose packing for nonspherical grains, Phys. Rev. E. 83 (2011) 051305.

[59] A. Bertei, C. Nicolella, Percolation theory in SOFC composite electrodes: Effects of porosity and particle size distribution on effective properties, J. Power Sources. 196 (2011) 9429–9436.

[60] B. Kenney, M. Valdmanis, C. Baker, J.G. Pharoah, K. Karan, Computation of TPB length, surface area and pore size from numerical reconstruction of composite solid oxide fuel cell electrodes, J. Power Sources. 189 (2009) 1051–1059.

[61] Y. Shi, Y. Zhang, Simulation of random packing of spherical particles with different size distributions, Appl. Phys. A. 92 (2008) 621–626.

[62] A.B. Yu, N. Standish, Porosity calculations of multi-component mixtures of spherical particles, Powder Technol. 52 (1987) 233–241.

[63] A. Bertei, C. Nicolella, A comparative study and an extended theory of percolation for random packings of rigid spheres, Powder Technol. 213 (2011) 100–108.

[64] C.L. Martin, D. Bouvard, Study on the cold compaction of composite powders by the discrete element method, Acta Mater. 51 (2003) 373–386.

[65] C.L. Martin, D. Bouvard, S. Shima, Study of particle rearrangement during powder compaction by the Discrete Element Method, J. Mech. Phys. Solids. 51 (2003) 667–693.

[66] C.L. Martin, L.C.R. Schneider, L. Olmos, D. Bouvard, Discrete element modeling of metallic powder sintering, Scr. Mater. 55 (2006) 425–428.

[67] K. Karan, Assessment of transport-limited catalyst utilization for engineering of ultra-low Pt loading polymer electrolyte fuel cell anode, Electrochem. Commun. 9 (2007) 747–753.

Appendix

5.A Calculus of the scalar moment of inertia

5.A.1 Analytical shapes

For particles which have an analytical expression of the shape (e.g., ellipsoids, cylinders), the calculus of the scalar moment of inertia J_i is made by using the analytical expression. Taken the local particle system of reference, that is, the system of reference $\left(\tilde{x},\tilde{y},\tilde{z}\right)$ oriented along the particle axes $\underline{\hat{x}}_i$, $\underline{\hat{y}}_i$ and $\underline{\hat{z}}_i$ and centered in the particle center of mass, the tensor of inertia $\tilde{\underline{\underline{J}}}_i$ is calculated as:

$$\tilde{\underline{\underline{J}}}_i = \int\int\int_{V_i} \left(\left(\underline{\tilde{r}} \cdot \underline{\tilde{r}} \right) \underline{\underline{I}} - \underline{\tilde{r}} \otimes \underline{\tilde{r}} \right) dV_i \qquad (5.A.1)$$

where $\underline{\tilde{r}} = (\tilde{x}, \tilde{y}, \tilde{z})^T$. In particular, it is convenient to choose a local frame whose axes are the principal axes of inertia for the particle (for example, for ellipsoids the local axes are oriented along the particle semiaxes): in such a case $\underline{\underline{\tilde{J}}}_i$ is a diagonal matrix.

Given the axis of rotation $\underline{\hat{M}}_i$ in the global system of reference, it can be reduced to the local frame by projecting its components on the particle orientation axes similarly to what done in Eq. (5.1), that is, $\underline{\tilde{\hat{M}}}_i = \left(\underline{\hat{M}}_i \cdot \underline{\hat{x}}_i, \underline{\hat{M}}_i \cdot \underline{\hat{y}}_i, \underline{\hat{M}}_i \cdot \underline{\hat{z}}_i\right)^T$. Then, the scalar moment of inertia is calculated as:

$$J_i = \left(\underline{\underline{\tilde{J}}}_i \cdot \underline{\tilde{\hat{M}}}_i\right) \cdot \underline{\tilde{\hat{M}}}_i \qquad (5.A.2)$$

5.A.2 Non–analytical shapes

When the particle shape cannot be represented by an analytical expression, e.g., an agglomerate of spheres, the scalar moment of inertia is calculated by considering the component spheres. The particle moment of inertia J_i is calculated by summing the moments of inertia of its component spheres, calculated with respect to the axis of rotation $\underline{\hat{M}}_i$ using the Huygens–Steiner theorem, as:

$$J_i = \sum_{k=1}^{n_c^{(i)}} \left(\frac{8}{15} \pi r_k^{(i)5} + \frac{4}{3} \pi r_k^{(i)3} b_k^{(i)2} \right) \qquad (5.A.3)$$

where $b_k^{(i)}$ represents the distance of the center of the component sphere $k^{(i)}$ from the axis of rotation, calculated as:

$$b_k^{(i)} = \left| \underline{c}_k^{(i)} - \underline{c}_i - t_k^{(i)} \underline{\hat{M}}_i \right| \quad \text{with} \quad t_k^{(i)} = \frac{\underline{\hat{M}}_i \cdot \left(\underline{c}_k^{(i)} - \underline{c}_i \right)}{\underline{\hat{M}}_i \cdot \underline{\hat{M}}_i} \qquad (5.A.4)$$

It is worth noting that Eq. (5.A.4) provides a good approximation of the particle moment of inertia if the shape is well represented by the component spheres in a non–overlapping configuration, in order to avoid to double count the volume shared by two overlapping component spheres.

5.B Check a point within a particle

5.B.1 Check a point within an ellipsoid

In order to check if a test point $\underline{P}$ is contained within the i–th ellipsoid, centered in $\underline{c}_i$, its coordinates are reported to the particle local system of reference by using Eq.

(5.1), obtaining $\underset{\sim}{\tilde{P}} = \left((\underline{P} - \underline{c}_i) \cdot \underline{\hat{x}}_i, (\underline{P} - \underline{c}_i) \cdot \underline{\hat{y}}_i, (\underline{P} - \underline{c}_i) \cdot \underline{\hat{z}}_i \right)^T$. For convenience, let us call the local coordinates of $\underline{\tilde{P}}$, $\tilde{x}_P$, $\tilde{y}_P$ and $\tilde{z}_P$.

Be $s_x^{(i)}$, $s_y^{(i)}$ and $s_z^{(i)}$ the semiaxes of the ellipsoid, the check of the point $\underline{\tilde{P}}$ consists in:

$$\left(\frac{\tilde{x}_P}{s_x^{(i)}} \right)^2 + \left(\frac{\tilde{y}_P}{s_y^{(i)}} \right)^2 + \left(\frac{\tilde{z}_P}{s_z^{(i)}} \right)^2 \leq 1 \tag{5.B.1}$$

If Eq. (5.B.1) is satisfied, the test point $\underline{P}$ is within the *i*–th ellipsoid, otherwise it is outside.

5.B.2 Check a point within a cylinder

Be $\underline{P}$ the test point to be checked in the *i*–th cylinder, which has a radius $R^{(i)}$ and a height $H^{(i)}$. The axis of the cylinder is oriented along its orientation axis $\underline{\hat{x}}_i$. The test point is within the cylinder if: i) its distance from the cylinder axis is smaller than the cylinder radius and ii) its projection on the cylinder axis is smaller than one half of the cylinder height.

The distance $b_P^{(i)}$ of the test point from the cylinder axis is calculated as in Eq. (5.A.4) by substituting $\underline{\hat{M}}_i$ with $\underline{\hat{x}}_i$ and $\underline{c}_k^{(i)}$ with $\underline{P}$. Thus, the first condition to be satisfied is $b_P^{(i)} \leq R^{(i)}$. The projection of $\underline{P}$ on the cylinder axis is calculated as $(\underline{P} - \underline{c}_i) \cdot \underline{\hat{x}}_i$, hence the second condition is satisfied if the inequality $\left| (\underline{P} - \underline{c}_i) \cdot \underline{\hat{x}}_i \right| \leq H^{(i)}/2$ is verified.

Chapter 6

Microstructural Modeling of Infiltrated Electrodes

This Chapter presents a packing algorithm for the reconstruction of infiltrated electrodes, which are an alternative type of microstructure for intermediate temperature SOFCs. To date, this framework represents one of the first studies of detailed microstructural modeling of infiltrated electrodes.

The model consists in: i) generation of the matrix of micrometer–sized particles, called backbone, through the drop–and–roll algorithm (see Chapter 4), ii) infiltration of nanoparticles onto the surface of backbone particles using a Monte Carlo method. The effective properties required by electrochemical models are evaluated.

The study shows that:

i. percolation thresholds can be predicted as a function of nanoparticle size;

ii. the TPB density in infiltrated electrodes may increase by 2 orders of magnitude if compared with conventional composite electrodes;

iii. percolation properties are highly sensitive to the volume fraction of nanoparticles.

This Chapter was adapted from the paper "Microstructural modeling and effective properties of infiltrated SOFC electrodes" by A. Bertei, J.G. Pharoah, D.A.W. Gawel and C. Nicolella, published in ECS Trans. 57 (2013) 2527–2536.

Abstract

A modeling framework for the microstructural modeling of infiltrated SOFC electrodes is presented. The model numerically reconstructs infiltrated electrodes through a sedimentation algorithm for the backbone generation and a novel Monte Carlo packing algorithm for the random infiltration. Effective properties are evaluated by means of Monte Carlo geometric analysis and finite volume method as a function of the loading and of the particle size of infiltrated particles. Infiltration into ion–conducting and composite backbones is analyzed in this study. Simulations show that the infiltration can lead to an increase in TPB density of about two orders of magnitude if compared with conventional composite electrodes. In addition, infiltration into monocomponent backbones can lead to a TPB density about twice the TPB achievable when infiltrating composite backbones. On the other hand, a critical loading of nanoparticles must be reached in monocomponent backbones while in a composite backbone the infiltration is always beneficial.

6.1 Introduction

One of the main goals for solid oxide fuel cells (SOFCs) consists in the reduction of operating temperature to a range of 500–800°C [1]. In the last decade the use of nano–structured electrodes produced by infiltration/impregnation techniques has been suggested as one of the possible ways [2].

The infiltration technique involves the deposition of nanoparticles into a pre–sintered backbone. Infiltrated electrodes show significant advantages if compared with conventional electrodes: a wide choice of catalyst materials as a result of a lower firing temperature, a good adhesion with the electrolyte, a high catalytic activity coupled with an enhanced electric conductivity [2]. Infiltration of nanoparticles into ion–conducting, mix–conducting and composite backbones have been experimentally studied revealing significant increases in power density [3–5].

The advantages of infiltrated electrodes are strictly related to their microstructural characteristics. So far, the optimization of infiltrated electrode microstructure has been done mainly empirically. Only a couple of studies have attempted to model the microstructural characteristics of infiltrated electrodes [6,7], even if relying on simplified percolation models. However, nowadays more advanced microstructural models, based on packing algorithms or on tomographic reconstruction, are available. So far, such advanced microstructural models have been applied to study mainly conventional electrodes [8,9].

In this study, a microstructural model for the numerical reconstruction of infiltrated electrodes is presented. The model is based on the combination of a conventional packing algorithm for the backbone reconstruction plus a novel Monte

Carlo algorithm to simulate the infiltration of nanoparticles. The study focuses on the evaluation of the effective properties of both ion–conducting and composite backbones infiltrated with electron–conducting nanoparticles as a function of the loading and the size of nanoparticles. Model parameters and working conditions are chosen in order to maximize the three–phase boundary density (TPB), in order to assess the maximum performance achievable by infiltrated electrodes.

6.2 Modeling

The modeling approach consists in three sequential steps: generation of the backbone structure (Section 6.2.1), infiltration of the backbone with nanoparticles (Section 6.2.2), evaluation of the effective properties of the resulting packing (Section 6.2.3).

6.2.1 Backbone generation

The backbone represents the pre–sintered electrode to be infiltrated by nanoparticles. It can be modeled as a random packing of micrometer–sized spherical particles [8].

The backbone generation is performed through a consolidated packing algorithm, the drop–and–roll algorithm [10]. One particle at a time is added into a cubic domain of specified dimensions with periodic boundary conditions in the horizontal directions. Each particle is dropped from a random point at the top of the domain, then it falls and rolls over previously placed particles until a stable position is reached. As the particle comes into rest, its position is fixed and a new particle is dropped. When simulating composite backbones, the desired volume fraction is enforced by assigning a weighted probability to the particle selection. The sintering is simulated by assigning a desired particle–particle contact angle, which eventually defines the backbone porosity.

Eventually the algorithm provides a virtual sample of the pre–sintered electrode used as backbone for the random infiltration.

6.2.2 Random infiltration

The novelty of this study is represented by the algorithm used to infiltrate nanoparticles into the backbone. The random infiltration follows a sequential Monte Carlo algorithm, which places nanoparticles onto the surface of backbone particles. Both the size of nanoparticles and the loading (that is, the volume fraction of nanoparticles) can be set in the algorithm.

The center of a nanoparticle is randomly placed on the surface of a backbone particle (see magnification in Figure 6.1). Then, the overlaps made by the nanoparticle are evaluated with respect to backbone particles and nanoparticles previously placed. A contacting particle is marked as overlapping if the corresponding contact angle exceeds a prescribed value, which is different for backbone and nanoparticles. If the number of overlaps is smaller than three, the nanoparticle is moved over the backbone surface in order to remove the overlaps, then overlaps are checked again. If the number of overlaps is equal or larger than three, the selected position is discarded since a nanoparticle cannot be placed in such a location without violating the contact angle constraints.

The procedure is repeated until the desired loading is reached. The procedure stops if, after a predefined large number of trials, a free position to place a nanoparticle is not found, meaning that the maximum loading has been reached. The maximum loading has to be intended as the loading corresponding to cover the backbone with a monolayer of nanoparticles. The algorithm does not allow the growth of multiple layers of nanoparticles. In fact, a second layer may reduce the TPB length [6], and this phenomenon is out of the scope of this study.

An example of an infiltrated electrode made on the basis of a monocomponent ion–conducting backbone is reported in Figure 6.1.

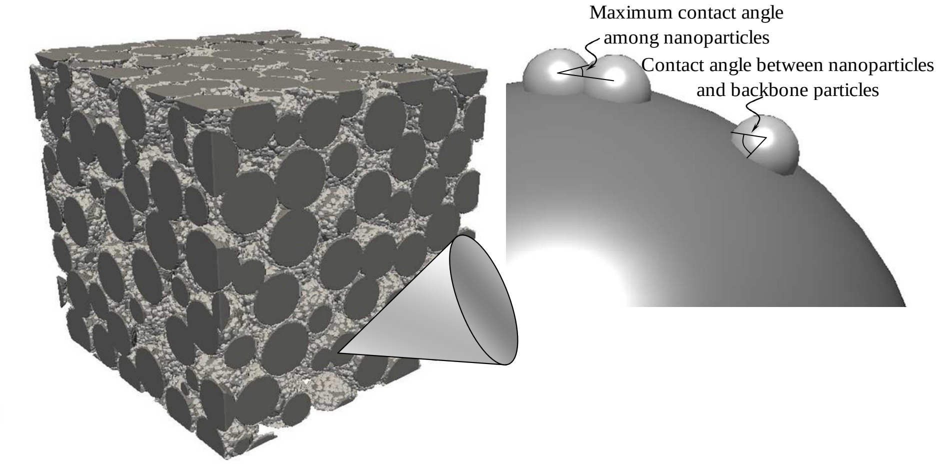

Figure 6.1 – Infiltrated electrode generated by the algorithm using a size ratio equal to 1/10 between nanoparticles and backbone particles. In the magnification, contact angles of a nanoparticle with backbone particles and other nanoparticles are defined.

6.2.3 Effective properties

The effective properties of the resulting packing are evaluated through Monte Carlo geometrical analysis as well as through finite volume simulations.

The percolation properties of backbone particles and nanoparticles are evaluated through the knowledge of the contact information of each particle within the packing. In this way, clusters of particles of the same type connected each other can be identified [11]. A cluster is percolating if it spans from the top to the bottom of the domain. The percolation fraction of a conducting phase is defined as the number fraction of particles belonging to percolating clusters over the total number of particles of such a phase.

The surface area of backbone particles before infiltration is evaluated by randomly generating thousands of test points on the surface of each sphere. The test point is then checked against other backbone particles: if the distance from the center of another sphere is smaller than the sphere radius, the test point is internal to the packing. In the other case, the test point is exposed to the pore space, thus it is accounted for in the calculation of the exposed area. A similar approach is used to evaluate the fraction of backbone surface covered by nanoparticles after the infiltration. The surface coverage fraction is defined as the fraction of backbone surface area covered by nanoparticles.

The packing porosity and the loading are evaluated by randomly generating thousands of test points within the domain. Test points falling within nanoparticles are accounted for the loading while points falling within the pore space are accounted for the porosity calculation.

The mean pore size is evaluated by using the chord length method [12]. According to Zalc et al. [13], the mean pore size is equal to the number–averaged chord length corrected by a factor which takes into account the nature of the redirecting collisions of the diffusion of a tracer in Knudsen regime.

The effective electric conductivity is evaluated with MicroFOAM [14], which uses the finite volume method to solve for the normalized boundary flux within the discretized structure. Choi et al. [14] validated MicroFOAM against a random walk simulation and found good agreement between the solutions when an appropriate discretization procedure was used to mesh the finite volumes.

The TPB length is computed through the knowledge of particle radius and position, following a technique similar to that used for surface area determination. A test point is generated on the perimeter of the plane of intersection connecting two different conducting particles. The test point, which represents a portion of the perimeter, is accounted for the TPB length calculation if it does not belong to a third particle. The procedure is repeated by moving the test point along the perimeter for all the planes of intersection. The procedure does not take into account the pore percolation because the gas phase is entirely connected in the range of porosity investigated in this study [8,13].

6.3 Results and discussion

The methods described in Section 6.2 were used to reconstruct and analyze infiltrated electrodes in the range of conditions reported in Table 6.1.

Two types of backbones were considered in this study: a monocomponent backbone, composed by ion–conducting particles, and a composite backbone, composed by a binary mixture of electron–conducting and ion–conducting particles 50–50% in volume. In both the cases, the backbone porosity was set to 40% and all the particles had the same size.

The infiltration considered electron–conducting nanoparticles with a size equal to 1/10, 1/15 and 1/20 the diameter of backbone particles. The contact angle between nanoparticles and backbone particles was tailored in order to place the center of nanoparticles exactly on the surface of backbone particles (see magnification in Figure 6.1). This constraint corresponds to set the contact angle between nanoparticles and backbone particles to 87.1°, 88.0° and 88.5° for the three nanoparticle sizes considered. The maximum contact angle among nanoparticles was set equal to 30°. These contact angles were chosen because they allowed the maximization of the TPB density.

A cubic domain with a side length equal to 8 times the backbone particle diameter was used. A sensitivity analysis revealed that this domain was big enough to make the results independent of the sample size. Results were averaged on three structures per setting. Dimensional results, such as the mean pore size and the TPB density, are reported in dimensionless form assuming a unitary backbone particle diameter.

Table 6.1 – Microstructural parameters used in the study.

Parameter	*Value*
Backbone porosity	0.40
Volume fraction of ion–conducting phase in the backbone	0.5, 1.0
Diameter ratio between nanoparticles and backbone particles	1/10, 1/15, 1/20
Maximum contact angle among nanoparticles	30°

6.3.1 Surface coverage

The fraction of external surface of backbone particles covered by nanoparticles is the main variable for determining the percolation and effective properties of the electrode.

As shown in Figure 6.2, given the nanoparticle size, as the loading increases, the surface coverage fraction increases. Independently of the size of nanoparticles, the maximum surface coverage fraction is about 0.68. The whole surface of backbone particles cannot be covered because the infiltration is a random process and due to the geometrical constraint given by the maximum allowed contact angle among nanoparticles.

As reported in Figure 6.2, the maximum surface coverage fraction corresponds to the maximum loading, which is larger as the size of nanoparticles increases. It is noteworthy that in reality it would be possible to continue the infiltration beyond the maximum loading, but it would correspond to create multi–layers of nanoparticles, with potential reduction in the TPB length [6].

In the remainder of this study, all the results are reported as a function of the surface coverage fraction. Figure 6.2 can be used to correlate the surface coverage fraction to the corresponding loading of nanoparticles.

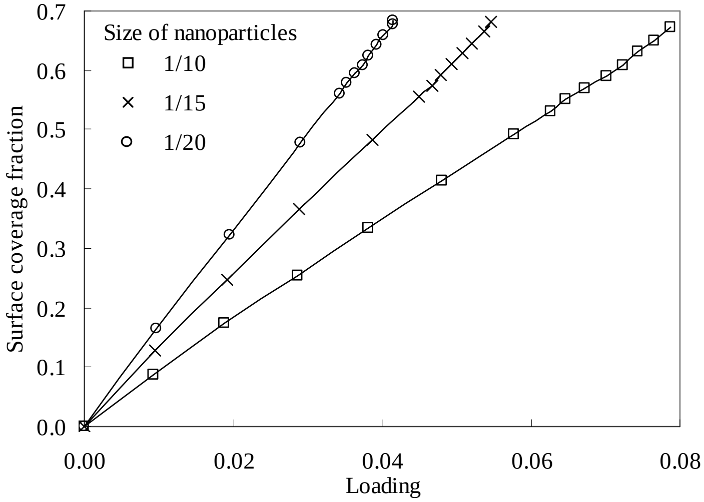

Figure 6.2 – Surface coverage fraction as a function of the loading of nanoparticles.

6.3.2 Percolating properties

Figure 6.3 shows the percolation fraction of infiltrated particles as a function of the surface coverage fraction for three sizes of nanoparticles.

In a monocomponent backbone (solid lines), nanoparticles have to overcome a critical threshold, called percolation threshold, in order to create a percolating path. The percolation threshold lies in the range 0.52–0.57 of surface coverage fraction depending on the size of nanoparticles. Beyond the percolation threshold, the percolation fraction of nanoparticles increases as the surface coverage increases until the maximum loading is reached.

On the other hand, in a composite backbone (dotted lines) the percolation fraction of nanoparticles is always bigger than 0.47, where 0.47 is the product of the solid volume fraction of electron–conducting particles, equal to 0.50, and the percolation fraction of electron–conducting backbone particles before infiltration, equal to 0.94 as resulting from simulations. In fact, nanoparticles are equally distributed on backbone particles, therefore at least the 47% of them are in contact with a percolating electron–conducting backbone particle. As a consequence of the positive percolating effect due to the electron–conducting backbone particles, given the surface coverage fraction, the percolation fraction of nanoparticles is larger in a composite backbone than in a monocomponent backbone (see Figure 6.3).

For both monocomponent and composite backbones, given the surface coverage fraction, the percolation fraction of nanoparticles increases as the size of nanoparticles increases. This phenomenon is due to the fact that bigger nanoparticles tend to percolate better than smaller nanoparticles over the surface of a sphere, as it can be demonstrated by percolation theory considerations [15].

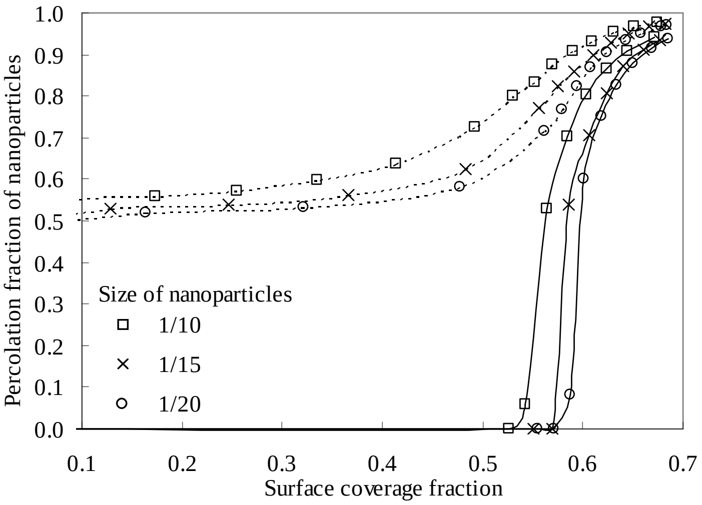

Figure 6.3 – Percolation fraction of nanoparticles as a function of the surface coverage fraction. Solid lines refer to a monocomponent backbone, dotted lines to a composite backbone.

6.3.3 Gas phase properties

Figure 6.4 shows the main geometric properties characterizing the gas phase as a function of the surface coverage fraction. Both the porosity and the mean pore size decrease as the surface coverage fraction and the size of nanoparticles increase. This behavior is reasonable since pores are filled by nanoparticles as the loading increases, which leads to a reduction in porosity and mean pore size.

For the set of conditions investigated in this study, the reduction in porosity does not lead to completely close the pores: the mean pore size is reduced by 14% in the worst case. Such a reduction should not compromise the effective transport properties, in particular the normalized effective diffusivity, which is the ratio between porosity and tortuosity [13]. Assuming that the effective diffusivity in the infiltrated electrode corresponds to the diffusivity of a backbone with equal porosity, using the correlation suggested by Berson et al. [12], the normalized effective diffusivity is 0.17 in the worst case (porosity of 0.32, corresponding to the maximum loading of the biggest nanoparticles considered), while it is 0.26 for the backbone before infiltration. Obviously, increasing the loading beyond the maximum loading would further reduce the porosity, leading to a possible significant reduction in gas phase effective properties.

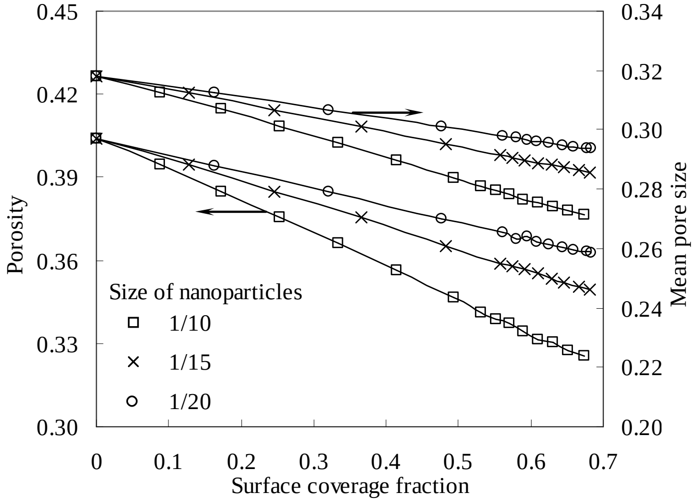

Figure 6.4 – Porosity and mean pore size as a function of the surface coverage fraction.

6.3.4 Effective electric conductivity

It is worth comparing the effective conductivity of electron–conducting nanoparticles with the effective conductivity of ion–conducting particles. In order to make the results comparable and independent of the specific material conductivity, the effective conductivities are normalized with the bulk conductivity of the considered phase.

In a monocomponent backbone, at the maximum loading the ratio between the normalized effective conductivity of nanoparticles and the normalized effective conductivity of the backbone is 0.143, 0.091 and 0.065 for a diameter ratio of 1/10, 1/15 and 1/20, respectively. Therefore, the conduction within the infiltrated phase is about an order of magnitude smaller than in the backbone, which is reasonable because the charges have to flow in surface–like path. As the size of nanoparticles increases, the normalized effective conductivity of the infiltrated phase increases:

this is attributed to the larger cross–section offered by bigger nanoparticles. It is noteworthy that the normalized effective conductivity of the electron–conducting phase for the biggest nanoparticle size considered in this study is comparable with the normalized effective conductivity of electron–conducting particles in a conventional composite electrode [14].

Since the specific conductivity of typical electron–conducting materials used in SOFC electrodes is usually orders of magnitude larger than the specific conductivity of the ion conductor, the electron conduction in infiltrated electrode should not be a limiting factor.

6.3.5 TPB length

Figure 6.5 shows the dimensionless TPB length per unit volume as a function of the surface coverage fraction for three sizes of nanoparticles.

For a composite backbone, when nanoparticles are not infiltrated (i.e., loading equal to 0), the dimensionless TPB density is 0.73: this is the contribution of backbone particles, equal to the TPB density of a conventional composite electrode. Increasing the loading leads to a slow increase in TPB until a surface coverage fraction of about 0.5, over which the TPB density increases more rapidly. On the other hand, in a monocomponent backbone a critical threshold must be overcome in order to develop a connected TPB length. These results are in agreement with the percolating properties shown in Figure 6.3.

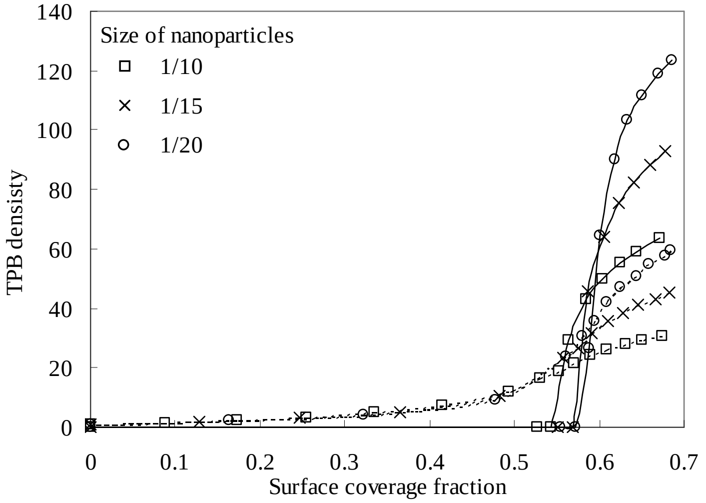

Figure 6.5 – TPB density as a function of the surface coverage fraction. Solid lines refer to a monocomponent backbone, dotted lines to a composite backbone.

Interesting information can be obtained looking at the maximum loading, where the percolation fraction of nanoparticles approaches 1 (see Figure 6.3). Figure 6.5 shows that at the maximum loading the TPB density scales with the inverse of the nanoparticle diameter for both composite and monocomponent backbones. In addition, the TPB density in a monocomponent backbone is more than twice the TPB density of a composite backbone. The factor 2 arises because in a composite backbone the percolating ion–conducting particles are about one half than in a fully ion–conducting backbone.

6.4 Conclusions

A modeling framework for the estimation of effective properties of infiltrated electrodes, based on the numerical reconstruction through packing algorithms, was presented in this study. Infiltration of nanoparticles into monocomponent and composite backbones was analyzed as a function of the loading and size of nanoparticles. Simulation parameters were set in order to maximize the TPB density.

Simulation results showed that in a monocomponent backbone a critical loading must be reached in order to create a percolating path of nanoparticles. The critical loading corresponds to a surface coverage fraction of 0.52–0.57, that means volume fraction of nanoparticles equal to 0.06 and 0.035 for size of nanoparticles equal to, respectively, 1/10 and 1/20 the diameter of backbone particles. On the other hand, more than half of nanoparticles are percolating when a composite backbone is used.

Simulations showed that the infiltration of a layer of nanoparticles does not lead to a significant reduction in porosity and gas transport properties. As a maximum, the mean pore size decreased by 14% while the effective diffusivity was halved in the worst case.

The infiltration led to increase the TPB density by even two orders of magnitude if compared with a conventional composite electrode. Simulations showed that the infiltration of nanoparticles into a monocomponent backbone can lead to a TPB density that is about twice the TPB density reached in the same conditions when infiltrating a composite backbone. However, while in a monocomponent backbone a critical loading must be reached, infiltration of nanoparticles into a composite backbone increased the TPB length for every loading.

Although the model allows the prediction of effective properties of infiltrated electrode, simulations revealed a strong sensitivity of the results on the size and the loading of nanoparticles. Furthermore, this high sensitivity is confined in a narrow range of loading. These conditions may make impracticable the prediction and the optimization of the microstructure of infiltrated electrodes, especially for monocomponent backbones.

Acknowledgements

Helpful discussions with Mr. Eric Hardjo (Fuel Cell Research Centre of Kingston – Ontario) and Dr. Dayadeep S. Monder (Indian Institute of Technology Hyderabad) are gratefully acknowledged.

References

[1] B.C.H. Steele, Materials for IT-SOFC stacks - 35 years R&D: the inevitability of gradualness?, Solid State Ionics. 134 (2000) 3–20.

[2] Z. Jiang, C. Xia, F. Chen, Nano-structured composite cathodes for intermediate-temperature solid oxide fuel cells via an infiltration/impregnation technique, Electrochim. Acta. 55 (2010) 3595–3605.

[3] T.Z. Sholklapper, C. Lu, C.P. Jacobson, S.J. Visco, L.C. De Jonghe, LSM-infiltrated solid oxide fuel cell cathodes, Electrochem. Solid-State Lett. 9 (2006) A376–A378.

[4] T.Z. Sholklapper, H. Kurokawa, C.P. Jacobson, S.. J. Visco, L.C. De Jonghe, Nanostructured solid oxide fuel cell electrodes, Nanoletters. 7 (2007) 2136–2141.

[5] A.N. Busawon, D. Sarantaridis, A. Atkinson, Ni infiltration as a possible solution to the redox problem of SOFC anodes, Electrochem. Solid-State Lett. 11 (2008) B186–B189.

[6] D. Ding, W. Zhu, J. Gao, C. Xia, High performance electrolyte-coated anodes for low-temperature solid oxide fuel cells: Model and experiments, J. Power Sources. 179 (2008) 177–185.

[7] E. Hardjo, D.S. Monder, K. Karan, Numerical modeling of nickel-impregnated porous YSZ-supported anodes and comparison to conventional composite Ni-YSZ electrodes, ECS Trans. 35 (2011) 1823–1832.

[8] B. Kenney, M. Valdmanis, C. Baker, J.G. Pharoah, K. Karan, Computation of TPB length, surface area and pore size from numerical reconstruction of composite solid oxide fuel cell electrodes, J. Power Sources. 189 (2009) 1051–1059.

[9] N.S.K. Gunda, H.-W. Choi, A. Berson, B. Kenney, K. Karan, J.G. Pharoah, et al., Focused ion beam-scanning electron microscopy on solid-oxide fuel-cell electrode: Image analysis and computing effective transport properties, J. Power Sources. 196 (2011) 3592–3603.

[10] A. Bertei, Chapter 4 of this Thesis, 2013.

[11] D. Bouvard, F.F. Lange, Relation between percolation and particle coordination in binary powder mixtures, Acta Metall. Mater. 39 (1991) 3083–3090.

[12] A. Berson, H.-W. Choi, J.G. Pharoah, Determination of the effective gas diffusivity of a porous composite medium from the three-dimensional reconstruction of its microstructure, Phys. Rev. E. 83 (2011) 026310.

[13] J.M. Zalc, S.C. Reyes, E. Iglesia, The effects of diffusion mechanism and void structure on transport rates and tortuosity factors in complex porous structures, Chem. Eng. Sci. 59 (2004) 2947–2960.

[14] H.-W. Choi, A. Berson, J.G. Pharoah, S.B. Beale, Effective transport properties of the porous electrodes in solid oxide fuel cells, Proc. Inst. Mech. Eng. Part A J. Power Energy. 225 (2011) 183–197.

[15] P.H.L. Martins, J.A. Plascak, Percolation on two- and three-dimensional lattices, Phys. Rev. E. 67 (2003) 046119.

Coupling between Microstructural and Electrochemical Modeling

Chapter 7

Integrated Microstructural–Electrochemical Modeling of Composite Electrodes

This Chapter presents an integrated microstructural–electrochemical model for SOFC composite electrodes. The microstructure of the electrodes is numerically reconstructed and analyzed through a Monte Carlo random–walk method to evaluate the effective properties, which are used in the continuum transport and reaction model. The study focuses on the cathode.

The study shows that:

i. the integration between microstructural and electrochemical models avoids the use of empirical or adjustable parameters, overcoming the limits of typical macro–modeling studies;

ii. the microstructural model accurately predicts effective properties in gas and solid phase in agreement with experimental data in a wide range of conditions;

iii. the lower bounds of particle size and porosity for composite cathodes are identified and related to the transition of gas diffusion to Knudsen regime.

This Chapter was adapted from the paper "Microstructural modeling for prediction of transport properties and electrochemical performance in SOFC composite electrodes" by A. Bertei, B. Nucci and C. Nicolella, published in Chem. Eng. Sci. 101 (2013) 175–190.

Abstract

A model for the description of transport and electrochemical processes in solid oxide fuel cell (SOFC) electrodes is presented in this study. Effective transport and reaction properties are evaluated using a Monte Carlo random–walk method on electrodes numerically reconstructed with a packing algorithm. This approach overcomes limitations of typical micro–modeling studies on SOFCs, wherein effective microstructural properties are estimated using empirical correlations or fitted on experimental data. Throughout the entire modeling framework in this study, no fitted or empirical parameters are used. Effective properties as a function of porosity and particle size are calculated and reported in dimensionless form to provide generality in their application. A good agreement with independent experimental data for both gas and solid phases is achieved. The model predictions can be used to improve the design of composite electrodes for solid oxide fuel cells. In particular, simulation results show that porosity lower than 0.20 and particle size smaller than 0.2μm should be avoided in the design of SOFC composite cathodes because, under these conditions, Knudsen effects limit the mass transport with a significant reduction in the electrode performance.

7.1 Introduction

Solid oxide fuel cells (SOFCs) have attracted research attention due to their expected high efficiency of energy conversion [1], low emission of pollutants [2], broad fuel flexibility [3,4] and capability to produce both heat and power [5]. A solid oxide fuel cell is an electrochemical device which converts the chemical energy of a fossil or renewable fuel into electric energy [6]. It consists of two electrodes, the anode for fuel and the cathode for air, separated by the electrolyte and connected into an electrical circuit. The electrolyte is a dense ion–conducting layer, which operates at relatively high temperatures (600–1000°C) [1]. At the cathode molecular oxygen is reduced by the electrons coming from the external circuit, forming oxygen ions. These are transported by the electrolyte towards the anode, where the fuel is oxidized.

In the last two decades modeling and simulation techniques have assisted the development of SOFC technology [7,8]. The modeling spans over a wide range of length scales, from the material and microstructural details [9], up to the electrode and cell levels [10–12] and to the system level [5,13].

A typical electrode is a porous layer wherein charge and chemical species are transported and react [14]. Figure 7.1 shows a scheme of a composite cathode, where molecular oxygen permeates through the thickness to react with electrons. The transport and electrochemical processes are usually modeled using micro–

models based on mass and energy balances [15,16]. Several aspects have been investigated and discussed: thermodynamics [17,18], mass transport phenomena [19,20], detailed reaction mechanisms [21,22].

Experimental studies have recognized that the microstructural characteristics significantly influence transport and reaction phenomena, affecting the electrode performance [23–25]. For example, reducing the particle size significantly enhances the number of reaction sites [26], which can be maximized by tailoring the electrode composition [24,25]. The porosity is another key factor: while a decrease in porosity initially leads to an increase in electrode efficiency [25], closure of pores and gas diffusion limitations can reduce the electrochemical performance below a critical limit [24,27].

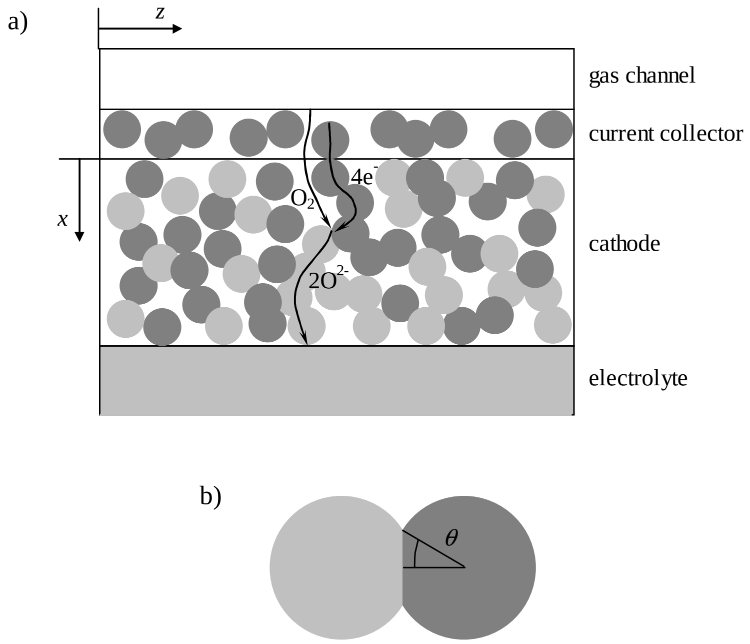

Figure 7.1 – a) Schematic view of a porous composite cathode. b) contact between two different conducting particles: θ is the contact angle.

In modeling studies, very often effective transport and reaction properties are estimated by using empirical correlations. In some cases, morphological parameters such as tortuosity, contact area between neighboring particles or mean pore diameter are taken as adjustable parameters to fit on experimental data [8]. In this way, the estimated or fitted transport properties may be unrealistic and not representative of the microstructure corresponding to the sample characteristics (i.e., composition, particle size, porosity). This may nullify the efforts made to describe very complex phenomena and reaction mechanisms.

Apart from the pioneering studies made by Sunde [9,28], only in the last few years the modeling of the electrode microstructure by means of particle–based packing algorithms has been adopted for SOFCs [29–32]. Such a technique is expected to improve the estimation of effective properties, reducing, if not eliminating, the number of adjustable parameters. In addition, if compared with empirical correlations, the microstructural simulation allows specific features of SOFC electrodes to be taken into account, such as the sintering effects and the particle size distribution [30]. Although the actual electrode microstructure is not exactly represented, the microstructural modeling provides a valuable tool for predicting the performance of conventional and alternative architectures [31].

It must be mentioned that an alternative method to estimate the microstructural properties consists in reconstructing the microstructure of actual samples through focused–ion–beam scanning–electron–microscope images or X–ray tomography [33–36]. These techniques provide a closer representation of the electrode microstructure, although they are not predictive (that is, real samples are required) and rely on the image resolution and post–processing analysis, which may cause possible uncertainties.

In this study, transport and reaction effective properties in SOFC composite electrodes are evaluated on microstructures numerically generated through a packing algorithm. A Monte Carlo random–walk method is adopted to calculate the effective transport properties in both gas and solid phases. Phase percolation and pore size characterization are also analyzed. The effects of porosity and particle size on effective properties are particularly investigated and compared with independent experimental data. Microstructural results are given in dimensionless form, providing generality in their application.

The evaluated effective properties are used in a model for the description of transport and electrochemical processes within composite electrodes, with special focus on the cathode. The sub–models describing mass and charge transport as well as the electrochemical reaction are presented in detail. The model is used to study the performance of the cathode as a function of morphological characteristics, in particular porosity and particle size. This enables the derivation of practical indications about conditions to be avoided when designing an SOFC cathode.

It is important to emphasize that, apart from the assumption of modeling the electrode microstructure as a random packing of spherical particles, throughout the entire modeling approach there are no empirical or adjusted parameters.

The Chapter is organized as follows. Section 7.2 is dedicated to the description of the microstructural models, from the numerical generation of the microstructure to the calculation of morphological and effective transport properties. In Section 7.3 the model of transport and reaction is presented. In Section 7.4 the results of the microstructural modeling are presented and compared with experimental data. Section 7.5 reports the results of the transport and reaction model applied to composite cathodes, where the connection between microstructural properties and electrode performance is analyzed. General conclusions and future research are summarized in Section 7.6.

7.2 Microstructural modeling

7.2.1 Packing generation

Binary random packings of spherical particles are numerically constructed by using a sedimentation algorithm also known as drop–and–roll [37–39]. In this section, only a brief description of the algorithm is summarized, more details can be found in a previous chapter of this thesis [40].

The packings are numerically generated by adding a particle at a time into a box domain of specified dimensions. Periodic boundary conditions are implemented in the horizontal directions to build an effectively infinite packing in the horizontal plane and avoiding wall effects [38]. Particles are sequentially dropped from a random point from the top of the domain. The desired composition is enforced by assigning a weighted probability to the particle selection according to the relative solid volume fractions of the binary mixture. The falling particle rolls over one or two already packed particles without friction, adhesion or inertia until either it touches the floor or it is stably supported by three other particles [41]. As the particle comes into rest, its position is fixed and a new particle is dropped into the domain. As the box is entirely filled, a portion with a thickness of six particle diameters is removed from both the top and the bottom of the domain to ensure the extinction of floor and wall effects [42]. The packing procedure produces a random loose packing with a weak anisotropy in the vertical direction imposed by the gravity force [43,44].

The degree of densification is determined by assigning the desired particle–particle contact angle (see Figure 7.1b), which defines the amount of particle overlap in each pair of contacts. The contact angle is kept constant throughout the structure during the packing generation. There is a one–to–one correspondence between porosity and contact angle, as discussed in Section 7.4.2.

The packing algorithm provides the center coordinates, the radius and the type of each packed sphere. These data enable the determination of the neighboring particles for each sphere in the packing and, consequently, the clusters of homologue particles connected to each other [45]. Clusters which provide a connected network of particles from the top to the bottom of the domain are marked as percolating [10]. The percolation fraction of each solid phase is defined as the number fraction of particles belonging to percolating networks over the total number of particles of such a phase [45,46].

The packing porosity and the solid volume fractions are determined through a Monte Carlo method, since the analytical computation of particle volumes is demanding when particles experience multiple overlaps [47]. A fixed number of points (200 per particle) are randomly and uniformly distributed within the domain. The porosity and the solid volume fractions are assumed to be equal to the number fraction of points falling, respectively, within the gas phase and within the solid phases.

7.2.2 Calculation of effective properties

Both gas diffusion and electric conduction in porous media are diffusive phenomena, obeying a Fick–type law. As a consequence, the calculation of the effective diffusivity in gas phase, as well as the effective electric conductivity in solid phases, can be performed by simulating the Brownian movements of tracers in their corresponding phases [48]. This study adopts a random–walk Monte Carlo simulation based on the mean–square displacement method [49–51].

7.2.2.1 Effective diffusivity in gas phase

A tracer (e.g., a molecule of a gaseous species) is randomly placed within the gas phase. The free path, that is the step length that the tracer has to cover, is randomly chosen from an exponential probability distribution [52] centered on the mean free path δ. Then, a random trajectory is selected [53]. The tracer moves of the free path, unless it collides with a solid particle. In such a case, the tracer is reflected according to the Knudsen cosine law [54], otherwise a new random trajectory and free path are chosen. Independent random number generators [55] are employed to pick uniformly distributed numbers used to select the initial tracer position, the random trajectory, the free path and the reflected trajectory [56].

The mean free path δ is calculated according to the definition of Knudsen number Kn [57]:

$$Kn = \frac{\delta}{d_{pore}} \tag{7.1}$$

where d_{pore} is the mean pore size, whose calculation is discussed in Section 7.2.3. The Knudsen number Kn is imposed in the method: a small value (e.g., $Kn \leq 10^{-2}$) is set to simulate a bulk diffusion regime, higher values (e.g., $Kn \geq 10$) to simulate diffusion in Knudsen regime.

The effective diffusivity is calculated from the mean square displacements $\langle R^2 \rangle$ of thousands of tracers as follows [48]:

$$D^{eff} = \frac{\langle R^2 \rangle \phi_g \gamma_g}{6t} \tag{7.2}$$

where t is the tracer travel time, ϕ_g represents the packing porosity and γ_g the pore percolation fraction. The calculation of the pore percolation fraction is discussed in Section 7.2.4. The product $\phi_g \gamma_g$ in Eq. (7.2) accounts for the volume excluded by packed spheres and closed pores. The travel time t is proportional to the total traveled distance s covered by the tracer as $s = vt$, where v is the mean molecular velocity. The total traveled distance is imposed in the method.

Eq. (7.2) is not directly applied in this study, rather a normalized effective diffusivity is calculated. The normalization accounts for the bulk diffusivity D_b, which, according to the gas kinetic theory [58], results as follows:

$$D_b = \frac{1}{3} \delta v \tag{7.3}$$

By dividing Eq. (7.2) by Eq. (7.3) and substituting the relationship between s and t ($s = vt$), as well as between Kn and δ (Eq. (7.1)), the normalized effective diffusivity $\tilde{D}^{eff}$ is obtained:

$$\tilde{D}^{eff} = \frac{D^{eff}}{D_b} = \frac{\langle R^2 \rangle \phi_g \gamma_g}{2Kn \cdot d_{pore} s} \tag{7.4}$$

The normalization makes $\tilde{D}^{eff}$ independent of the gas species. On the other hand, the normalized effective diffusivity depends on the Knudsen number. $\tilde{D}^{eff}$ approaches the effective bulk diffusivity or the effective Knudsen diffusivity, both normalized by D_b, for Kn approaching, respectively, 0 or ∞ [51].

As a final remark, tracers are generated in the central portion of the packing, far from both the top and the bottom of the domain. In fact, the collision of tracers with upper and lower domain boundaries may affect the calculation of the mean–square displacement. In order to further reduce this phenomenon, domains with a square base and a height to side length ratio equal to three are used in this study.

7.2.2.2 Tortuosity factor

When dealing with porous media, the tortuosity factor τ is typically used to characterize the diffusion process within the pores. The tortuosity factor is defined as the square of the tortuosity [59].

Zalc et al. [50] demonstrated that, if properly calculated, the tortuosity factor is a purely geometric parameter, function of the pore microstructure only. As a consequence, the tortuosity factor depends neither on the diffusion regime (i.e., independent of Knudsen number) nor on the gaseous species. This happens if the proper mean pore size d_{pore} is used to calculate the Knudsen number, as discussed in Section 7.2.3.

According to Zalc et al. [50], in this study the tortuosity factor is calculated as follows:

$$\tau = \frac{1}{1+Kn}\frac{\phi_g \gamma_g}{\tilde{D}^{eff}} \tag{7.5}$$

where the normalized effective diffusivity defined Eq. (7.4) is used. It is worth noting that while $\tilde{D}^{eff}$ depends on the Knudsen number, Eq. (7.5) allows τ to be independent of the Knudsen regime.

The tortuosity factor characterizes both ordinary and Knudsen diffusion. The tortuosity factor rules also the pressure–driven viscous flow through the porous media [59], taking part in the calculation of the permeability as discussed in Section 7.3.3.

7.2.2.3 Effective electric conductivity in solid phases

The random walk approach described in Section 7.2.2.1 is also used to determine the effective electric conductivity of the solid phases.

A tracer (e.g., an electron or an ion) is generated within a percolating particle of the considered solid phase J. The tracer is randomly moved within the phase, following an elastic reflection law when it collides with the external surface of a particle or with the plane separating the particle from another particle belonging to a different solid phase. The collision of tracers with upper and lower domain boundaries are avoided by generating them in the central portion of the domain, which has a height to side length ratio equal to three.

An equivalent Knudsen number Kn^{eq} is used to calculate the free path, similarly to what described in Section 7.2.2.1 for the gas phase. The equivalent Knudsen number is defined as the ratio between the mean free path and the mean particle diameter $\bar{d}_J$. The equivalent Knudsen number is an input parameter to be set. To simulate a bulk diffusion regime a small value of Kn^{eq} (e.g., $Kn^{eq} \leq 10^{-2}$) must be used, since Knudsen diffusion of charged species in solid phase is not physically realistic.

The normalized effective conductivity $\tilde{\sigma}_J^{eff}$, which is the ratio of the effective and the bulk conductivity of the considered solid phase J, is calculated similarly to Eq. (7.4) as follows:

$$\tilde{\sigma}_J^{eff} = \frac{\langle R^2 \rangle \phi_J \gamma_J}{2Kn^{eq} \bar{d}_J s} \tag{7.6}$$

where ϕ_J and γ_J represent, respectively, the volume fraction and the percolation fraction of phase J. The normalized effective conductivity characterizes the conduction of charged species within the considered phase and it is a function of the microstructure only.

7.2.3 Pore size characterization

The mean pore size d_{pore}, required for the estimation of the Knudsen number and the effective diffusivity (see Section 7.2.2.1), cannot be directly derived from the packing algorithm.

Several methods have been employed to determine the pore characteristic length, such as the sphere growth [30,60] and the chord length method [61]. The mean pore size must capture the statistics of the length distribution between particle external surfaces and the nature of the redirecting collisions in Knudsen regime, while be independent of the gas diffusion regime [50]. Derjaguin [62] proposed an approach, later extended by Levitz [63], to determine the mean pore size as:

$$d_{pore} = \langle l \rangle \left(\frac{\langle l^2 \rangle}{2\langle l \rangle^2} - \beta \right) \tag{7.7}$$

where $\langle l \rangle$ and $\langle l^2 \rangle$ represent, respectively, the number–averaged chord length and the mean–square chord length. In this study, the chords are numerically computed selecting a random point on the surface of a particle, choosing a random trajectory and evaluating the distance required to touch another particle.

The β factor captures the nature of redirecting collisions and is defined as [50]:

$$\beta = -\sum_{m=1}^{\infty} \langle \cos \vartheta_m \rangle \tag{7.8}$$

where $\langle \cos \vartheta_m \rangle$ is the average cosine of the angles between trajectory segments separated by m collisions with particles. In this study, the sum in Eq. (7.8) is computed using the first 12 terms according to the suggestion of Zalc et al. [50].

In isotropic random packings of spheres, the chord length distribution is expected to be exponential [51,61,63], therefore the ratio $\langle l^2 \rangle / 2\langle l \rangle^2$ becomes unity in Eq. (7.7). The β factor, which depends on the model of reflection on particle surface, is expected to approach 0 or 0.3077 for, respectively, elastic reflection or diffuse reflection (i.e., obeying the Knudsen cosine law) [50,51].

In this study, Eq. (7.7) is used to calculate the mean pore size. Eq. (7.7) has been shown to be the proper way to determine the pore characteristic length in random packings of spheres for porosity higher than 0.10, making the tortuosity factor τ independent of the diffusion transport regime [50,51].

7.2.4 Pore percolation

The pore percolation fraction is the ratio between open porosity and total porosity. The open porosity provides a continuous path for gas molecules moving from the top to the bottom of the domain within the gas phase. The pore percolation fraction is thus related to the transport properties in gas phase (see Eqs. (7.4) and (7.5)).

The pore percolation is determined by using a grid based technique [30]. The box domain is overlaid with a cartesian grid composed by cubic cells. Each cell is assigned to belong to the gas phase if more than half of its volume resides in a pore. The cell void fraction is calculated by uniformly distributing test points within the cell and calculating the number fraction of them which belong to the gas phase.

The process produces a three–dimensional lattice of void cells representing the gas phase. The lattice is analyzed to identify the clusters of neighboring cells connected to each other through their faces, as similarly done for site percolation in simple cubic lattices [64–66]. The Hoshen–Kopelman labeling technique [67] is used in this study to identify the clusters of cells. Only the clusters spanning throughout the whole vertical direction of the packing are marked as percolating. The pore percolation fraction γ_g is defined as the number fraction of cells belonging to percolating clusters over the total number of void cells.

7.2.5 TPB length

The three–phase boundary (TPB) is the contact perimeter between two solid particles, belonging to different conducting phases (i.e., electron–conducting and ion–conducting), exposed to the gas phase. In SOFC electrodes, the TPB is the place where reaction occurs [14].

The generation algorithm (see Section 7.2.1), in addition to particle information, also provides the center coordinates, radius and orientation of the planes of intersection which separate each pair of overlapping particles. Since particles are spherical, these planes of intersection are circles, which may be crossed by other planes of intersection, especially for low porosities. The analytical calculation of the contact perimeter is possible provided that there is no more than a triple intersection of spheres in the same point [30,47]. Since an intersection of more than three particles cannot be excluded *a priori*, the TPB length calculation is performed by means of the technique described below.

A test point is generated on the perimeter of the plane of intersection connecting two conducting particles. The test point is accounted for the TPB length calculation if it does not belong to a third particle. The procedure is repeated by moving the test point along the perimeter of the plane of intersection through a rotation around the normal axis of the plane. The effective perimeter exposed to the gas phase is equal to the number fraction of accepted test points times the perimeter length of the circle. The total TPB length is evaluated by repeating the procedure for all the planes of intersection. The connected TPB length is similarly calculated, by considering the planes of intersection connecting percolating particles only.

It is noteworthy that the procedure described above does not take into account the pore percolation because, as discussed in Section 7.4.3.1, the gas phase is entirely connected in the range of porosity investigated in this study.

7.3 Transport and reaction modeling

7.3.1 General aspects and model assumptions

Within an SOFC porous composite electrode, the electrochemical reaction between a gaseous species (e.g., oxygen in the cathode, hydrogen in the anode) and charged species in solid phase (i.e., electrons and oxygen ions) takes place in conjunction with transport of mass and charge. In this study, the transport and reaction modeling focuses on the cathode, although the same approach can be used for the anode.

A schematic representation of the cathode is reported in Figure 7.1a for a planar cell configuration. The cathode is the composite layer between the electrolyte and the current collector. The electrolyte is a dense ion–conducting layer while the current collector is a porous layer which collects and uniformly distributes electrons coming from the external circuit [68]. The current collector is exposed to the gas channel, which supplies air to the electrode. Molecular oxygen permeates along the *x*–coordinate to reach the cathode, wherein it is consumed. As a result, the oxygen partial pressure in the channel decreases along the *z*–coordinate.

The reaction taking place within the cathode is the electrochemical reduction of molecular oxygen into oxygen ions by means of electrons, according to the following stoichiometry:

$$O_{2(g)} + 4e^{-}_{(el)} \rightarrow 2O^{2-}_{(io)} \tag{7.9}$$

The reaction, apart from describing the molecular oxygen consumption, represents the conversion of the current from the electronic form into the ionic form. Charged species are transported by different conducting phases, namely by an electron–conductor (*el*) and by an ion–conductor (*io*). Typical conducting materials are the strontium–doped lanthanum manganite (LSM) as electronic conductor and the yttria–stabilized zirconia (YSZ) as ionic conductor [14]. The reaction may take place at any TPB provided that all the three phases are percolating.

The reacting system is described through mass conservation equations expressed for the three reaction participants and for nitrogen. Although the microstructural details are readily available from the microstructural modeling (see Section 7.2.1), the balance equations are not resolved in the reconstructed electrode. While recently different authors have incorporated transport and reaction phenomena within the reconstructed microstructure [69–72], in this study the transport and reaction model is developed by using the continuum approach, which describes the composite structure as a homogeneous continuum of the three involved phases [10,18,73]. The homogenization requires the use of effective transport and geometrical properties, which are evaluated according to Section 7.2.

The following further assumptions are adopted:

i. steady–state conditions;

ii. heat effects associated to Joule dissipation and reaction are considered negligible, resulting in uniform temperature in the whole electrode [12,74];

iii. the morphological effective properties are assumed constant throughout the electrode volume;

iv. only a cross section of the cathode along the length of the channel is modeled: this results in a 1D model in the axial coordinate *x*. Different degrees of oxygen consumption along the gas channel are accounted for by varying the oxygen partial pressure as boundary condition;

v. no mixed ionic–electronic conduction in the electron–conducting and ion–conducting phases [12,18];

vi. the electrochemical reaction described in Eq. (7.9) is assumed to occur at the three–phase boundary, that is at the contact perimeter between percolating electron–conducting and ion–conducting particles exposed to the gas phase [12,75];

vii. surface diffusion is not accounted for in the evaluation of molar fluxes since it is broadly accepted that surface transport phenomena are limited within the proximity of the TPB region [18,75], so that they can be included in the reaction mechanism [68,76].

7.3.2 Governing equations and boundary conditions

The transport and reaction model consists of a set of partial–differential equations, representing the conservation of the three reacting species (i.e., molecular oxygen, electrons and oxygen ions) and of the inert gas.

Considering steady–state conditions, the balance equations, on a molar basis, for electrons (*e*), oxygen ions (*o*), molecular oxygen (*O*) and nitrogen (*I*) result as follows:

$$\frac{dN_e}{dx} = -\frac{i_{TPB}\lambda_{TPB}^c}{F} \tag{7.10}$$

$$\frac{dN_o}{dx} = \frac{i_{TPB}\lambda_{TPB}^c}{2F} \tag{7.11}$$

$$\frac{dN_O}{dx} = -\frac{i_{TPB}\lambda_{TPB}^c}{4F} \tag{7.12}$$

$$\frac{dN_I}{dx} = 0 \tag{7.13}$$

where N_i represents the molar flux of the species *i* and *F* the Faraday constant.

The source terms in Eqs. (7.10–7.12) account for the production and consumption of the species as a consequence of the electrochemical reaction (Eq. (7.9)) at the TPBs. The term $i_{TPB}\lambda_{TPB}^c$ represents the current exchanged per unit of electrode volume, which is positive when molecular oxygen is consumed in the reaction. This term is the product of the current density per unit of TPB length i_{TPB} and the connected TPB length per unit volume λ_{TPB}^c. While the latter is a morphological parameter, function of the microstructure only and evaluated according to Section 7.2.5, i_{TPB} represents the reaction rate, as discussed in Section 7.3.5.

The set of balance equations Eqs. (7.10–7.13) is coupled with the following boundary conditions (refer also to Figure 7.1a):

$$x = 0 \quad \text{(current collector interface)} \quad \begin{cases} N_e = \dfrac{I_c}{F} \\ N_o = 0 \\ y_O = y_O^{ch} \\ P = P^{ch} \end{cases} \tag{7.14a}$$

$$x = L_c \quad \text{(electrolyte interface)} \quad \begin{cases} N_e = 0 \\ N_o = \dfrac{I_c}{2F} \; \text{and} \; V_{io} = 0 \\ N_O = 0 \\ N_I = 0 \end{cases} \tag{7.14b}$$

At the current collector interface, the oxygen ion flux is set to 0 because the current collector is a purely electron–conducting material. The inlet electron flux corresponds to the total current density I_c. Both pressure P and oxygen molar fraction y_O are set equal to the gas stream conditions within the gas channel. In fact, due to its high porosity, the current collector does not offer significant resistance to mass transport and can be neglected [77].

At the electrolyte interface (L_c is the cathode thickness), gaseous fluxes are null as well as the electron flux, since the electrolyte is a dense ion–conducting layer. On the other hand, the outlet oxygen ion flux accounts for the total current density. Since the absolute electric potential of a phase is determined up to an additive constant [18], the electric potential of the ion–conducting phase V_{io} is set at 0 V at the electrolyte interface as reference point [12]. For consistency, for every applied current density, the electric potential of the electron–conducting phase V_{el} at $x = 0$ equals the absolute value of overall cathode overpotential η_c. Note that the cathode overpotential is the main performance index since it encompasses the resistances involved in all the processes occurring within the electrode, such as reaction (i.e., charge transfer at the TPB), mass transport and charge transport.

According to the sign convention used in Eq. (7.14), a positive current density I_c corresponds to molecular oxygen consumption, that is, to conversion of electrons into oxygen ions.

It is noteworthy that the transport and reaction model here presented has been extensively validated with experimental data in a previous chapter of this thesis [77].

7.3.3 Gas transport

In this study, mass transport within the pores is described according to the dusty–gas model [78,79]. Such a model comprises convection and both ordinary and Knudsen diffusion. Suwanwarangkul et al. [20] found that the dusty–gas model is more accurate to predict mass transport in SOFC electrodes than the extended Fick model and the Stefan–Maxwell model.

Due to the high temperature and relatively low pressure used in SOFC applications, ideal gas behavior is assumed. According to the dusty–gas model, molar fluxes of gaseous species are calculated as a function of pressure and oxygen molar fraction as follows:

$$N_O\left(\frac{1}{D_{K,O}^{eff}}+\frac{1-y_O}{D_{O-I}^{eff}}\right)=\frac{y_O}{D_{O-I}^{eff}}N_I-\frac{P}{\Re T}\frac{dy_O}{dx}-\frac{y_O}{\Re T}\left(1+\frac{P}{\mu}\frac{B}{D_{K,O}^{eff}}\right)\frac{dP}{dx} \tag{7.15a}$$

$$N_I\left(\frac{1}{D_{K,I}^{eff}}+\frac{y_O}{D_{O-I}^{eff}}\right)=\frac{1-y_O}{D_{O-I}^{eff}}N_O+\frac{P}{\Re T}\frac{dy_O}{dx}-\frac{1-y_O}{\Re T}\left(1+\frac{P}{\mu}\frac{B}{D_{K,I}^{eff}}\right)\frac{dP}{dx} \tag{7.15b}$$

where $\Re$ is the ideal gas constant and T the absolute temperature.

Effective diffusion coefficients in Eq. (7.15) are calculated by correcting for open porosity and tortuosity factor as follows [51]:

$$D_{O-I}^{eff}=\frac{\phi_g\gamma_g}{\tau}D_{O-I} \tag{7.16}$$

$$D_{K,i}^{eff}=\frac{\phi_g\gamma_g}{\tau}D_{K,i} \qquad \text{where} \quad D_{K,i}=\frac{1}{3}d_{pore}\sqrt{\frac{8\Re T}{\pi M_i}} \quad (i = O, I) \tag{7.17}$$

where M_i is the molecular weight of species i. D_{O-I}^{eff} and $D_{K,i}^{eff}$ represent the effective diffusivity in the limit of, respectively, bulk ordinary diffusion (i.e., $Kn \to 0$) and Knudsen diffusion (i.e., $Kn \to \infty$). According to Section 7.2.2.2, the same tortuosity factor is used to correct both ordinary and Knudsen effective diffusivities, differently from what suggested by other authors [80–83]. The binary diffusion coefficient D_{O-I} in Eq. (7.16) is calculated by using the Fuller correlation [84] while the dynamic viscosity μ in Eq. (7.15) according to the Herning and Zipperer method [84].

The permeability coefficient B in Eq. (7.15) is calculated as [78,79]:

$$B=\frac{\phi_g\gamma_g}{\tau}\frac{d_{pore}^{\;2}}{32} \tag{7.18}$$

In this study, the mean pore size d_{pore} is proposed to be used as the characteristic length to describe also the permeability of the media. Note that d_{pore} was defined in Section 7.2.3 to make the tortuosity factor independent of the Knudsen number. Even though in principle the use of d_{pore} to calculate the permeability cannot be theoretically justified, comparison of simulation results with experimental data in Section 7.4.3.3 suggests that Eq. (7.18) provides a good estimation of the permeability.

7.3.4 Charge transport

The transport of charged species, that is, electrons and oxygen ions, in their respective conducting phases is assumed to follow the Ohm's law [10,18,85]:

$$N_e = \frac{\sigma_{el}^{eff}}{F}\frac{dV_{el}}{dx} \tag{7.19}$$

$$N_o = \frac{\sigma_{io}^{eff}}{2F}\frac{dV_{io}}{dx} \tag{7.20}$$

In Eqs. (7.19) and (7.20), σ_{el}^{eff} and σ_{io}^{eff} represent, respectively, the effective electric conductivity of the electron–conducting and ion–conducting phases. Effective conductivities are calculated by multiplying the bulk conductivity of the pure material by the normalized effective conductivity, which is evaluated according to Eq. (7.6).

The flux of oxygen ions should be more realistically depicted as the flux of oxygen vacancies [14], which depends on the gradient of both electric potential (migration) and oxygen vacancy concentration (diffusion). However, the oxygen vacancy concentration is high in ion–conducting materials used in SOFCs. The oxygen vacancy concentration can be considered as a constant during charge transfer processes, making negligible the diffusive component of the flux of oxygen ions [12,18].

7.3.5 Electrochemical kinetics

The reaction given in Eq. (7.9) represents the global stoichiometry of the molecular oxygen electrochemical reduction. A complex kinetic scheme, involving several elementary reaction steps and intermediates, is expected. Several efforts have been made to elucidate the reaction pathway of oxygen reduction in SOFC composite cathodes [76,86–88]. A comprehensive review can be found in Adler [14], who, however, concludes that there is not general agreement about the reaction mechanism.

A detailed reaction mechanism of Eq. (7.9) is not required for the purposes of this study, a global macro–kinetics is enough. In the literature, several global expressions for the electrochemical oxygen reduction have been proposed [21,85,89,90]. Such kinetic expressions are tailored for the materials used in this study, that is, LSM and YSZ. In this study, two expressions are selected, reported by Kenney and Karan [68] and by Nam and Jeon [11], and summarized in Table 7.1. These kinetic expressions were experimentally obtained by, respectively, van Heuveln and Bouwmeester [76] and Radhakrishnan et al. [88], who performed measurements in model electrode configurations over a wide range of temperature, overpotential and oxygen partial pressure.

Table 7.1 – Global kinetic expressions for molecular oxygen reduction (Eq. (7.9)). The first expression is taken from Kenney and Karan [68], the second one from Nam and Jeon [11].

Expression	*Parameters*
$i_{TPB} = i_0\left[\exp\left(\alpha_a \frac{F}{\Re T}\eta\right) - \exp\left(-\alpha_c \frac{F}{\Re T}\eta\right)\right]$	$\alpha_a = 1.5$ $\alpha_c = 0.5$ $P_O^{ref} = 0.21\,\text{bar}$
$i_0 = i_0^{ref}\left(\frac{P_O}{P_O^{ref}}\right)^{\zeta} \exp\left[-\frac{E_a}{\Re}\left(\frac{1}{T} - \frac{1}{T^{ref}}\right)\right]$	$T^{ref} = 945°\text{C}$ $i_0^{ref} = 2.5\cdot10^{-4}\,\text{A}\cdot\text{m}^{-1}$ $E_a = 1.40\cdot10^{5}\,\text{J}\cdot\text{mol}^{-1}$ $\zeta = 0.375$
$i_{TPB} = i_0\left[\exp\left(\frac{2F}{\Re T}\eta\right) - \exp\left(-\frac{2F}{\Re T}\eta\right)\right]$	$E_a = 1.45\cdot10^{5}\,\text{J}\cdot\text{mol}^{-1}$
$i_0 = \frac{\Re T}{4F}\frac{P_O^{\zeta}}{0.00136}\exp\left(-\frac{E_a}{\Re T}\right)$	$\zeta = 0.25$

In Table 7.1, P_O represents the oxygen partial pressure (i.e., $P_O = y_O P$), η the overpotential, ζ the apparent oxygen reaction order, E_a the activation energy, α_a and α_a the transfer coefficients. The expressions are written in the direction of molecular oxygen consumption (i.e., $i_{TPB} > 0$) for positive overpotential.

For both the expressions, the activation overpotential η accounts for the potential drop between electron–conducting and ion–conducting phases as follows [18]:

$$\eta = -\frac{\Re T}{4F}\ln\left(\frac{P_O^{OC}}{P_O}\right) - V_{el} + V_{io} \tag{7.21}$$

The leftmost term in the right side of Eq. (7.21) represents the equilibrium potential step, which depends on gas phase concentration. P_O^{OC} represents the oxygen partial pressure in the channel corresponding to the open–circuit conditions.

The dependence of the current density on oxygen partial pressure and overpotential is formally different for the two expressions in Table 7.1. However, they predict similar results, which are fairly in agreement with our previous studies [77,91]. Further details on the equivalence of the two kinetic expressions are given in Section 7.5.1.

7.4 Microstructural modeling results

7.4.1 Verification of the mean–square displacement method on periodic structures

The random walk simulation method (RW) described in Section 7.2.2 was applied to evaluate the effective diffusivity and conductivity in a periodic lattice in order to assess its numerical verification. As a comparison, a finite element method (FEM) was used, solving the Fick law equation within the corresponding computational domain (i.e., gas phase or solid phase). In FEM simulations, the effective properties (diffusivity and conductivity) were evaluated as the ratio between the flux calculated in the lattice of the conducting phase (i.e., gas phase for diffusivity calculations, solid phase for conductivity calculations) and the flux calculated in an equivalent continuum domain constituted by the conducting phase only.

A unit cell of a body–centered cubic lattice (BCC) was used as reference. The lattice porosity was reduced from $\phi_g = 1 - \pi\sqrt{3}/8 \approx 0.32$, corresponding to rigid particles, by increasing the contact angle among the particles, that is, by uniformly increasing their radius. FEM results were obtained by refining the grid until mesh–independent results were reached. In RW simulations, 5000 tracers were used, traveling for a total distance *s* equal to 20000 times the domain length, which corresponded in average to an effective displacement equal to 2–4 times the particle diameter. In order to be consistent with the FEM, which simulated a bulk diffusion, an imposed Knudsen number of 10^{-3} was used in RW simulations for both gas and solid phases.

Numerical results are shown in Figure 7.2 as a function of porosity. As the porosity decreases, the effective gas diffusivity decreases while the effective solid conductivity increases. The latter behavior is consistent with the results obtained by Siu and Lee [92].

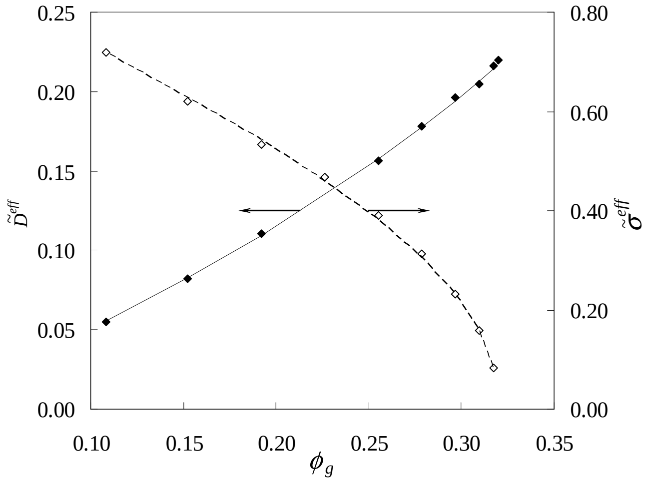

Figure 7.2 – Effective gas diffusivity and solid conductivity in a BCC lattice as a function of porosity: lines represent FEM results while marks numerical results of the mean–square displacement method.

The good agreement between the two series of results points out that the mean–square displacement method accurately evaluates the effective properties in both gas and solid phases.

7.4.2 Random packings investigated

Random packings of particles were numerically constructed by using the packing algorithm described in Section 7.2.1. Although the algorithm can simulate packings with the desired size distribution, in this study monosized particles were used to obtain general behaviors rather than distribution–specific results and because experimental data for validation are available in the literature for monosized random packings of spheres. Binary mixtures of electron–conducting and ion–conducting particles were simulated with equal solid volume fraction, that is, $\psi_{el} = \psi_{io} = 0.50$. This composition, used experimentally by several research groups [25,27,93], was chosen because it maximizes the TPB length when particles of the same size are used [30,94].

The desired packing porosity was reached by tailoring the contact angle. Figure 7.3 shows the relationship between the porosity and the contact angle: as the contact angle increases, the porosity decreases. The range of porosity investigated in this study falls between 0.10 and 0.40, except for Section 7.4.3.1, where porosities below 0.10 are also analyzed.

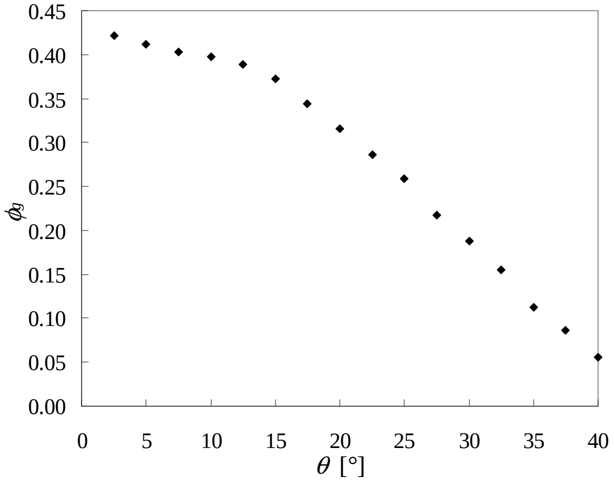

Figure 7.3 – Relationship between porosity and contact angle for simulated random packings of monosized spherical particles.

Regarding the computational domain, unless otherwise specified, a box domain with a square base and a height to side length ratio equal to three was used (see Section 7.2.2.1). The base side length was equal to 16 times the particle diameter, so that the generated packings were representative samples of the electrode microstructure [26,30,51,95].

Due to the randomness of the structure generation, numerical results were averaged on 5 structures. Different authors [30,51] used a larger number of samples (e.g., 20). However, in this study the relative standard deviations obtained by averaging results on 5 structures were generally below 2%, which was accepted as a reasonable precision if compared with possible errors introduced by model assumptions and simplifications. Due to the small standard deviation of numerical results, error bars are not displayed in the figures reported in Section 7.4, because smaller than the size of the markers.

7.4.3 Gas phase effective properties

7.4.3.1 Gas phase connectivity

The pore percolation was evaluated by using the grid based method described in Section 7.2.4. The domain was overlaid with cubic cells with a side length in the order of 0.02–0.10 times the mean pore size. This grid resolution enabled the accurate calculation of the pore percolation in the whole range of porosity investigated. In fact, as a comparison, the porosity calculated by summing up the volumes of the void cells differed from the packing porosity, estimated with the Monte Carlo method (see Section 7.2.1), by less than 0.4%. In order to limit the computational time and the memory requirements, smaller packings of particles were used in this section, corresponding to cubic domains with side length equal to 10 times the particle diameter.

Figure 7.4 shows the pore percolation fraction γ_g as a function of porosity in packings of monosized spherical particles. In the range of porosity 0.10–0.40 the percolation fraction is constantly equal to 1, which means that the gas phase is entirely connected. Below $\phi_g = 0.10$ the pore percolation fraction sharply decreases and the gas phase becomes not percolating for porosities below 0.04: $\phi_g = 0.04$ corresponds to the gas phase percolation threshold, value consistent with Zalc et al. [50] results.

The fact that the pore percolation fraction γ_g is equal to 1 within the range of porosity investigated in this study, i.e., $\phi_g = 0.10$–0.40, simplified the calculation of effective properties. The random walk simulation applied to the gas phase could be performed by placing tracers in any point within the gas phase, due to the absence of closed pores. Similarly, the calculation of the TPB length was performed without accounting for the pore percolation, as described in Section 7.2.5.

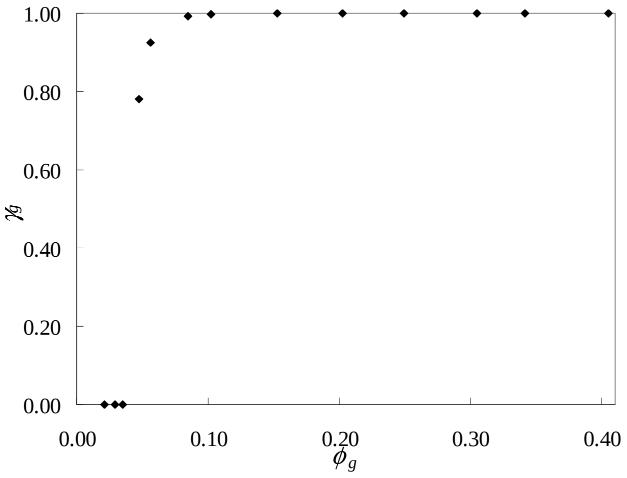

Figure 7.4 – Pore percolation fraction as a function of porosity in monosized random packings of spherical particles.

7.4.3.2 Effective diffusivity and tortuosity factor

The effective diffusivity and tortuosity factor in gas phase were determined by applying the mean–square displacement method described in Sections 7.2.2.1 and 7.2.2.2. In the random walk simulations, 20000 tracers were used, traveling for an effective displacement equal in average to 6 particle diameters, which corresponded to 19–43 times the mean pore size for, respectively, $\phi_g = 0.40$ and $\phi_g = 0.10$. As discussed in Section 7.2.2.2, the tortuosity factor is independent of the Knudsen number. Therefore, in simulations the Knudsen number was arbitrarily set to 10^{-2}, representing a bulk diffusion regime.

The tortuosity factor as a function of porosity is shown in Figure 7.5 with solid marks. Numerical results obtained by Zalc et al. [50] are also reported, who used a mean–square displacement method applied to numerically generated packings similar to those simulated in this study. Figure 7.5 also reports experimental data obtained by Currie [96], who measured the effective diffusivity in random packings of monosized rigid glass spheres.

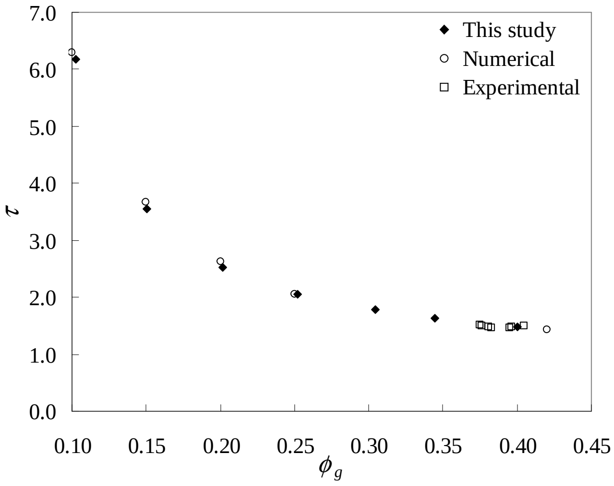

Figure 7.5 – Tortuosity factor as a function of porosity in monosized random packings of spheres. Numerical results obtained in this study through the random walk simulation are reported with solid marks. Circles represent the numerical results obtained by Zalc et al. [50] on generated random packings of spheres. Experimental data of packings of rigid glass spheres by Currie [96] are marked with squares.

The tortuosity factor increases monotonically as the porosity decreases, in particular more sharply for $\phi_g < 0.20$. The increase in the tortuosity factor contributes to reduce the factor $\phi_g \gamma_g / \tau$, which appears as a correction term for both effective diffusivity and permeability in Eqs. (7.16–7.18). While $\phi_g \gamma_g / \tau = 0.27$ for porosity equal to 0.40, the ratio falls down to 0.0167 for $\phi_g = 0.10$, which approximately corresponds to a second order power–law behavior, in agreement with Berson et al. [51] results.

Figure 7.5 shows that the results obtained in this study are consistent with those produced by Zalc et al. [50]. The comparison with experimental values [96] is satisfactory as well, even though limited to a small range of porosity close to the rigid packing limit. A broader comparison with experimental data is given in Section 7.4.3.3 regarding the permeability coefficient.

7.4.3.3 Mean pore size and permeability

The mean pore size was evaluated according to Section 7.2.3. It is the characteristic length used to calculate the Knudsen number (see Eq. (7.1)) and takes part in the determination of the permeability according to Eq. (7.18).

In this study, $5 \cdot 10^5$ chords were used to calculate the number–averaged and mean–square chord length in Eq. (7.7). The β factor in Eq. (7.8) was averaged on a minimum of $3 \cdot 10^7$ particle collisions, according to Zalc et al. [50] suggestion.

Since the mean pore size scales with the particle diameter [94] and the permeability with the square of particle diameter [97], d_{pore} and B are normalized as follows:

$$\tilde{d}_{pore} = \frac{d_{pore}}{d_{part}} \tag{7.22}$$

$$\tilde{B} = \frac{B}{d_{part}^{\;2}} \tag{7.23}$$

The normalization makes the two variables independent of the particle size, giving more generality to the results.

Figure 7.6 reports the normalized mean pore size and the normalized permeability as a function of porosity. d_{pore} and B can be extracted for any specific case by multiplying the normalized values by the specific particle size. Experimental data of normalized permeability, measured by Bosl et al. [97] in beds of sintered glass beads with negligible Knudsen effects, are also reported.

According to Figure 7.6, the mean pore size increases as the porosity increases. The permeability increases with porosity as well, but the dependence is stronger, corresponding to a power law $\tilde{B} \approx \phi_g^{3.3}$.

Experimental data of normalized permeability evaluated by Bosl et al. [97] are in very good agreement with numerical results obtained in this study. This means that the mean pore size, calculated according to Eq. (7.7), is also the characteristic pore dimension to describe the pressure–driven viscous flow, as proposed in Section 7.3.3. Secondarily, this gives sound indications that both the tortuosity factor and mean pore size were correctly predicted by the microstructural models, since the permeability is a function of both d_{pore} and τ according to Eq. (7.18).

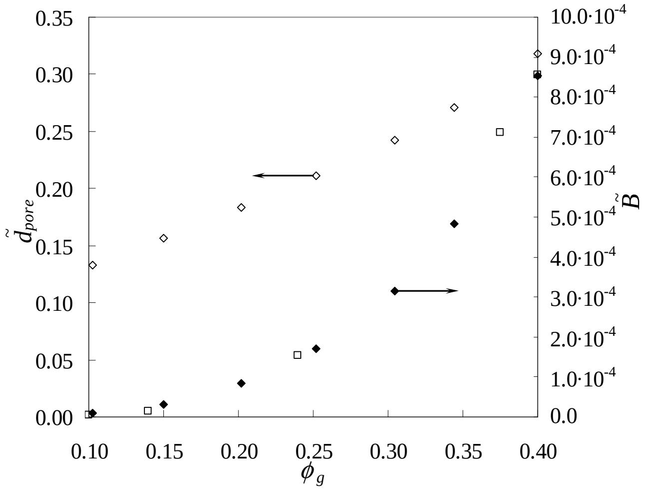

Figure 7.6 – Normalized mean pore size (void marks, leftmost axis) and normalized permeability (solid marks, rightmost axis) as a function of porosity in monosized random packings of spheres. Experimental values of normalized permeability of sintered glass beads obtained by Bosl et al. [97] are reported with squares.

7.4.4 Solid phase effective properties

7.4.4.1 Solid phase connectivity

The percolation fraction of electron–conducting and ion–conducting phases were evaluated through the knowledge of the nearest neighbors of each particle, which made possible to identify the percolating clusters (see Section 7.2.1). Since monosized binary mixtures with equal composition were investigated (see Section 7.4.2), the percolation fraction of the electron–conducting phase was equal to that of the ion–conducting phase, i.e., $\gamma_{el} = \gamma_{io}$.

Simulations showed that as the porosity decreases from 0.40 to 0.10, the percolation fraction of conducting particles increases from 0.972 to 0.997. This is a consequence of the larger number of contacts per particle provided by the increase in the contact angle as shown previously in this thesis [40]. Even in the limit of rigid spheres (i.e., ϕ_g approaching 0.42), the percolation fraction is high, even though not as high as that of the gas phase (see Section 7.4.3.1).

7.4.4.2 Effective conductivity

The normalized effective conductivity of the solid phases were determined by applying the mean–square displacement method described in Section 7.2.2.3, calculated according to Eq. (7.6). The number of tracers used in the simulations was 20000, traveling for an effective displacement equal in average to 10 particle diameters. An equivalent Knudsen number of 10^{-2} was set, corresponding to a bulk diffusion regime.

Figure 7.7 shows the normalized effective conductivity evaluated in mono–component and binary random packings as a function of porosity. In the second case, since both particle size and composition of electron–conducting and ion–conducting phases were identical, the normalized effective conductivities of both the phases are equal. Figure 7.7 also reports the normalized effective electric conductivity of mono–component packings of sintered spherical powders, made of stainless steel or copper, measured by Koh and Fortini [98].

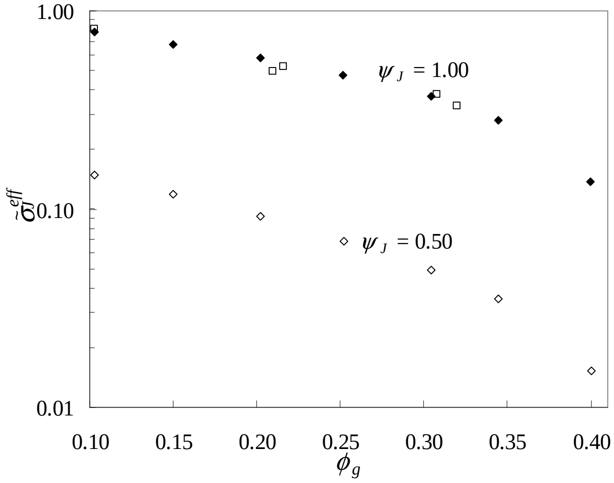

Figure 7.7 – Normalized effective conductivity as a function of porosity in mono–component and binary packings of spheres. Experimental data on mono–component random packings obtained by Koh and Fortini [98] are represented with squares.

For both ψ_J = 1.00 and ψ_J = 0.50, the normalized effective electric conductivity decreases as the porosity increases. This behavior is mainly attributed to the decrease in the contact angle among the particles, according to Figure 7.3. In fact, the normalized effective conductivity for both ψ_J = 1.00 and ψ_J = 0.50 falls down to zero as the porosity approaches the value corresponding to rigid particles. This behavior is analogous of that reported in Figure 7.2 for the BCC lattice, where the decrease in conductivity with porosity is essentially due to the smaller contact angle [92,99]. Obviously, in random packings also the tortuosity of conducting paths may vary with the porosity, as well as multiple parallel paths can be activated as particles make more contacts each other, as highlighted by the increase in the percolation fraction described in Section 7.4.4.1.

As recently pointed out by Sanyal et al. [31], the contact angle must be taken into account in the evaluation of the effective conductivity in random packings. As a consequence, semi–empirical correlations, in which the contact angle is not explicitly taken into account, usually do not provide accurate predictions [31,73].

The considerations exposed above are supported by the good agreement between simulation results and experimental data [98] for mono–component sintered packings presented in Figure 7.7. In addition, simulation results are fairly in agreement with numerical results obtained by Choi et al. [100] for monosized packings of sintered spheres at different solid volume fractions.

The satisfactory agreement with experimental data reached for effective properties in both gas and solid phases (see Figures 7.6 and 7.7) points out that the structures generated in this study were representative of real random packings of particles.

7.4.5 TPB length

The total and connected TPB lengths in numerically generated packings were evaluated according to the technique described in Section 7.2.5. Both total and connected TPB lengths were referred per unit volume and normalized with the particle diameter. The normalization considers that the TPB length per unit volume scales with the inverse of the square of the particle size [26,94,101]. The normalized lengths result as follows:

$$\tilde{\lambda}_{TPB}^{x} = \lambda_{TPB}^{x} \cdot d_{part}^{\ 2} \ (x = c, t) \tag{7.24}$$

In Figure 7.8, normalized total and connected TPB lengths are reported as a function of porosity. Note that $\tilde{\lambda}_{TPB}^{c} < \tilde{\lambda}_{TPB}^{t}$ since the former accounts for the percolation fractions of electron–conducting and ion–conducting phases, which are both smaller than 1 as discussed in Section 7.4.4.1. However, the gap between total and connected TPB lengths decreases as the porosity decreases.

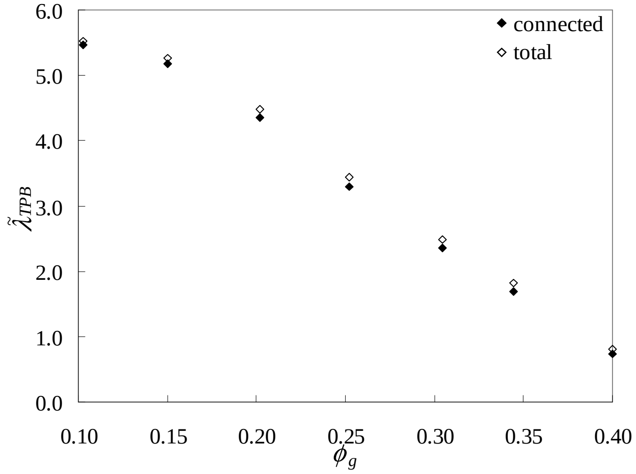

Figure 7.8 – Normalized TPB length per unit volume as a function of porosity in binary mixtures of monosized spheres with same volume composition.

As the porosity decreases, the TPB length increases. This behavior is reasonable because the TPB length per unit volume is proportional to: i) the number of particles per unit volume, ii) the number of contacts between electron–conducting and ion–conducting particles, and iii) the sine of the contact angle [94]. Simulations revealed that all these quantities increase as the porosity decreases. While the first two variables were found to increase almost linearly as the porosity decreases, the sine of the contact angle behaves differently. The relationship between $\sin(\theta)$ and porosity can be extracted from Figure 7.3. The dependence of $\sin(\theta)$ on porosity was found to be responsible of the decrease in the slope (in absolute value) of the TPB length for $\phi_g < 0.15$, as reported in Figure 7.8.

7.5 Transport and reaction model results

7.5.1 Model input parameters

The transport and reaction model described in Section 7.3 was applied to simulate porous composite cathodes in a broad range of porosity and particle size.

The conducting materials used in the simulations were strontium–doped lanthanum manganite (LSM) as electronic conductor and yttria–stabilized zirconia (YSZ) as ion–conducting phase. These materials are commonly used in SOFC composite cathodes, their transport and catalytic properties have been extensively studied [14,88,93].

Table 7.2 summarizes the main model parameters and operating conditions used in this study, which are typical for SOFC composite cathodes. For example, the composition used in the study is the same adopted by Barbucci et al. [93], that is similar to that used at Forschungszentrum Jülich [25] and at the Risø National Laboratory [27]. The ranges of particle size and porosity investigated comprise the design parameters used in several studies, for example Tsai and Barnett [24] used particle size equal to 0.28–0.97μm and porosity equal to 0.22–0.40, Haanappel et al. [25] used particle size equal to about 0.5μm while Barbucci et al. [93] used particle size equal to 0.3μm and porosity equal to about 0.4. Simulations were performed at 800°C and with an applied current density of $4000\mathrm{A\cdot m^{-2}}$. These values were chosen in the range of typical working conditions in the current state–of–the–art SOFCs [102–106]. Different oxygen molar fractions in gas channel were tested to simulate different degrees of oxygen consumption along the gas channel. However, the open–circuit conditions were kept fixed with $P_O^{OC} = 0.21$ bar.

Table 7.2 – Model parameters and operating conditions.

Parameter	*Value*
Working conditions	
Temperature T	800°C
Channel pressure P^{ch}	1.0bar
Channel oxygen molar fraction y_O^{ch}	0.10–0.21
Applied current density I_c	$4000\mathrm{A\cdot m^{-2}}$
Materials	
Electron–conducting phase *el*	LSM
Bulk electric conductivity at 800°C σ_{el}	$3.01\cdot 10^{4}\mathrm{S\cdot m^{-1}}$ [11]
Ion–conducting phase *io*	YSZ
Bulk ionic conductivity at 800°C σ_{io}	$2.26\mathrm{S\cdot m^{-1}}$ [11]
Microstructural parameters	
Particle diameter d_{part}	0.05–1.0μm
Porosity ϕ_g	0.10–0.40
Solid volume fraction of electron–conducting phase ψ_{el}	0.50

The electric properties of LSM and YSZ were taken from Nam and Jeon [11], physical properties of the gas phase from Todd and Young [84]. Microstructural parameters, such as the mean pore size or the connected TPB length, were calculated from the results obtained in Section 7.4.

Two global kinetic expressions (see Table 7.1) were considered in the simulations. In the full range of conditions investigated, the relative difference between the predicted values of cathode overpotential, evaluated according to the two expressions, was less than 10% as a maximum. The relative difference was in average smaller than 5%, even less for conditions governed by mass transport limitations, which are of primary interest in this study. Therefore, both the expressions are equivalent, since they predict similar results in the range of conditions investigated. In the remainder of this work, only numerical results obtained by using the Kenney and Karan [68] kinetic expression are presented.

7.5.2 Cathode overpotential versus thickness

The thickness is one of the key geometrical parameters which affect the electrode performance [10,23,107]. As the thickness increases, the number of reaction sites increases. On the other hand, molecular oxygen, electrons and oxygen ions have to cover a longer distance to reach/leave the reaction sites. While a larger number of reaction sites lead to a reduction in cathode overpotential, the ohmic drops and the concentration gradients in gas phase increase in thicker electrodes. A minimum of cathode overpotential is expected, corresponding to the optimal thickness. This feature has already been analyzed in the literature, even though without an accurate microstructural modeling [10,90].

Figure 7.9 shows the cathode overpotential as a function of thickness, for different porosities, as a result of simulations. In Figure 7.9a, the particle size is equal to 1.0μm, in Figure 7.9b to 0.1μm. In both cases, the oxygen partial pressure in the gas channel was set to 0.21bar.

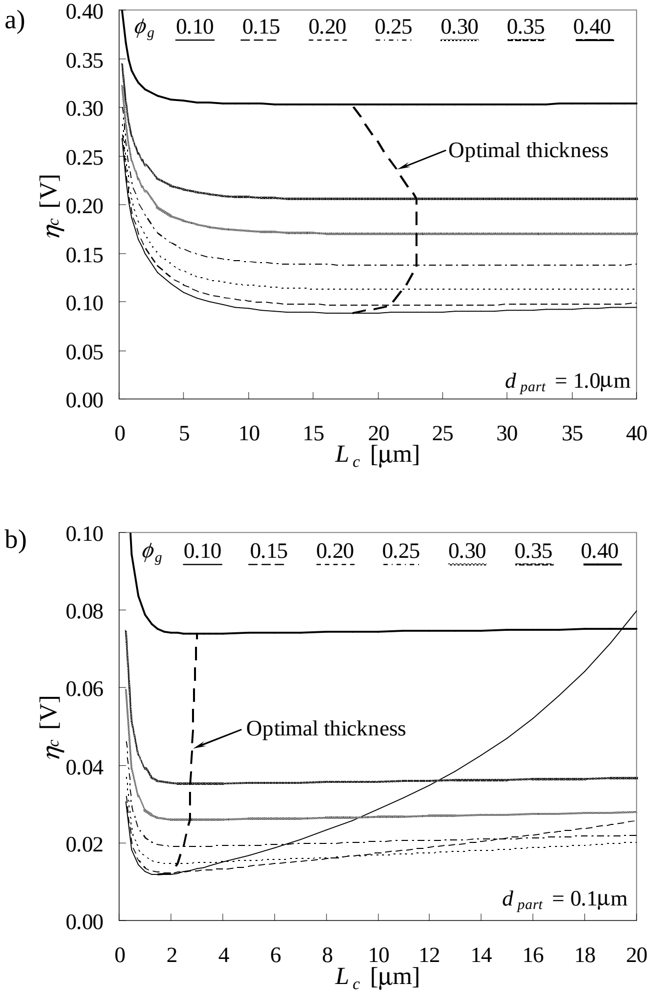

Figure 7.9 – Cathode overpotential as a function of thickness for different porosities: a) particle size equal to 1.0μm, b) particle size equal to 0.1μm. In both the simulations, cathodes with equal volume fractions of LSM and YSZ were considered, the temperature was set to 800°C, the applied current density to 4000A·m^{-2}, the oxygen partial pressure in the channel to 0.21bar.

Figure 7.9 shows that, given the porosity and the particle size, the electrode overpotential exhibits a minimum as a function of thickness as expected. Taking as an example Figure 7.9a, the increase in cathode overpotential with thickness beyond the minimum condition is rather small. Such an increase is mainly due to the additional resistance to gas transport offered by an electrode thicker than the optimum one. Indeed, the slope of the curves increase as the porosity decreases, as highlighted in Figure 7.9b.

This behavior is confirmed in Figure 7.10, which reports the current exchanged per unit volume as a function of the normalized axial coordinate $\tilde{x} = x / L_c$ for three electrode thicknesses. The current exchanged per unit volume is equal to the product $i_{TPB}\lambda^c_{TPB}$ and is related to the reaction rate per unit volume. Figure 7.10 shows that the reaction does not take place uniformly within the thickness but mainly occurs near the electrode–electrolyte interface (i.e., $\tilde{x} = 1$), especially for thick electrodes. Therefore, molecular oxygen must permeate throughout the whole electrode thickness to reach the reaction zone. This phenomenon led to the increase in cathode overpotential for thick electrodes as described above.

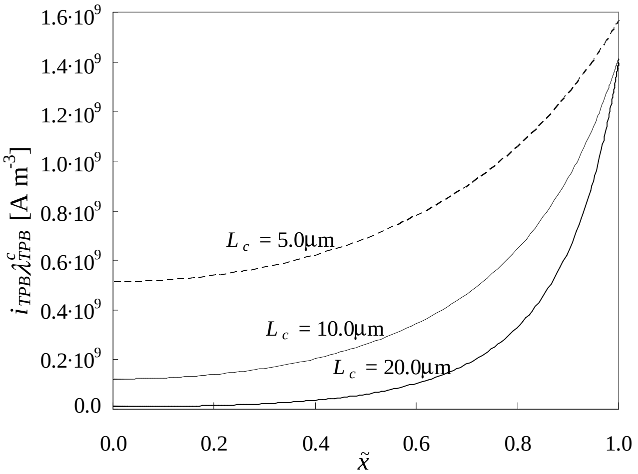

Figure 7.10 – Distribution of the current exchanged per unit volume as a function of the normalized axial coordinate for three electrode thicknesses. The conditions used in the simulation are reported in Table 7.2 with particle size equal to 0.5μm, porosity equal to 0.20 and oxygen partial pressure in the channel equal to 0.21bar.

7.5.3 Effect of porosity and particle size

According to Figure 7.9, as the porosity decreases, the minimum of cathode overpotential η_c decreases. On the other hand, for electrodes thicker than the optimal thickness, the decrease in porosity may lead to a sharp increase in overpotential (see especially Figure 7.9b).

This behavior is explained by considering the double effect of a reduction in porosity on microstructural properties: i) effective conductivities and TPB length increase (see Sections 7.4.4.2 and 7.4.5), but ii) the effective diffusivity, the mean pore size and the permeability decrease (see Sections 7.4.3.2 and 7.4.3.3). The increase in λ_{TPB}^{c}, σ_{el}^{eff} and σ_{io}^{eff} contributes to reduce the cathode overpotential, because a larger density of reaction sites are available and charge transport properties are enhanced. On the other hand, the reduction of transport properties in gas phase limits the supply of molecular oxygen, leading to an increase in cathode overpotential. The first phenomenon is dominant when the thickness is small and close to the optimal condition, the second one becomes significant when the thickness is larger.

The reduction in particle size has a similar effect on the cathode overpotential of that described for porosity. However, both effective electric conductivities and tortuosity factor do not depend on particle size.

These considerations explain why the optimal thickness generally decreases as the porosity and the particle size decrease (see the dotted lines in Figure 7.9). In the optimal conditions there are no significant mass transfer limitations, therefore the optimal thickness is ruled by the density of TPBs and by the effective electric conductivities. Since they increase with decreasing porosity and particle size, the optimal thickness decreases as ϕ_g and d_{part} decrease.

According to Section 7.4.3.3, as the porosity and the particle size decrease, the mean pore size decreases. As d_{pore} decreases, the diffusion regime passes from the continuum to the Knudsen regime, where Knudsen diffusion dominates on ordinary diffusion. The oxygen Knudsen diffusivity is smaller than the ordinary diffusivity: for the conditions simulated in this study, the ratio $D_{K,O}^{eff} / D_{O-I}^{eff}$ is equal to 0.405 when $Kn_O = 1$. Since $D_{K,O}^{eff} / D_{O-I}^{eff} \propto Kn_O^{-1}$ and, according to Eq. (7.1), $d_{pore} \propto Kn_O^{-1}$, it results that the ratio $D_{K,O}^{eff} / D_{O-I}^{eff} \propto d_{pore}$. As d_{pore} decreases, as a consequence of a reduction in porosity or in particle size, the diffusion of molecular oxygen slows down dramatically. Thus, the sharp increase in cathode overpotential for $\phi_g = 0.10$ and 0.15 in the rightmost part of Figure 7.9b is due to the reduction in the mean pore size, leading to the transition of gas transport from continuum to Knudsen regime.

7.5.4 Minimum cathode overpotential

In an SOFC electrode, the efficiency of energy conversion is maximized when the overpotential is reduced as low as possible. The minimum overpotential corresponds to the optimal electrode thickness, which depends on porosity and particle size as discussed in the previous section.

According to Figure 7.9b, the optimal electrode can be rather thin when small particles are used. Depending on the fabrication technique adopted, thicknesses of the order of 1–2μm are difficult to realize. While very efficient electrodes can be theoretically predicted, technological limitations must be considered for their fabrication. According to the current state–of–the–art, considering the most common fabrication techniques and the flatness requirements [108], the minimum thickness achievable is in the order of 5μm [109].

Figure 7.11 shows the minimum cathode overpotential as a function of particle size for different porosities. The minimum overpotential was calculated for the optimal thickness if larger than 5μm, otherwise the overall overpotential corresponding to a 5μm thick cathode was considered. Figure 7.11a reports the simulation results assuming an oxygen partial pressure in the gas channel of 0.21bar, Figure 7.11b assuming 0.10bar.

Looking at the rightmost part of Figure 7.11a, the minimum cathode overpotential monotonically decreases as the particle size and the porosity decrease. This behavior is consistent with the results described in Section 7.5.3. On the other hand, the leftmost region of the figure shows a different behavior: while for ϕ_g = 0.20–0.40 the cathode overpotential decreases as the particle size decreases, for ϕ_g = 0.10–0.15 an opposite trend is highlighted. The increase in the minimum cathode overpotential for small porosities and particle sizes is due to the mass transport limitations, corresponding to the Knudsen transport regime as discussed in Section 7.5.3.

Similar conclusions can be drawn regarding Figure 7.11b, corresponding to a lower oxygen partial pressure in the feed. The increase in cathode overpotential for small particle sizes when ϕ_g = 0.10–0.15 is even larger. This behavior is reasonable since mass transfer limitations are expected to be higher in this operating condition. Furthermore, given the porosity and the particle size, the minimum cathode overpotential is in average 0.03V larger than the corresponding value for P_O^{ch} = 0.21bar. Such a difference is in part due to the equilibrium potential step in Eq. (7.21), which arises when an oxygen partial pressure smaller than the open–circuit condition is fed to the electrode.

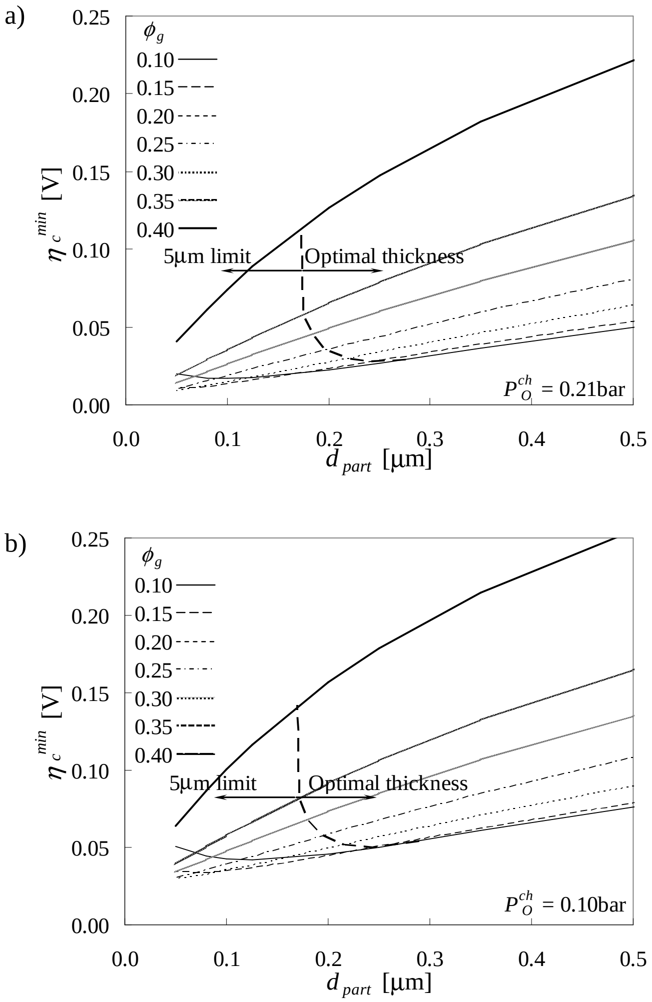

Figure 7.11 – Minimum cathode overpotential as a function of particle size for different porosities. The minimum corresponds to the optimal thickness if larger than 5μm, otherwise the overall overpotential at 5μm was considered. Cathodes with equal volume fractions of LSM and YSZ were considered, the temperature was set to 800°C, the applied current density to 4000A·m^{-2}. The oxygen partial pressure in the channel was a) 0.21bar, b) 0.10bar.

7.5.5 Final considerations and suggestions for design

The simulation results shown in the previous sections make possible to draw conclusions about the optimal electrode design, in particular about conditions which should be avoided.

Figure 7.11 suggests to avoid particles smaller than 0.2μm. In fact, according to Section 7.5.3, Knudsen effects may arise, leading to detrimental mass transfer limitations.

The porosity should be reduced as low as possible. In fact, according to Figures 7.4 and 7.9b, mass transfer limitations arise only for very small porosities and for thicknesses far beyond the optimal thickness. The lower porosity limit is in the order of 0.20. Smaller porosities could not guarantee a significant increase in performance and may even lead to a higher cathode overpotential.

These recommendations hold also for electrodes thinner than 5μm. According to Figure 7.9b, for $\phi_g < 0.20$ and $d_{part} < 0.2\mu m$, the cathode overpotential sharply increases for thicknesses higher than the optimal condition. This strong sensitivity to geometrical and morphological parameters should be avoided. In case of adopting bi–layer cathodes, with a functional layer composed of smaller particles at the electrolyte interface [110], the thickness of such a layer should not exceed 2μm according to Figure 7.9b.

Considering the lower limits of porosity and particle size suggested by the analysis, equal respectively to 0.20 and 0.2μm, for an oxygen partial pressure of 0.21bar and a current density of $4000A\cdot m^{-2}$ the minimum cathode overpotential is equal to about 0.03V (Figure 7.9a), which corresponds to a cathode resistance of $7.5\cdot 10^{-6}\Omega\cdot m^2$. In the same operating conditions, the cathodes prepared by Barbucci et al. [93], our experimental benchmark, having a porosity of about 0.4 and a particle size of 0.3μm, showed a minimum cathode overpotential of 0.105V. Therefore, the optimization of the microstructure can allow the reduction of the overall electrode overpotential by a factor 3.5. In addition, the optimized microstructure shows a performance slightly better than the typical range of cathode resistance considered for SOFC applications, equal to $10\cdot 10^{-6}$–$40\cdot 10^{-6}\Omega\cdot m^2$ [111].

The considerations expressed above are drawn looking at the electrode efficiency only. Other requirements are also important, such as the life of the component, the fabrication cost, the reproducibility. Technological issues, such as grain growth during the sintering process or operation [112–114], may force to use a particle size bigger than the lower limit suggested in this study. As a consequence, provided the validity of the models, the performance predicted in this study may be considered as the best that a real electrode may reach.

7.6 Conclusions

This study presented a modeling framework for the calculation of effective transport and reaction properties for SOFC composite electrodes. The effective properties were used in a transport and reaction model to study the electrode performance as a function of morphological and geometrical characteristics. No fitted or empirical parameters were used in this modeling framework.

The effect of porosity and particle size on microstructural properties was addressed. Predicted results were compared with independent experimental data, highlighting a satisfactory agreement for both gas phase and solid phase properties. Predicted values of tortuosity factor, permeability, mean pore size, phase connectivity, effective conductivity and TPB length per unit volume were reported in dimensionless form to be used in a broader and general context.

The transport and reaction model was used to evaluate the performance of porous composite SOFC cathodes. Typical operating conditions (temperature equal to 800°C, current density equal to $4000\mathrm{A\cdot m^{-2}}$) and conducting materials (LSM and YSZ) were chosen to perform the simulations. The model predicted a minimum of electrode overpotential as a function of thickness revealing that, in the range of porosity and particle size investigated, the increase in overpotential beyond the optimal thickness was due to gas transport limitations. Model results showed that these limitations became more significant as both porosity and particle size decreased. This behavior was related to the transition of gas diffusion from continuum to Knudsen regime, which negatively affected the electrode efficiency. This result held also for different oxygen partial pressures.

From a numerical study on the optimal conditions as a function of porosity and particle size, it was found that porosity lower than 0.20 and particle size smaller than 0.2μm should be avoided in cathode design. Furthermore, if a functional layer was inserted near the electrolyte interface, its thickness is proposed to be smaller than 2μm. These design indications are tailored for the specific conducting materials considered in the study, therefore appreciable discrepancies may result when using materials having different electrochemical properties.

The broad capability of the presented modeling approach makes it attractive for the study of every reacting porous media. The models can be used to support experimental analyses, especially if coupled with other reconstruction techniques [33,34], or as a design tool. For SOFC applications, the model could be extended to study the functional degradation due to particle coarsening and grain agglomeration in both cathode and anode [114,115].

Future research will further investigate the correlation between microstructural properties and electrochemical performance. The effects of specific particle size distributions on effective properties and electrode efficiency will be addressed, as well as novel and unconventional architectures such as functionally graded and engineered electrodes.

Nomenclature

Glossary

B	permeability [m^2]
$\tilde{B}$	normalized permeability
$\bar{d}_J$	mean particle diameter of phase *J* (*J* = *el*, *io*) [m]
d_{part}	particle diameter [m]
d_{pore}	mean pore size [m]
$\tilde{d}_{pore}$	normalized mean pore size
D_b	bulk diffusivity [m$^2\cdot$s^{-1}]
D^{eff}	effective diffusivity [m$^2\cdot$s^{-1}]
$\tilde{D}^{eff}$	normalized effective diffusivity
$D_{K,i}$	Knudsen diffusivity of species *i* (*i* = *O*, *I*) [m$^2\cdot$s^{-1}]
$D_{K,i}^{eff}$	effective Knudsen diffusivity of species *i* (*i* = *O*, *I*) [m$^2\cdot$s^{-1}]
D_{O-I}	binary diffusion coefficient of *O*–*I* gas mixture [m$^2\cdot$s^{-1}]
D_{O-I}^{eff}	effective binary diffusion coefficient of *O*–*I* gas mixture [m$^2\cdot$s^{-1}]
E_a	activation energy [J$\cdot$mol^{-1}]
F	Faraday constant [C$\cdot$mol^{-1}]
i_0	exchange current per unit of TPB length [A$\cdot$m^{-1}]
i_{TPB}	current density per unit of TPB length [A$\cdot$m^{-1}]
I_c	current density per unit of electrode area [A$\cdot$m^{-2}]
Kn	Knudsen number (for gas phase)
Kn^{eq}	equivalent Knudsen number (for solid phase)
$\langle l \rangle$	number–averaged chord length [m]
$\langle l^2 \rangle$	mean–square chord length [m^2]
L_c	electrode thickness [m]
M_i	molecular weight of species *i* (*i* = *O*, *I*) [kg$\cdot$mol^{-1}]
N_i	molar flux of species *i* (*i* = *e*, *o*, *O*, *I*) [mol$\cdot$m$^{-2}\cdot$s^{-1}]
P	pressure [Pa]
P_O	oxygen partial pressure [Pa]
$\Re$	ideal gas constant [J$\cdot$mol$^{-1}\cdot$K^{-1}]
$\langle R^2 \rangle$	mean–square displacement of tracers [m^2]
s	total traveled distance covered by a tracer [m]
T	temperature [K]
v	mean molecular velocity [m$\cdot$s^{-1}]
V_J	electric potential of conducting phase *J* (*J* = *el*, *io*) [V]

x	axial electrode coordinate [m]
$\tilde{x}$	normalized axial electrode coordinate
y_i	molar fraction of species *i* (*i* = *O*, *I*)
α_a	transfer coefficient (anodic)
α_c	transfer coefficient (cathodic)
β	factor defined in Eq. (7.8)
γ_J	percolation fraction of phase *J* (*J* = *g*, *el*, *io*)
δ	mean free path [m]
ζ	reaction order of molecular oxygen
η	overpotential [V]
η_c	overall electrode overpotential [V]
η_c^{min}	minimum overall electrode overpotential [V]
θ	contact angle [°]
λ_{TPB}^{c}	connected TPB length per unit volume [m^{-2}]
$\tilde{\lambda}_{TPB}^{c}$	normalized connected TPB length per unit volume
λ_{TPB}^{t}	total TPB length per unit volume [m^{-2}]
$\tilde{\lambda}_{TPB}^{t}$	normalized total TPB length per unit volume
μ	gas dynamic viscosity [$\mathrm{kg}\cdot\mathrm{m}^{-1}\cdot\mathrm{s}^{-1}$]
σ_J^{eff}	effective electric conductivity of phase *J* (*J* = *el*, *io*) [$\mathrm{S}\cdot\mathrm{m}^{-1}$]
$\tilde{\sigma}_J^{eff}$	normalized effective electric conductivity of phase *J* (*J* = *el*, *io*)
τ	tortuosity factor
ϕ_J	volume fraction of phase *J* (*J* = *g*, *el*, *io*)
ψ_J	solid volume fraction of phase *J* (*J* = *el*, *io*)

Superscripts

ch	gas conditions within gas channel
OC	open–circuit conditions
ref	reference conditions

Subscripts

e	electrons
el	electron–conducting phase
g	gas phase
io	ion–conducting phase
I	inert gas (e.g., nitrogen)
o	oxygen ions

O	molecular oxygen

Abbreviations

BCC	body–centered cubic
FEM	finite element method
LSM	strontium–doped lanthanum manganite
RW	random walk
YSZ	yttria–stabilized zirconia

Acknowledgements

Helpful discussion with Dr. Alessandra Sanson and Dr. Elisa Mercadelli, of the Institute of Science and Technology for Ceramics, National Research Council of Italy, is gratefully acknowledged. Special thanks to Dr. Jon G. Pharoah and Dr. Hae–Won Choi, Queen's University of Kingston – Ontario, who provided the original version of the packing algorithm.

References

[1] S.C. Singhal, K. Kendall, High temperature solid oxide fuel cells: fundamentals, design and applications, Elsevier, Oxford, 2003.

[2] S.C. Singhal, Advances in solid oxide fuel cell technology, Solid State Ionics. 135 (2000) 305–313.

[3] E. Achenbach, E. Riensche, Methane/steam reforming kinetics for solid oxide fuel cells, J. Power Sources. 52 (1994) 283–288.

[4] R.J. Kee, H. Zhu, D.G. Goodwin, Solid-oxide fuel cells with hydrocarbon fuels, Proc. Combust. Inst. 30 (2005) 2379–2404.

[5] J. Palsson, A. Selimovic, L. Sjunnesson, Combined solid oxide fuel cell and gas turbine systems for efficient power and heat generation, J. Power Sources. 86 (2000) 442–448.

[6] J. Larminie, A. Dicks, Fuel Cell Systems Explained, Wiley, New York, 2003.

[7] K.N. Grew, W.K.S. Chiu, A review of modeling and simulation techniques across the length scales for the solid oxide fuel cell, J. Power Sources. 199 (2012) 1–13.

[8] M. Andersson, J. Yuan, B. Sundén, Review on modeling development for multiscale chemical reactions coupled transport phenomena in solid oxide fuel cells, Appl. Energy. 87 (2010) 1461–1476.

[9] S. Sunde, Monte Carlo simulations of polarization resistance of composite electrodes for solid oxide fuel cells, J. Electrochem. Soc. 143 (1996) 1930–1939.

[10] P. Costamagna, P. Costa, V. Antonucci, Micro-modelling of solid oxide fuel cell electrodes, Electrochim. Acta. 43 (1998) 375–394.

[11] J.H. Nam, D.H. Jeon, A comprehensive micro-scale model for transport and reaction in intermediate temperature solid oxide fuel cells, Electrochim. Acta. 51 (2006) 3446–3460.

[12] H. Zhu, R.J. Kee, Modeling distributed charge-transfer processes in SOFC membrane electrode assemblies, J. Electrochem. Soc. 155 (2008) B715–B729.

[13] W.L. Becker, R.J. Braun, M. Penev, M. Melaina, Design and technoeconomic performance analysis of a 1MW solid oxide fuel cell polygeneration system for combined production of heat, hydrogen, and power, J. Power Sources. 200 (2012) 34–44.

[14] S.B. Adler, Factors governing oxygen reduction in solid oxide fuel cell cathodes., Chem. Rev. 104 (2004) 4791–4843.

[15] P. Aguiar, C.S. Adjiman, N.P. Brandon, Anode-supported intermediate temperature direct internal reforming solid oxide fuel cell. I: model-based steady-state performance, J. Power Sources. 138 (2004) 120–136.

[16] V.M. Janardhanan, O. Deutschmann, Numerical study of mass and heat transport in solid-oxide fuel cells running on humidified methane, Chem. Eng. Sci. 62 (2007) 5473–5486.

[17] H. Zhu, R.J. Kee, Thermodynamics of SOFC efficiency and fuel utilization as functions of fuel mixtures and operating conditions, J. Power Sources. 161 (2006) 957–964.

[18] W.G. Bessler, S. Gewies, M. Vogler, A new framework for physically based modeling of solid oxide fuel cells, Electrochim. Acta. 53 (2007) 1782–1800.

[19] W. Lehnert, J. Meusinger, F. Thom, Modelling of gas transport phenomena in SOFC anodes, J. Power Sources. 87 (2000) 57–63.

[20] R. Suwanwarangkul, E. Croiset, M.W. Fowler, P.L. Douglas, E. Entchev, M.A. Douglas, Performance comparison of Fick’s, dusty-gas and Stefan–Maxwell models to predict the concentration overpotential of a SOFC anode, J. Power Sources. 122 (2003) 9–18.

[21] H. Zhu, R.J. Kee, V.M. Janardhanan, O. Deutschmann, D.G. Goodwin, Modeling elementary heterogeneous chemistry and electrochemistry in solid-oxide fuel cells, J. Electrochem. Soc. 152 (2005) A2427–A2440.

[22] S. Gewies, W.G. Bessler, Physically based impedance modeling of Ni/YSZ cermet anodes, J. Electrochem. Soc. 155 (2008) B937–B952.

[23] M. Juhl, S. Primdahl, C. Manon, M. Mogensen, Performance/structure correlation for composite SOFC cathodes, J. Power Sources. 61 (1996) 173–181.

[24] T. Tsai, S.A. Barnett, Effect of LSM-YSZ cathode on thin-electrolyte solid oxide fuel cell performance, Solid State Ionics. 93 (1997) 207–217.

[25] V.A.C. Haanappel, J. Mertens, D. Rutenbeck, C. Tropartz, W. Herzhof, D. Sebold, et al., Optimisation of processing and microstructural parameters of LSM cathodes to improve the electrochemical performance of anode-supported SOFCs, J. Power Sources. 141 (2005) 216–226.

[26] Q. Cai, C.S. Adjiman, N.P. Brandon, Modelling the 3D microstructure and performance of solid oxide fuel cell electrodes: Computational parameters, Electrochim. Acta. 56 (2011) 5804–5814.

[27] M.J. Jørgensen, S. Primdahl, C. Bagger, M. Mogensen, Effect of sintering temperature on microstructure and performance of LSM–YSZ composite cathodes, Solid State Ionics. 139 (2001) 1–11.

[28] S. Sunde, Monte Carlo simulations of conductivity of composite electrodes for solid oxide fuel cells, J. Electrochem. Soc. 143 (1996) 1123–1132.

[29] L.C.R. Schneider, C.L. Martin, Y. Bultel, L. Dessemond, D. Bouvard, Percolation effects in functionally graded SOFC electrodes, Electrochim. Acta. 52 (2007) 3190–3198.

[30] B. Kenney, M. Valdmanis, C. Baker, J.G. Pharoah, K. Karan, Computation of TPB length, surface area and pore size from numerical reconstruction of composite solid oxide fuel cell electrodes, J. Power Sources. 189 (2009) 1051–1059.

[31] J. Sanyal, G.M. Goldin, H. Zhu, R.J. Kee, A particle-based model for predicting the effective conductivities of composite electrodes, J. Power Sources. 195 (2010) 6671–6679.

[32] A. Abbaspour, J.-L. Luo, K. Nandakumar, Three-dimensional random resistor-network model for solid oxide fuel cell composite electrodes, Electrochim. Acta. 55 (2010) 3944–3950.

[33] J.R. Izzo, A.S. Joshi, K.N. Grew, W.K.S. Chiu, A. Tkachuk, S.H. Wang, et al., Nondestructive reconstruction and analysis of SOFC anodes using X-ray computed tomography at sub-50 nm resolution, J. Electrochem. Soc. 155 (2008) B504–B508.

[34] J.R. Wilson, A.T. Duong, M. Gameiro, H.-Y. Chen, K. Thornton, D.R. Mumm, et al., Quantitative three-dimensional microstructure of a solid oxide fuel cell cathode, Electrochem. Commun. 11 (2009) 1052–1056.

[35] P.R. Shearing, J. Golbert, R.J. Chater, N.P. Brandon, 3D reconstruction of SOFC anodes using a focused ion beam lift-out technique, Chem. Eng. Sci. 64 (2009) 3928–3933.

[36] H. Iwai, N. Shikazono, T. Matsui, H. Teshima, M. Kishimoto, Quantification of SOFC anode microstructure based on dual beam FIB-SEM technique, J. Power Sources. 195 (2010) 955–961.

[37] E.M. Tory, B.H. Church, M.K. Tam, M. Ratner, Simulated random packing of equal spheres, Can. J. Chem. Eng. 51 (1973) 484–493.

[38] W.M. Visscher, M. Bolsterli, Random packing of equal and unequal spheres in two and three dimensions, Nature. 239 (1972) 504–507.

[39] W.S. Jodrey, E.M. Tory, Simulation of random packing of spheres, J. Simul. 32 (1979) 1–12.

[40] A. Bertei, Chapter 4 of this Thesis, 2013.

[41] Y. Shi, Y. Zhang, Simulation of random packing of spherical particles with different size distributions, Appl. Phys. A. 92 (2008) 621–626.

[42] R. Ben Aïm, P. Le Goff, Effet de paroi dans les empilements désordonnés de sphères et application à la porosité de mélanges binaires, Powder Technol. 1 (1968) 281–290.

[43] A. Bezrukov, M. Bargiel, D. Stoyan, Statistical analysis of simulated random packings of spheres, Part. Part. Syst. Charact. 19 (2002) 111–118.

[44] G.T. Nolan, P.E. Kavanagh, Computer simulation of random packing of hard spheres, Powder Technol. 72 (1992) 149–155.

[45] D. Bouvard, F.F. Lange, Relation between percolation and particle coordination in binary powder mixtures, Acta Metall. Mater. 39 (1991) 3083–3090.

[46] A. Bertei, C. Nicolella, A comparative study and an extended theory of percolation for random packings of rigid spheres, Powder Technol. 213 (2011) 100–108.

[47] K.D. Gibson, H.A. Scheraga, Volume of the intersection of three spheres of unequal size. A simplified formula, J. Phys. Chem. 91 (1987) 4121–4122.

[48] A. Einstein, Investigations on the theory of the Brownian movement, Dover, New York, 1926.

[49] L.M. Schwartz, J.R. Banavar, Transport properties of disordered continuum systems, Phys. Rev. B. 39 (1989) 11965–11970.

[50] J.M. Zalc, S.C. Reyes, E. Iglesia, The effects of diffusion mechanism and void structure on transport rates and tortuosity factors in complex porous structures, Chem. Eng. Sci. 59 (2004) 2947–2960.

[51] A. Berson, H.-W. Choi, J.G. Pharoah, Determination of the effective gas diffusivity of a porous composite medium from the three-dimensional reconstruction of its microstructure, Phys. Rev. E. 83 (2011) 026310.

[52] J.H. Hildebrand, An introduction to kinetic theory, Reinhold, New York, 1963.

[53] G. Marsaglia, Choosing a point from the surface of a sphere, Ann. Math. Stat. 43 (1972) 645–646.

[54] J. Greenwood, The correct and incorrect generation of a cosine distribution of scattered particles for Monte-Carlo modelling of vacuum systems, Vacuum. 67 (2002) 217–222.

[55] B.A. Wichmann, I.D. Hill, Algorithm AS 183: an efficient and portable pseudo-random number generator, J. R. Stat. Soc. Ser. C (Applied Stat. 31 (1982) 188–190.

[56] J.E. Gentle, Random number generation and Monte Carlo methods, Springer, New York, 2003.

[57] M. Knudsen, Die Gesetze der Molekularströmung und der inneren Reibungsströmung der Gase durch Röhren, Ann. Phys. 333 (1909) 75–130.

[58] E.H. Kennard, Kinetic theory of gases, McGraw-Hill, New York, 1938.

[59] N. Epstein, On tortuosity and the tortuosity factor in flow and diffusion through porous media, Chem. Eng. Sci. 44 (1989) 777–779.

[60] S. Torquato, Random heterogeneous materials: microstructure and macroscopic properties, Springer, New York, 2002.

[61] B. Lu, S. Torquato, Chord-length and free-path distribution functions for many-body systems, J. Chem. Phys. 98 (1993) 6472–6482.

[62] B. Derjaguin, Measurement of the specific surface of porous and disperse bodies by their resistance to the flow of rarefied gases, Prog. Surf. Sci. 45 (1994) 337–340.

[63] P. Levitz, Knudsen diffusion and excitation transfer in random porous media, J. Phys. Chem. 97 (1993) 3813–3818.

[64] M.S. Watanabe, Percolation with a periodic boundary condition: The effect of system size for crystallization in molecular dynamics, Phys. Rev. E. 51 (1995) 3945–3951.

[65] J.-P. Hovi, A. Aharony, Scaling and universality in the spanning probability for percolation, Phys. Rev. E. 53 (1996) 235–253.

[66] M. Masihi, P.R. King, P. Nurafza, Effect of anisotropy on finite-size scaling in percolation theory, Phys. Rev. E. 74 (2006) 042102.

[67] J. Hoshen, R. Kopelman, Percolation and cluster distribution. I. Cluster multiple labeling technique and critical concentration algorithm, Phys. Rev. B. 14 (1976) 3438–3445.

[68] B. Kenney, K. Karan, Engineering of microstructure and design of a planar porous composite SOFC cathode: A numerical analysis, Solid State Ionics. 178 (2007) 297–306.

[69] P.R. Shearing, Q. Cai, J.I. Golbert, V. Yufit, C.S. Adjiman, N.P. Brandon, Microstructural analysis of a solid oxide fuel cell anode using focused ion beam techniques coupled with electrochemical simulation, J. Power Sources. 195 (2010) 4804–4810.

[70] C. Kreller, M. Drake, S.B. Adler, H.-Y. Chen, H.-C. Yu, K. Thornton, et al., Modeling SOFC cathodes based on 3-D representations of electrode microstructure, ECS Trans. 35 (2011) 815–822.

[71] K. Matsuzaki, N. Shikazono, N. Kasagi, Three-dimensional numerical analysis of mixed ionic and electronic conducting cathode reconstructed by focused ion beam scanning electron microscope, J. Power Sources. 196 (2011) 3073–3082.

[72] T. Carraro, J. Joos, B. Rüger, A. Weber, E. Ivers-Tiffée, 3D finite element model for reconstructed mixed-conducting cathodes: I. Performance quantification, Electrochim. Acta. 77 (2012) 315–323.

[73] A. Bertei, Chapter 3 of this Thesis, 2013.

[74] G.M. Goldin, H. Zhu, R.J. Kee, D. Bierschenk, S.A. Barnett, Multidimensional flow, thermal, and chemical behavior in solid-oxide fuel cell button cells, J. Power Sources. 187 (2009) 123–135.

[75] M. Mogensen, S. Skaarup, Kinetic and geometric aspects of solid oxide fuel cell electrodes, Solid State Ionics. 86-88 (1996) 1151–1160.

[76] F.H. van Heuveln, H.J.M. Bouwmeester, Electrode properties of Sr-doped $LaMnO_3$ on yttria-stabilized zirconia. II. Electrode kinetics, J. Electrochem. Soc. 144 (1997) 134–140.

[77] A. Bertei, Chapter 2 of this Thesis, 2013.

[78] E.A. Mason, A.P. Malinauskas, Gas transport in porous media: the dusty-gas model, Elsevier, Amsterdam, 1983.

[79] D. Arnošt, P. Schneider, Dynamic transport of multicomponent mixtures of gases in porous solids, Chem. Eng. J. Biochem. Eng. J. 57 (1995) 91–99.

[80] M. Tassopoulos, D.E. Rosner, Simulation of vapor diffusion in anisotropic particulate deposits, Chem. Eng. Sci. 47 (1992) 421–443.

[81] V.N. Burganos, Gas diffusion in random binary media, J. Chem. Phys. 109 (1998) 6772–6779.

[82] W. Kast, C.-R. Hohenthanner, Mass transfer within the gas-phase of porous media, Int. J. Heat Mass Transf. 43 (2000) 807–823.

[83] O. Geier, S. Vasenkov, J. Karger, Pulsed field gradient nuclear magnetic resonance study of long-range diffusion in beds of NaX zeolite: Evidence for different apparent tortuosity factors in the Knudsen and bulk regimes, J. Chem. Phys. 117 (2002) 1935–1938.

[84] B. Todd, J.B. Young, Thermodynamic and transport properties of gases for use in solid oxide fuel cell modelling, J. Power Sources. 110 (2002) 186–200.

[85] J. Deseure, Y. Bultel, L. Dessemond, E. Siebert, Theoretical optimisation of a SOFC composite cathode, Electrochim. Acta. 50 (2005) 2037–2046.

[86] E. Siebert, A. Hammouche, M. Kleitz, Impedance spectroscopy analysis of La1-xSrxMnO3-yttria-stabilized zirconia electrode kinetics, Electrochim. Acta. 40 (1995) 1741–1753.

[87] E.P. Murray, T. Tsai, S.A. Barnett, Oxygen transfer processes in (La,Sr)MnO_3/Y_2O_3-stabilized ZrO_2 cathodes: an impedance spectroscopy study, Solid State Ionics. 110 (1998) 235–243.

[88] R. Radhakrishnan, A. V. Virkar, S.C. Singhal, Estimation of charge-transfer resistivity of $La_{0.8}Sr_{0.2}MnO_3$ cathode on $Y_{0.16}Zr_{0.84}O_2$ electrolyte using patterned electrodes, J. Electrochem. Soc. 152 (2005) A210–A218.

[89] W.Y. Lee, D. Wee, A.F. Ghoniem, An improved one-dimensional membrane-electrode assembly model to predict the performance of solid oxide fuel cell including the limiting current density, J. Power Sources. 186 (2009) 417–427.

[90] S. Farhad, F. Hamdullahpur, Optimization of the microstructure of porous composite cathodes in solid oxide fuel cells, AIChE J. 58 (2012) 1248–1261.

[91] A. Barbucci, M. Carpanese, A.P. Reverberi, G. Cerisola, M. Blanes, P.L. Cabot, et al., Influence of electrode thickness on the performance of composite electrodes for SOFC, J. Appl. Electrochem. 38 (2008) 939–945.

[92] W.W.M. Siu, S.H.-K. Lee, Effective conductivity computation of a packed bed using constriction resistance and contact angle effects, Int. J. Heat Mass Transf. 43 (2000) 3917–3924.

[93] A. Barbucci, M. Paola Carpanese, M. Viviani, N. Vatistas, C. Nicolella, Morphology and electrochemical activity of SOFC composite cathodes: I. Experimental analysis, J. Appl. Electrochem. 39 (2009) 513–521.

[94] A. Bertei, C. Nicolella, Percolation theory in SOFC composite electrodes: Effects of porosity and particle size distribution on effective properties, J. Power Sources. 196 (2011) 9429–9436.

[95] S.A. Barnett, J.S. Cronin, K. Yakal-Kremski, Studies of solid oxide fuel cell electrode evolution using 3D tomography, in: F. Lefebvre-Joud (Ed.), 10th Eur. SOFC Forum, Lucerne - Switzerland, 2012: pp. A0603–A0613.

[96] J.A. Currie, Gaseous diffusion in porous media. Part 2. - Dry granular materials, Br. J. Appl. Phys. 11 (1960) 318–324.

[97] W.J. Bosl, J. Dvorkin, A. Nur, A study of porosity and permeability using a lattice Boltzmann simulation, Geophys. Res. Lett. 25 (1998) 1475–1478.

[98] J.C.Y. Koh, A. Fortini, Prediction of thermal conductivity and electrical resistivity of porous metallic materials, Int. J. Heat Mass Transf. 16 (1973) 2013–2022.

[99] A. V. Gusarov, T. Laoui, L. Froyen, V.I. Titov, Contact thermal conductivity of a powder bed in selective laser sintering, Int. J. Heat Mass Transf. 46 (2003) 1103–1109.

[100] H.-W. Choi, A. Berson, J.G. Pharoah, S.B. Beale, Effective transport properties of the porous electrodes in solid oxide fuel cells, Proc. Inst. Mech. Eng. Part A J. Power Energy. 225 (2011) 183–197.

[101] D. Chen, Z. Lin, H. Zhu, R.J. Kee, Percolation theory to predict effective properties of solid oxide fuel-cell composite electrodes, J. Power Sources. 191 (2009) 240–252.

[102] N. Christiansen, S. Primdahl, M. Wandel, S. Ramousse, A. Hagen, Status of the solid oxide fuel cell development at Topsoe Fuel Cell A/S and Risø DTU, in: F. Lefebvre-Joud (Ed.), 10th Eur. SOFC Forum, Lucerne - Switzerland, 2012: pp. A0411–A0419.

[103] M. Bertoldi, O. Bucheli, S. Modena, A. V. Ravagni, Development and manufacturing of SOFC-based products at SOFCpower SpA, in: F. Lefebvre-Joud (Ed.), 10th Eur. SOFC Forum, Lucerne - Switzerland, 2012: pp. A0428–A0436.

[104] A. Mai, B. Iwanschitz, R. Denzler, U. Weissen, D. Haberstock, V. Nerlich, et al., Progress in the development of the Hexis' SOFC stack and the Galileo 1000 N micro-CHP system, in: F. Lefebvre-Joud (Ed.), 10th Eur. SOFC Forum, Lucerne - Switzerland, 2012.

[105] K. Haltiner, R. Kerr, Latest update on Delphi's solid oxide fuel cell stack for transportation and stationary applications, in: F. Lefebvre-Joud (Ed.), 10th Eur. SOFC Forum, Lucerne - Switzerland, 2012.

[106] B. Borglum, E. Tang, M. Pastula, Solid oxide fuel cell development at Versa Power Systems, in: F. Lefebvre-Joud (Ed.), 10th Eur. SOFC Forum, Lucerne - Switzerland, 2012: pp. A0513–A0517.

[107] C. Nicolella, A. Bertei, M. Viviani, A. Barbucci, Morphology and electrochemical activity of SOFC composite cathodes: II. Mathematical modelling, J. Appl. Electrochem. 39 (2008) 503–511.

[108] J. Myung, H.J. Ko, H. Park, M. Hwan, S. Hyun, Fabrication and characterization of planar-type SOFC unit cells using the tape-casting/lamination/co-firing method, Int. J. Hydrogen Energy. 37 (2012) 498–504.

[109] F. Tietz, H.-P. Buchkremer, D. Stöver, Components manufacturing for solid oxide fuel cells, Solid State Ionics. 152-153 (2002) 373–381.

[110] Q. Su, D. Yoon, Y.N. Kim, W. Gong, A. Chen, S. Cho, et al., Effects of interlayer thickness on the electrochemical and mechanical properties of bi-layer cathodes for solid oxide fuel cells, J. Power Sources. 218 (2012) 261–267.

[111] N.H. Menzler, F. Tietz, S. Uhlenbruck, H.P. Buchkremer, D. Stöver, Materials and manufacturing technologies for solid oxide fuel cells, J. Mater. Sci. 45 (2010) 3109–3135.

[112] H.S. Song, W.H. Kim, S.H. Hyun, J. Moon, J. Kim, H.-W. Lee, Effect of starting particulate materials on microstructure and cathodic performance of nanoporous LSM-YSZ composite cathodes, J. Power Sources. 167 (2007) 258–264.

[113] M. Shah, P.W. Voorhees, S.A. Barnett, Time-dependent performance changes in LSCF-infiltrated SOFC cathodes: The role of nano-particle coarsening, Solid State Ionics. 187 (2011) 64–67.

[114] J.S. Cronin, J.R. Wilson, S.A. Barnett, Impact of pore microstructure evolution on polarization resistance of Ni-Yttria-stabilized zirconia fuel cell anodes, J. Power Sources. 196 (2011) 2640–2643.

[115] W. Zhou, H. Shi, R. Ran, R. Cai, Z. Shao, W. Jin, Fabrication of an anode-supported yttria-stabilized zirconia thin film for solid-oxide fuel cells via wet powder spraying, J. Power Sources. 184 (2008) 229–237.

Chapter 8

Integrated Microstructural–Electrochemical Modeling of SOFC Cells

This Chapter presents an integrated microstructural–electrochemical model for cells in a SOFC stack. The microstructure of the electrodes (both functional layers and current collectors) is numerically reconstructed to evaluate the effective properties. The electrochemical model, applied in the whole cell and in the feeding channels, allows the prediction of the current–voltage behavior. The study focuses on anode–supported SOFCs produced by the Forschungszentrum Jülich.

The study shows that:

i. the integrated model allows a *from–powder–to–power* approach, validated by the good agreement with experimental data without any fitted parameter;

ii. the model allows the physical interpretation of the cell behavior revealing the contribution of each microscopic process in the macroscopic performance;

iii. practical design indications can be obtained by running the model.

This Chapter was adapted from the paper "Electrochemical simulation of planar solid oxide fuel cells with detailed microstructural modeling" by A. Bertei, J. Mertens and C. Nicolella, submitted to Electrochimica Acta in December 2013.

Abstract

A quasi–two–dimensional physically–based model for the description of transport and reaction in planar solid oxide fuel cells (SOFCs) is presented in this study. Electrochemistry and transport phenomena in the cell are locally described in 2D using mass conservation equations and well–established global electrokinetics, coupled with the 1D representation of gas channels in both co–flow and counter–flow configurations. The key feature of the model consists in the numerical reconstruction, through packing algorithms, of the three–dimensional microstructure of each porous layer for an accurate evaluation of the effective properties. Coupling of a detailed microstructural modeling into the cell–level electrochemical model allows the prediction of the polarization behavior from the knowledge of operating conditions and powder characteristics, thus eliminating the need for empirical correlations and adjusted parameters, which is typically the weak point of existing cell–level models. The framework is used for the simulation of a short stack of anode–supported cells with LSM–based cathode and 1.5mm thick anode support, developed and tested by Forschungszentrum Jülich. The effective properties of each layer are calculated and compared with available experimental data. A good agreement is also reached when comparing simulated and experimental polarization curves under different operating conditions without fitting any parameter. Simulations show that at 800°C the activation resistance in the cathode functional layer is the main contribution to the cell overpotential. In addition, the model suggests that gas concentration effects at the anode play an important role on the global electrochemical response. The study shows that quantitative predictions can be obtained using this integrated approach, making it an attractive tool to assist the SOFC development.

8.1 Introduction

Solid oxide fuel cells (SOFCs) are energy conversion devices which offer clear advantages if compared with conventional power systems, such as low emission of pollutants [1], high efficiency [2] and fuel flexibility [3], making them attractive for use in both stationary and mobile applications [4]. Recent advances in manufacturing techniques and improvements in cell lifetime have led this technology close to be launched on the market [5–7].

SOFC development is currently assisted by modeling and simulation techniques [8], which help researchers to understand the complex interactions between electrochemical phenomena and material properties over different length scales [9]. In particular, much efforts have been done to model the electrochemical behavior of cells within a stack [10,11]. Cell–level models describe the chemical and electrochemical phenomena occurring within an SOFC, with the goal to relate the global cell response (e.g., the cell current–voltage characteristic) to the microscopic processes occurring within the cell components, such as the transport of reactants and products within the pores of the electrodes and the local kinetic electrochemical phenomena. This allows researchers to interpret the experimental results and to predict the system performance.

Several cell–level models have been developed in the past. Aguiar et al. [12] proposed a dynamic model for anode–supported SOFCs, consisting of mass and energy balances applied on the fuel and air channels. Zhu et al. [11] and Janardhanan and Deutschmann [13] adopted a continuum approach based on local balance equations in the membrane–electrode assembly, focusing on the elementary kinetics of internal reforming. A similar approach was adopted by Bessler et al. [14], who presented a physically–based modeling framework for the description of kinetics and transport of species over different length scales. Specific studies were performed by Pramuanjaroenkij et al. [15], who investigated the effect of the electrolyte thickness on the cell current–voltage characteristic, and by Andersson et al. [16], who considered the electrochemical reactions spread on the active three–phase boundaries within the electrode volume in order to identify the extension of the reaction zones.

In all the models mentioned above, the microstructure of porous electrodes was represented with less detail than chemical and electrochemical phenomena, so that effective properties, such as the tortuosity of the gas phase or the effective electric conductivity, were evaluated with simplified percolation models or empirical correlations [17,18] if not treated as fitting parameters to match experimental results [8]. In this way, unrealistic values could be assumed or the properties could be not representative of the microstructure corresponding to the sample characteristics, eventually nullifying the efforts made in the description of complex electrochemical phenomena [19]. In fact, particle–based models [20] and even simple percolation models [17] suggest that the cell global electrochemical performance is significantly affected by microstructural characteristics [21], as also supported by experimental evidences [22–24]. Therefore, an integrated approach, which incorporates a detailed microstructural description of electrodes, can represent an improvement in the cell–level modeling, as shown for electrodes in button cell configuration in Chapter 7.

In this context, models in which transport and reaction equations are solved within an electrode microstructure reconstructed with tomographic techniques [25–27] satisfy the need for a detailed morphological description. However, this method is not predictive since existing samples are required. Moreover, to date the computational effort is too high to implement such an approach for a whole cell within a stack.

In this study, a mechanistic quasi–2D cell–level model incorporating a detailed microstructural description of porous composite electrodes is presented. The microstructure of the electrodes is numerically reconstructed in three dimensions with packing algorithms, providing the effective properties needed by the electrochemical cell–level model with reduced or no adjustable or fitted morphological parameters. The framework, although general in its description, is applied to study the anode–supported planar cells produced by the Forschungszentrum Jülich in F–design, with LSM–YSZ cathode and Ni–YSZ anode, which are among the most efficient, reliable and well–characterized cells produced nowadays [28].

The study is organized as follows. In Section 8.2 the modeling approach is presented, describing both the microstructural model and the electrochemical model. Results from the microstructural modeling are discussed in Section 8.3 while in Section 8.4 the electrochemical results are reported. General conclusions are summarized in Section 8.5.

8.2 Modeling

Figure 8.1 represents a generic planar anode–supported cell, composed of an anode supporting layer, an anode functional layer, an electrolyte, a cathode functional layer and a cathode current collector. Figure 8.1 also shows the gas channels at both sides of the cell, which provide hydrogen and oxygen to the anodic and cathodic compartments, respectively.

During cell operation, hydrogen and oxygen are consumed along the channel length to take part to the electrochemical reactions occurring within the electrodes. Perpendicularly to the gas flow in the channels, hydrogen and oxygen permeate through the porous structures of the anode and the cathode, respectively, to react as follows:

$$H_{2(g)} + O^{2-}_{(io)} \rightarrow H_2O_{(g)} + 2e^{-}_{(ela)} \tag{8.1}$$

$$\frac{1}{2}O_{2(g)} + 2e^{-}_{(elc)} \rightarrow O^{2-}_{(io)} \tag{8.2}$$

Note that in Eqs. (8.1) and (8.2) composite electrodes are assumed: mixed ionic–electronic conductors are not considered in this study.

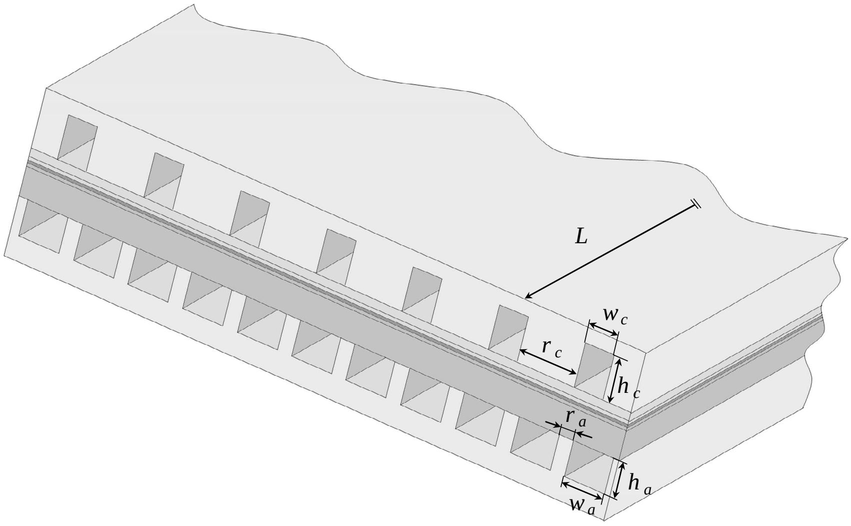

Figure 8.1 – Representation of the cell geometry modeled in this study, with the cathodic side represented at the top and the anodic side at the bottom. The dimensions of gas channels and interconnect ribs are indicated. The thickness of the five cell layers is not to scale for visualization purposes.

In composite electrodes, both the anodic and cathodic electrochemical reactions are supposed to occur in the proximity of the three–phase boundary (TPB) among the porous phase, the electron–conducting phase and the ion–conducting phase [29,30]. The TPB sites are spread in the volume of the cathode and anode functional layers. Oxygen ions are produced at the cathode and transported, through the electrolyte, towards the anode, wherein they are consumed. Electrons, flowing in the external circuit from the anode to the cathode, reach/leave the TPB sites passing through the interconnect ribs and the electronic paths within the cathode current collector and the anode supporting layer. In a planar cell the current globally flows perpendicularly to the gas flow in the channels.

Focusing on cell compartments, while the electrolyte is a dense layer of a ion–conducting ceramic material such as yttria–stabilized zirconia (YSZ) [31], the other four layers are porous in order to allow the transport of gas species. The cathode and anode functional layers are composite layers, made of an ion–conducting phase (the same of the electrolyte) and an electron–conducting phase, typically nickel at the anode [32,33] and strontium–doped lanthanum manganite (LSM) at the cathode [30,34]. The particles of the electron–conducting and ion–conducting materials are randomly mixed and sintered to extend the TPB length [3,29,30].

In an anode–supported SOFC, the anode supporting layer has the main aim to mechanically support the cell while providing high electric conductivity and gas permeability [33,35]. The materials are the same of the anode functional layer in order to ensure a small mismatch in the expansion coefficient [36], although higher porosity and coarser particles are typically adopted [37,38]. Similarly to the anode supporting layer, the cathode current collector is characterized by high permeability and electric conductivity, serving as gas and current distributor to the cathode functional layer [24,39], but its thickness is significantly lower than that of the anode supporting layer.

The cell configuration described above has been the standard design (F–design) adopted by the Forschungszentrum Jülich as a benchmark for testing purposes and stationary applications in the last ten years [40,41]. The same design is considered in the model presented in the following Sections.

8.2.1 Microstructural modeling

The goal of the microstructural model is the evaluation of the morphological properties of the electrodes starting from the powder characteristics. It consists of a packing algorithm to numerically reconstruct the microstructure of the electrodes in three dimensions (Section 8.2.1.1) and a Monte Carlo method to evaluate the effective properties (Section 8.2.1.2). The resulting effective properties are used as input parameters in the electrochemical model.

8.2.1.1 Structure generation

According to the description provided in Section 8.2, the electrodes can be fairly represented as random packings of overlapping spherical particles, as also assumed by several modeling studies [17,20,42–45]. Virtual samples of electrode microstructures are generated through a packing algorithm known as drop–and–roll algorithm [46,47]. Only a brief description of the method is summarized in this Section, as full details of the implementation and algorithm validation are reported in previous Chapters [19,48].

The algorithm mimics the deposition of spherical particles within a box of specified dimensions by sequentially dropping spheres from a random location at the top of the domain. Each falling particle rolls over one or two already placed particles without inertia or friction until a stable position on the top of three particles or on the floor is reached. The procedure is repeated by dropping new particles until the domain is completely filled. For binary mixtures, the type and size of each incoming particle are selected before dropping the sphere according to a weighted probability corresponding to the electrode composition. In order to extinguish wall and floor effects, periodic boundary conditions are applied in the horizontal directions while a layer of six particle diameters is removed from the top and the bottom of the domain [46,49].

The densification introduced by the sintering process is simulated by partly overlapping the particles. The degree of particle overlap is tailored through the definition of a maximum angle of contact among the particles, kept constant throughout the structure during the packing generation [48]. However, the sintering process can also lead to produce electrodes with large porosity (say, greater than 40%, as in the cathode of the present study) when pore–formers and other organic additives are added to the powders before the electrode deposition [50,51]. Pore–formers are represented in the algorithm as spherical particles, dropped during the packing generation, which eventually vanish leaving holes in the final structure [42,43,52]. After the disappearance of pore–former particles the algorithm also checks if the structure is mechanically stable, that is, if there are not unstable particles [48]. In all the structures generated in this study the stability criterion is met. The angle of contact and the pore–former volume fraction contribute to determine the packing porosity: lowering the angle of contact while increasing the amount of pore–formers lead to increase the electrode porosity as discussed in previous Chapters [19,48].

A particular characteristic of the anode microstructure is represented by the morphological modifications introduced by the reduction of nickel oxide into nickel. Ni–YSZ cermet anodes are usually prepared by mixing the YSZ powder with a precursor of nickel, such as nickel oxide, reduced to nickel upon exposure to fuel gases [33,37,38]. The same procedure is mimicked by the algorithm: first the 'green' anode microstructure is generated by sequentially dropping NiO and YSZ particles, then NiO particles are shrunk, keeping fixed their center coordinates, by a factor which accounts for both the mass and density change related to the reduction to nickel. The resulting structure is considered as representative of the anode microstructure.

Although the algorithm presents some features specifically tailored for the conducting materials considered in this study, it is sufficiently general to numerically reconstruct the microstructure of the porous layers, composite or not, adopted in SOFCs, independently of the material, particle size and porosity.

8.2.1.2 Structure analysis

The numerically reconstructed electrodes generated with the packing algorithm described in Section 8.2.1.1 are analyzed to obtain the effective transport and geometrical properties of interest. Only a brief summary of the methods employed are reported here, more details can be found in the previous Chapter of this thesis.

The effective transport properties, such as the gas phase effective diffusivity and the effective electric conductivity, are evaluated in each reconstructed layer through a Monte Carlo random–walk method [53,54]. For the calculation of the effective gas diffusivity, thousands of tracers are generated within the pores, wherein they move following a Brownian motion. At each movement each tracer moves of the free path, chosen from an exponential probability distribution centered on the mean free path. When a tracer hits a particle, it is reflected on the particle surface according to the Knudsen cosine law [55]. As soon as the tracer has covered a prescribed distance, the displacement between the initial and final tracer positions is measured. The effective diffusivity is evaluated from the mean square displacements of thousands of tracers by applying the Einstein equation [56]. In addition, the tortuosity factor of the gas phase can be easily derived from the ratio between porosity and effective diffusivity [53]. The same approach is adopted to calculate the effective electric conductivity of the electron–conducting and ion–conducting phases, but in such a case tracers randomly move within percolating particles of each conducting phase. In addition, an elastic reflection law is used when tracers hit the particle external surface or the boundary with particles of different phase [19].

Other geometrical properties can be extracted from the reconstructed layers. The pore size distribution is determined through the chord length method, that is, by randomly drawing chords in the pore space among solid particles [54]. According to Zalc et al. [53], the mean pore size is calculated from the number–averaged chord length corrected by the statistics of the chord distribution and the nature of the tracer redirecting collisions.

In composite layers, such as the anode and cathode functional layers, the TPB length is calculated as the contact perimeter between electron–conducting and ion–conducting particles [20,52]. The computation is performed by generating test points on the perimeter of the plane of intersection connecting two particles of different type. The test point, representative of a fraction of the perimeter length, is accounted for the TPB calculation if it does not belong to a third particle. The procedure is repeated for all the pairs of contacting particles of different type. In particular, only the TPB length generated by percolating electron–conducting and ion–conducting particles is considered since only the connected TPB is potentially active for the electrochemical reactions [30,52].

The methods described above allow an accurate and coherent prediction of all the effective properties required by the electrochemical model, which is presented in the following Section.

8.2.2 Electrochemical modeling

The electrochemical model describes the transport and reaction of species in the cell and feeding channels through conservation equations. Although some researchers solve mass and charge balances directly in the three–dimensional reconstructed electrodes [25–27], in this study the conservation equations are written adopting the continuum approach [57,58] in order to minimize the computational cost. In the continuum approach the porous nature of the electrodes is described as a homogeneous continuum, with particle–level detail represented through effective properties, assumed uniform within each layer and evaluated using the microstructural model described in Section 8.2.1.

The whole three–dimensional structure of the stack, as depicted in Figure 8.1, is not represented in the electrochemical model: only a 2D slice of a cell along the length *L*, representative of the repeating unit of the SOFC system [15,16], is considered. Furthermore, the gas flow in the channels is modeled in one dimension because, due to their small height and width, the transversal phenomena are usually negligible if compared with the transport along the longitudinal direction [14,59]. The resulting computational domain of the electrochemical model is schematized in Figure 8.2. Although the reduction of the problem from a three–dimensional to a quasi–two–dimensional one does not allow the model to capture some details, such as the uneven distribution of gases and current under the ribs [39,60], this simplification represents a reasonable compromise to substantially reduce the computational cost while considering the main characteristic phenomena occurring in the system.

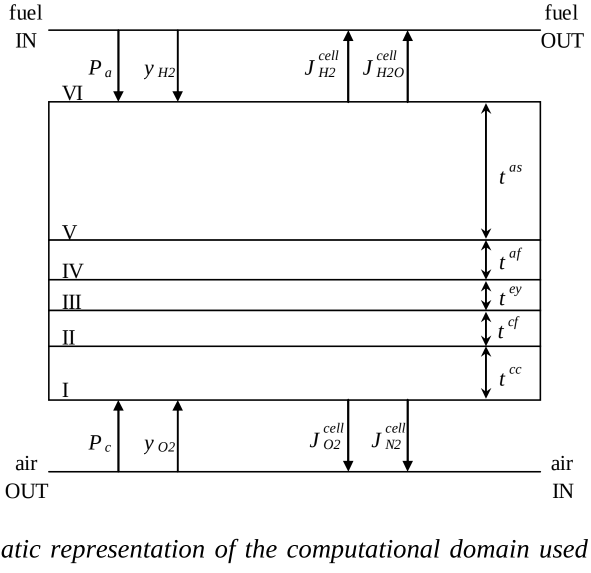

Figure 8.2 – Schematic representation of the computational domain used in this study: 2D for the cell, 1D for the gas channels (counter–flow configuration). The thickness of each layer in the cell is indicated, as well as the coupling of boundary conditions at the cell–channel interfaces.

The electrochemical model consists of a set of mass and charge balance equations describing the transport and reaction phenomena occurring within the cell and the channels. For the purposes of this study, steady–state conditions are considered. In addition, uniform temperature is assumed throughout the cell due to the small size of the stack investigated, as experimentally verified by Bertoldi et al. [61], whose set up is considered in this study as discussed in Section 8.4.

The conservation equations for the reacting species within the cell and the channels are reported, respectively, in Sections 8.2.2.1 and 8.2.2.2, while Section 8.2.2.3 provides the boundary conditions needed to couple the cell to the channels.

8.2.2.1 Transport and reaction in the cell

Within the cell, hydrogen is consumed at the anode side according to Eq. (8.1) while, at the cathode, molecular oxygen is converted into oxygen ions as in Eq. (8.2). Since composite electrodes are considered, both the reactions are assumed to occur at the TPBs of electron–conducting and ion–conducting particles spread in the functional layers [16,29,57]. In this Section, the balance equations for anode, electrolyte and cathode are presented.

The set of equations Eqs. (8.3a–8.6a) represents the mass and charge balances for the species participating to hydrogen oxidation (Eq. (8.1)) in the anode, which are hydrogen (*H2*), gaseous water (*H2O*), electrons (*e*) and oxygen ions (*O*). The corresponding molar fluxes are reported in Eqs. (8.3b–8.6b).

$$\nabla \cdot \underline{J}_{H2} = -\frac{i_a \lambda_{TPB}^{af}}{2F} \tag{8.3a}$$

$$\underline{J}_{H2}\left(\frac{1}{D_{K,H2}^{eff,af}} + \frac{1-y_{H2}}{D_{H2/H2O}^{eff,af}}\right) = \\ = \frac{y_{H2}}{D_{H2/H2O}^{eff,af}}\underline{J}_{H2O} - \frac{P_a}{RT}\nabla y_{H2} - \frac{y_{H2}}{RT}\left(1+\frac{B^{af}}{D_{K,H2}^{eff,af}}\frac{P_a}{\mu_a}\right)\nabla P_a \tag{8.3b}$$

$$\nabla \cdot \underline{J}_{H2O} = \frac{i_a \lambda_{TPB}^{af}}{2F} \tag{8.4a}$$

$$\underline{J}_{H2O}\left(\frac{1}{D_{K,H2O}^{eff,af}} + \frac{y_{H2}}{D_{H2/H2O}^{eff,af}}\right) = \\ = \frac{1-y_{H2}}{D_{H2/H2O}^{eff,af}}\underline{J}_{H2} + \frac{P_a}{RT}\nabla y_{H2} - \frac{1-y_{H2}}{RT}\left(1+\frac{B^{af}}{D_{K,H2O}^{eff,af}}\frac{P_a}{\mu_a}\right)\nabla P_a \tag{8.4b}$$

$$\nabla \cdot \underline{J}_e = \frac{i_a \lambda_{TPB}^{af}}{F} \tag{8.5a}$$

$$\underline{J}_e = \frac{\sigma_{ela} \kappa_{ela}^{eff,af}}{F} \nabla V_{ela} \tag{8.5b}$$

$$\nabla \cdot \underline{J}_O = -\frac{i_a \lambda_{TPB}^{af}}{2F} \tag{8.6a}$$

$$\underline{J}_O = \frac{\sigma_{io} \kappa_{io}^{eff,af}}{2F} \nabla V_{io} \tag{8.6b}$$

The equations are written for the anode functional layer (superscript *af*), although the same equations hold also for anode supporting layer (change the superscripts with *as*).

The terms in the right side of Eqs. (8.3a–8.6a) account for the consumption and production of species at the TPB according to Eq. (8.1). The term λ_{TPB}^{af} represents the TPB length per unit volume, evaluated as described in Section 8.2.1.2, while i_a is the current density per unit of TPB length, whose kinetic expression is discussed at the end of this Section. A positive current density is considered when hydrogen is consumed and water is produced.

The transport of charged species, Eqs. (8.5b–8.6b), is assumed to follow the Ohm's law [14,17,57]. Effective conductivities for both electron–conducting and ion–conducting phases are considered by multiplying the bulk conductivity of pure materials by the normalized conductivity factors, evaluated according to Section 8.2.1.2. Note that no mixed ionic–electronic conduction is considered, as commonly accepted for the couple of materials (i.e., Ni and YSZ) considered in this study [17,29,57].

The molar fluxes of gas species within the pores, Eqs. (8.3b–8.4b), are calculated using the dusty–gas model [62–64] as a function of pressure and hydrogen molar fraction. The dusty–gas model takes into account both diffusion (both ordinary and Knudsen diffusion) and convection. Ideal gas behavior is assumed for both hydrogen and water according to the high temperature and relatively low pressure [59]. Effective diffusion coefficients are calculated correcting for the porosity and tortuosity factor of the gas phase as follows:

$$D_{H2/H2O}^{eff,af} = \frac{\phi^{af}}{\tau^{af}} D_{H2/H2O}^{af} \tag{8.7}$$

$$D_{K,s}^{eff,af} = \frac{\phi^{af}}{\tau^{af}} \frac{1}{3} d_{pore}^{af} \sqrt{\frac{8RT}{\pi M_s}} \quad \text{with } s = H2, H2O \tag{8.8}$$

where the binary diffusion coefficient is evaluated using the Fuller correlation [65]. The permeability coefficient B^{af} is calculated as [19]:

$$B^{af} = \frac{\phi^{af}}{\tau^{af}} \frac{\left(d_{pore}^{af}\right)^2}{32} \tag{8.9}$$

where the mean pore size is evaluated according to Section 8.2.1.2.

A similar approach is adopted at the cathode side, where balance equations for molecular oxygen (*O2*), nitrogen (*N2*), electrons (*e*) and oxygen ions (*O*) are considered according to the stoichiometry of the oxygen reduction reaction in Eq. (8.2). The set of balance equations, written for the cathode functional layer (superscript *cf*), is reported in Eqs. (8.10a–8.13a) as follows:

$$\nabla \cdot \underline{J}_{O2} = -\frac{i_c \lambda_{TPB}^{cf}}{4F} \tag{8.10a}$$

$$\underline{J}_{O2} \left(\frac{1}{D_{K,O2}^{eff,cf}} + \frac{1 - y_{O2}}{D_{O2/N2}^{eff,cf}} \right) =$$

$$= \frac{y_{O2}}{D_{O2/N2}^{eff,cf}} \underline{J}_{N2} - \frac{P_c}{RT} \nabla y_{O2} - \frac{y_{O2}}{RT} \left(1 + \frac{B^{cf}}{D_{K,O2}^{eff,cf}} \frac{P_c}{\mu_c} \right) \nabla P_c \tag{8.10b}$$

$$\nabla \cdot \underline{J}_{N2} = 0 \tag{8.11a}$$

$$\underline{J}_{N2} \left(\frac{1}{D_{K,N2}^{eff,cf}} + \frac{y_{O2}}{D_{O2/N2}^{eff,cf}} \right) =$$

$$= \frac{1 - y_{O2}}{D_{O2/N2}^{eff,cf}} \underline{J}_{O2} + \frac{P_c}{RT} \nabla y_{O2} - \frac{1 - y_{O2}}{RT} \left(1 + \frac{B^{cf}}{D_{K,N2}^{eff,cf}} \frac{P_c}{\mu_c} \right) \nabla P_c \tag{8.11b}$$

$$\nabla \cdot \underline{J}_e = -\frac{i_c \lambda_{TPB}^{cf}}{F} \tag{8.12a}$$

$$\underline{J}_e = \frac{\sigma_{elc} \kappa_{elc}^{eff,cf}}{F} \nabla V_{elc} \tag{8.12b}$$

$$\nabla \cdot \underline{J}_O = \frac{i_c \lambda_{TPB}^{cf}}{2F} \tag{8.13a}$$

$$\underline{J}_O = \frac{\sigma_{io}\kappa_{io}^{eff,cf}}{2F}\nabla V_{io} \tag{8.13b}$$

The terms on the right side of Eqs. (8.10a–8.13a) represent the source terms, which are positive when oxygen is consumed. This sign convention is coherent with the one used at the anode: positive current for both hydrogen and oxygen consumption. Similarly to what done for the anode, the transport of charged species (Eqs. (8.12b–8.13b)) follows the Ohm's law and the gas transport (Eqs. (8.10b–8.11b)) is described by the dusty–gas model. In particular, Eqs. (8.7–8.9) are applied to evaluate the diffusion coefficients for oxygen and nitrogen as well as the permeability considering the effective properties of the cathode functional layer.

The same set of balance and transport equations Eqs. (8.10–8.13) is considered also for the cathode current collector layer (change the superscript *cf* with *cc*), although with some simplifications. Indeed, the current collector is a porous layer of electron–conducting phase only [24,39,66,67], therefore the balance equation for oxygen ions in the ion–conducting phase (Eq. (8.13)) is not considered. In addition, no TPB is present, therefore all the source terms in the right sides of Eqs. (8.10a–8.12a) are set to 0.

The only phenomenon occurring in the electrolyte is the transport of oxygen ions and no reaction occurs within this layer. Therefore, the mass conservation equation for oxygen ions results as follows:

$$\nabla \cdot \underline{J}_O = 0 \tag{8.14a}$$

$$\underline{J}_O = \frac{\sigma_{io}}{2F}\nabla V_{io} \tag{8.14b}$$

Note that, similarly to Eqs. (8.6b) and (8.13b), Eq. (8.14b) describes the charge transport in a dense medium according to the Ohm's law.

The final considerations for the cell model regard the kinetic expressions for the evaluation of the current densities i_a and i_c for both the anode and the cathode. For the specific materials considered in this study, i.e., Ni and YSZ at the anode and LSM and YSZ at the cathode, detailed reaction mechanisms have been proposed in the past by several research groups, see for example Refs. [11,58,68–70] for hydrogen oxidation reaction and Refs. [30,71,72] for oxygen reduction reaction. However, for the purpose of this study, detailed electrochemical kinetics are not required. Instead, global reaction kinetics are used, which often work remarkably well in cell–level models [73].

The reaction rate of the hydrogen oxidation reaction at the cermet Ni–YSZ anode is assumed to follow the global expression proposed by Goodwin et al. [73], reported in Eq. (8.15). Such an expression is the refinement of a reaction scheme proposed by the same group in previous studies [11,57], which is similar to the one used by De Boer [74] according to the authors. The reaction mechanism includes five elementary reactions and it is simplified to a global expression assuming the hydrogen spillover as the rate–determining step [11,73]. The global expression was satisfactorily validated with experimental data obtained in patterned electrodes by Mizusaki et al. [75], showing a good agreement especially for typical conditions of fuel cell operation [73].

$$i_a = i_{a0}\left\{\exp\left((1+\alpha_a)\frac{F\eta_a}{RT}\right)-\exp\left(-\beta_a\frac{F\eta_a}{RT}\right)\right\} \tag{8.15a}$$

$$i_{a0} = i_{a0}^{ref}\exp\left[-\frac{E_a^{act}}{R}\left(\frac{1}{T}-\frac{1}{T_a^{ref}}\right)\right]\frac{\left(\dfrac{P_a y_{H2}}{P_{H2}^*}\right)^{\frac{1-\alpha_a}{2}}\left(\dfrac{P_a(1-y_{H2})}{1.013\cdot 10^5}\right)^{\frac{1+\alpha_a}{2}}}{1+\left(\dfrac{P_a y_{H2}}{P_{H2}^*}\right)^{0.5}} \tag{8.15b}$$

$$\eta_a = -\frac{RT}{2F}\ln\left(\frac{y_{H2,IN}}{y_{H2}}\frac{1-y_{H2}}{1-y_{H2,IN}}\right)-(V_{io}-V_{ela}) \tag{8.15c}$$

$$P_{H2}^* = \frac{A_{des}\Gamma^2\sqrt{2\pi RTM_{H2}}}{\gamma_0}\exp\left(-\frac{E_{des}}{RT}\right) \tag{8.15d}$$

Going into the details, Eq. (8.15a) represents a modified Butler–Volmer expression, in which the current density depends on the anodic activation overpotential η_a. The activation overpotential, reported in Eq. (8.15c), accounts for the potential drop between ion–conducting and electron–conducting phase as well as the equilibrium potential step [14], which depends on the local gas concentration in comparison with the open–circuit conditions, equal to the inlet conditions in the fuel channel [76]. The exchange current density i_{a0} depends on the local oxygen and water partial pressures as in Eq. (8.15b), where P_{H2}^* represents a reference pressure representative of the hydrogen adsorption/desorption equilibrium [11]. Note that the kinetic expression Eq. (8.15a) is written in the direction of positive current density (i.e., water production) for positive activation overpotential.

A similar approach is used at the composite LSM–YSZ cathode for the description of the oxygen reduction reaction. The global kinetic expression proposed by Kenney and Karan [39] is used in this work, as summarized in Eq. (8.16). Such an expression comes from the mechanism proposed by van Heuveln and Bouwmeester [72], who performed measurements in patterned electrodes in a wide range of experimental conditions. As discussed in the previous Chapter of this thesis [19], the kinetic expression in Eq. (8.16) generally agrees with the global kinetics proposed by Radhakrishnan et al. [71] as used by Nam and Jeon [18].

$$i_c = i_{c0}\left\{\exp\left(\alpha_c \frac{F\eta_c}{RT}\right) - \exp\left(-\beta_c \frac{F\eta_c}{RT}\right)\right\} \tag{8.16a}$$

$$i_{c0} = i_{c0}^{ref}\,\exp\left[-\frac{E_c^{act}}{R}\left(\frac{1}{T} - \frac{1}{T_c^{ref}}\right)\right]\left(\frac{P_c y_{O2}}{P_{O2}^{ref}}\right)^{\varsigma} \tag{8.16b}$$

$$\eta_c = -\frac{RT}{4F}\ln\left(\frac{P_{c,IN}\, y_{O2,IN}}{P_c y_{O2}}\right) - \left(V_{elc} - V_{io}\right) \tag{8.16c}$$

Eq. (8.16a) represents a Butler–Volmer expression where the exchange current density depends on the local oxygen partial pressure (Eq. (8.16b)) while the activation overpotential (Eq. (8.16c)) comprises both the potential difference between conducting phases and the equilibrium potential step. The sign convention used in Eq. (8.16a) is coherent with the one used in Eq. (8.15a), that is, a positive activation overpotential leads to a positive current density representative of oxygen consumption.

Therefore, both the kinetic expressions adopted in this study, Eqs. (8.15) and (8.16), come from the selection of reliable complete reaction schemes found in the literature reduced to global kinetics, derived and validated in patterned electrodes. Note that while the electrochemical model proposed in Eqs. (8.3–8.14) is generally valid for SOFCs with porous composite electrodes with no mixed ionic/electronic conduction, the kinetic expressions in Eqs. (8.15) and (8.16) are strictly valid for the couples of materials considered in this study, that is Ni–YSZ and LSM–YSZ.

8.2.2.2 Transport in channels

Within the fuel and air channels, gases are transported along the channel length and permeate transversely into the electrodes to participate to the electrochemical reactions. As already discussed in Section 8.2.2, channels are represented in one dimension because only the phenomena occurring along the longitudinal direction (*x*) are relevant. In particular, channels with rectangular cross–section are considered (see Figure 8.1).

The conservation equations related to the anode channel are represented by the set of partial differential equations in Eqs. (8.17–8.19), comprising the conservation of mass, hydrogen and momentum as follows:

$$\frac{d\tilde{J}_a}{dx}=\frac{w_a+r_a}{w_a h_a}\left(J_{H2}^{cell}M_{H2}+J_{H2O}^{cell}M_{H2O}\right) \tag{8.17a}$$

$$\tilde{J}_a=\rho_a v_a \tag{8.17b}$$

$$\frac{d\tilde{J}_{H2,a}}{dx}=\frac{w_a+r_a}{w_a h_a}J_{H2}^{cell}M_{H2} \tag{8.18a}$$

$$\tilde{J}_{H2,a}=\rho_a v_a \tilde{y}_{H2}-D_{H2/H2O}\left(1+Pe_a^2\frac{\delta_a}{210}\right)\rho_a\frac{d\tilde{y}_{H2}}{dx} \tag{8.18b}$$

$$\frac{d}{dx}\left(\rho_a {v_a}^2-\frac{4}{3}\mu_a\frac{dv_a}{dx}\right)=-\frac{dP_a}{dx}-\frac{2(w_a+h_a)}{w_a h_a}\tau_{w,a} \tag{8.19}$$

Both the conservation equations of mass and hydrogen, written on mass basis (note the ˜ over the fluxes), account for the local exchange of hydrogen and water with the cell on the right side of Eqs. (8.17a) and (8.18a). As discussed later in Section 8.2.2.3, J_{H2}^{cell} and J_{H2O}^{cell} represent the molar fluxes of hydrogen and water, respectively, coming out from the anode supporting layer (i.e., positive flux if oriented from the cell towards the channel). The term $(w_a+r_a)/(w_a h_a)$ plays as a geometric correction term [14,59], which takes into account that while the hydrogen oxidation (and therefore the generation of the fluxes J_{H2}^{cell} and J_{H2O}^{cell}) occurs in the whole cell width, anode channels occupy only a fraction $w_a/(w_a+r_a)$ of the cell width, as represented in Figure 8.1.

The mass flux of hydrogen in Eq. (8.18b) takes into account both convection and diffusion, the latter sometimes erroneously neglected in cell–level models [11,12,77,78] as pointed out by Bessler and Gewies [59]. In addition to the Fick diffusion, Eq. (8.18b) accounts also for the Taylor–Aris axial dispersion [79,80] in rectangular ducts for laminar flow, where the Peclet number is calculated as follows [81]:

$$Pe_a=\frac{v_a\min(w_a,h_a)}{D_{H2/H2O}} \tag{8.20}$$

and the dimensionless factor δ_a, under the dilute mixture assumption, depends only on the h_a/w_a ratio as in Dutta et al. [81].

Eq. (8.19) represents the momentum equation for a compressible flow. Due to the small Reynolds numbers during normal operation, the gas flow is in laminar regime, as anticipated during the description of Eq. (8.18b). In these conditions, the shear–stress factor at the wall $\tau_{w,a}$ on the right side of Eq. (8.19) can be calculated as [59]:

$$\tau_{w,a} = \frac{1}{8}\frac{2(w_a + h_a)}{w_a h_a}(\mathrm{Re}\, f)_a \mu_a v_a \tag{8.21}$$

where the product between Reynolds number and friction factor (*Ref*)$_a$ is calculated as a function of the height over width ratio h_a/w_a and local wall Reynolds number according to Yuan et al. [82]. The wall Reynolds number $Re_{w,a}$, reported in Eq. (8.22), represents the dimensionless injection velocity of water and hydrogen on the channel wall at the interface with the anode supporting layer. Note that the wall Reynolds number is different from the Reynolds number Re_a, which describes the flow regime in the channel.

$$\mathrm{Re}_{w,a} = \frac{w_a + r_a}{w_a}\left(J_{H2}^{cell} M_{H2} + J_{H2O}^{cell} M_{H2O}\right)\frac{D_{h,a}}{\mu_a} \quad \text{with} \quad D_{h,a} = 4\frac{w_a h_a}{2(w_a + h_a)} \tag{8.22}$$

In Eq. (8.22), $D_{h,a}$ represents the channel hydraulic diameter. The dynamic viscosity of the gas mixture μ_a in Eqs. (8.19), (8.21) and (8.22) is calculated with the Herning and Zipperer method according to the local gas composition [65].

The same approach is used for the conservation of mass, oxygen and momentum in the cathode channel. For the sake of completeness, the full set of conservation equations Eqs. (8.23–8.25) is reported below. The sign convention is for a co–flow configuration while equations for a counter–flow configuration can be obtained from Eqs. (8.23–8.25) by changing the sign of each term in a spatial derivative. The definitions of Peclet number Pe_c, shear–stress factor at the wall $\tau_{w,c}$ and wall Reynolds number $Re_{w,c}$ are not reported because they can be easily derived from Eqs. (8.20–8.22) by substituting the subscripts *a*, *H2* and *H2O* with *c*, *O2* and *N2*.

$$\frac{d\tilde{J}_c}{dx} = \frac{w_c + r_c}{w_c h_c}\left(J_{O2}^{cell} M_{O2} + J_{N2}^{cell} M_{N2}\right) \tag{8.23a}$$

$$\tilde{J}_c = \rho_c v_c \tag{8.23b}$$

$$\frac{d\tilde{J}_{O2,c}}{dx} = \frac{w_c + r_c}{w_c h_c} J_{O2}^{cell} M_{O2} \tag{8.24a}$$

$$\tilde{J}_{O2,c} = \rho_c v_c \tilde{y}_{O2} - D_{O2/N2}\left(1 + Pe_c^2 \frac{\delta_c}{210}\right)\rho_c \frac{d\tilde{y}_{O2}}{dx} \tag{8.24b}$$

$$\frac{d}{dx}\left(\rho_c {v_c}^2 - \frac{4}{3}\mu_c \frac{dv_c}{dx}\right) = -\frac{dP_c}{dx} - \frac{2(w_c + h_c)}{w_c h_c}\tau_{w,c} \tag{8.25}$$

The set of equations Eqs. (8.17–8.25) reported above is sufficiently general to be applied for the description of one–dimensional gas flow in cathode and anode channels, provided that the flow regime be laminar and the channel cross–section be rectangular as in Figure 8.1.

8.2.2.3 Boundary conditions and performance indexes

The transport and reaction models of cell (Section 8.2.2.1) and channels (Section 8.2.2.2) are coupled through appropriate boundary conditions as schematically represented in Figure 8.2.

The source terms in mass and species conservation equations in anode and cathode channels (Eqs. (8.17a–8.18a) and (8.23a–8.24a)) are linked to the gas molar fluxes calculated in the cell using the dusty–gas model as follows:

$$J_{H2}^{cell} = \underline{J}_{H2} \cdot \underline{n} \quad \text{and} \quad J_{H2O}^{cell} = \underline{J}_{H2O} \cdot \underline{n} \tag{8.26a}$$

$$J_{O2}^{cell} = \underline{J}_{O2} \cdot \underline{n} \quad \text{and} \quad J_{N2}^{cell} = \underline{J}_{N2} \cdot \underline{n} \tag{8.26b}$$

Eq. (8.26a) is applied at the interface between anode supporting layer and anode channel (boundary VI), while Eq. (8.26b) is applied at the interface between cathode current collector and cathode channel (boundary I). In Eq. (8.26) $\underline{n}$ represents a normal versor oriented outwards (i.e., from the cell to the channel).

From a mathematical point of view, gas fluxes at the boundary of the cell provide the source terms to be implemented in mass conservation equations in the channels, as represented by the arrows in Figure 8.2. On the other hand, at the electrode–channel interfaces, the total pressure and the species molar fractions calculated in the channels provide the Dirichlet boundary conditions for the cell. In particular, the hydrogen and oxygen molar fraction at boundaries VI and I are required to match those in the anode and cathode channels, respectively. Note that no boundary–layer resistance to mass transfer between cell and channel is considered, indeed it can be proven that, due to the small height of the channels, the transversal diffusive flux of gas species is fast enough to supply the cell without creating significant molar fraction gradients along the channel height.

Additional boundary conditions for the channels are the inlet conditions: pressure, hydrogen or oxygen molar fraction and velocity are specified. Open boundary conditions are implemented at the outlets. For the cell, no–flux conditions for electrons and gas species are applied at the electrode–electrolyte interfaces (boundaries III and IV) since the electrolyte is a dense ion–conducting layer. Similarly, no–flux conditions for oxygen ions are applied at boundaries VI and II (remember that the cathode current collector is insulating to ion transport).

Since the absolute electric potential of a phase is determined up to an additive constant, the electric potential of the electron–conducting phase at boundary I is set at zero as reference point, that is, V_{elc} = 0V [14,57]. Note that model results are not affected by this reference choice. The cell potential V_{cell} is imposed as a boundary condition at the anode side (boundary VI). In particular, the electric potential of the electron–conducting phase at boundary VI is set as $V_{ela} = \eta_{cell}$, where η_{cell} represents the cell overpotential, defined as follows:

$$\eta_{cell} = OCV - V_{cell} \tag{8.27a}$$

$$OCV = E^{\circ} - \frac{RT}{2F}\ln\left(\frac{1-y_{H2,IN}}{y_{H2,IN}}\left(\frac{1.013\cdot 10^{5}}{P_{c,IN}\,y_{O2,IN}}\right)^{1/2}\right) \tag{8.27b}$$

In Eq. (8.27), the *OCV* represents the open–circuit voltage, calculated according to the Nernst law as in Eq. (8.27b) considering the gas inlet conditions and the standard electromotive force *E*° calculated at the operating temperature [2].

Note that, throughout the model, the electric potential V_{ela} represents the real potential that could be measured with a voltmeter plus the *OCV*, which is consistent with the boundary condition $V_{ela} = \eta_{cell}$. Therefore, V_{ela} is a relative electric potential conveniently defined for modeling purposes so that $V_{ela} = \eta_{cell}$ = 0V at open circuit conditions. Similarly, the electric potential of the ion–conducting phase V_{io} is a relative potential that equals 0V at open circuit. These definitions of relative potentials V_{ela} and V_{io} are consistently applied throughout the model, from the boundary condition in Eq. (8.27a) to the definitions of activation overpotentials in Eqs. (8.15c) and (8.16c). The use of relative potentials is particularly useful, if not necessary, because the absolute potential of the ion–conducting phase and the standard electromotive forces of reactions Eqs. (8.1) and (8.2) are inaccessible [14]. Mathematically, the use of reference potentials corresponds to shifting them by a constant reference [57], operation which has no impact on the model results [19,76].

The full set of Eqs. (8.3–8.25) is mathematically closed by the boundary conditions described above, therefore it can be numerically solved. Additional expressions for the evaluation of physical and electrochemical properties for the specific set of conducting materials and reactants used in this study are reported in Table 8.1. From the model solution, some important outputs and performance indexes can be easily calculated. The current density per unit of cell surface *I* is calculated from the integration of $i_c\lambda_{TPB}^{cf}/L$ in the cathode functional layer. The fuel utilization factor can be calculated as the ratio of the hydrogen consumed in the cell over the hydrogen fed to the cell [2]. The oxygen utilization factor is similarly defined. Both these utilization factors can be calculated from the inlet and outlet fluxes in anode and cathode channels as follows:

Table 8.1 – Physical and electrochemical properties for the gas species (H2, H2O, O2, N2) and conducting materials (LSM, YSZ, Ni) used in this study.

Parameter	*Value*
Physical properties gas phase	
μ_m $(m = a,c)$	$\frac{y_{s1}\mu_{s1}M_{s1}^{0.5}+(1-y_{s1})\mu_{s2}M_{s2}^{0.5}}{y_{s1}M_{s1}^{0.5}+(1-y_{s1})M_{s2}^{0.5}}$ $\mathrm{kg\cdot m^{-1}\cdot s^{-1}}$ [65] $s_1, s_2 = \begin{cases} H2, H2O \quad for\ m = a \\ O2, N2 \quad for\ m = c \end{cases}$
$D_{H2,H2O}$	$\frac{0.0143\cdot T^{1.75}}{P_a\left(6.12^{1/3}+13.1^{1/3}\right)^2}\sqrt{\frac{1/M_{H2}+1/M_{H2O}}{2000}}$ $\mathrm{m^2\cdot s^{-1}}$ [65]
$D_{O2,N2}$	$\frac{0.0143\cdot T^{1.75}}{P_c\left(16.3^{1/3}+18.5^{1/3}\right)^2}\sqrt{\frac{1/M_{O2}+1/M_{N2}}{2000}}$ $\mathrm{m^2\cdot s^{-1}}$ [65]
Physical properties solid phase	
σ_{ela} (Ni)	$3.27\cdot 10^6 - 1065.3\cdot T$ $\mathrm{S\cdot m^{-1}}$ [18]
σ_{elc} (LSM)	$8.855\cdot 10^7 \exp(-1082.5/T)/T$ $\mathrm{S\cdot m^{-1}}$ [18]
σ_{io} (YSZ)	$3.34\cdot 10^4 \exp(-10300/T)$ $\mathrm{S\cdot m^{-1}}$ [18]
Thermochemistry	
$-\Delta H°$ (800°C)	$248.266\mathrm{kJ\cdot mol^{-1}}$ [2]
$E°$ (800°C)	0.978V [2]
Anode kinetics Eq. (8.15)	
i_{0a}^{ref}	$4.092\cdot 10^{-2}\mathrm{A\cdot m^{-1}}$ [73]
$\alpha_a - \beta_a$	0.3 – 0.7 [73]
E_a^{act}	$120\mathrm{kJ\cdot mol^{-1}}$ [57]
T_a^{ref}	700°C [73]
A_{des}	$5.59\cdot 10^{15}\mathrm{s\cdot m^2\cdot mol^{-1}}$ [11]
E_{des}	$88.12\mathrm{kJ\cdot mol^{-1}}$ [11]
Γ	$2.6\cdot 10^{-5}\mathrm{mol\cdot m^{-2}}$ [11]
γ_0	0.01 [11]
Cathode kinetics Eq. (8.16)	
i_{0c}^{ref}	$2.5\cdot 10^{-4}\mathrm{A\cdot m^{-1}}$ [39]
$\alpha_c - \beta_c$	1.5 – 0.5 [39]
E_c^{act}	$140\mathrm{kJ\cdot mol^{-1}}$ [39]
T_c^{ref}	945°C [39]
P_{O2}^{ref}	0.21atm [39]
ζ	0.375 [39]

$$U_{H2} = \frac{\tilde{J}_{H2,a,IN} - \tilde{J}_{H2,a,OUT}}{\tilde{J}_{H2,a,IN}} \tag{8.28a}$$

$$U_{O2} = \frac{\tilde{J}_{O2,c,IN} - \tilde{J}_{O2,c,OUT}}{\tilde{J}_{O2,c,IN}} \tag{8.28b}$$

The electrical efficiency ε is a measure of the electric energy produced by the cell compared with the heat that would be produced by burning the fuel, calculated as [2]:

$$\varepsilon = \frac{U_{H2} V_{cell} 2F}{-\Delta H^\circ} \tag{8.29}$$

where $-\Delta H^\circ$ is the lower heating value of hydrogen combustion.

Another important parameter which characterizes the fuel cell operation is the air–to–fuel ratio, which reflects the amount of oxidizer supplied to the system in relation to the amount stoichiometrically required [12]. In this study, a molar oxygen–to–hydrogen ratio $r_{O2/H2}$ is adopted, defined as follows:

$$r_{O2/H2} = \frac{F_{air} y_{O2,IN}}{F_{fuel} y_{H2,IN}} = \frac{U_{H2}}{2U_{O2}} \tag{8.30}$$

where F_{air} and F_{fuel} represent, respectively, the molar flows of air and fuel (i.e., H_2–H_2O mixture) fed to the SOFC stack. Due to the stoichiometry of the reactions represented in Eqs. (8.1) and (8.2), $r_{O2/H2} > 0.5$ represents a working condition with excess of oxygen while $r_{O2/H2} < 0.5$ a condition with deficiency of oxygen.

8.2.3 Specific considerations on the cell investigated

The integrated microstructural–electrochemical model presented in Sections 8.2.1 and 8.2.2 is sufficiently general to be applied for simulating planar SOFCs with composite electrodes in both co–flow and counter–flow configurations. However, as already anticipated in the previous Sections, the model is specifically used in this study to analyze anode–supported cells produced by the Forschungszentrum Jülich in F–design, with LSM–YSZ cathode and Ni–YSZ anode. Therefore, some parameters as well as some model simplifications are tailored for the specific system under consideration.

The morphological and geometrical input parameters are taken from the literature and reported in Tables 8.2 and 8.3, respectively. Due to lack of specific data and in order to simplify the analysis, only the mean diameters of the particle size distribution for each phase in each layer were considered, although the packing algorithm described in Section 8.2.1.1 can in principle simulate polydisperse powders. Similarly, mean values of the thickness of each layer were considered, although a small scattering, minimized through a proper quality assurance [83], is normal. An additional simplification concerns the anode channel, which is replaced with a wire mesh in the Jülich F–design [40,84]. An equivalent rectangular channel is assumed by considering a channel height h_a equal to the real height occupied by the wire, a channel width w_a equal to the wire pitch and a ratio $w_a/(w_a+r_a)$ equal to the void fraction of the wire mesh. In this way, the set of Eqs. (8.17–8.22), written for rectangular ducts, still holds. However, as a consequence of this simplification, the calculated dispersion factor coefficient δ_a (Eq. (8.18b)) and shear–stress factor at the wall $\tau_{w,a}$ (Eqs. (8.19) and (8.21)) might differ from the real ones.

Table 8.2 – Microstructural information of the anode–supported Jülich cell (F–design) simulated in this study. n.a. means not available.

Parameter	*Cathode current collector (cc)*	*Cathode functional layer (cf)*	*Electrolyte (ey)*	*Anode functional layer (af)*	*Anode supporting layer (as)*
el material	LSM[*] [24]	LSM[*] [66]	/	Ni[†] [37]	Ni[†] [37]
io material	/	8YSZ [66]	8YSZ [24]	8YSZ [37]	8YSZ [37]
ψ_{el}	1.0 [24]	0.475[§] [66]	0.0 [24]	0.397[†] [37]	0.397[†] [37]
d_{el} [μm]	11.6 [24]	0.52 [66]	/	0.97[†] [85]	1.5[†‡] [37]
d_{io} [μm]	/	0.34 [66]	/	1.164 [85]	n.a.
ϕ	0.42[#]	0.42 [86]	0.0 [24]	0.235[†] [85]	0.43[†] [37]
t [μm]	60 [87]	10 [66]	10 [24]	12 [85]	1500 [24]
fabrication method	screen printing [87]	screen printing [87]	vacuum slip casting [24]	vacuum slip casting [24]	Coat–mix® [37]

[*] LSM is $La_{0.65}Sr_{0.3}MnO_{3-\delta}$.

[#] Supposed equal to ϕ^{cf} according to the experimental results of Mertens et al. [67].

[§] Corresponding to LSM–YSZ 50–50% in weight.

[†] Values after reduction of NiO to Ni. The corresponding fraction of NiO–YSZ before reduction is 56–44% in weight.

[‡] Ni and YSZ particles are aggregated in elongated agglomerates with average diameter equal to 60μm and shape factor 0.7 [37].

Another specific feature of the cell investigated consists in the set of conducting materials adopted by the Forschungszentrum Jülich for F–design, which are LSM (in particular $La_{0.65}Sr_{0.3}MnO_{3-\delta}$ [24]) and Ni as electron–conducting phases and 8YSZ as ionic conductor. As a consequence, the procedure described in Section 8.2.1.1 to mimic reduction of NiO to Ni is specific for cermet anodes prepared via nickel oxide as a precursor of nickel. In addition, as already anticipated in Section 8.2.2.1, the kinetic expressions reported in Eqs. (8.15) and (8.16) and related parameters summarized in Table 8.1 are specific for the conducting materials used in the functional layers, therefore they must be replaced if the couples of materials differ from LSM–YSZ and Ni–YSZ.

Table 8.3 – Geometric parameters of anode and cathode channels for the anode–supported Jülich cell (F–design) simulated in this study.

Parameter	*Cathode channel*	*Anode channel*
h [mm]	1.5 [40]	1.2 [84]
w [mm]	1.0 [40]	1.4^*
r [mm]	2.0 [40]	0.47^*
L [mm]	$90^\#$ [61]	$90^\#$ [61]

* Equivalent values evaluated according to the considerations reported in Section 8.2.3, corresponding to the wire mesh geometry as in Peksen [84].

\# The cell is square with nominal dimensions 100mm·100mm, the active area is 90mm·90mm. In agreement with Bertoldi et al. [61], the current density is referred per unit of active area.

8.3 Microstructural results

The microstructural model presented in Section 8.2.1 is used to numerically reconstruct and evaluate the effective properties of the porous layers of the anode–supported Jülich cell. The main microstructural information of the cell analyzed, used as input parameters for the numerical reconstruction, is reported in Table 8.2.

A box domain with a minimum side length equal to 16 particle diameters was used, which is fairly accepted as a representative domain of the electrode microstructure [19,54,88]. In the Monte Carlo random–walk method (see Section 8.2.1.2), 20000 tracers travelling for a distance equivalent to at least 6 particle diameters were used to evaluate the gas phase tortuosity factor and the effective conductivity factor of each phase [19]. A bulk diffusion regime was simulated by adopting a Knudsen number of 10^{-2}. Results were averaged on three microstructures per layer.

Table 8.4 collects all the results of the microstructural modeling for the conditions summarized in Table 8.2. In the following Sections 8.3.1–8.3.4, further details and comments on the estimated effective properties are reported.

Table 8.4 – Effective properties calculated from the microstructural modeling for the conditions summarized in Table 8.2 (only the electrolyte and the anode supporting layer were not simulated). n.a. means not available.

Parameter	*Cathode current collector (cc)*	*Cathode functional layer (cf)*	*Electrolyte (ey)*	*Anode functional layer (af)*	*Anode supporting layer (as)*
ϕ	0.422	0.421	/	0.237	0.430 [37]
τ	1.520	1.516	/	2.225	3.225 [38]
d_{pore} [μm]	4.647	0.172	/	0.225	1.480 [38]
B [μm^2]	$1.874\cdot 10^{-1}$	$2.557\cdot 10^{-4}$	/	$1.667\cdot 10^{-4}$	$1.2\cdot 10^{-2}$ [37]
κ_{el}^{eff}	0.1944	0.0095	/	0.0282	0.0346 [37]
κ_{io}^{eff}	/	0.0382	/	0.1239	n.a.
λ_{TPB} [μm^{-2}]	/	4.608	/	3.243	n.a.

8.3.1 Anode supporting layer

The anode supporting layer was not simulated in this study because its microstructure cannot be represented as a random packing of spherical particles, as assumed in Section 8.2.1.1. In fact, the dry powders, prepared through the Coat–mix® fabrication process, consist of tiny rigid agglomerates (about 60μm in diameter) in which both conducting phases are distributed homogeneously [37]. All the necessary effective properties used in this study were measured by Simwonis et al. [37] and Haanappel et al. [38] and are reported in Table 8.4.

The porosity of the anode supporting layer is larger than that of the functional layer (0.430 compared with 0.237) because the supporting layer must allow a fast gas transport from the anode channel to the functional layer, wherein hydrogen oxidation occurs. The tortuosity factor τ^{as}, equal to 3.225, is about twice the tortuosity factor of a random packing of monosized sintered spherical particles for the same porosity [19,53,54]. Such a high value can be attributed to the particle agglomeration, indeed Bertei et al. [89] recently pointed out that the tortuosity factor in simulated random packings of agglomerates is larger than in random packings of spheres. However, the permeability coefficient B^{as} is sufficiently high to allow a rapid gas transport throughout the thickness of the anode supporting layer [37]. Note that the measured permeability coefficient is only 1.32 times larger than the one that could be estimated using Eq. (8.9), result which shows the wide applicability of such an equation.

The effective conductivity factor for the electron–conducting phase $\kappa_{ela}^{eff,as}$ is larger than that simulated in the anode functional layer (see Section 8.3.2), although the order of magnitude is the same for both the values. This result is unusual because both the layers have the same solid volume fraction of nickel while the functional layer has a smaller porosity, therefore a larger conductivity should be expected for the functional layer. This effect may be due to the particular morphological characteristics resulting from the Coat–mix® preparation process, which indeed was selected by the Forschungszentrum Jülich also because it provides a larger electronic conductivity if compared with the supporting layers prepared through tape–casting technique [37].

The effective conductivity factor of the ion–conducting phase and the TPB length per unit volume were neither measured nor simulated. However, these properties are not strictly required by the electrochemical model in the specific conditions simulated in this study. In fact, as discussed in Section 8.4.2.1, no reaction and so no ion transport take place in the anode supporting layer, therefore model results are independent of the specific values set for $\kappa_{io}^{eff,as}$ and λ_{TPB}^{as}.

8.3.2 Anode functional layer

The properties of the anode functional layer were estimated with the methods described in Section 8.2.1 on numerically reconstructed structures based on the input parameters reported in Table 8.2. Note that, based on the microstructural information reported in Table 8.2, the functional layer simulated in this study is the same one reconstructed by Joos et al. [85] through three–dimensional tomographic techniques, therefore a comparison with their results can be performed.

Among the input parameters, the diameters of Ni and YSZ particles after reduction were taken from Joos et al. [85]. The ratio $d_{ela}^{af} / d_{io}^{af}$ is equal to 0.833, close to 0.838, which is the diameter ratio that should be expected between Ni particles after reduction and NiO particles before reduction. Therefore, in the simulation, the 'green' microstructure was generated considering YSZ and NiO particles of 1.164μm (that is, equal to the diameter of YSZ particles), then NiO particles were shrunk by a factor 0.838 to account for NiO reduction (i.e., change in both density and molecular weight) as described in Section 8.2.1.1. The resulting microstructure was finally analyzed according to the methods described in Section 8.2.1.2.

No pore–formers were introduced in the structure generation to the reach the porosity of the functional layer. The corresponding tortuosity factor is 2.225, which is lower than in the supporting layer as discussed in Section 8.3.1, but it is fairly in agreement with the tortuosity factor of a random packing of monosized spherical particles with the same porosity [19,53]. A similar consideration can be drawn for the pore size, whose ratio with YSZ and Ni particle diameter is 0.193 and 0.230, respectively. However, d_{pore}^{af} differs from the one reported by Joos et al. [85], corresponding to 0.922μm. The discrepancy may be attributed to the method that they apply to calculate the pore diameter in the reconstructed electrode, which is based on measuring the maximum distance between pore walls: while this method can be fairly accurate to estimate the size of the particles, which show a convex shape, it could overestimate the pore size, since pores are usually non–convex in SOFC electrodes. The value of the pore size reported in Table 8.4, i.e., obtained in this study, was used in Eq. (8.9) to evaluate the permeability coefficient, which is 2 orders of magnitude smaller than in the anode supporting layer.

Simulations show that the effective conductivity factor for the ion–conducting phase is significantly larger than that of the electron–conducting phase. This is a reasonable consequence of the reduction of NiO particles, which leads to a reduction in both connectivity and volume fraction of Ni particles. The TPB length per unit volume calculated in this study, equal to 3.243μm^{-2}, fairly agrees with the one measured by Joos et al. [85], which falls between 1.88 and 2.49μm^{-2} (note that the range is due to the uncertainties related to the unknown percolation state of particles close to the domain boundaries in the tomographic reconstruction). Considering both the simplifications introduced in the microstructural models described in Section 8.2.1 as well as the possible errors in the detection of the TPB in the tomographically reconstructed structure, the comparison suggests that the microstructural model presented in this study provides reasonable predictions of effective properties in cermet anodes.

8.3.3 Cathode functional layer

The microstructure of the cathode functional layer, consisting of LSM and YSZ particles, was numerically reconstructed according to the methods described Section 8.2.1 to estimate its effective properties. The input parameters used in the reconstruction are mainly taken from Mertens et al. [66], as summarized in Table 8.2. In particular, ground and not calcinated YSZ powder was considered in this study, because it represents a benchmark for the cathodes fabricated by the Forschungszentrum Jülich [24,67,90].

The porosity of the cathode functional layer was estimated by Ananyev et al. [86] through the analysis of SEM images applying different segmentation and filtering methods. The estimated porosity, equal to 0.42, is relatively high if compared with the typical porosity of random close packings of spherical particles [48,91,92], suggesting that the specific preparation process resulted in an increase in porosity with respect to what might be expected. Although no specific pore–former particles were added during the cathode preparation [66], binders and other organic additives introduced in the paste for screen printing might have contributed to affect the resulting electrode porosity as they vanish during the sintering similarly to what pore–formers do [36]. As described in Section 8.2.1.1, the structure generation algorithm does not directly simulate the presence of such organic additives, however the corresponding increase in porosity can be taken into account by assimilating their effect through a corresponding amount of pore–formers.

When pore–formers are accounted for in the structure generation, two input parameters are required to specify the porosity: the maximum angle of contact among the particles, which takes into account the particle overlap introduced during the sintering (see Section 8.2.1.1), and the volume fraction of pore–formers. Mathematically speaking, an infinite set of these two input parameters can lead to a final porosity of 0.42. Due to the lack of additional morphological information regarding the real particle overlap in the cathode functional layer, the maximum angle of contact was set to 15°, as commonly accepted in several modeling studies [17,18,39,93]. As a consequence of this choice, the solid volume fraction of pore–former particles had to be assigned to 0.093 in order to meet the porosity value. In Section 8.4.1 a sensitivity analysis on this couple of parameters is performed and discussed.

The effective properties calculated under the conditions described above are reported in Table 8.4. The tortuosity factor, equal to 1.516, is slightly larger than the value obtained in a random packing of monosized spherical particles without pore–formers [19,53]. In fact, given the porosity, pore–formers and other organic additives introduce a few big pores in the medium, resulting in a decrease in the constriction factor [94,95], so in an increase in the tortuosity factor. The ratio ϕ^{cf}/τ^{cf}, corresponding to the effective diffusivity factor, is equal to 0.278, which is reasonably close to 0.32 measured by Mertens et al. [67]. The difference between these two values is attributed in part to the simplifications introduced in the model (e.g., particles are assumed to be spherical, the effect of binders and organic additives is assimilated to a small amount of pore–formers), in part to the uncertainties regarding the morphological characteristics of the electrode, such as possible errors in the estimation of the porosity from SEM images as described by Ananyev et al. [86].

The TPB length per unit volume and effective conductivity factors $\kappa_{elc}^{eff,cf}$ and $\kappa_{io}^{eff,cf}$ are in the same order of magnitude of those in the anode functional layer. Model simulations predict that $\kappa_{elc}^{eff,cf}$ is approximately 4 times smaller than $\kappa_{io}^{eff,cf}$.

This result is reasonable because the volume fraction of the electron–conducting phase is smaller than that of the ion–conducting phase. In addition, electron–conducting particles are bigger than ion–conducting particles and, typically, in a random mixture bigger particles percolate worse than smaller ones [52,96].

8.3.4 Cathode current collector

The cathode current collector was numerically reconstructed considering the input parameters reported in Table 8.2. In the reconstruction, the same maximum angle of contact and volume fraction of pore–formers used for the simulation of the cathode functional layer were used. Table 8.4 shows the effective properties evaluated according to the methods described in Section 8.2.1.2.

The porosity and tortuosity factor of the cathode current collector do not differ significantly from those of the cathode functional layer, therefore the ratio ϕ^{cc}/τ^{cc} is almost equal to ϕ^{cf}/τ^{cf}. This result is in agreement with the experimental measurements performed by Mertens et al. [67]. Both the permeability coefficient and the effective electric conductivity factor are much larger than those in the cathode functional layer. Such a result is reasonable because bigger particles are used in the current collector and because no ion–conducting particles are present. High permeability and electric conductivity are desired features in the cathode current collector, therefore model results justify the experimental efforts made by Forschungszentrum Jülich to optimize the cathode layers [24].

8.4 Electrochemical results

In this Section, the electrochemical model described in Section 8.2.2 is applied to simulate the polarization behavior of an anode–supported Jülich cell with LSM–based cathode (F–design) considering the microstructural and geometrical properties evaluated in Section 8.3. In particular, in Section 8.4.1 the model is first validated against experimental data obtained in a short 4–cell stack in counter–flow configuration [61], then a sensitivity analysis on the only uncertain parameter is presented and discussed. In Section 8.4.2 the model is used to analyze the effect of different operating conditions in order to investigate the electrochemical behavior of anode–supported cells.

8.4.1 Model validation

The model validation is performed against the experimental polarization curves measured by Bertoldi et al. [61] in a 4–cell short stack, whose geometric properties and operating conditions are reported in Tables 8.3 and 8.5, respectively. The effective properties calculated in Section 8.3, reported in Table 8.4, are considered. The effects of variation of both fuel and air flow rates as well as of the water content in the fuel stream are analyzed. Note that all the results are referred to the voltage of a single cell V_{cell}, therefore assuming that all the cells behave identically, as also verified by Bertoldi et al. [61].

Table 8.5 – Reference operating conditions considered in model validation (Section 8.4.1) for the 4–cell stack as reported by Bertoldi et al. [61]. These reference conditions are labeled as C1, following the same nomenclature in Bertoldi et al.

Parameter	*Value*
T	800°C
$P_{a,IN}$	1.0atm
$y_{H2,IN}$	0.965
F_{fuel}	$8\text{Nl}\cdot\text{min}^{-1*}$
$P_{c,IN}$	1.0atm
$y_{O2,IN}$	0.210
F_{air}	$10\text{Nl}\cdot\text{min}^{-1*}$

[*] The corresponding inlet velocities in the anode and cathode channels are calculated as, respectively, 1.617 and $3.639\text{m}\cdot\text{s}^{-1}$.

Figure 8.3 shows the current–voltage characteristic of the cell at different flow rates of air and fuel. The molar oxygen–to–hydrogen ratio $r_{O2/H2}$ is kept fixed at 0.272. Simulation results are reported with lines while experimental data with marks. For all the curves, as the current density increases, the voltage decreases monotonically as a consequence of the larger activation, ohmic and concentration overpotentials. Given a current density, as the flow rates decrease, V_{cell} decreases: this is due to the reduced feed of reactants (i.e., H_2 and O_2), therefore at a given I, i.e., at a given consumption rate, the molar fractions of hydrogen and oxygen decrease, leading to larger equilibrium potential steps in Eqs. (8.15c) and (8.16c), that is, to larger concentration overpotentials. In order to compensate the reduced chemical driving force, the electrochemical driving force η_{cell} must increase to hold the same current density, explaining why a smaller V_{cell} is obtained as F_{air} and F_{fuel} decrease.

Note that in the working conditions corresponding to Figure 8.3, the oxygen supply is limiting, that is, hydrogen is fed in excess since $r_{O2/H2} < 0.5$. However, the limiting current is not observed in Figure 8.3 because experimentally the polarization was stopped at $V_{cell} = 0.6\text{V}$ [61] in order to prevent the anode from reoxidation [97,98].

Figure 8.3 shows that simulation results reproduce quantitatively the polarization behavior. The agreement is almost perfect for $F_{fuel} = 8\text{Nl}\cdot\text{min}^{-1}$ while worsens for smaller F_{fuel}. The agreement is still satisfactory considering the morphological simplifications adopted and the absence of fitted parameters (remember that just a parameter, namely the angle of contact in the cathode, was assigned, as anticipated in Section 8.3.3 and further discussed at the end of this Section).

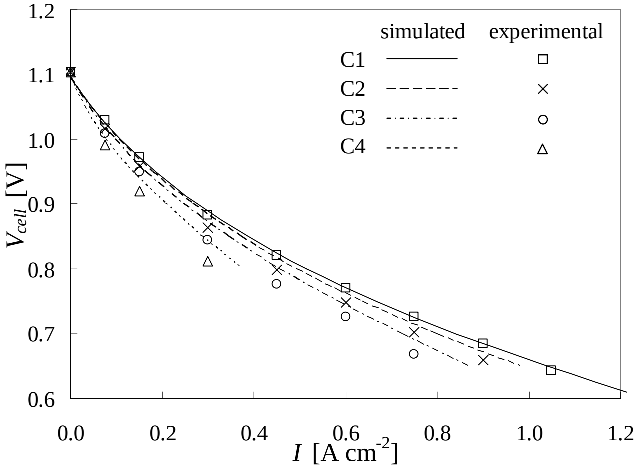

Figure 8.3 – Polarization curves of the 4–cell stack considered in this study at different flow rates of fuel and air at a given $r_{O2/H2} = 0.272$. *Simulation results are reported with lines, experimental results measured by Bertoldi et al. [61] are represented with marks. The corresponding operating conditions are reported in Table 8.5. The nomenclature of the series is the same one used by Bertoldi et al. and reported as follows: C1 (*$F_{fuel} = 8Nl{\cdot}min^{-1}$, $F_{air} = 10Nl{\cdot}min^{-1}$*), C2 (*$F_{fuel} = 6Nl{\cdot}min^{-1}$, $F_{air} = 7.5Nl{\cdot}min^{-1}$*), C3 (*$F_{fuel} = 4Nl{\cdot}min^{-1}$, $F_{air} = 5Nl{\cdot}min^{-1}$*), C4 (*$F_{fuel} = 2Nl{\cdot}min^{-1}$, $F_{air} = 2.5Nl{\cdot}min^{-1}$*).*

Figure 8.4 shows the polarization curves at different molar fractions of water in the fuel feed. According to the Nernst law in Eq. (8.27b), the OCV decreases as $y_{H2,IN}$ decreases: this behavior is quantitatively satisfied both experimentally and numerically in Figure 8.4 at $I = 0\text{A}{\cdot}\text{cm}^{-2}$. This thermodynamic effect holds also for $I > 0$, as experimentally observed in Figure 8.4: given the current density, V_{cell} at $y_{H2,IN} = 0.915$ is smaller than at $y_{H2,IN} = 0.965$.

However, the Figure also shows that the gap between the two experimental polarization curves decreases as I increases, as also reproduced by the simulated curves: the ratio $-dV_{cell}/dI$ is smaller for $y_{H2,IN} = 0.915$ than for $y_{H2,IN} = 0.965$. This behavior can be explained by using the model, which provides a twofold reason. A smaller $y_{H2,IN}$ reduces the absolute value of the equilibrium potential step in Eq. (8.15c), which leads to reduce the cell overpotential η_{cell}. Secondarily, considering Eq. (8.15b) at a constant pressure (note that the model predicts an almost constant pressure, equal to $P_{a,IN}$, in the whole anodic compartment), the exchange current density i_{a0} increases as y_{H2} decreases, which also contributes to lower η_{cell} at a given

I. These results are in agreement with previous research on Ni–YSZ electrodes: the catalytic effect of water on the kinetic rate of hydrogen oxidation has been experimentally proven by several research groups [68,99] while others have pointed out the role of concentration effects [100,101]. Since the model is able to reproduce such a behavior, there are sound indications that both the selected kinetic expression and the mathematical description of gas transport are representative of the physics and electrochemistry of the cell. It must be mentioned that F_{air} in E2 is larger than in E1: this also contributes to decrease the gap between the two polarization curves, although such a contribution is negligible. Running the model by imposing the conditions F_{fuel} = 8Nl·min^{-1}, F_{air} = 10Nl·min^{-1} and $y_{H2,IN}$ = 0.915, so that there is only a difference in $y_{H2,IN}$ between E1 and such a working condition, produces a current–voltage characteristic almost coincident with the E2 represented in Figure 8.4, showing that the decrease in the gap between E1 and E2 is due to the kinetic and concentration effects on the anode side as discussed above.

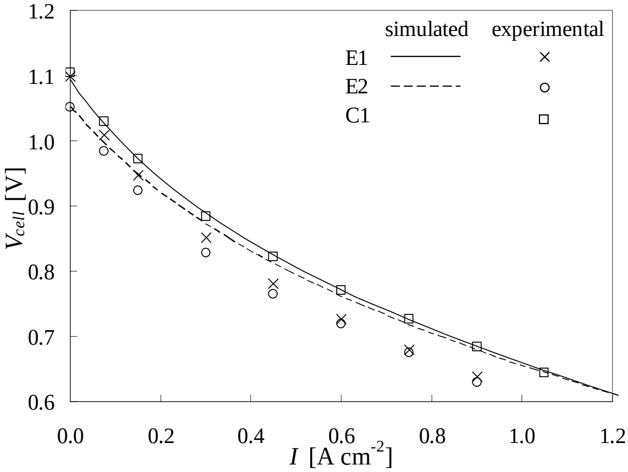

Figure 8.4 – Polarization curves of the 4–cell stack at different molar fractions of water in the fuel feed. Simulation results are reported with lines, experimental results [61] are represented with marks. The corresponding operating conditions are reported in Table 8.5 and as follows: E1 (F_{fuel} = 8Nl·min^{-1}, F_{air} = 10Nl·min^{-1}, $y_{H2,IN}$ = 0.965), E2 (F_{fuel} = 8Nl·min^{-1}, F_{air} = 16Nl·min^{-1}, $y_{H2,IN}$ = 0.915). For reference, the experimental data measured in condition C1, nominally equal to E1, are also reported.

Looking at Figure 8.4, the agreement between simulated and experimental polarization curves is only qualitative because simulated curves do not match experimental ones, as occurred in Figure 8.3. This difference may be due to the degradation of the cells during the experiments performed by Bertoldi et al. [61], as clearly represented in Figure 8.4: the series C1 was experimentally obtained before the series E1. Although the working conditions are the same, experimentally the series E1 shows a worse performance than C1 since, given V_{cell}, a reduced I is produced. This evidence indicates a degradation of the cell, although the reason is unknown and not reported in the experimental study. The modeling of such a degradation phenomenon, though interesting, is out of the scope of this study. Therefore, although a quantitative comparison between simulated and experimental polarization curves is not possible in Figure 8.4, the qualitative agreement and the discussion reported above on the nature of the decrease in the gap between polarization curves E1 and E2 support the validity of the model. In addition, considering also the good agreement reached in Figure 8.3, there are sound indications that the proposed model can quantitatively predict the stack performance starting from the knowledge of the powder information.

As discussed in Section 8.3.3, the reconstruction of both the cathode functional layer and cathode current collector was subject to the assumption of a parameter, that is, the maximum angle of contact among the particles, arbitrarily set to 15° following the suggestion of previous research on this topic [17,18,39,93]. Figure 8.5 shows the sensitivity of the cell polarization behavior on this uncertain parameter for the operating condition C1. In particular, three maximum angles of contacts are considered, 8°, 15° (the reference one) and 30°, whose corresponding solid volume fractions of pore–formers, used to represent the increase in porosity due to binders and other organic additives, are 0.050, 0.093, 0.260, respectively. The microstructures of the cathode functional layer and cathode current collector were simulated as described in Section 8.2.1, then the resulting effective properties were used as input parameters in the electrochemical model to produce the results reported in Figure 8.5.

Figure 8.5 shows that different angles of contact lead to different current–voltage characteristics, in particular the performance increases as the angle of contact increases. This is a consequence of the variation in the effective properties in the cathodic layers. In particular, in the cathode functional layer the TPB length increases from 2.006 to 9.050μm^{-2} as θ^{cf} increases from 8° to 30°. A similar trend is shown by the effective conductivity factors: for example, $\kappa_{io}^{eff,cf}$ increases from 0.0186 to 0.0535 while $\kappa_{elc}^{eff,cc}$ from 0.0999 to 0.2999 as the angle of contact varies from 8° to 30°. About the porous phase, τ^{cf} and τ^{cc} increase as the maximum angle of contact increases. In fact, increasing θ^{cf} (and θ^{cc}, which is equal to θ^{cf}) leads to smaller pores among the particles as a consequence of the enhanced densification [48] but, at the same time, the increase in the solid volume fraction of pore–formers, necessary to keep the same porosity, introduces larger pores in the medium. This results in a smaller constriction factor, proportional to the square of the ratio between smallest and largest pore diameters [94,95], which eventually leads to increase the tortuosity factors. In particular, the ratios ϕ^{cf}/τ^{cf} and ϕ^{cc}/τ^{cc} pass from about 0.292 at $\theta^{cf} = \theta^{cc} = 8°$ to about 0.235 at $\theta^{cf} = \theta^{cc} = 30°$.

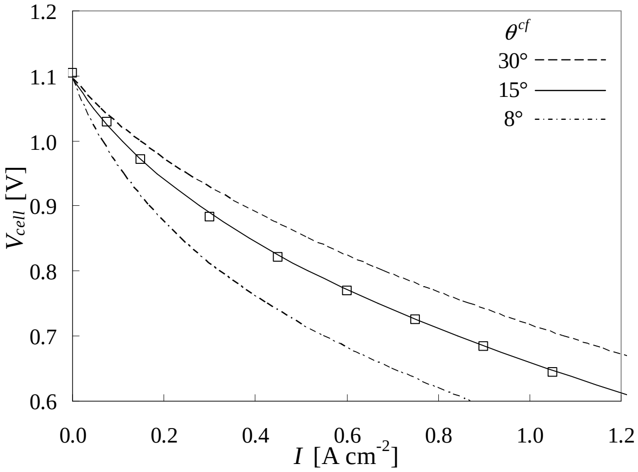

Figure 8.5 – Sensitivity analysis on the uncertain parameter ϕ^{cf}, the maximum angle of contact among the particles in the cathode functional layer and cathode current collector. The operating conditions C1 are considered. The squares represent experimental data [61] while lines model predictions at different angles of contact.

According to Section 8.3.3, Mertens et al. [67] measured a ratio ϕ^{cf}/τ^{cf} of 0.32. Note that the model is not able to reproduce this experimental value, regardless of the angle of contact used in the simulation, in part as a consequence of model simplifications such as assimilating binders and organic additives to pore–formers, in part due to possible errors in the determination of the porosity by SEM analysis by Ananyev et al. [86] as already pointed out in Section 8.3.3. It is interesting to note that the larger the angle of contact, the smaller the ϕ^{cf}/τ^{cf} ratio. This behavior can suggest that large angles of contacts, such as 30°, are unlikely because the ϕ^{cf}/τ^{cf} ratio would scarcely agree with the measured value. On the other hand, smaller angles of contact, as 8°, are representative of a weak sintering degree, resulting in low TPB density and effective conductivity as shown above. Therefore, an angle of contact of 8° or smaller is unlikely as well in an optimized cathode such as the Jülich one.

Although there are not direct proofs that the choice of setting the maximum angle of contact to 15° be correct, the indications just pointed out reasonably justify the assumption $\theta^{cf} = \theta^{cc} = 15°$. Hence, the sensitivity analysis supports the soundness of the model and of the choice of the only uncertain morphological parameter. The results reported in Figures 8.3–8.5 suggest that the modeling framework presented in this study is able to fairly reproduce the steady–state behavior of an SOFC stack despite its morphological simplifications, in particular the strongest one, that is, that particles are spherical.

8.4.2 Model simulations

In this Section the model is used to gain a deeper insight into the anode–supported Jülich cell, simulating the steady–state behavior in conditions different from those analyzed in Section 8.4.1. In particular, different operating conditions (Sections 8.4.2.1–8.4.2.3) and cell geometry (Section 8.4.2.4) are discussed. The microstructural characteristics of the anode and cathode layers are not varied, therefore the effective properties evaluated in Section 8.3 and reported in Table 8.4 are used also in this Section.

8.4.2.1 Effect of air flow rate

In the model validation (Section 8.4.1) the effect of a variation of F_{fuel} and F_{air} was discussed. However, in such an analysis the molar oxygen–to–hydrogen ratio remained fixed to $r_{O2/H2} = 0.272$. In this Section, the effect of $r_{O2/H2}$ is examined through a systematic variation of the air flow rate at a given F_{fuel}. In particular, larger $r_{O2/H2}$ than that used in Section 8.4.1 are simulated: an oxygen–to–hydrogen ratio smaller than 0.5, as the one adopted by Bertoldi et al. [61], is atypical, because in such a condition oxygen is the limiting reactant. Usually air is fed in excess to the cell [2,12] since there is no economic value to recover unreacted oxygen, while there is in unused hydrogen. For the same reason, in this and in the following Sections F_{fuel} is set to $4\text{Nl}\cdot\text{min}^{-1}$ (i.e., condition C3 in Figure 8.3), differently from the reference flow rate of $8\text{Nl}\cdot\text{min}^{-1}$ adopted by Bertoldi et al. [61] as reported in Table 8.5. In fact, at 0.7V, for the operating condition C1 the hydrogen utilization is equal to 24.3%, which is too low for a real SOFC system dedicated to energy production. On the other hand, U_{H2} is equal to 40.8% for condition C3 at 0.7V, which is closer to a real plant condition while giving further ground of improvement.

Figure 8.6 shows the simulated polarization curves at different molar oxygen–to–hydrogen ratios. The maximum oxygen–to–hydrogen ratio analyzed corresponds to an air flow rate of $16\text{Nl}\cdot\text{min}^{-1}$, that is, to an inlet air velocity in the air channel of $5.823\text{m}\cdot\text{s}^{-1}$, which is the maximum velocity tested experimentally by Bertoldi et al. [61].

The Figure shows that at a given current density, V_{cell} increases as $r_{O2/H2}$ increases. This is a result of the smaller concentration overpotential at the cathode, mathematically represented by the reduction, in absolute value, in the equilibrium potential step in Eq. (8.16c). Note that the improvement in cell performance levels off at high oxygen–to–hydrogen ratios because the oxygen molar fraction tends to become uniform in the cathode, resulting in negligible effects of the equilibrium potential step. Therefore, provided that a sufficient oxygen feed be guaranteed in order to minimize the effect of concentration overpotential on the cathode side, the air flow rate can be used to control the temperature without significantly affecting the electrochemical performance [2,12,16]. On the other hand, the upper bound of air flow rate is determined by the constraints about the pressure drops on the air channel: as an example, for $r_{O2/H2}$ = 0.870 the model predicts a cathodic pressure drop of 0.46kPa, almost independent of the cell potential.

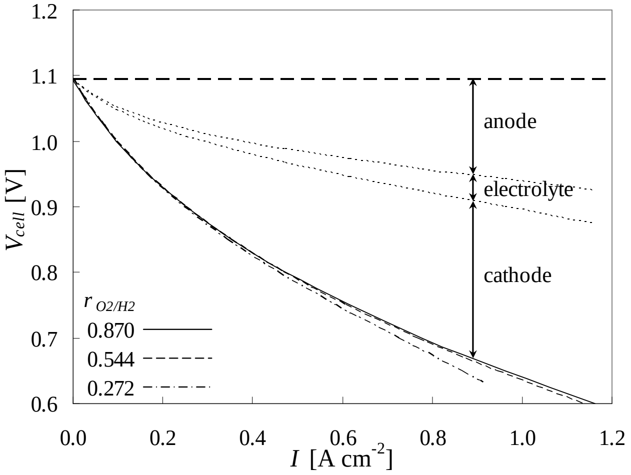

Figure 8.6 – Effect of the oxygen–to–hydrogen ratio on the polarization curve. F_{fuel} *is kept constant to 4Nl·min*$^{-1}$ *while* F_{air} *is varied to 5, 10 and 16Nl·min*$^{-1}$*, corresponding to* $r_{O2/H2}$ *of 0.272, 0.544 and 0.870, respectively. The other operating conditions are the same reported in Table 8.5, effective properties are kept equal to those summarized in Table 8.4.*

The model also allows the identification of the sources of energy loss in the cell. Figure 8.6 shows that the main energy loss is concentrated at the cathode, which contributes for the 56.6% of the cell overpotential at 0.7V for $r_{O2/H2}$ = 0.870. In the same conditions, the anode contributes for the 34.8%. This predicted distribution of overpotential is in agreement with several experimental observations, which indicate the LSM–YSZ cathode as the main source of irreversibility in anode–supported SOFCs [2,24,30]. In particular, model simulations show that, for $r_{O2/H2}$ = 0.870 at V_{cell} = 0.7V, the active thickness (that is, the thickness wherein the 99% of the current is converted) is equal to 9.4μm in the cathode side while 2.3μm in the anode side. It is noteworthy that the active thickness on the cathode side extends for almost the whole thickness of the cathode functional layer, indicating that the thickness and microstructural characteristics experimentally identified by Haanappel et al. [24] as the optimum ones are confirmed by the model. On the other hand, the smaller active thickness identified on the anode side suggests that the hydrogen oxidation reaction occurs completely within the anode functional layer (i.e., no reaction occurs in the anode supporting layer, as anticipated in Section 8.3.1) and it is not a limiting factor for cell operation. In particular, simulations show that the major contribution to anode overpotential is related to the concentration overpotential, which is markedly larger than kinetic and ohmic losses because the thick anode support yields a significant gradient of hydrogen molar fraction along the anode thickness.

The model allows the interpretation of other interesting features of the cell electrochemical behavior. Figure 8.6 shows that at low current density the polarization curves exhibit a parabolic behavior, which is also present in all the experimental curves in Figures 8.3 and 8.4. Such a shape is often attributed to the activation of electrochemical reactions, that is, to the nonlinear Butler–Volmer kinetic expression [2,15]. In reality, simulations show that even if both cathodic and anodic kinetics (Eqs. (8.15a) and (8.16a)) were linearized, the parabolic shape would remain, although less pronounced. The model suggests that such a parabolic behavior is mainly due to the non–linearity introduced by gas concentration effects, that is, due to the equilibrium potential steps in Eqs. (8.15c) and (8.16c), rather then to the exponential form of the Butler–Volmer kinetics in Eqs. (8.15a) and (8.16a). This result was already pointed out by Bessler and Gewies [59], this study confirms their findings, showing how a physically–based model can be useful to avoid misinterpretation of experimental observations.

8.4.2.2 Effect of flow configuration

Jülich cells are typically run in counter–flow [40,41,61], which is expected to be more efficient than the co–flow configuration because it provides, in average, a higher driving force. However, often co–flow configuration is preferred for planar SOFCs because it prevents from steep temperature gradients and uneven thermal stresses [2,12]. In this Section, the comparison between co–flow and counter–flow arrangements is performed by using the electrochemical model by conveniently changing the flow direction in the air channel (Eqs. (8.23–8.25)) and the corresponding boundary conditions. The operating condition F_{fuel} = 4Nl·min^{-1} with $r_{O2/H2}$ = 0.870, identified as the best one in Section 8.4.2.1, is taken as reference.

Figure 8.7 shows the distribution of the current density at the electrolyte–anode functional layer interface along the cell length x for counter–flow and co–flow configurations. The cell voltage is equal to 0.7V. The Figure shows that, in both conditions, the current production is larger at the inlet of the fuel feed (x = 0) and monotonically decreases along the channel axial direction. Such a trend is expected because as hydrogen is consumed along the cell length its molar fraction decreases in the gas phase, resulting in larger concentration overpotentials (i.e., larger equilibrium potential step in Eq. (8.15c)) which slow down the current production.

Note that a similar depletion of oxygen occurs in the air channel, although less pronounced since air is fed in excess to the cell as $r_{O2/H2} > 0.5$. The Figure shows that at $x = 0$ the local current density is larger in co–flow than in counter–flow configuration: this is due to the larger driving force because both the fuel and the oxidizer are fresh at the fuel inlet in co–flow configuration. Due to the simultaneous depletion of hydrogen and oxygen, the local current density decreases more sharply in co–flow than in counter–flow so that, in average, the mean current density produced in counter–flow arrangement is slightly larger than in co–flow, 0.778A·cm^{-2} versus 0.774A·cm^{-2}, respectively. These values of mean current density highlight that, in these operating conditions, the two flow configurations practically show an almost coincident electrochemical performance. This is due to the small fuel utilization, equal to 43.4% in counter–flow configuration at 0.7V.

The counter–flow configuration is considered also in the following Sections in order to allow a direct comparison with results obtained in Sections 8.4.1 and 8.4.2.1.

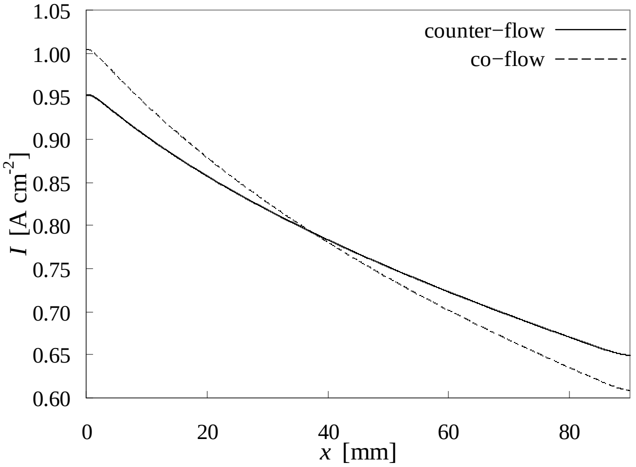

Figure 8.7 – Local current density at the electrolyte–anode functional layer interface simulated at $V_{cell} = 0.7V$ in counter–flow (solid line) and co–flow (dotted line) configurations. The operating conditions are those reported in Table 8.5 with the exception of $F_{fuel} = 4Nl\cdot min^{-1}$ and $F_{air} = 16Nl\cdot min^{-1}$.

8.4.2.3 Effect of temperature

As reported in Section 8.2.2, uniform temperature is assumed in the cell due to the small size of the stack under consideration. This assumption is reasonable since Bertoldi et al. [61] proved experimentally that the increase in cell temperature with increasing current density (up to 1A·cm^{-2}) was quite similar in all the test conditions and restricted to 10–20°C with respect to the operating temperature at OCV. In addition, they verified that no particular variation in temperature between different cells was evident and thus the effect of larger thermal gradients could be neglected. In these conditions, it is worth analyzing the effect of a small variation in operating temperature with the model.

Figure 8.8a shows the polarization behavior at three different operating temperatures. The operating conditions are those reported in Table 8.5 considering $F_{fuel} = 4\text{Nl}\cdot\text{min}^{-1}$ and $F_{air} = 16\text{Nl}\cdot\text{min}^{-1}$.

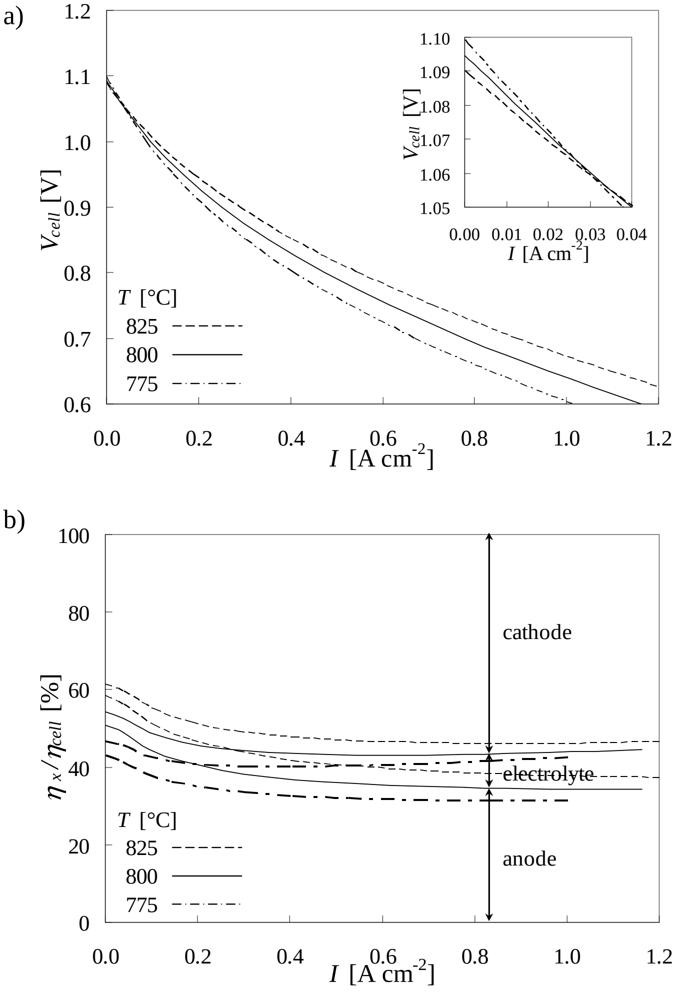

Figure 8.8 – Effect of the operating temperature on the polarization behavior of the simulated stack. Three different operating temperatures are considered, represented with different lines. The operating conditions are those reported in Table 8.5 with the exception of $F_{fuel} = 4\text{Nl}\cdot\text{min}^{-1}$ *and* $F_{air} = 16\text{Nl}\cdot\text{min}^{-1}$*. a) Polarization curves (also a magnification around OCV is reported); b) relative contribution of each compartment (i.e., anode, electrolyte and cathode) to the whole cell overpotential as a function of the current density.*

At I = 0, the higher the temperature, the smaller the OCV, as predicted by the Nernst law Eq. (8.27b). However, for I > 0.05A·cm^{-2}, the higher the temperature, the higher the current density at a given V_{cell}. This behavior is mainly due to the larger exchange currents (i_{a0} and i_{c0}) and ionic conductivity σ_{io}, which are thermally activated and increase as the temperature increases (see Eqs. (8.15b) and (8.16b) and Table 8.1).

Figure 8.8b shows additional information to clarify the results described above. In particular, increasing the temperature leads to a decrease in the relative contribution of the cathode to the whole cell overpotential at the expenses of the anode. According to Section 8.4.2.1, the cathode resistance is mainly ruled by the activation overpotential while the anode by gas concentration effects: an increase in operating temperature speeds up the cathodic exchange current i_{c0} much more than the diffusion coefficients $D_{H2/H2O}$, $D_{K,H2}$, $D_{K,H2O}$ (see their weak temperature dependence in Table 8.1 and Eq. (8.8)) and the anodic exchange current i_{a0}, as $E_c^{act} > E_a^{act}$ (see Table 8.1). Interestingly, Figure 8.8b can also be interpreted in the opposite direction: as the temperature decreases, the activation losses in the cathode become dominant. This observation justifies the adoption of materials different from LSM and YSZ for applications designed for T < 800°C [36,87,102].

Another interesting result shown in Figure 8.8b is the comparison of relative contributions at I = 0: the anodic contribution is larger at I = 0 than at higher current densities. This is attributed to the catalytic effect of water on the hydrogen oxidation kinetics, topic already introduced in Section 8.4.1: as the current density increases, more water is produced within the anode, which increases i_{a0} speeding up the oxidation reaction kinetics, so reducing the anode resistance with respect to OCV condition. This interpretation is supported by the model results: at 800°C, the active thickness at OCV in the anode functional layer is almost twice larger than at 0.7V.

Coming back to Figure 8.8a, there is a final remark to be pointed out. Comparing the polarization curves at 800°C and 825°C, in the latter operating condition the current density is, in average, 15% larger than that produced at 800°C at the same cell voltage. Even assuming that experimental data used in Section 8.4.1 could have been affected by a maximum temperature gradient of 20°C, as discussed at the beginning of this Section, the error introduced in simulation results by the assumption of uniform temperature would have been smaller than 15%. Note that such an error would be fairly reasonable when modeling an SOFC at the stack level, and it would be smaller than the error accepted during the sensitivity analysis on the maximum angle of contact in Section 8.4.1. In other words, the comparison between the sensitivity analysis reported in Section 8.4.1 and the simulation performed in this

Section shows that the global electrochemical behavior of the cell is more sensitive to errors in the estimation of microstructural details rather then on simplifications related to operating conditions. This observation confirms once again the importance of a detailed microstructural modeling integrated into a cell–level electrochemical model, which is the main point introduced in this study.

8.4.2.4 Effect of cell geometry

In this Section the model is used to analyze the effect of modifications of the cell geometry on the current–voltage characteristic of the system. In particular, in the first simulation the size of the cell is increased to the nominal area 200mm·200mm (the active area is 190mm·190mm), which is the size expected for power stacks [40,41,103]. A second independent analysis concerns the thickness of the anode supporting layer, which is reduced to 500μm as planned by the Forschungszentrum Jülich in order to adapt the manufacturing line to industrial necessities adopting the tape–casting technique [41,87]. These simulations are also useful to highlight and discuss about some limits of the proposed model, such as the assumption of uniform temperature and the reduction of the three–dimensional geometry to a two–dimensional domain, both introduced in Section 8.2.2.

Figure 8.9 shows the polarization behavior of two cells differing in their size only. The operating conditions for the shortest cell are those used in the previous Sections, that is, those reported in Table 8.5 with F_{fuel} = 4Nl·min^{-1} and $r_{O2/H2}$ = 0.870. For the biggest cell, the inlet velocities of fuel and air in the feeding channels are set equal to those used in the shortest cell, that is, 0.809m·s^{-1} and 5.823m·s^{-1}, respectively. Note that while this operating condition ensures that the gas flow in the channels is the same in both the cells, a reduced feed of reactants per unit of cell area is supplied in the largest cell.

Figure 8.9 shows that the performance worsens as the size of the cell increases while keeping the same inlet velocities: the produced current density is reduced of about 15–20% at the same voltage. This effect is due to the larger utilization of fuel and oxygen as a consequence of a reduced feed of reactants per unit of cell area. At V_{cell} = 0.7V, the fuel utilization is equal to 43.4% for L = 0.09m while equal to 74.2% for L = 0.19m. The larger U_{H2} and U_{O2} indicate that y_{H2} and y_{O2} are in average smaller within their respective functional layers, thus resulting in larger concentration overpotentials (see Eqs. (8.15c) and (8.16c)) which are the responsible of the decrease in the global cell performance. On the other hand, the larger fuel utilization has the beneficial effect to increase the electrical efficiency, as deducible from Eq. (8.29) and reported in Figure 8.9: the maximum efficiency rises from 29.7% to 45.4%. Note that at 800°C the thermodynamic efficiency limit, equal to $\Delta G°/\Delta H°$, corresponds to 76.0% based on the lower heating value.

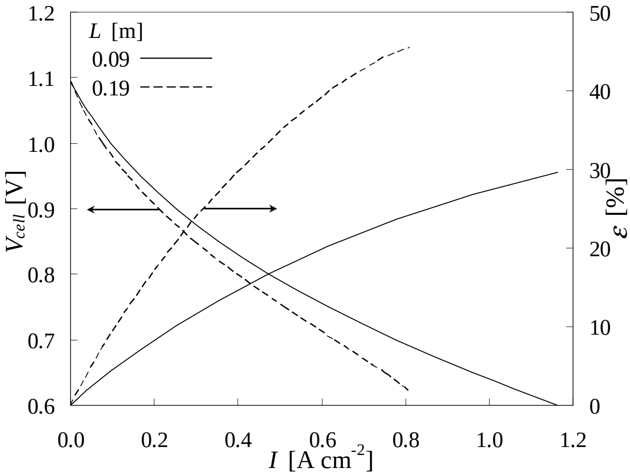

Figure 8.9 – Effect of the cell length on the polarization behavior of the simulated stack. On the right axis, the electrical efficiency, based on the lower heating value, is reported. The operating conditions are those summarized in Table 8.5, with $r_{O2/H2} = 0.870$ *and an inlet velocity of fuel stream equal to* $0.809 \mathrm{m \cdot s^{-1}}$ *for both the cell lengths.*

It is noteworthy that the polarization behavior of the biggest cell substantially matches that of the shortest cell if the inlet velocities of fuel and air are proportionally increased by a factor 0.19/0.09 in order to keep the same feed of reactants per unit of cell area. In this operating condition, the fuel inlet velocity for the biggest cell is raised to $1.707 \mathrm{m \cdot s^{-1}}$. The velocity in the air channels increases accordingly, leading to a maximum Reynolds number Re_c equal to about 100, which is still below the critical Reynolds number of turbulent transition in rectangular ducts [104]. Therefore, this simulation (not reported in Figure 8.9) shows that the good performance reached by the shortest cell can be recovered by the largest one when supplying the same amount of reactants per unit of cell area, obviously at the expenses of a smaller fuel utilization.

It must be pointed out that the electrochemical performance for the bigger cell size could be even slightly better than that predicted by the model in Figure 8.9. In fact, as the size of the cell increases, the heat associated to Joule heating and electrochemical reactions may result in a potential temperature increase along the fuel flow direction, which can boost the current production [60]. Obviously, while this is beneficial from a performance point of view, temperature gradients should be minimized to avoid thermo–mechanical stresses, for example tailoring the air flow rate as discussed in Section 8.4.2.1. However, such a phenomenon cannot be described by the model since uniform temperature is assumed (see Section 8.2.2). The analysis of thermal effects on the electrochemical behavior in big stacks, based on the integration of the heat balance in model equations, with effective thermal conductivities properly evaluated on numerically reconstructed microstructures, will be subject of a future extension of the model.

Forschungszentrum Jülich plans to reduce the thickness of the anode supporting layer to 500μm, instead of 1500μm as reported in Table 8.2, for a twofold reason: the application of a manufactory technique scalable to industrial level, such as the tape–casting, and the saving of material [41,87]. The effect of the reduction of t^{as} is reported in Figure 8.10. Even though the anode supporting layer produced by tape–casting shows some different microstructural characteristics [85], the same effective properties reported in Table 8.4 are considered in this study in order to have, if not quantitative information, at least preliminary indications on the possible effects on the electrochemical behavior. The simulated operating conditions are the same used above in this Section.

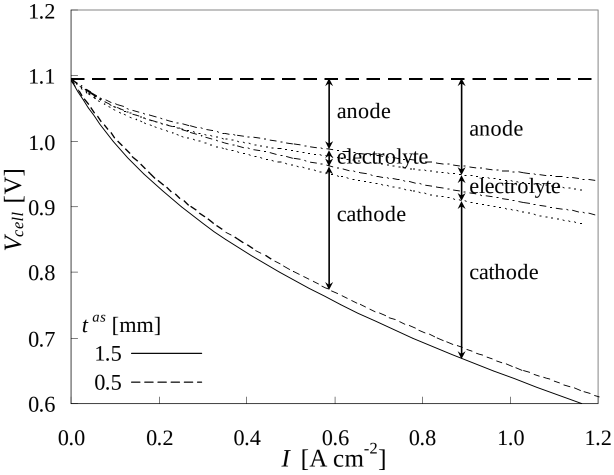

Figure 8.10 – Effect of the thickness of the anode supporting layer on the polarization behavior of the cell. The operating conditions are those reported in Table 8.5 with the exception of F_{fuel} = 4Nl·min^{-1} and F_{air} = 16Nl·min^{-1}.

Figure 8.10 shows that reducing t^{as} leads to a slight improvement in the performance. This is due to the shorter diffusion length for both hydrogen and water to reach/leave the anode functional layer, reduced by a factor 3. For a current density of 0.8A·cm^{-2}, y_{H2} at the electrolyte–anode functional layer interface at $x = L/2$ is 0.687 for t^{as} = 0.5mm while 0.624 t^{as} = 1.5mm, indicating that in the former condition the supply of hydrogen and the removal of water are facilitated, resulting in a smaller concentration overpotential as the equilibrium potential step in Eq. (8.15c) decreases in absolute value. The corresponding reduction in anode overpotential is also visible in Figure 8.10.

Hence, simulations suggest that such a geometric modification should not significantly affect the electrochemical response of the cell. This conclusion is correct provided that the thinner anode supporting layer could still guarantee a uniform gas and electron distribution on the whole cell area, which is realistic if considering the characteristics of the wire mesh (see Section 8.2.3). However, the model cannot catch this detail because the full three–dimensional geometry of the system is not represented in the electrochemical model. Therefore, although at the present simulations suggest to pursue in the reduction of the thickness of the anode supporting layer, saving material and so reducing cost and weight of the stack, a more detailed analysis is required, which will be subject of future investigations.

Concluding, while in this Section some geometric modifications to the Jülich cell analyzed were investigated, some limits of the model were identified suggesting, as an improvement, to include the heat balance in the model equations and to consider transversal phenomena occurring along the direction neglected in the current electrochemical model.

8.5 Conclusions

A quasi–two–dimensional model for the description of the electrochemical behavior of planar SOFCs in a stack was presented. The novel feature introduced in this study consists in integrating a detailed microstructural modeling of the porous layers for the estimation of the effective properties, such as TPB length, tortuosity factor, permeability, effective conductivity. This integrated approach is fully predictive and allows a coherent and rigorous simulation of the cell polarization behavior starting from the knowledge of powder characteristics and operating conditions only, enabling a substantial reduction of the number of uncertain parameters.

The modeling framework was used to simulate the microstructure and the polarization behavior of a short stack of anode–supported planar cells produced by the Forschungszentrum Jülich with LSM–based cathode (F–design) without any fitted or adjusted parameter. The comparison of predicted effective properties with available experimental data, either measured or evaluated on SEM images, revealed discrepancies in the order of 30% as a maximum, which is a reasonable accuracy if considering the complexity of the system. The good agreement between simulated and experimental polarization curves pointed out that the model can quantitatively reproduce the experimental data with good accuracy without any fitting.

The model revealed that gas concentration effects, especially on the anode side, are responsible of both the parabolic shape of the curve near OCV and the reduced polarization resistance as the water molar fraction in the fuel stream increases. The main contribution to cell overpotential was identified in the activation losses in the cathode functional layer. Simulations suggest that the cell performance can be improved by enhancing the catalytic activity of the cathode, especially for intermediate temperature applications, while possibly reducing the thickness of the anode supporting layer.

The sensitivity analysis performed on the only uncertain morphological parameter, that is, the angle of contact among the particles in the cathode, showed that the global electrochemical response of the system is typically more sensitive to microstructural modifications rather then on variations in operating conditions. This shows the importance of a detailed microstructural modeling coupled with an electrochemical cell–level model, which is the main point highlighted in this study.

Concluding, this study showed that quantitative information of the whole cell electrochemical behavior can be predicted starting from the knowledge of operating conditions and powder characteristics when a detailed microstructural model is coupled with an electrochemical model. The integrated model can be used as a physically–based interpretative tool of experimental data and as a design tool to optimize the system. Future research will be dedicated to overcome the limits of the present study, mainly related to the assumption of uniform temperature (not applicable for the simulation of big stacks), through the integration of the heat balance in the set of model equations. In addition, the electrochemistry of mixed ionic–electronic conducting cathodes will be investigated, in order to make the model applicable for the current generation of Jülich LSCF–based anode–supported cells.

Nomenclature

Glossary

A_{des}	pre–exponential factor of hydrogen desorption kinetics [$s \cdot m^2 \cdot mol^{-1}$]
B^{la}	permeability in the layer *la* (*la* = *af*, *as*, *cf*, *cc*) [m^2]
d_p^{la}	mean particle size of phase *p* (*p* = *ela*, *elc*, *io*) in the layer *la* (*la* = *af*, *as*, *cf*, *cc*) [m]
d_{pore}^{la}	mean pore size in the layer *la* (*la* = *af*, *as*, *cf*, *cc*) [m]
$D_{h,j}$	channel hydraulic diameter (*j* = *a*, *c*) [m]
$D_{K,s}^{eff,la}$	effective Knudsen diffusivity of species *s* (*s* = *H2*, *H2O*, *O2*, *N2*) in the layer *la* (*la* = *af*, *as*, *cf*, *cc*) [$m^2 \cdot s^{-1}$]
$D_{s1/s2}$	binary diffusivity of the pair of species *s1/s2* (*s1/s2* = *H2/H2O*, *O2/N2*) [$m^2 \cdot s^{-1}$]

$D_{s1/s2}^{eff,la}$	effective binary diffusivity of the pair of species *s1/s2* (*s1/s2* = *H2/H2O*, *O2/N2*) in the layer *la* (*la* = *af*, *as*, *cf*, *cc*) [m^{2}·s^{-1}]
E°	standard electromotive force [V]
E_{des}	activation energy of hydrogen desorption kinetics [J·mol^{-1}]
E_{j}^{act}	activation energy (*j* = *a*, *c*) [J·mol^{-1}]
f_{j}	friction factor (*j* = *a*, *c*)
F	Faraday constant [C·mol^{-1}]
F_{air}	molar flow rate of air [mol·s^{-1}]
F_{fuel}	molar flow rate of fuel [mol·s^{-1}]
h_{j}	channel height (*j* = *a*, *c*) [m]
i_{j}	current density per unit of TPB length (*j* = *a*, *c*) [A·m^{-1}]
i_{j0}	exchange current per unit of TPB length (*j* = *a*, *c*) [A·m^{-1}]
i_{j0}^{ref}	exchange current per unit of TPB length at the reference temperature (*j* = *a*, *c*) [A·m^{-1}]
I	current density per unit of cell area [A· m^{-2}]
$\underline{J}_{s}$	molar flux of species *s* (*s* = *H2*, *H2O*, *O2*, *N2*, *e*, *O*) [mol·m^{-2}·s^{-1}]
$\underline{\tilde{J}}_{s}$	mass flux of species *s* (*s* = *H2*, *H2O*, *O2*, *N2*, *e*, *O*) [kg·m^{-2}·s^{-1}]
J_{s}^{cell}	molar flux of species *s* (*s* = *H2*, *H2O*, *O2*, *N2*) at the cell–channel interface [mol·m^{-2}·s^{-1}]
L	cell length [m]
M_{s}	molecular weight of species *s* (*s* = *H2*, *H2O*, *O2*, *N2*) [kg· mol^{-1}]
$\underline{n}$	normal versor oriented from cell to channel
OCV	open–circuit voltage [V]
P_{j}	pressure (*j* = *a*, *c*) [Pa]
P_{H2}^{*}	reference pressure of hydrogen adsorption/desorption equilibrium [Pa]
P_{O2}^{ref}	reference oxygen partial pressure [Pa]
Pe_{j}	Peclet number (*j* = *a*, *c*)
r_{j}	interconnect rib width (*j* = *a*, *c*) [m]
$r_{O2/H2}$	molar oxygen–to–hydrogen ratio
R	ideal gas constant [J· mol^{-1}· K^{-1}]
Re_{j}	Reynolds number (*j* = *a*, *c*)
$Re_{w,j}$	wall Reynolds number (*j* = *a*, *c*)
t^{la}	thickness of the layer *la* (*la* = *af*, *as*, *cf*, cc, ey) [m]
T	operating temperature [K]
T_{j}^{ref}	reference temperature for reaction kinetics (*j* = *a*, *c*) [K]
U_{s}	utilization factor (*s* = *H2*, *O2*)

v_j	mass–averaged gas velocity ($j = a, c$) [m·s^{-1}]
V_{cell}	cell potential [V]
V_p	electric potential of phase p ($p = ela, elc, io$) [V]
w_j	channel width ($j = a, c$) [m]
x	coordinate along the longitudinal direction [m]
y_s	molar fraction of gas species s ($s = H2, H2O, O2, N2$)
$\tilde{y}_s$	mass fraction of gas species s ($s = H2, H2O, O2, N2$)
α_j	first transfer coefficient ($j = a, c$)
β_j	second transfer coefficient ($j = a, c$)
γ_0	sticking probability of hydrogen adsorption kinetics
Γ	surface site density [mol·m^{-2}]
δ_j	dimensionless factor of Taylor–Aris axial dispersion ($j = a, c$)
$-\Delta G°$	standard Gibbs free energy of hydrogen combustion [J·mol^{-1}]
$-\Delta H°$	lower heating value of hydrogen combustion [J·mol^{-1}]
ε	electrical efficiency
ζ	reaction order oxygen in cathode kinetics
η_{cell}	cell overpotential [V]
η_j	activation overpotential ($j = a, c$) [V]
θ^{la}	maximum angle of contact among the particles in the layer la ($la = af, as, cf,$ cc) [°]
$\kappa_p^{eff,la}$	effective conductivity factor of phase p ($p = ela, elc, io$) in the layer la ($la = af, as, cf, cc$)
λ_{TPB}^{la}	TPB length per unit volume in the layer la ($la = af, as, cf, cc$) [m^{-2}]
μ_j	gas dynamic viscosity ($j = a, c$) [kg·m^{-1}·s^{-1}]
ρ_j	gas density ($j = a, c$) [kg·m^{-3}]
σ_p	conductivity of phase p ($p = ela, elc, io$) [S·m^{-1}]
τ^{la}	tortuosity factor in the layer la ($la = af, as, cf, cc$)
$\tau_{w,j}$	shear–stress factor at the wall ($j = a, c$) [N·m^{-2}]
ϕ^{la}	porosity of the layer la ($la = af, as, cf, cc$)
ψ_{el}	solid volume fraction of electronic phase el ($el = ela, elc$) after sintering

Superscripts

af	anode functional layer
as	anode supporting layer
cc	cathode current collector
cf	cathode functional layer
ey	electrolyte

Subscripts

a	anodic
c	cathodic
e	electron
ela	electron–conducting phase in the anode (e.g., Ni)
elc	electron–conducting phase in the cathode (e.g., LSM)
H2	hydrogen
H2O	water
io	ion–conducting phase (e.g., YSZ)
IN	inlet conditions
N2	nitrogen
O	oxygen ions
O2	oxygen

Abbreviations

LSM	strontium–doped lanthanum manganite
TPB	three–phase boundary length
YSZ	yttria–stabilized zirconia

Acknowledgements

Helpful discussions with Prof. Wolfgang G. Bessler (Offenburg University of Applied Science) and Dr. Dino Klotz (Karlsruhe Institute of Technology – IWE) are gratefully acknowledged. Special thanks to Maxim Ananyev (Institute of High–Temperature Electrochemistry) for providing morphological data on the Jülich cell. The original version of the drop–and–roll packing algorithm was provided by Dr. Jon G. Pharoah (Fuel Cell Research Centre of Kingston – Ontario).

References

[1] S.C. Singhal, Advances in solid oxide fuel cell technology, Solid State Ionics. 135 (2000) 305–313.

[2] J. Larminie, A. Dicks, Fuel Cell Systems Explained, Wiley, New York, 2003.

[3] R.J. Kee, H. Zhu, D.G. Goodwin, Solid-oxide fuel cells with hydrocarbon fuels, Proc. Combust. Inst. 30 (2005) 2379–2404.

[4] S.C. Singhal, K. Kendall, High temperature solid oxide fuel cells: fundamentals, design and applications, Elsevier, Oxford, 2003.

[5] M.C. Williams, J.P. Strakey, W.A. Surdoval, The U.S. Department of Energy, Office of Fossil Energy Stationary Fuel Cell Program, J. Power Sources. 143 (2005) 191–196.

[6] K. Horiuchi, Current status of national SOFC projects in Japan, ECS Trans. 57 (2013) 3–10.

[7] S.D. Vora, SECA program overview and status, ECS Trans. 57 (2013) 11–19.

[8] M. Andersson, J. Yuan, B. Sundén, Review on modeling development for multiscale chemical reactions coupled transport phenomena in solid oxide fuel cells, Appl. Energy. 87 (2010) 1461–1476.

[9] K.N. Grew, W.K.S. Chiu, A review of modeling and simulation techniques across the length scales for the solid oxide fuel cell, J. Power Sources. 199 (2012) 1–13.

[10] R. Bove, S. Ubertini, Modeling solid oxide fuel cell operation: Approaches, techniques and results, J. Power Sources. 159 (2006) 543–559.

[11] H. Zhu, R.J. Kee, V.M. Janardhanan, O. Deutschmann, D.G. Goodwin, Modeling elementary heterogeneous chemistry and electrochemistry in solid-oxide fuel cells, J. Electrochem. Soc. 152 (2005) A2427–A2440.

[12] P. Aguiar, C.S. Adjiman, N.P. Brandon, Anode-supported intermediate temperature direct internal reforming solid oxide fuel cell. I: model-based steady-state performance, J. Power Sources. 138 (2004) 120–136.

[13] V.M. Janardhanan, O. Deutschmann, Numerical study of mass and heat transport in solid-oxide fuel cells running on humidified methane, Chem. Eng. Sci. 62 (2007) 5473–5486.

[14] W.G. Bessler, S. Gewies, M. Vogler, A new framework for physically based modeling of solid oxide fuel cells, Electrochim. Acta. 53 (2007) 1782–1800.

[15] A. Pramuanjaroenkij, S. Kakaç, X. Yang Zhou, Mathematical analysis of planar solid oxide fuel cells, Int. J. Hydrogen Energy. 33 (2008) 2547–2565.

[16] M. Andersson, J. Yuan, B. Sundén, SOFC modeling considering electrochemical reactions at the active three phase boundaries, Int. J. Heat Mass Transf. 55 (2012) 773–788.

[17] P. Costamagna, P. Costa, V. Antonucci, Micro-modelling of solid oxide fuel cell electrodes, Electrochim. Acta. 43 (1998) 375–394.

[18] J.H. Nam, D.H. Jeon, A comprehensive micro-scale model for transport and reaction in intermediate temperature solid oxide fuel cells, Electrochim. Acta. 51 (2006) 3446–3460.

[19] A. Bertei, Chapter 7 of this Thesis, 2013.

[20] B. Kenney, M. Valdmanis, C. Baker, J.G. Pharoah, K. Karan, Computation of TPB length, surface area and pore size from numerical reconstruction of composite solid oxide fuel cell electrodes, J. Power Sources. 189 (2009) 1051–1059.

[21] J. Sanyal, G.M. Goldin, H. Zhu, R.J. Kee, A particle-based model for predicting the effective conductivities of composite electrodes, J. Power Sources. 195 (2010) 6671–6679.

[22] M. Juhl, S. Primdahl, C. Manon, M. Mogensen, Performance/structure correlation for composite SOFC cathodes, J. Power Sources. 61 (1996) 173–181.

[23] T. Tsai, S.A. Barnett, Effect of LSM-YSZ cathode on thin-electrolyte solid oxide fuel cell performance, Solid State Ionics. 93 (1997) 207–217.

[24] V.A.C. Haanappel, J. Mertens, D. Rutenbeck, C. Tropartz, W. Herzhof, D. Sebold, et al., Optimisation of processing and microstructural parameters of LSM cathodes to improve the electrochemical performance of anode-supported SOFCs, J. Power Sources. 141 (2005) 216–226.

[25] D. Kanno, N. Shikazono, N. Takagi, K. Matsuzaki, N. Kasagi, Evaluation of SOFC anode polarization simulation using three-dimensional microstructures reconstructed by FIB tomography, Electrochim. Acta. 56 (2011) 4015–4021.

[26] T. Carraro, J. Joos, B. Rüger, A. Weber, E. Ivers-Tiffée, 3D finite element model for reconstructed mixed-conducting cathodes: I. Performance quantification, Electrochim. Acta. 77 (2012) 315–323.

[27] P.R. Shearing, Q. Cai, J.I. Golbert, V. Yufit, C.S. Adjiman, N.P. Brandon, Microstructural analysis of a solid oxide fuel cell anode using focused ion beam techniques coupled with electrochemical simulation, J. Power Sources. 195 (2010) 4804–4810.

[28] L. Blum, W. a. Meulenberg, H. Nabielek, R. Steinberger-Wilckens, Worldwide SOFC technology overview and benchmark, Int. J. Appl. Ceram. Technol. 2 (2005) 482–492.

[29] M. Mogensen, S. Skaarup, Kinetic and geometric aspects of solid oxide fuel cell electrodes, Solid State Ionics. 86-88 (1996) 1151–1160.

[30] S.B. Adler, Factors governing oxygen reduction in solid oxide fuel cell cathodes., Chem. Rev. 104 (2004) 4791–4843.

[31] J.W. Fergus, Electrolytes for solid oxide fuel cells, J. Power Sources. 162 (2006) 30–40.

[32] J.B. Goodenough, Y.-H. Huang, Alternative anode materials for solid oxide fuel cells, J. Power Sources. 173 (2007) 1–10.

[33] W.. Zhu, S.. Deevi, A review on the status of anode materials for solid oxide fuel cells, Mater. Sci. Eng. A. 362 (2003) 228–239.

[34] S.P. Jiang, Development of lanthanum strontium manganite perovskite cathode materials of solid oxide fuel cells: a review, J. Mater. Sci. 43 (2008) 6799–6833.

[35] A. V. Virkar, J. Chen, C.W. Tanner, J.-W. Kim, The role of electrode microstructure on activation and concentration polarizations in solid oxide fuel cells, Solid State Ionics. 131 (2000) 189–198.

[36] N.H. Menzler, F. Tietz, S. Uhlenbruck, H.P. Buchkremer, D. Stöver, Materials and manufacturing technologies for solid oxide fuel cells, J. Mater. Sci. 45 (2010) 3109–3135.

[37] D. Simwonis, H. Thülen, F.J. Dias, A. Naoumidis, D. Stöver, Properties of Ni/YSZ porous cermets for SOFC anode substrates prepared by tape casting and coat-mix process, J. Mater. Process. Technol. 92-93 (1999) 107–111.

[38] V.A.C. Haanappel, J. Mertens, J. Malzbender, Characterisation of Ni-cermets SOFCs with varying anode densities, J. Power Sources. 171 (2007) 789–792.

[39] B. Kenney, K. Karan, Engineering of microstructure and design of a planar porous composite SOFC cathode: A numerical analysis, Solid State Ionics. 178 (2007) 297–306.

[40] L. Blum, H.-P. Buchkremer, S. Gross, A. Gubner, L.G.J. (Bert) de Haart, H. Nabielek, et al., Solid oxide fuel cell development at Forschungszentrum Juelich, Fuel Cells. 7 (2007) 204–210.

[41] L. Blum, L.G.J. (Bert) de Haart, J. Malzbender, N.H. Menzler, J. Remmel, R. Steinberger-Wilckens, Recent results in Jülich solid oxide fuel cell technology development, J. Power Sources. 241 (2013) 477–485.

[42] Q. Cai, C.S. Adjiman, N.P. Brandon, Investigation of the active thickness of solid oxide fuel cell electrodes using a 3D microstructure model, Electrochim. Acta. 56 (2011) 10809–10819.

[43] Y. Nishida, S. Itoh, A modeling study of porous composite microstructures for solid oxide fuel cell anodes, Electrochim. Acta. 56 (2011) 2792–2800.

[44] A. Abbaspour, J.-L. Luo, K. Nandakumar, Three-dimensional random resistor-network model for solid oxide fuel cell composite electrodes, Electrochim. Acta. 55 (2010) 3944–3950.

[45] D. Chen, Z. Lin, H. Zhu, R.J. Kee, Percolation theory to predict effective properties of solid oxide fuel-cell composite electrodes, J. Power Sources. 191 (2009) 240–252.

[46] W.M. Visscher, M. Bolsterli, Random packing of equal and unequal spheres in two and three dimensions, Nature. 239 (1972) 504–507.

[47] E.M. Tory, B.H. Church, M.K. Tam, M. Ratner, Simulated random packing of equal spheres, Can. J. Chem. Eng. 51 (1973) 484–493.

[48] A. Bertei, Chapter 4 of this Thesis, 2013.

[49] R. Ben Aïm, P. Le Goff, Effet de paroi dans les empilements désordonnés de sphères et application à la porosité de mélanges binaires, Powder Technol. 1 (1968) 281–290.

[50] D. Dong, J. Gao, X. Liu, G. Meng, Fabrication of tubular NiO/YSZ anode-support of solid oxide fuel cell by gelcasting, J. Power Sources. 165 (2007) 217–223.

[51] J.J. Haslam, A.-Q. Pham, B.W. Chung, J.F. DiCarlo, R.S. Glass, Effects of the use of pore formers on performance of an anode supported solid oxide fuel cell, J. Am. Ceram. Soc. 88 (2005) 513–518.

[52] A. Bertei, C. Nicolella, Percolation theory in SOFC composite electrodes: Effects of porosity and particle size distribution on effective properties, J. Power Sources. 196 (2011) 9429–9436.

[53] J.M. Zalc, S.C. Reyes, E. Iglesia, The effects of diffusion mechanism and void structure on transport rates and tortuosity factors in complex porous structures, Chem. Eng. Sci. 59 (2004) 2947–2960.

[54] A. Berson, H.-W. Choi, J.G. Pharoah, Determination of the effective gas diffusivity of a porous composite medium from the three-dimensional reconstruction of its microstructure, Phys. Rev. E. 83 (2011) 026310.

[55] J. Greenwood, The correct and incorrect generation of a cosine distribution of scattered particles for Monte-Carlo modelling of vacuum systems, Vacuum. 67 (2002) 217–222.

[56] A. Einstein, Investigations on the theory of the Brownian movement, Dover, New York, 1926.

[57] H. Zhu, R.J. Kee, Modeling distributed charge-transfer processes in SOFC membrane electrode assemblies, J. Electrochem. Soc. 155 (2008) B715–B729.

[58] S. Gewies, W.G. Bessler, Physically based impedance modeling of Ni/YSZ cermet anodes, J. Electrochem. Soc. 155 (2008) B937–B952.

[59] W.G. Bessler, S. Gewies, Gas concentration impedance of solid oxide fuel cell anodes II. channel geometry, J. Electrochem. Soc. 154 (2007) B548–B559.

[60] M. Andersson, H. Paradis, J. Yuan, B. Sundén, Three dimensional modeling of an solid oxide fuel cell coupling charge transfer phenomena with transport processes and heat generation, Electrochim. Acta. 109 (2013) 881–893.

[61] M. Bertoldi, T. Zandonella, V.A.C. Haanappel, J. Mertens, J. Remmel, L.G.J. de Haart, Demonstration of a 4-Cells SOFC stack under different experimental conditions, J. Fuel Cell Sci. Technol. 5 (2008) 011004.

[62] E.A. Mason, A.P. Malinauskas, Gas transport in porous media: the dusty-gas model, Elsevier, Amsterdam, 1983.

[63] R. Krishna, J.A. Wesselingh, The Maxwell-Stefan approach to mass transfer, Chem. Eng. Sci. 52 (1997) 861–911.

[64] R. Suwanwarangkul, E. Croiset, M.W. Fowler, P.L. Douglas, E. Entchev, M.A. Douglas, Performance comparison of Fick’s, dusty-gas and Stefan–Maxwell models to predict the concentration overpotential of a SOFC anode, J. Power Sources. 122 (2003) 9–18.

[65] B. Todd, J.B. Young, Thermodynamic and transport properties of gases for use in solid oxide fuel cell modelling, J. Power Sources. 110 (2002) 186–200.

[66] J. Mertens, V.A.C. Haanappel, C. Tropartz, W. Herzhof, H.P. Buchkremer, The electrochemical performance of anode-supported SOFCs with LSM-type cathodes produced by alternative processing routes, J. Fuel Cell Sci. Technol. 3 (2006) 125–130.

[67] J. Mertens, V.A.C. Haanappel, C. Wedershoven, H.-P. Buchkremer, Sintering behavior of (La,Sr)MnO_3 type cathodes for planar anode-supported SOFCs, J. Fuel Cell Sci. Technol. 3 (2006) 415–421.

[68] A. Bieberle, L.P. Meier, L.J. Gauckler, The electrochemistry of Ni pattern anodes used as solid oxide fuel cell model electrodes, J. Electrochem. Soc. 148 (2001) A646–A656.

[69] A. Bieberle, L.J. Gauckler, State-space modeling of the anodic SOFC system Ni , H_2–H_2O|YSZ, Solid State Ionics. 146 (2002) 23–41.

[70] W.G. Bessler, A new computational approach for SOFC impedance from detailed electrochemical reaction–diffusion models, Solid State Ionics. 176 (2005) 997–1011.

[71] R. Radhakrishnan, A. V. Virkar, S.C. Singhal, Estimation of charge-transfer resistivity of $La_{0.8}Sr_{0.2}MnO_3$ cathode on $Y_{0.16}Zr_{0.84}O_2$ electrolyte using patterned electrodes, J. Electrochem. Soc. 152 (2005) A210–A218.

[72] F.H. van Heuveln, H.J.M. Bouwmeester, Electrode properties of Sr-doped $LaMnO_3$ on yttria-stabilized zirconia. II. Electrode kinetics, J. Electrochem. Soc. 144 (1997) 134–140.

[73] D.G. Goodwin, H. Zhu, A.M. Colclasure, R.J. Kee, Modeling electrochemical oxidation of hydrogen in Ni-YSZ pattern anodes, J. Electrochem. Soc. 156 (2009) B1004–B1021.

[74] B. De Boer, SOFC Anode: Hydrogen oxidation at porous nickel and nickel/yttria-stabilized zirconia cermet electrodes, University of Twente, The Netherlands, 1998.

[75] J. Mizusaki, H. Tagawa, T. Saito, K. Kamitani, T. Yamamura, K. Hirano, et al., Preparation of nickel pattern electrodes on YSZ and their electrochemical properties in H_2-H_2O atmospheres, J. Electrochem. Soc. 141 (1994) 2129–2134.

[76] A. Bertei, Chapter 3 of this Thesis, 2013.

[77] P. Costamagna, A. Selimovic, M. Del Borghi, G. Agnew, Electrochemical model of the integrated planar solid oxide fuel cell (IP-SOFC), Chem. Eng. J. 102 (2004) 61–69.

[78] B. Morel, J. Laurencin, Y. Bultel, F. Lefebvre-Joud, Anode-supported SOFC model centered on the direct internal reforming, J. Electrochem. Soc. 152 (2005) A1382–A1389.

[79] G. Taylor, Dispersion of soluble matter in solvent flowing slowly through a tube, Proc. R. Soc. London A. 219 (1953) 186–203.

[80] R. Aris, On the dispersion of a solute in a fluid flowing through a tube, Proc. R. Soc. London A. 235 (1956) 67–77.

[81] D. Dutta, A. Ramachandran, D.T.J. Leighton, Effect of channel geometry on solute dispersion in pressure-driven microfluidic systems, Microfluid. Nanofluidics. 2 (2006) 275–290.

[82] J. Yuan, M. Rokni, B. Sundén, Simulation of fully developed laminar heat and mass transfer in fuel cell ducts with different cross-sections, Int. J. Heat Mass Transf. 44 (2001) 4047–4058.

[83] V.A.C. Haanappel, M.J. Smith, A review of standardising SOFC measurement and quality assurance at FZJ, J. Power Sources. 171 (2007) 169–178.

[84] M. Peksen, A coupled 3D thermofluid–thermomechanical analysis of a planar type production scale SOFC stack, Int. J. Hydrogen Energy. 36 (2011) 11914–11928.

[85] J. Joos, M. Ender, I. Rotscholl, N.H. Menzler, A. Weber, E. Ivers-Tiffée, Quantification of Ni/YSZ-anode microstructure parameters derived from FIB-tomography, in: F. Lefebvre-Joud (Ed.), 10th Eur. SOFC Forum, Lucerne - Switzerland, 2012: pp. B0578–B0589.

[86] M. Ananyev, A. Gavrilyuk, D. Bronin, R. Steinberger-Wilckens, J. Mertens, SOFC degradation quantification using image analysis, in: K.A. Friedrich (Ed.), Eur. Fuel Cell Forum 2011, Lucerne - Switzerland, 2011: pp. B0421–B0434.

[87] V.A.C. Haanappel, N. Jordan, A. Mai, J. Mertens, J.M. Serra, F. Tietz, et al., Advances in research, development, and testing of single cells at Forschungszentrum Jülich, J. Fuel Cell Sci. Technol. 6 (2009) 021302.

[88] Q. Cai, C.S. Adjiman, N.P. Brandon, Modelling the 3D microstructure and performance of solid oxide fuel cell electrodes: Computational parameters, Electrochim. Acta. 56 (2011) 5804–5814.

[89] A. Bertei, B. Nucci, C. Nicolella, Effective transport properties in random packings of spheres and agglomerates, Chem. Eng. Trans. 32 (2013) 1531–1536.

[90] V.A.C. Haanappel, A. Mai, J. Mertens, Electrode activation of anode-supported SOFCs with LSM- or LSCF-type cathodes, Solid State Ionics. 177 (2006) 2033–2037.

[91] G.T. Nolan, P.E. Kavanagh, Computer simulation of random packing of hard spheres, Powder Technol. 72 (1992) 149–155.

[92] D.G. Scott, Packing of spheres: Packing of equal spheres, Nature. 188 (1960) 908–909.

[93] A. Bertei, Chapter 2 of this Thesis, 2013.

[94] L. Holzer, D. Wiedenmann, B. Münch, L. Keller, M. Prestat, P. Gasser, et al., The influence of constrictivity on the effective transport properties of porous layers in electrolysis and fuel cells, J. Mater. Sci. 48 (2013) 2934–2952.

[95] D. Wiedenmann, L. Keller, L. Holzer, J. Stojadinović, B. Münch, L. Suarez, et al., Three-dimensional pore structure and ion conductivity of porous ceramic diaphragms, AIChE J. 59 (2013) 1446–1457.

[96] J.H. Yu, G.W. Park, S. Lee, S.K. Woo, Microstructural effects on the electrical and mechanical properties of Ni–YSZ cermet for SOFC anode, J. Power Sources. 163 (2007) 926–932.

[97] J.P. Neidhardt, M. Henke, W.G. Bessler, Kinetic modeling of nickel oxidation is SOFC anodes, ECS Trans. 35 (2011) 1621–1629.

[98] J.P. Neidhardt, R.J. Kee, W.G. Bessler, Electrode reoxidation in solid-oxide cells: detailed modeling of nickel oxide film growth, ECS Trans. 57 (2013) 2573–2582.

[99] A. Leonide, Y. Apel, E. Ivers-Tiffée, SOFC modeling and parameter identification by means of impedance spectroscopy, ECS Trans. 19 (2009) 81–109.

[100] V. Sonn, A. Leonide, E. Ivers-Tiffée, Combined deconvolution and CNLS fitting approach applied on the impedance response of technical Ni⁄8YSZ cermet electrodes, J. Electrochem. Soc. 155 (2008) B675–B679.

[101] M. Vogler, H. Störmer, D. Gerthsen, A. Utz, A. Weber, E. Ivers-Tiffée, et al., Electrochemistry and mechanism of hydrogen oxidation at Ni/YSZ

patterned anodes, in: P. Connor (Ed.), 9th Eur. SOFC Forum, Lucerne - Switzerland, 2010: pp. 0994–09103.

[102] V.A.C. Haanappel, J. Mertens, A. Mai, Performance improvement of (La,Sr)MnO_3 and (La,Sr)(Co,Fe)O_3-type anode-supported SOFCs, J. Fuel Cell Sci. Technol. 3 (2006) 263–270.

[103] R. Steinberger-Wilckens, L. Blum, H.-P. Buchkremer, S. Gross, L.G.J. (Bert) de Haart, K. Hilpert, et al., Overview of the development of solid oxide fuel cells at Forschungszentrum Juelich, Int. J. Appl. Ceram. Technol. 3 (2006) 470–476.

[104] I. Tosun, D. Uner, C. Ozgen, Critical Reynolds number for newtonian flow in rectangular ducts, Ind. Eng. Chem. Res. 27 (1988) 1955–1957.

Chapter 9

Conclusions

This Chapter summarizes the main achievements of the thesis and provides the general conclusions of the study. Possible improvements and further applications of the presented modeling framework are also discussed.

The main points to be highlighted are:

i. the proposed integrated microstructural–electrochemical modeling framework allows a *from–powder–to–power* approach, that is, the prediction of the system performance from the same measurable and controllable parameters used in reality without the need for empirical, fitted of adjusted parameters;

ii. the framework allows the physically–based interpretation of experimental observations, such as the strong coupling between electrochemical behavior and morphological characteristics, and can be used as a tool to optimize the SOFC design;

iii. the models can be extended to take into account microstructure evolution (i.e., functional degradation of the electrodes), heat balance and mixed ionic–electronic conducting materials at the electrodes.

9.1 Survey of main results

This thesis presented an integrated modeling framework to describe the interaction between microstructure and electrochemical behavior of SOFCs. Several modeling tools at the microstructural and electrochemical cell levels were developed, combined and applied, showing that the models can quantitatively reproduce the strong coupling between the morphological characteristics of the electrodes and the electrochemical behavior of the whole fuel cell system.

At the microstructural level, several particle–based algorithms able to numerically reconstruct the three–dimensional microstructure of porous electrodes were presented and discussed. These algorithms were developed to take into account the main morphological features of SOFC electrodes, such as the polydispersion of particle size and, more importantly, the effects of sintering phenomena, which cause the densification of the structure through particle overlap and the formation of additional pores when pore–former particles are introduced.

Packing algorithms were adopted in this thesis to simulate conventional porous electrodes (Chapter 4) and nanostructured electrodes (Chapter 6) under the assumption that particles were spherical. A more general packing algorithm, able to reconstruct random packings of nonspherical particles, was proposed in Chapter 5 in order to take into account specific features which may arise in SOFC electrodes, such as particle agglomeration and the distortion of particle shape from the spherical one. A Monte Carlo random–walk method (Chapter 7) was developed in order to calculate the effective transport properties (e.g., effective conductivity, tortuosity factor) and the specific geometric properties (e.g., three–phase boundary length, mean pore size) of the reconstructed electrodes.

Using this approach, all the main morphological features and electrode architectures could be properly simulated. Quantitative information, such as percolation thresholds, three–phase boundary length and effective transport properties, could be accurately predicted. In addition, the approach allowed the substantial reduction, if not the elimination, of free parameters, avoiding the need for empirical correlations or the use of percolation models, both of which were found to provide limited information (Chapter 4) or inaccurate predictions (Chapter 3) if compared with detailed particle–based models.

The microstructural models were specifically validated in Chapter 7 against well–characterized experimental data. Effective transport properties in both gas (i.e., permeability) and solid phase (i.e., effective conductivity) of random packings of sintered spherical particles were predicted and compared with experimental measurements in a wide range of porosity. The excellent agreement found for both gas and solid phase properties without any fitted or adjusted parameter attested the soundness of the proposed particle–based models.

Electrochemical models were developed at both electrode level for button cell configuration (Chapters 2, 3 and 7) and at cell level to simulate the behavior of a cell within a stack (Chapter 8). A physically–based approach was considered, consisting of mass and charge balances applied within the membrane–electrode assembly and the feeding channels. The transport of gaseous and charged species in porous media as well as the reaction at the contact points between different conducting phases were considered through mechanistic models, as an example the dusty–gas model to describe convention and diffusion (both ordinary and Knudsen diffusion) of gas species within the pores of the electrodes. The mechanistic approach was found to be applicable for conventional materials commonly used for high temperature fuel cells and also for unconventional SOFC configurations (Chapter 3).

The solution of model equations provided the steady–state and the transient electrochemical behavior of the electrode or the cell. The steady–state response was useful to evaluate the system efficiency and to assess how different phenomena contributed to affect the SOFC performance, such as the effects of mass transfer limitations discussed in Chapters 7 and 8. Dynamic simulations, performed to reproduce impedance spectra, allowed a physical interpretation of experimental results and the identification of basic processes occurring at microscopic scale as in Chapter 2. In addition, the knowledge of the local distribution of field variables (e.g., concentrations, electric potentials, pressure), which are not available experimentally, made the model capable to provide a closer understanding of all the microscopic processes occurring in the system, thus proving information regarding kinetic aspects (Chapter 2), active thicknesses (Chapters 2 and 8) and limiting factors (Chapter 7).

Microstructural and electrochemical models were integrated at both electrode (Chapter 7) and cell (Chapter 8) levels, providing a modeling framework able to describe the coupling between morphological characteristics and electrochemical behavior. The approach was validated in Chapter 8, showing that the integrated model was capable to reproduce and predict the macroscopic behavior of an SOFC stack produced by the Forschungszentrum Jülich, which nowadays represents a worldwide benchmark, in a wide range of operating conditions without the need for fitted parameters.

9.2 General conclusions

The main goal of the thesis consisted in the integration of the microstructural modeling into the mechanistic description of reaction and transport phenomena at electrode and cell level. This integration allowed us to build a modeling framework *from–powder–to–power*, that is, capable to reproduce and predict the SOFC macroscopic response, such as the current–voltage relationship, from the knowledge of powder characteristics and operating conditions, which are the same measurable and controllable parameters available in reality.

Within this framework, no empirical, fitted or adjustable parameters are required, feature which makes the modeling tool widely applicable in a broad range of conditions. In particular, the microstructural and the electrochemical models developed are sufficiently general to quantitatively reproduce all the main electrode configurations, morphological features and conducting materials currently adopted for SOFC applications.

The integrated microstructural–electrochemical model is fully predictive and does not require real samples. When specific measurements are available, the model can be used as an interpretative tool of experimental data, otherwise it can be applied as a design tool to improve the cell performance by optimizing the geometrical and microstructural parameters.

The thesis showed that there is a strong coupling between electrode microstructure and cell electrochemical behavior: morphological characteristics may affect the system performance more significantly than some material properties or operating conditions. Only a model capable to reproduce such a strong coupling can provide quantitative information and sound predictions. By using the proposed modeling framework, the cell performance can be substantially improved by optimizing the electrode microstructure and taking into account the influence on the all processes occurring at the microscopic scale.

9.3 Outlook

The integrated microstructural–electrochemical models proposed in this thesis provide a sound and validated basis for the mechanistic description of solid oxide fuel cells, from the microstructural to the cell level, and for the prediction of system performance for a wide variety of operating conditions and electrode architectures. However, in the framework of multi–scale modeling and due to inherent complexity of SOFCs, further improvements and integrations are still possible.

The most significant aspect to be added to the model is the description of the microstructural modifications of the electrode microstructure occurring during operation, such as grain growth, coarsening and agglomeration of particles. To date these phenomena are supposed to be the main processes which lead to performance degradation and limit the lifetime of SOFCs. The modeling of the electrode microstructural evolution can be included into the particle–based models presented in this thesis by applying discrete element methods or kinetic Monte Carlo methods. Comparison of the numerically reconstructed microstructures with samples analyzed through computer tomography will assess the validity of the numerical models. Then, coupling the electrochemical models will allow the prediction of the temporal evolution of the cell performance, providing a rapid alternative to long–term ageing tests.

An important improvement concerns the introduction of the heat balance in the cell electrochemical model, with corresponding effective thermal conductivities evaluated through the Monte Carlo random–walk method. To date, the effective thermal properties of porous electrodes are evaluated using empirical correlations which usually overestimate the effective thermal conductivity. With the heat balance, also the temperature distribution throughout the cell will be predictable. This information be useful to assess the arise of thermal stresses and to investigate the effects of temperature gradients on the electrochemistry. The solution of the heat balance will also provide the outputs necessary to integrate the model in process simulators in order to evaluate the thermal efficiency of the fuel cell system.

Finally, the model can be extended to take into account mixed ionic–electronic conductors instead of composite electrodes, making it attractive for the next generation of intermediate temperature SOFCs. In practice, the extension will concern only a modification of the reaction kinetics and of the charge transport model, therefore it could be easily accommodated.